

*Surface-Compartmentalized  
worm-like Crystalline-Core Micelles:  
Preparation and Applications*

Doctoral Thesis

submitted to obtain the academic degree of Doctor of Natural Sciences  
(Dr. rer. nat.) of the Bayreuth Graduate School of Mathematical and Natural  
Sciences (BayNAT) of the University of Bayreuth

*Christian Hils*

from *Rottweil*

Bayreuth, 2021



This doctoral thesis was prepared at the department of Macromolecular Chemistry II at the University of Bayreuth from November 2018 until August 2021 and was supervised by Prof. Dr. Andreas Greiner.

This is a full reprint of the thesis submitted to obtain the academic degree of Doctor of Natural Sciences (Dr. rer. nat.) and approved by the Bayreuth Graduate School of Mathematical and Natural Sciences (BayNAT) of the University of Bayreuth.

Date of submission: 26<sup>th</sup> August 2021

Date of defence: 17<sup>th</sup> March 2022

Acting director: Prof. Dr. Hans Keppler

Doctoral committee:

Prof. Dr. Andreas Greiner	(reviewer)
Prof. Dr. Mukundan Thelakkat	(reviewer)
Prof. Dr. Birgit Weber	(chairman)
Prof. Dr. Markus Retsch	



*Wer aufhört, besser zu werden, hat aufgehört, gut zu sein.*

*Philip Rosenthal*



---

## Table of Contents

<b>List of Publications</b>	<b>III</b>
<b>Summary</b>	<b>V</b>
<b>Zusammenfassung</b>	<b>IX</b>
<b>1. Introduction</b>	<b>1</b>
1.1 Crystallization-Driven Self-Assembly	1
1.2 Surface-Compartmentalized Micelles	5
1.2.1 Patchy Micelles	6
1.2.2 Block Co-Micelles	11
1.2.3 Janus Micelles	13
1.2.4 Application of Surface-Compartmentalised Micelles	16
1.3 Objective of the Thesis	19
1.4 References	21
<b>2. Thesis Overview</b>	<b>31</b>
2.1 Influence of Patch Size and Chemistry on the Catalytic Activity of Patchy Hybrid Nonwovens	32
2.2 Converting Poly(Methyl Methacrylate) into a Triple-Responsive Polymer	35
2.3 Hierarchical Superstructures by Combining Crystallization-Driven and Molecular Self-Assembly	37
2.4 Frustrated Microparticle Morphologies of a Semicrystalline Triblock Terpolymer in 3D Soft Confinement	39
2.5 Janus or Patchy: Who Wins the Battle in Crystallization-Driven Self-Assembly of Double Crystalline Triblock Terpolymers?	43
2.6 Individual Contributions to Joint Publications	45

<b>3. Influence of Patch Size and Chemistry on the Catalytic Activity of Patchy Hybrid Nonwovens</b>	<b>49</b>
<b>4. Converting Poly(Methyl Methacrylate) into a Triple-Responsive Polymer</b>	<b>95</b>
<b>5. Hierarchical Superstructures by Combining Crystallization-Driven and Molecular Self-Assembly</b>	<b>121</b>
<b>6. Frustrated Microparticle Morphologies of a Semicrystalline Triblock Terpolymer in 3D Soft Confinement</b>	<b>143</b>
<b>7. Janus or Patchy: Who Wins the Battle in Crystallization-Driven Self-Assembly of Double Crystalline Triblock Terpolymers?</b>	<b>177</b>
<b>8. Outlook</b>	<b>197</b>
<b>Glossary</b>	<b>199</b>
<b>Acknowledgement</b>	<b>203</b>
<b>Appendix</b>	<b>205</b>
<b>(Eidestättliche) Versicherung und Erklärung</b>	<b>251</b>

## List of Publications

1. Hils, C., Dulle, M., Sitaru, G., Gekle, S., Schöbel, J., Frank, A., Drechsler, M., Greiner A., Schmalz, H.  
**Influence of Patch Size and Chemistry on the Catalytic Activity of Patchy Hybrid Nonwovens**  
*Nanoscale Adv.*, **2020**, *2*, 438-452.
2. Hils, C., Fuchs, E., Eger, F., Schöbel, J., Schmalz, H.  
**Converting Poly(Methyl Methacrylate) into a Triple-Responsive Polymer**  
*Chem. Eur. J.*, **2020**, *26*, 5611 – 5614.
3. Göbel, C., Hils, C., Drechsler, M., Baabe, D., Greiner, A., Schmalz, H., Weber, B.  
**Confined Crystallization of Spin-Crossover Nanoparticles in Block-Copolymer Micelles**  
*Angew. Chem. Int. Ed.*, **2020**, *59*, 5765-5770.
4. Verkoyen, P., Dreier, P., Bros, M., Hils, C., Schmalz, H., Seiffert, S., Frey, H.  
**"Dumb" pH-Independent and Biocompatible Hydrogels Formed by Copolymers of Long-Chain Alkyl Glycidyl Ethers and Ethylene Oxide**  
*Biomacromolecules*, **2020**, *21*, 3152-3162.
5. Dai, X., Qiang, X., Hils, C., Schmalz, H., Gröschel, A. H.  
**Frustrated Microparticle Morphologies of a Semicrystalline Triblock Terpolymer in 3D Soft Confinement**  
*ASC Nano*, **2021**, *15*, 1111-1120.

6. Hils, C., Manners, I., Schöbel, J., Schmalz, H.  
**Crystalline-Core Patchy Micelles: Self-Assembly Concepts, Properties and Applications**  
*Polymers*, **2021**, *13*, 1481.
  
7. Frank, A., Hils, C., Weber, M., Kreger, K., Schmalz, H., Schmidt, H. W.  
**Hierarchical Superstructures by Combining Crystallization-Driven and Molecular Self-Assembly**  
*Angew. Chem. Int. Ed.*, **2021**, DOI: 10.1002/anie.202105787

## Summary

Crystallization-driven self-assembly (CDSA) of block copolymers with one crystallizable block has emerged as an outstanding method for the preparation of worm-like crystalline-core micelles (*w*CCMs) with tailored properties. The use of ABC triblock terpolymers with a semi-crystalline core-forming polyethylene (PE) middle block and incompatible end blocks of polystyrene (PS) and poly(methyl methacrylate) (PMMA) or poly(*N,N*-dialkylaminoethyl methacrylamides) (PDxA, alkyl = methyl, *iso*-propyl) leads to a patch-like microphase-separated corona, resulting in so-called patchy *w*CCMs. These micelles are characterized by an excellent interfacial activity and can be used as efficient templates for the embedding of nanoparticles or as hybrids in heterogeneous catalysis due to their functional corona patches.

Based on these highly promising properties, this doctoral thesis addressed the preparation as well as functionalization of surface-compartmentalized micelles with a semi-crystalline PE core, with the aim to exploit new applications for these interesting materials.

First, the influence of patch size and chemistry on the catalytic activity of gold nanoparticle (AuNP) loaded patchy hybrid nonwovens in the alcoholysis of silanes was studied. The patchy hybrid nonwovens were produced by coaxial electrospinning, employing PS as core and patchy *w*CCMs with functional PDxA patches in the corona, followed by loading with preformed citrate-stabilized AuNPs. Here, the accessibility of the patches for the reactants, i.e., its swellability in the employed solvent (*n*-butanol), turned out as the most decisive factor, resulting in a pronounced induction period and longer reaction times in the first catalysis cycles and for the more polar PDMA patches, respectively. Besides, even after 10 consecutive cycles no loss of catalytic activity occurred, demonstrating the excellent reusability of this catalysis system.

Moreover, solubility studies on PDxA homopolymers (*x* = methyl, ethyl or *iso*-propyl) in aqueous media of different pH revealed a double responsive behaviour (pH and temperature) that can be tuned by varying the alkyl substituents at the tertiary amino-groups. While PDMA is soluble over a broad pH and temperature range, PDEA and PDiPA show a pH dependent LCST (lower critical solution temperature)-type phase behaviour. Solubility can also be switched reversibly by CO<sub>2</sub>, and multivalent counter anions can induce a simultaneous LCST-

and UCST (upper critical solution temperature)-type behaviour upon proper choice of pH. Notably, the investigated PDxA homopolymers were produced by post polymerization amidation of PMMA and can even be employed on bulk PMMA samples for surface functionalization, showing that this approach is widely applicable to PMMA and respective block copolymers to introduce stimuli-responsivity in a highly efficient and facile way.

A new concept for the construction of hierarchical superstructures was developed, harnessing the well-defined patch functionality (tertiary amino-groups) of patchy fibres produced by coaxial electrospinning. The functional patches can initiate the molecular self-assembly of a benzene-1,3,5-tricarboxamide (BTA) from the surface of the fibres to yield a fir tree-like superstructure, where the patchy fibres form the core (branch) and the BTA assemblies the respective needles. A prerequisite for the formation of defined superstructures by this combination of CDSA with molecular self-assembly is the chemical match between the tertiary amino-groups in the surface patches of the fibres and the periphery of the BTA.

Amphiphilic worm-like Janus micelles with a superior interfacial activity could be realised by CDSA using a PS-*b*-PE-*b*-PEO (PEO = poly(ethylene oxide)) triblock terpolymer. Here, the strong incompatibility of the two end blocks combined with the ability of the PEO corona to crystallize is the key for the formation of a Janus-type corona instead of the entropically more favoured patchy structure. The presence of a Janus-type corona was proven by transmission electron microscopy studies using staining agents of different selectivity with respect to the PS and PEO corona blocks. In addition, the Janus micelles showed a distinct different morphology compared to that of  $w$ CCMs with a patchy PS/PMMA corona after dialysis in a non-solvent for the PS blocks.

Finally, CDSA of PS-*b*-PE-*b*-PMMA triblock terpolymers in the confinement of emulsion droplets (toluene in water) followed by solvent evaporation opens a new way toward internally structured microparticles. Controlling the interplay between CDSA and microphase separation allows to direct self-assembly to yield different well-defined morphologies. If CDSA to patchy  $w$ CCMs occurs simultaneously to solvent evaporation, lenticular microparticles with a compartmentalized hexagonal cylinder lattice were formed. If, however, solvent evaporation takes place first at elevated temperatures (CDSA is hindered), differently oriented lamellar morphologies (e.g., bud-like, double staircase, spherocone) can arise because of microphase separation taking place prior to crystallization. Hence, upon cooling, the PE block can only

crystallize within the confinement of the lamellar morphology, being preformed upon solvent evaporation.

This doctoral thesis shows the enormous potential of CDSA for the preparation of patchy and Janus micelles and further fields of application for these surface-compartmentalized micelles could be opened. Additionally, other exciting applications are conceivable, as will be explained in the chapter outlook.



## Zusammenfassung

Die kristallisationsgetriebene Selbstassemblierung (engl. „*crystallization-driven self-assembly*“, CDSA) von Blockcopolymeren mit einem kristallisierbaren Block hat sich als herausragende Methode für die Herstellung von wurmartigen Mizellen mit kristallinem Kern (*wCCMs*) erwiesen. Die Verwendung von ABC-Triblockterpolymeren mit einem teilkristallinen kernbildenden Mittelblock aus Polyethylen (PE) und inkompatiblen Endblöcken aus Polystyrol (PS) und Polymethylmethacrylat (PMMA) oder Poly(*N,N*-dialkylaminoethylmethacrylamiden) (PDxA, Alkyl = Methyl, *iso*-Propyl) führt zu einer patch-artigen, mikrophasenseparierten Corona, sogenannten „patchy“ *wCCMs*. Diese Mizellen zeichnen sich durch eine ausgezeichnete Grenzflächenaktivität aus und können, aufgrund ihrer funktionellen Corona-Struktur, als effizienter Träger für die Fixierung von Nanopartikeln oder in Form von Hybriden in der heterogenen Katalyse verwendet werden.

Basierend auf diesen vielversprechenden Eigenschaften befasste sich diese Doktorarbeit mit der Herstellung und Funktionalisierung von oberflächenkompartimentierten Mizellen mit einem teilkristallinen PE-Kern, um neue Anwendungen für diese interessanten Materialien zu erschließen.

Zunächst wurde der Einfluss der Mizellengröße und der chemischen Zusammensetzung in Hinblick auf die katalytische Aktivität von mit Goldnanopartikeln (AuNP) beladenen patchy Hybridfasermatten bei der Alkoholyse von Silanen untersucht. Die patchartig oberflächenstrukturierten Hybridfasermatten wurden durch koaxiales Elektrosponnen hergestellt, wobei PS als Kern und patchy Mizellen mit funktionellen PDxA-Domänen in der Corona verwendet wurden, gefolgt von der Beladung mit vorgeformten Citrat-stabilisierten AuNP. Dabei erwies sich die Zugänglichkeit für die Reaktanten, welche auf das Quellverhalten der Ketten (PDxA) im verwendeten Lösungsmittel (*n*-Butanol) zurückzuführen ist, als entscheidender Faktor. Dies führte in den ersten Katalysezyklen bzw. für die polareren PDMA-Domänen zu einer ausgeprägten Induktionszeit und längeren Reaktionszeiten. Außerdem trat auch nach zehn aufeinanderfolgenden Zyklen kein Verlust der katalytischen Aktivität auf, was die ausgezeichnete Wiederverwendbarkeit und effektive Fixierung der AuNP dieses Katalysesystems belegt.

Darüber hinaus ergaben Löslichkeitsstudien an PDxA-Homopolymeren (x = Methyl, Ethyl oder *iso*-Propyl) in wässrigen Medien mit unterschiedlichem pH-Wert eine doppelte Stimuliabhängigkeit (pH und Temperatur), welche durch Variation der Alkylsubstituenten an den tertiären Aminogruppen eingestellt werden kann. Während PDMA über einen breiten pH- und Temperaturbereich löslich ist, zeigen PDEA und PDiPA ein pH-abhängiges LCST-Phasenverhalten (engl. „*lower critical solution temperature*“). Die Löslichkeit kann ebenso durch Kohlenstoffdioxid reversibel verändert werden. Mehrwertige Gegenanionen können bei geeigneter Wahl des pH-Werts ein gleichzeitiges LCST- und UCST-Verhalten (engl. „*upper critical solution temperature*“) hervorrufen. Die untersuchten PDxA Homopolymere wurden durch Amidierung von PMMA (polymeranalog) hergestellt: Ferner konnte diese Methode sogar auf eine PMMA-Scheibe angewendet werden, was sich in einer Oberflächenfunktionalisierung widerspiegelte. Dieser Ansatz zeigt, dass auf hocheffiziente und einfache Weise Stimuli-Responsivität in PMMA und entsprechende Blockcopolymere eingefügt werden kann.

Des Weiteren wurde ein neues Konzept für den Aufbau hierarchischer Überstrukturen entwickelt, bei dem die gut definierte Funktionalität der Korona-Domänen (tertiäre Aminogruppen) der mittels koaxialem Elektrosplennen hergestellten patchy Fasern genutzt wird. Die funktionellen Bereiche sind dabei in der Lage die molekulare Selbstorganisation eines 1,3,5-Benzoltricarboxamids (BTA) von der Oberfläche der Fasern aus zu initiieren, um eine tannenbaumartige Überstruktur zu erhalten. Dabei bilden die patchy Fasern den Kern (Ast) und die assemblierten BTA-Strukturen die jeweiligen Nadeln. Eine Voraussetzung für die Bildung dieser definierten Überstrukturen, die durch Kombination von CDSA und molekularer Selbstorganisation entstanden sind, ist die chemische Übereinstimmung der tertiären Aminogruppen in den Korona-Domänen der verwendeten Mizellen, welche sich an der Oberfläche der Fasern und den Seitenarmen des BTA befinden.

Amphiphile, wurmartige Janus-Mizellen mit einer ausgezeichneten Grenzflächenaktivität konnten durch CDSA unter Verwendung eines PS-*b*-PE-*b*-PEO (PEO = Polyethylenoxid) Triblockterpolymers realisiert werden. Hier ist die starke Inkompatibilität der beiden Endblöcke, in Kombination mit der Möglichkeit der Kristallisation der PEO-Korona, der Schlüssel für die Ausbildung einer janusartigen Korona anstelle der entropisch günstigeren patchartigen Struktur. Die Existenz einer Janus-Korona wurde durch transmissionselektronenmikroskopische Untersuchungen, unter Verwendung von Kontrastiermitteln mit unterschiedlicher Selektivität in Bezug auf die PS- und PEO-Domänen der Korona, nachgewiesen.

Ergänzend zeigten die Janus-Mizellen nach der Dialyse in einem Nicht-Lösungsmittel für die PS-Blöcke eine deutlich abweichende Morphologie zu den  $w$ CCMs mit patchartiger PS/PMMA-Korona.

Darüber hinaus eröffnet die CDSA von PS-*b*-PE-*b*-PMMA-Triblockterpolymeren, welche in Emulsionströpfchen (Toluol in Wasser) eingeschlossen sind, einen neuen Weg zu intern strukturierten Mikropartikeln durch die Verdampfung des Lösungsmittels. Mit Hilfe der Steuerung des Zusammenspiels zwischen CDSA und Mikrophasentrennung kann die Selbstorganisation so gesteuert werden, dass verschiedene wohldefinierte Morphologien entstehen. Erfolgt die CDSA zu patchy  $w$ CCMs gleichzeitig mit der Verdampfung des Lösungsmittels, so bilden sich linsenförmige Mikropartikel mit kompartimentierten hexagonalen Zylindergittern aus. Findet jedoch zuerst die Lösungsmittelverdampfung bei höheren Temperaturen statt, wodurch die CDSA behindert wird, können durch die vor der Kristallisation stattfindende Mikrophasentrennung unterschiedlich orientierte lamellare Morphologien (z. B. knospenartig, Doppeltreppe, Sphärokon) entstehen. Aufgrund dessen kann der PE-Block beim Abkühlen nur innerhalb der begrenzten lamellaren Morphologie kristallisieren.

Diese Dissertation zeigt das enorme Potenzial der CDSA, in Hinblick auf die Herstellung von patchartigen und Janus-Mizellen, auf. Weitere Anwendungsfelder für diese oberflächenkompartimentierten Mizellen konnten dabei erschlossen werden. Darüber hinaus werden mehrere potenzielle Anwendungen im Kapitel „*Outlook*“ erläutert.



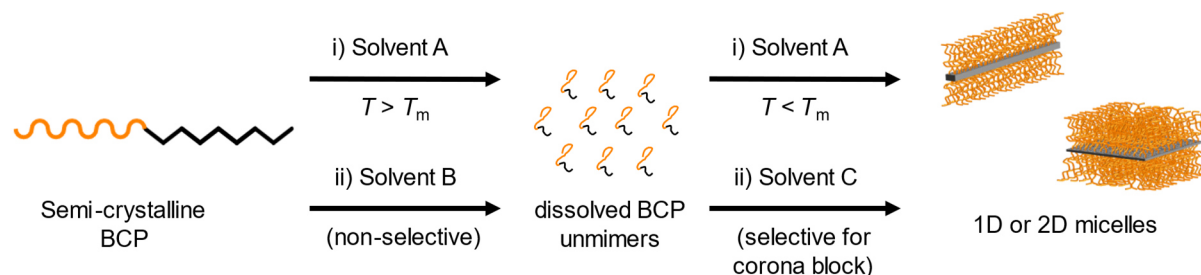
# 1 Introduction

## 1.1 Crystallization-Driven Self-Assembly

The discovery of living anionic polymerization by *Szwarc* opened the way toward well-defined block copolymers (BCPs) in the 1950s.<sup>[1,2]</sup> The first self-assembly studies based on polystyrene-*block*-poly(methyl methacrylate) (PS-*b*-PMMA) BCPs in solution were reported in the 1960s.<sup>[3,4]</sup> Since then, focus was mainly laid on the self-assembly of amorphous coil-coil BCPs in selective solvents. Only a few reports dealt with crystalline-coil BCPs employing poly(ethylene oxide) (PEO) as crystallizable core-forming block.<sup>[5,6]</sup> A theoretical description of self-assembly of crystalline-coil BCPs was given in 1991.<sup>[7]</sup> Anisotropic micellar structures based on crystalline-coil BCPs, such as one-dimensional (1D) fibre-like micelles<sup>[8]</sup> or two-dimensional (2D) platelets<sup>[7,9–11]</sup>, were first realised in the late 1990s. In 2000, the creation of micellar nanoparticles (NPs) with non-spherical 1D or 2D morphologies was unequivocally demonstrated by comparative solution self-assembly studies of BCPs with crystallizable poly(ferrocenyl dimethylsilane) (PFS) segments and related BCPs with amorphous core-forming blocks by *Manners* and *Winnik* et al.<sup>[12,13]</sup> BCP self-assembly processes in which core crystallization plays a dominant role and serves as additional strong driving force for micelle formation are now commonly referred to as crystallization-driven self-assembly (CDSA).<sup>[14–16]</sup> Studies on CDSA of crystallizable BCPs in selective solvents have significantly gained importance in the past two decades. Here, mainly cylindrical or platelet-like micelles were described, employing semi-crystalline or liquid crystalline core-forming blocks such as PFS,<sup>[8,17–19]</sup> poly(ferrocenyl methylsilane),<sup>[20]</sup> poly(ferrocenyl diethylsilane),<sup>[21]</sup> poly(ferrocenyl dimethylgermane) (PFG),<sup>[22]</sup> other polymetallocenes,<sup>[23,24]</sup> polyethylene (PE),<sup>[25–35]</sup> syndiotactic polypropylene,<sup>[36]</sup> PEO,<sup>[37–39]</sup> oligo(ethylene sulfide),<sup>[40,41]</sup> polyesters (poly( $\epsilon$ -caprolactone) or poly(*L*-lactide) (PLLA)),<sup>[42–51]</sup> polycarbonate,<sup>[52]</sup> poly(2-*iso*-propyl-2-oxazoline),<sup>[52]</sup> polyacrylonitrile,<sup>[53]</sup> liquid crystalline polymers,<sup>[54–56]</sup> and various conjugated polymers (e.g. poly(3-hexyl thiophene) (P3HT) and oligo(*p*-phenylene vinylene) (OPV))<sup>[57–62]</sup>.

The two common procedures for the preparation of 1D and 2D micelles using CDSA are temperate or non-solvent induced crystallization (Scheme 1.1). The first approach requires a solvent that is a good solvent for both blocks at temperatures above the melting temperature of the semi-crystalline core-forming block ( $T > T_m$ ) and selective for the corona block at  $T < T_m$ .

Consequently, molecularly dissolved BCP chains are obtained at  $T > T_m$ . Cooling to or below the crystallization temperature ( $T_c$ ) of the semi-crystalline block leads to its insolubility and crystallization starts. In the second method, the BCP is dissolved in a non-selective solvent. Next, the molecularly dissolved unimers are added to a selective solvent for the corona block. This leads to a collapse of the core-forming block and induces CDSA. Generally, this approach leads to the formation of polydisperse fibrous or platelet-like micelles.<sup>[63]</sup>



**Scheme 1.1.** General procedures employed for the preparation of micelles with crystalline cores *via* CDSA. Dissolving the semi-crystalline BCP in a (i) selective solvent or (ii) non-selective solvent leads to unimers at  $T > T_m$ . After cooling ( $T < T_m$ ) or addition to a selective solvent for the corona block crystallization towards 1D or 2D micelles occurs.

The preparation of well-defined 1D or 2D assemblies with controlled dimension, narrow size distribution, and tailored corona structures can be achieved by the so-called living CDSA.<sup>[13,16,63–65]</sup> Similar to the living polymerisation of monomers, CDSA can be performed in a living manner. For this procedure small micellar fragments, the so-called seeds, are used in analogy to initiators for living polymerization processes. In order to obtain these micellar fragments, polydisperse cylindrical micelles are produced using conventional CDSA. These micelles are fragmented by ultrasound to obtain the seeds. Because of this technique, the seed micelles are also termed "stub-like" micelles. Afterwards, unimers are added to these seed micelles and aged for 5 days to obtain uniform fibres (Figure 1.1a). Figures 1.1b-e show transmission electron microscopy (TEM) images of cylindrical micelles prepared from poly(*L*-lactide)-*block*-poly(*N*-isopropylacrylamide) (PLLA-*b*-PNIPAm) BCPs employing different unimer/seed ratios. The length of the cylindrical micelles increases with the unimer/seed ratio (Figure 1.1f) and, notably, shows a linear dependence on the unimer/seed ratio owing to the living character of this method (Figure 1.1g). Analogously to the molecular weight dispersity in living polymerisation techniques, the length dispersity for living CDSA is very low ( $L_w/L_n$  typically well below 1.1; where  $L_n$  is the number-average and  $L_w$  the weight-average of the micelle length).

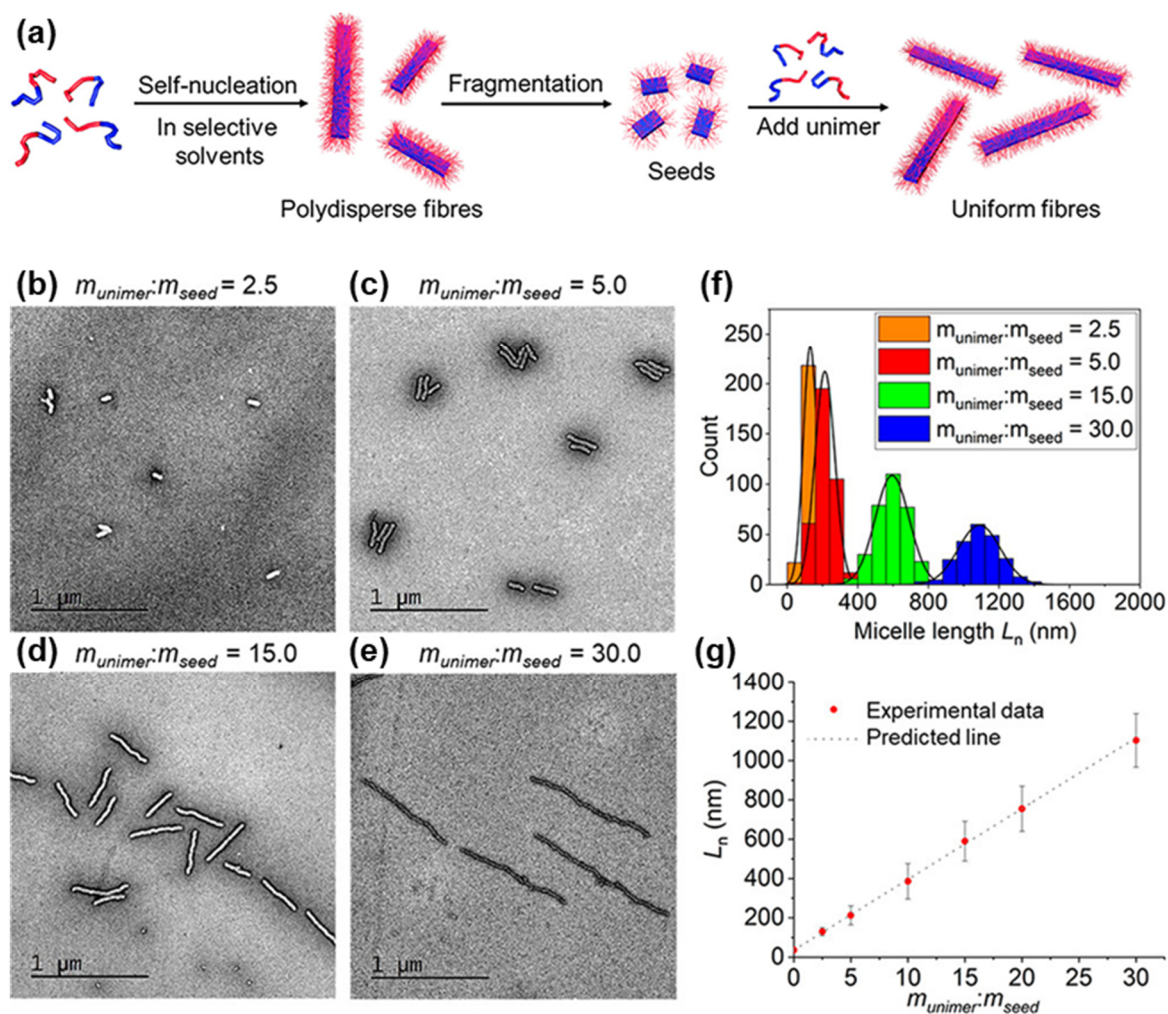
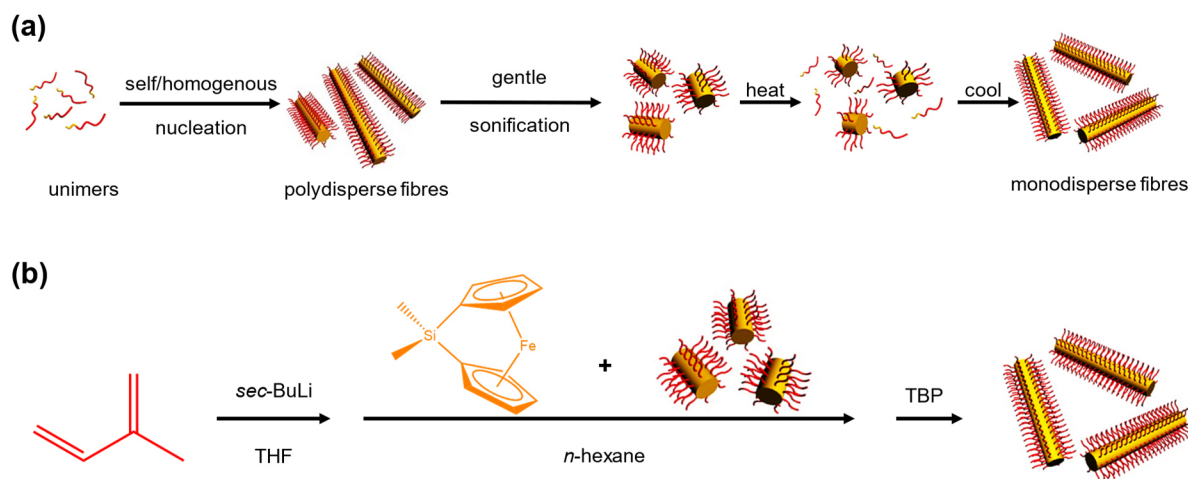


**Figure 1.1.** (a) Schematic representation of the preparation of uniform fibres by living CDSA applying a seeded-growth method. TEM micrographs of samples (aged for 5 days) of uniform PLLA<sub>47</sub>-*b*-PNIPAm<sub>267</sub> (index denotes the number average degree of polymerization) micelles prepared by seeded growth from seed micelles ( $L_n = 36$  nm,  $L_w/L_n = 1.10$ ,  $\sigma/L_n: 0.26$ ) in 2,2,2-trifluoroethanol/ethanol with unimer-to-seed mass ratios of (b) 2.5, (c) 5.0, (d) 15.0, and (e) 30.0, respectively. (f) Contour length histograms of micelle length distributions for the different applied unimer/seed ratios; (g) plot of number-average micelle length vs.  $m_{\text{unimer}}/m_{\text{seed}}$  (the error bars represent the standard deviation). TEM samples were stained with uranyl acetate. Reproduced from Ref. [49] (Copyright 2019) with permission of the *American Chemical Society*.

Living CDSA can also be realized with spherical crystalline-core micelles (sCCMs)<sup>[25]</sup> as seeds or by self-seeding.<sup>[54,66,67]</sup> The latter approach also uses small micellar fragments which are heated in dispersion to a specific annealing temperature ( $T_a$ ). At this temperature the crystalline cores are almost completely molten/dissolved and only a few crystallites survive and act as seeds in the subsequent CDSA upon cooling (Scheme 1.2a). Hence, the length of the micelles can be controlled by a proper choice of  $T_a$ . If  $T_a$  is too high, the crystalline cores will melt/dissolve completely and no crystallites could act as seeds. On the other hand, if  $T_a$  is too

low the crystalline cores will not melt/dissolve and the length distribution of the employed micellar fragments remains rather disperse. Consequently, between these two limiting cases an increase in micelle length is observed with increasing  $T_a$  as the proportion of surviving crystallites decreases accordingly. The excellent control over size and size distribution in living CDSA opened the way to the construction of complex micellar assemblies such as branched micelles,<sup>[68]</sup> platelet-shaped micelles and comicelles,<sup>[45,69–73]</sup> or patchy and block comicelles<sup>[25,64,74–77]</sup>.

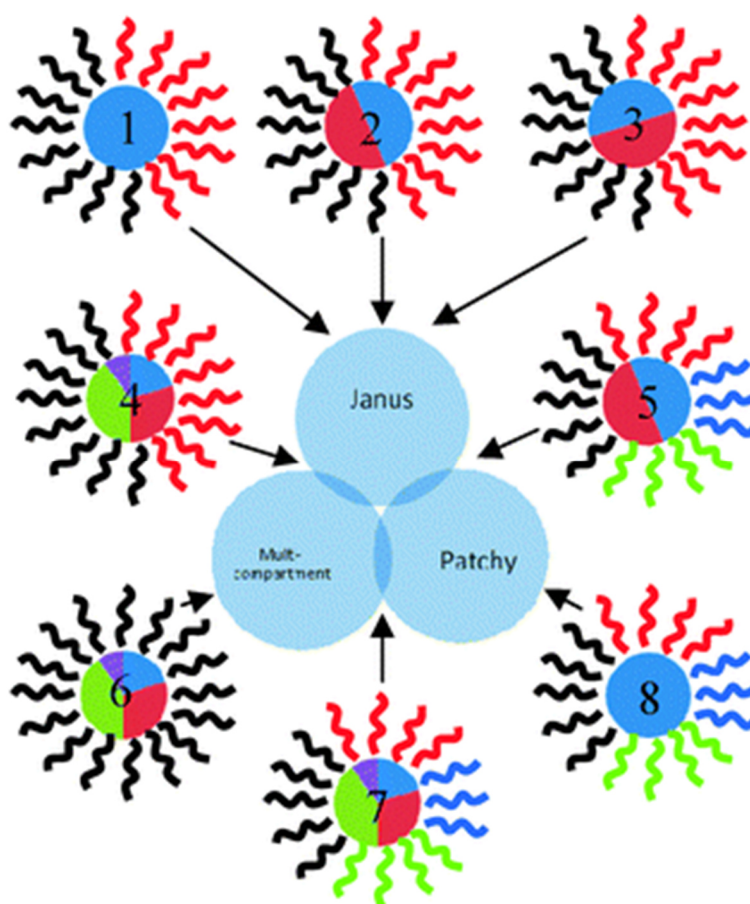


**Scheme 1.2.** (a) Self-seeding concept for living CDSA enabling the preparation of fibre-like micelles with defined length and narrow length distribution. (b) Living polymerisation-induced CDSA utilizing micellar seeds throughout anionic polymerisation of the PFS block. After complete conversion, the reaction was stopped with 4-*tert*-butylphenol (TBP). (a) Reproduced from Ref. <sup>[68]</sup> (Copyright 2015) with permission of the *American Chemical Society*.

One disadvantage of this seed-based method is the low amount of fibre-like micelles that can be produced because rather dilute solutions have to be used. This issue can be overcome by the living polymerisation-induced CDSA approach (Scheme 1.2b),<sup>[23,78,79]</sup> which enables the production of uniform fibre-like micelles with concentrations up to 10 – 20% (w/w solids) within a few hours. Utilizing the photo-induced *cis-trans* isomerization in OPV-based BCPs living CDSA can even be stimulated by light.<sup>[58]</sup>

## 1.2 Surface-Compartmentalized Micelles

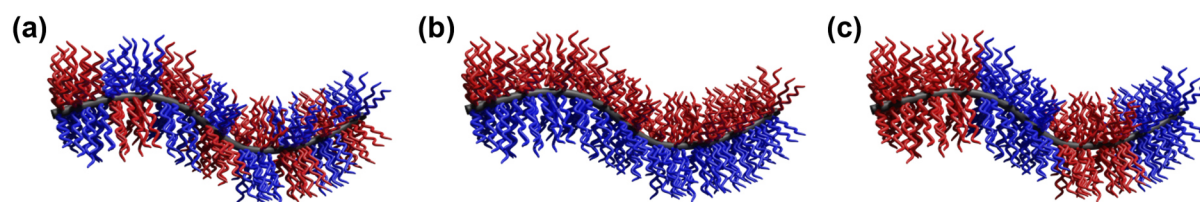
Anisotropic polymeric micelles can be classified into the following three categories, as shown in Scheme 1.3: Surface-compartmentalized micelles, multicompartment core micelles (MCMs) and a combination of both.<sup>[80]</sup> By definition, MCMs are micellar assemblies, which have a solvophilic corona and a solvophobic core. The different subdomains in the micelle core have different properties, so they behave like separate compartments.<sup>[81,82]</sup> Commonly, MCMs are produced by hierarchical self-assembly of suitable building blocks, giving access to a variety of different geometries.<sup>[83–98]</sup>



**Scheme 1.3.** Representations of anisotropic Janus, patchy and multicompartment polymer micelles. Reproduced from Ref. <sup>[80]</sup> (Copyright 2011) with permission of the *Royal Society of Chemistry*.

Surface-compartmentalized micelles can be classified into micelles with a patch-like microphase-separated (patchy) corona, featuring several compartments of different chemistry and/or polarity, or Janus-type micelles (two opposing faces with different chemistry and/or polarity). Scheme 1.4 illustrates the structures which cylindrical (or worm-like) micelles can form. Based on the previously mentioned classification, block comicelles with a block-like

arrangement of several ( $> 2$ ) surface compartments along the cylindrical longitudinal axis can be considered a special case of patchy micelles.



**Scheme 1.4.** Representations of a cylindrical (a) patchy, (b) Janus and (c) block micelle.

### 1.2.1 Patchy Micelles

For the preparation of patchy micelles and polymersomes based on amorphous coil-coil BCPs, three main strategies can be applied: i) Self-assembly of ABC triblock terpolymers with incompatible A and C blocks in selective solvents for the end blocks,<sup>[99–105]</sup> ii) coassembly of AB and CD diblock copolymers with selective interactions between the B and C blocks (such as hydrogen bonding, ionic interactions, solvophobic interactions),<sup>[106–109]</sup> leading to patchy micelles with an insoluble mixed B/C core, and iii) coassembly of AB and BC diblock copolymers,<sup>[110–113]</sup> where the B block forms the insoluble core. Most of the works report spherical micelles or polymersomes with a patchy corona and only a few describe the preparation of one-dimensional (worm-shaped, cylindrical) assemblies with a patchy, compartmentalized corona, although their existence is predicted for mixed polymer brushes by simulations.<sup>[114–117]</sup> Rare but very interesting examples are poly(*tert*-butyl acrylate)-*block*-poly(2-cinnamoyloxyethyl methacrylate)-*block*-poly(glyceryl monomethacrylate) (*PtBA-b-PCEMA-b-PGMA*) and *PnBA-b-PCEMA-b-PtBA* (*PnBA* = poly(*n*-butyl acrylate)) triblock terpolymers.<sup>[99,100,102]</sup> The preparation of micelles by self-assembly was done by dissolving the triblock terpolymers in a good solvent for all blocks. The subsequent addition of methanol, which is a non-solvent for the middle block, induces the micelle formation. Initially, cylindrical micelles with a patchy corona are formed as an intermediate stage. Here, small circular patches of *PtBA* blocks are formed in a corona consisting mainly of *PGMA* or *PnBA*. Further addition of methanol, which decreases the solubility of the *PtBA* block further, allows these cylinders to become double and triple helices through hierarchical self-assembly. Besides, CDSA is a very versatile tool for the preparation of well-defined cylindrical micelles with controlled length and length distribution and has proven to be a valuable method for the production of patchy cylindrical micelles.

The most common route to patchy micelles with crystalline cores is CDSA of linear ABC triblock terpolymers with a crystallizable middle block.<sup>[118]</sup> The driving force for corona segregation in CDSA of triblock terpolymers is the incompatibility of the corona forming blocks. This influences the average width of the patches and leads to an alternating, chessboard-like arrangement of the corona patches.<sup>[119]</sup> In 2008, patchy worm-like crystalline-core micelles (*wCCMs*) based on triblock terpolymers with a semi-crystalline PE middle block and two incompatible amorphous outer blocks (PS and PMMA) were reported for the first time.<sup>[120]</sup> The self-assembly mechanism of these PS-*b*-PE-*b*-PMMA (SEM) triblock terpolymers has been studied in detail and will be described in the following.<sup>[28]</sup>

First, the SEM triblock terpolymers are added to a good solvent for the amorphous blocks and heated above the melting temperature of the semi-crystalline PE block in the given solvent (Figure 1.2a). Depending on the solvent quality for the PE middle block, different micelle morphologies are produced. The SEM triblock terpolymers are molecularly dissolved as unimers in a good solvent for the molten PE block (THF or toluene). In poor solvents for PE (1,4-dioxane or dimethylacetamide), however, spherical micelles with an amorphous molten PE core are obtained because of the collapse of the PE block. Cooling of the unimer solution (good solvent) or the dispersion (spherical micelles in a poor solvent) leads to nucleation of the PE crystallization. In good solvents, the nuclei are stable and able to initiate bidirectional 1D epitaxial growth of the remaining unimers to form *wCCMs*. In poor solvents, the final morphology is dictated by the spherical shape of the micelles. Due to this, the crystallization of PE occurs exclusively in the confinement of the micellar core, resulting in the formation of *sCCMs*. In both cases, the micelles obtained exhibit a patchy, microphase-separated structure of the corona. This is more noticeable in the case of *wCCMs*, which might be attributed to the more dense chain packing in the corona of worm-like micelles with respect to that of spherical micelles (Figure 1.2b, c). Using TEM<sup>[28]</sup> an almost alternating arrangement of the PS and PMMA patches in the corona can be deduced, which was also confirmed by small-angle neutron scattering studies.<sup>[119]</sup>

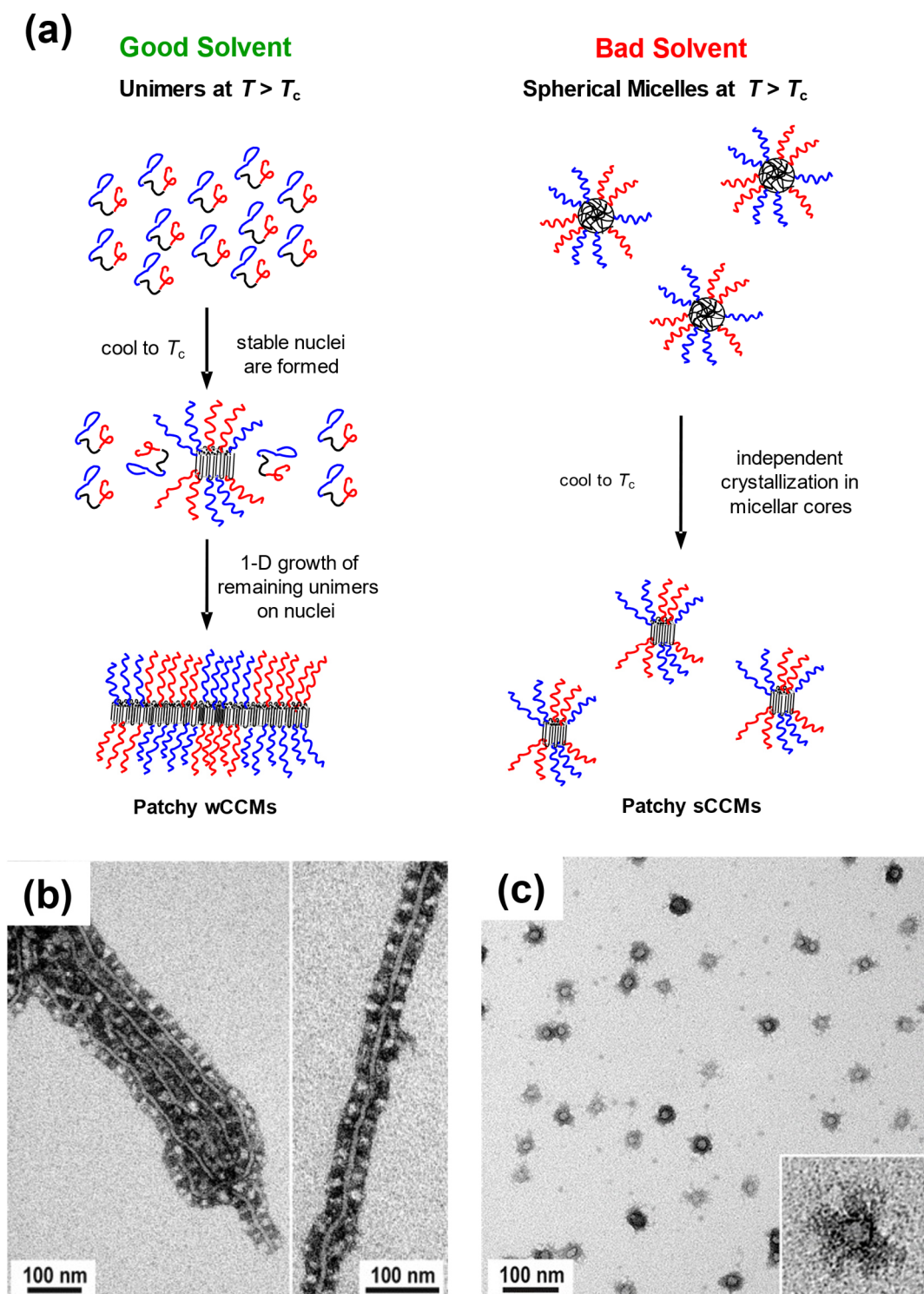


**Figure 1.2.** (a) Schematic representation of the proposed mechanism for the formation of patchy wCCMs and sCCMs from SEM triblock terpolymers (PS blocks are depicted in blue, PE in black and PMMA in red). TEM micrographs of (b) patchy  $S_{340}E_{700}M_{360}$  wCCMs produced *via* CDSA in THF and subsequent annealing at 45 °C for 3 h and (c) patchy  $S_{340}E_{700}M_{360}$  sCCMs formed in dimethylacetamide (average degrees of polymerisation are given as subscripts;  $RuO_4$  vapour was employed for selective staining of PS, which appears dark). Reproduced from Ref. [28] (Copyright 2011) with permission of the *American Chemical Society*.

A simple possibility to adjust the size of the PS and PMMA corona patches is to randomly cocrystallize a SEM triblock terpolymer with a corresponding PS-*b*-PE-*b*-PS (SES) triblock copolymer that carries two PS end blocks.<sup>[121]</sup> A systematic increase in the SES content led to a decrease in the PMMA patch size (Figure 1.3).

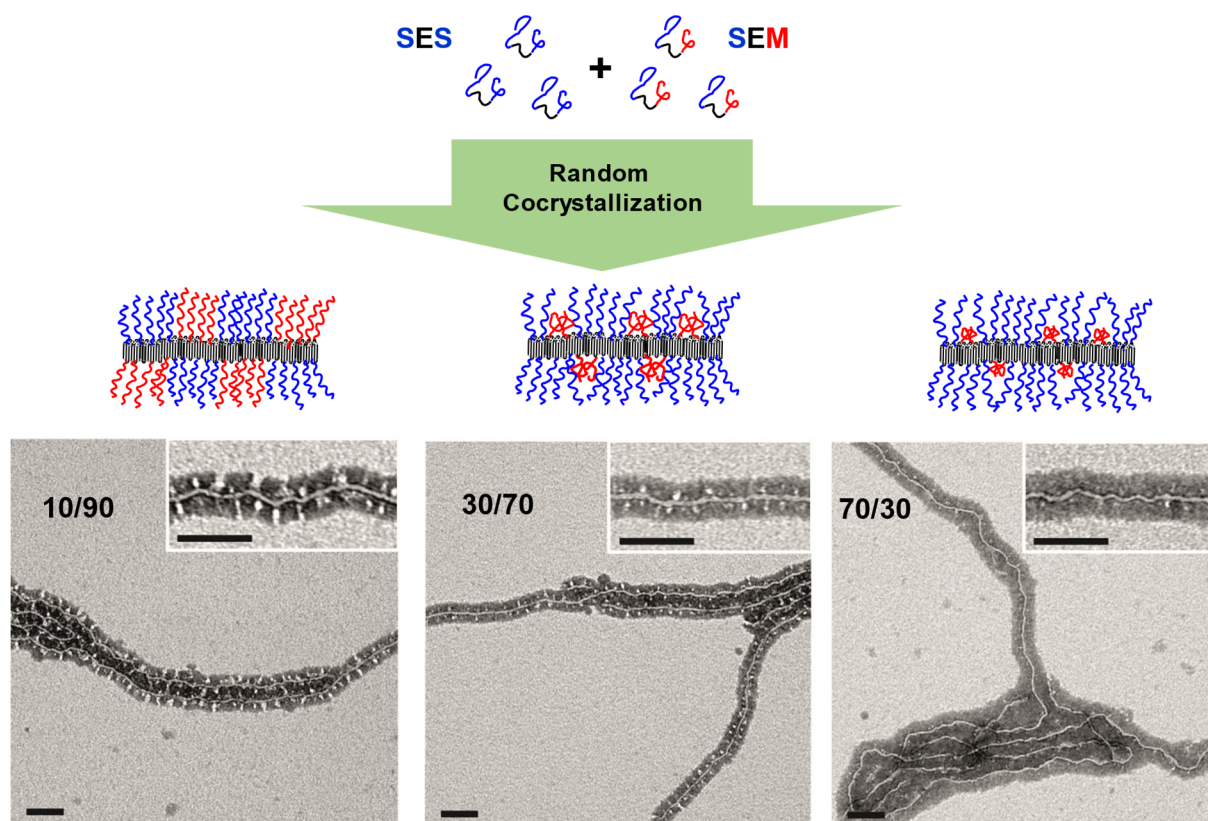


**Figure 1.3.** Adjustment of the size of corona patches by random cocrystallization of a SES triblock copolymer and a SEM triblock terpolymer. TEM micrographs of patchy *w*CCMs in THF. Prepared by cocrystallization of  $S_{380}E_{880}S_{390}$  with  $S_{340}E_{700}M_{360}$  (subscripts denote the respective average degrees of polymerisation). With increasing amount of  $S_{380}E_{880}S_{390}$  the PMMA corona patches (bright areas) decrease (scale bars: 100 nm). PS was selectively stained with  $RuO_4$  and appears dark. Reproduced from Ref. <sup>[121]</sup> (Copyright 2012) with permission of Elsevier.

Various attempts have been made to replace the PE block with another crystallizable block to produce patchy *w*CCMs, but so far only PFS based block copolymers are suitable. Successful examples include triblock terpolymers of PS-*b*-PFS-*b*-PMMA (Figure 1.4a), PS-*b*-PFS-*b*-PMVS (PMVS = poly(methylvinylsiloxane)) and PI-*b*-PFS-*b*-PMMA (PI = polyisoprene)<sup>[122,123]</sup> as well as  $\mu$ -ABC miktoarm star terpolymers containing a crystallizable PFS block (Figure 1.4b).<sup>[124]</sup> Surprisingly, living CDSA was slower for all investigated triblock terpolymers compared to PFS-containing diblock copolymers. This might be attributed to the

comparatively high steric hindrance due to the two corona blocks surrounding the core-forming block, or the choice of solvent, which did not support the crystallization of the PFS block sufficiently. Varying the corona chain length (ratio of core to total corona block) in PS-*b*-PFS-*b*-PMMA triblock terpolymers and cocrystallization of the resulting triblock terpolymers resulted in block comicelles with a patchy corona. Notably, the different corona thicknesses were still visible in TEM analysis (Figure 1.4c, d).

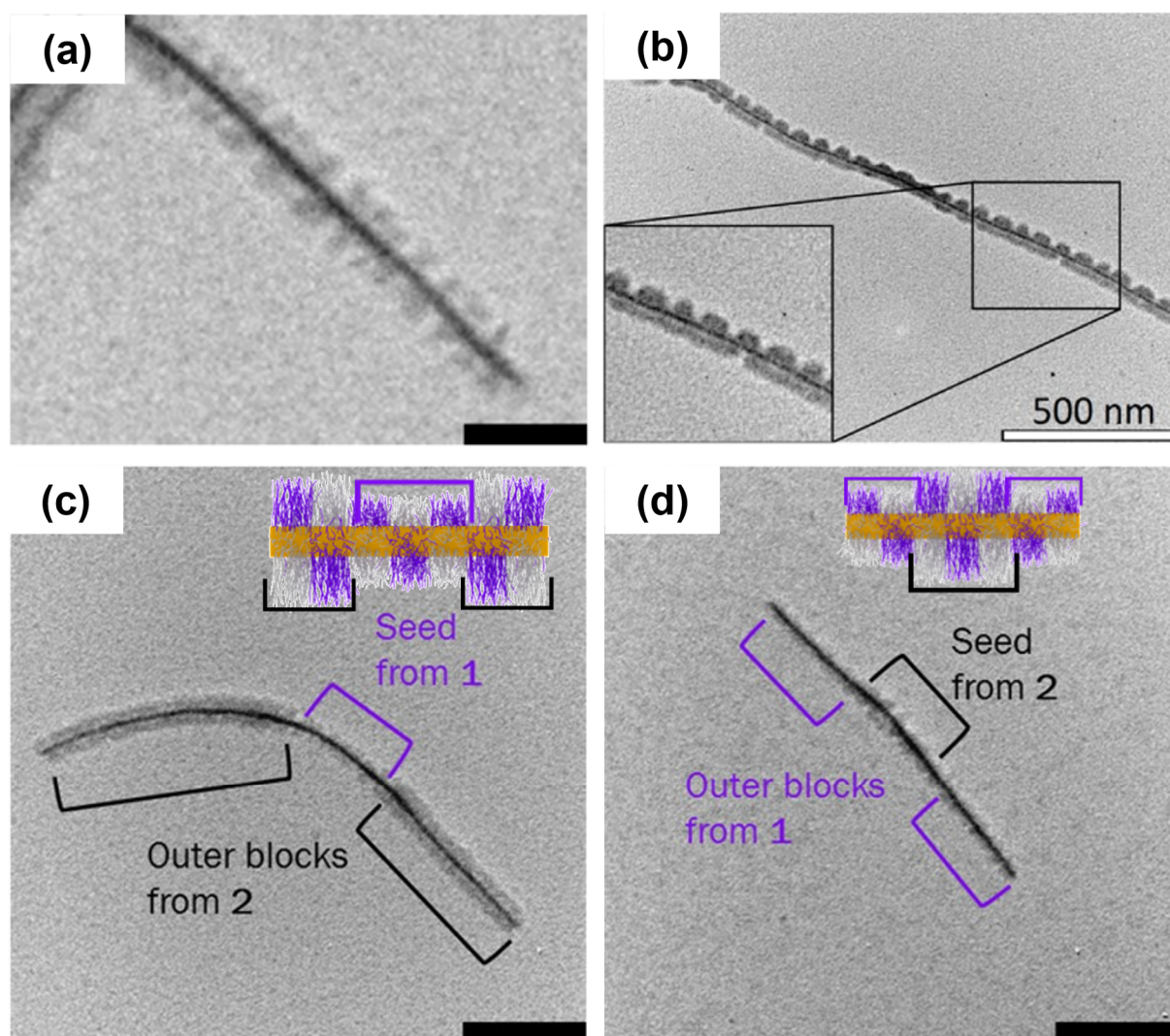


**Figure 1.4.** (a) PFS based cylindrical micelles with patchy corona. (b) Patchy micelles formed by CDSA of a  $\mu$ -SIF (PS-*arm*-PI-*arm*-PFS) miktoarm star terpolymer in ethyl acetate. (c, d) Patchy ABA-type triblock comicelles with a patchy PS/PMMA corona and a crystalline PFS core produced in acetone (scale bars = 100 nm). In (c, d), triblock terpolymers with PMMA and PS blocks of different lengths were used to modify the width of the patchy corona in the middle and outer blocks of the triblock comicelles (in the sketches PS is depicted in light grey and PMMA in purple). (a, c and d) Reprinted from Ref.<sup>[122]</sup> (Copyright 2017) (b) Reprinted from Ref.<sup>[124]</sup> (Copyright 2014) and with permission of the *American Chemical Society*.

Simultaneous coassembly of PFS-based diblock copolymers represents an alternative way to produce patchy cylindrical CCMs. However, the resulting micelles have a block-like rather

than alternating arrangement of their corona patches. Due to this peculiarity, this approach can be considered a special case of patchy CCMs. In 2014, these patchy block comicelles, resulting from the cocrystallization of linear and brush-like BCPs with a crystalline, core-forming PFS block, were reported for the first time.<sup>[125]</sup> The preparation of these comicelles is not limited to sterically demanding coblocks, but can be induced by sufficiently different *Flory-Huggins* interaction parameters between the corona-forming blocks.<sup>[126]</sup> One study investigated the competitive seeded-growth kinetics of the simultaneous cocrystallization of diblock copolymers with different corona blocks. Here, the growth rate of the unimers can be slowed down by small differences in chemical composition or employing long corona-forming chains. Furthermore, the block ratio of the core-forming compared to the corona-forming block plays an important role.<sup>[127]</sup>

### 1.2.2 Block Comicelles

Block comicelles represent a special type of patchy CCMs, since the sequential arrangement of the surface compartments and the precisely adjustable size of the blocks usually leads to larger corona segments than is typically observed for patchy CCMs. Similarly to the synthesis of BCPs, block-type CCMs are prepared by sequential living CDSA. The peculiarity of this process is that the micelles' termini remain "active" after the completion of unimer addition, whereby the addition of another type of unimer leads to the formation of a block-like structure (Figure 1.5a).<sup>[64,128]</sup> Because of this feature, it is possible to precisely adjust the block length by the amount of unimers added. In analogy to living polymerisation, unimers have to fulfil certain requirements for successful cocrystallization, as the reactivity of the first unimer limits the choice of the second. For example, the semi-crystalline micelle cores need compatibility for epitaxial crystallization, i.e. they should have a similar crystal lattice spacing.<sup>[129,130]</sup> Diblock copolymers bearing the same crystallizable block are commonly used to fulfil this requirement. This was first demonstrated for PFS-containing diblock copolymers to generate B-A-B triblock comicelles.<sup>[64]</sup> Furthermore, heteroepitaxial growth of PFG-containing diblock copolymers could be induced by CDSA using different PFS-containing seed micelles.<sup>[22,71,79]</sup> Due to the small difference in the crystal lattice spacing of the two core-forming blocks (ca. 6 %), tri- and pentablock comicelles as well as 2D coassemblies can be realised.

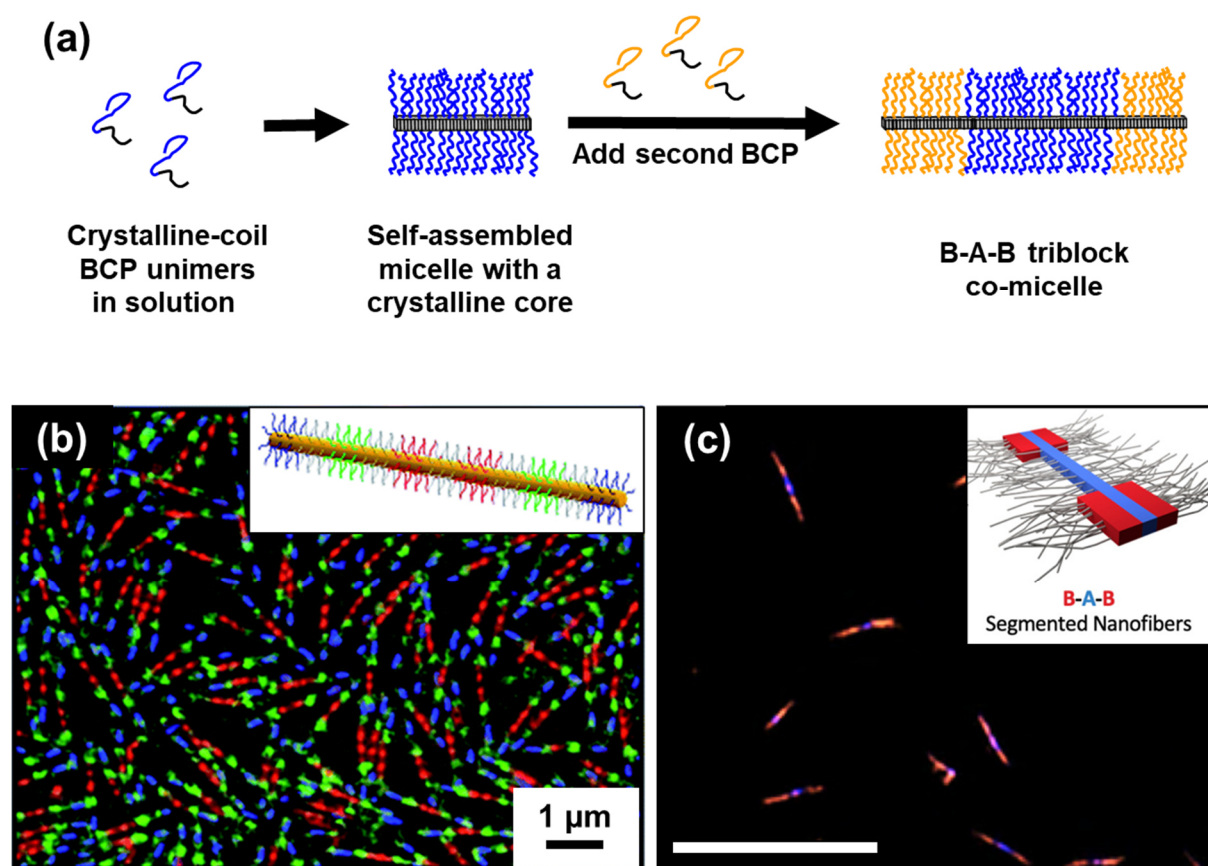


**Figure 1.5.** Preparation of B–A–B triblock comicelles by sequential living CDSA in selective solvents for the corona blocks. (b) Structured illumination microscopy micrograph of symmetrical 11-block comicelles with red, green, and blue fluorescent corona blocks separated by non-fluorescent polydimethylsiloxane spacer blocks. (c) Laser-scanning confocal microscopy micrograph of solid-state, donor–acceptor, coaxial heterojunction nanowires based on B–A–B segmented nanofibers with a semi-crystalline poly(di-*n*-hexylfluorene) (PDHF) core (depicted in blue) and a semi-crystalline poly(3-(2'-ethylhexyl)thiophene) (P3EHT) shell (depicted in red) in the outer corona blocks, taken with both blue (PDHF) and red (P3EHT) channels (scale bar: 10  $\mu\text{m}$ ). Blue emission from the central PDHF core, as well as red/orange emission from the outer P3EHT segments, due to *Förster resonance energy transfer* were observed. (a) Adapted from <sup>[76]</sup>, (b) Reprinted from Ref. <sup>[63]</sup> (Copyright 2021) with permission of the *Royal Society of Chemistry* and (c) reprinted from Ref.<sup>[55]</sup> (Copyright 2020) with permission of the *American Chemical Society*.

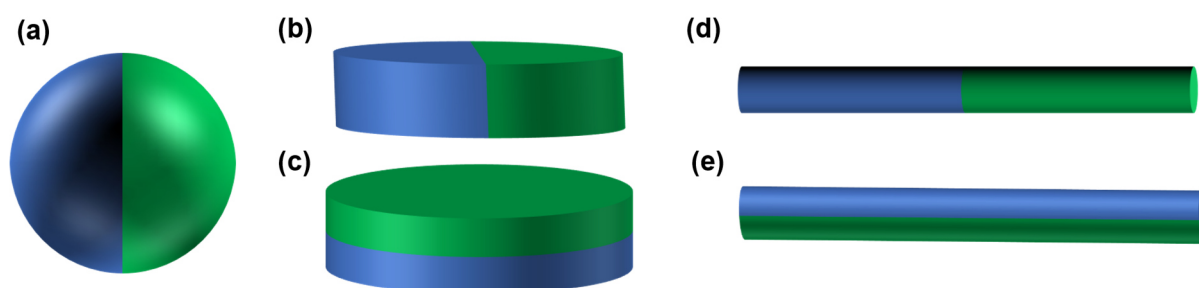
A myriad of 1D, PFS-containing block comicelles, with tailored number, length and composition of corona blocks, can be realized through living CDSA.<sup>[128,131–136]</sup> The accessibility of centrosymmetric and non-centrosymmetric block comicelles leads to a broad structural complexity.<sup>[76]</sup> An important step in the development of block comicelles was made by introducing fluorescent corona blocks. These can be used to create barcode and RGB micelles (Figure 1.5b).<sup>[63,74,137]</sup> Previously, producing cylindrical nanomaterials with accurate, colour-tuneable compartments of predictable length and number was a challenge. By replacing the PFS block with a poly(di-*n*-hexylfluorene) (PDHF) block, it is possible to obtain

fluorescence in the semi-crystalline core of the micelles.<sup>[75]</sup> Even solid-state donor-acceptor heterojunctions induced by secondary crystallization in one of the corona blocks can be achieved (Figure 1.5c).<sup>[55]</sup> These materials have a high potential for applications in optoelectronics, device manufacturing and sensor technology.<sup>[138]</sup>

Block comicelles have also been realised with various other semi-crystalline, core-forming blocks, including for example PFG,<sup>[22,71,79]</sup> polycarbonate,<sup>[52,139]</sup> poly(3-heptylselenophene),<sup>[57]</sup> P3HT,<sup>[140]</sup> OPV,<sup>[58,141,141,142]</sup> PLLA,<sup>[49]</sup> and PE<sup>[25]</sup>. Even more complex micelle architectures such as double-headed and single-headed spear-like micelles,<sup>[143]</sup> scarf-like micelles,<sup>[22]</sup> diamond-fibre hybrid structures<sup>[69]</sup> or platelets with different shapes (rectangular, quasi-hexagonal and diamond-platelet micelles)<sup>[70–73]</sup> can be accomplished.

### 1.2.3 Janus micelles

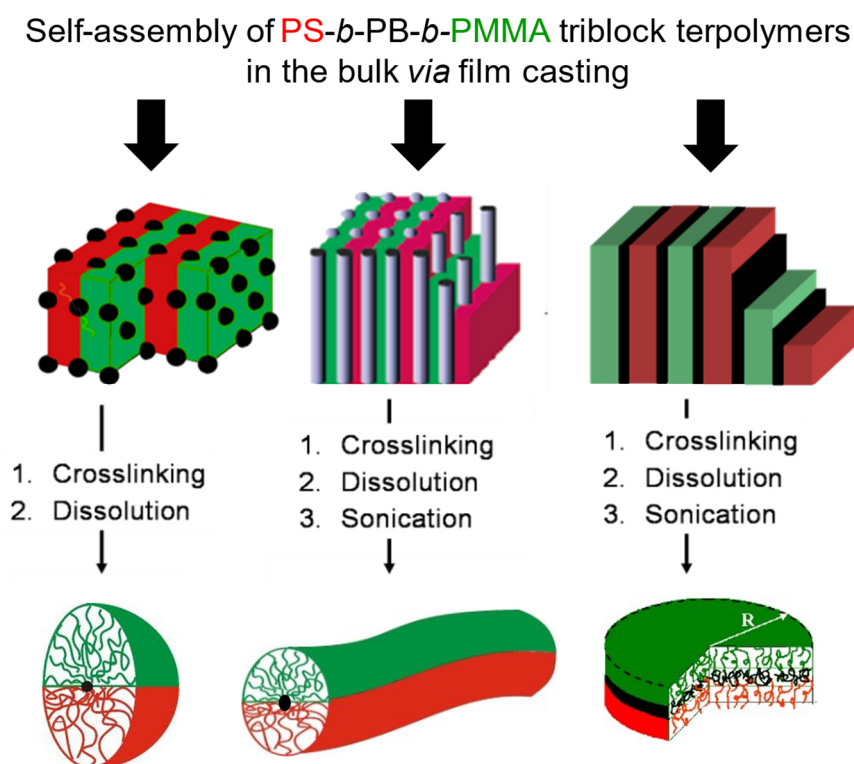
The nomenclature of these particles is based on the two-faced Roman god Janus.<sup>[144,145]</sup> These particles have two opposing faces with different polarity or chemistry. Janus particles can be classified into three classes, which give information about their morphology. Class one contains three-dimensional (3D) objects (spheres). Here, the respective half-shells of the sphere can only exist in one configuration (Scheme 1.5a). 2D (disc-shaped) and 1D (cylindrical) Janus particles can exist in two different configurations.<sup>[146]</sup> Here, the two different “faces” are arranged horizontally (Scheme 1.5b, d) or vertically (Scheme 1.5c, e) with respect to the objects long axis.



**Scheme 1.5.** Overview of possible Janus type particle configurations: spheres (a), discs (b + c) and cylinders (d + e).

For the preparation of amorphous Janus-type micelles, ABC triblock terpolymers are the most widely used materials.<sup>[144]</sup> The basic approach is to freeze the middle block B by covalent or non-covalent cross-linking, while the immiscible blocks A and C separate and point in different

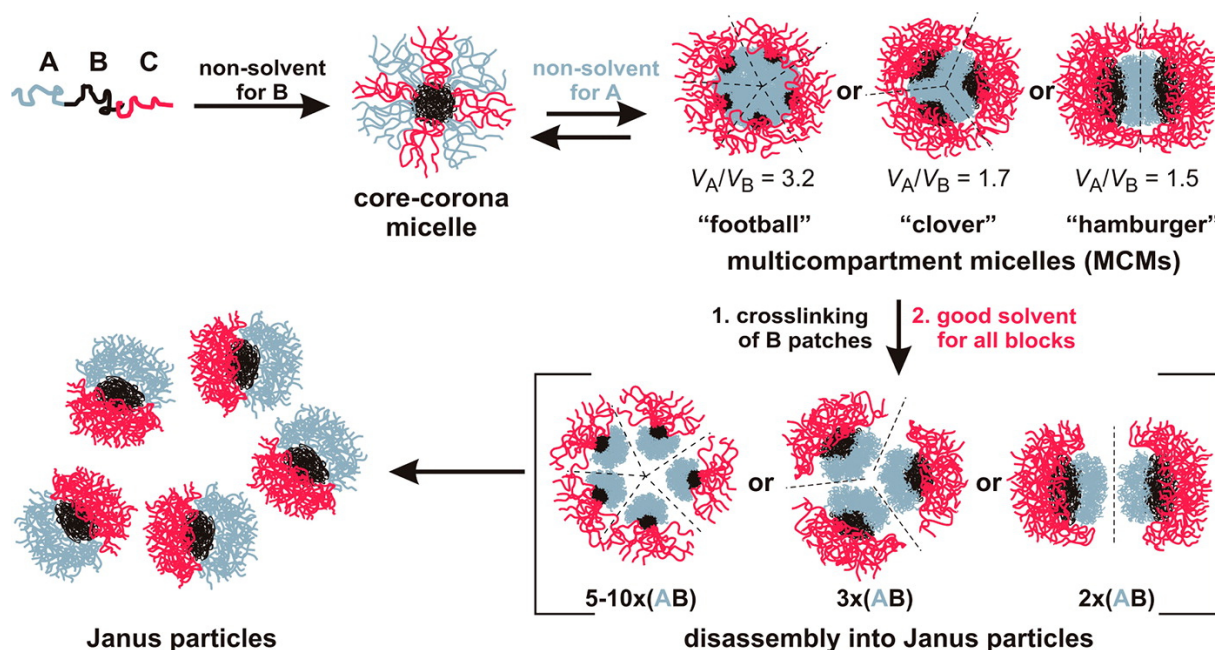
directions. In the early 2000s, amorphous Janus micelles were prepared by *Müller* and co-workers starting from polystyrene-*block*-polybutadiene-*block*-poly(methyl methacrylate) (PS-*b*-PB-*b*-PMMA) triblock terpolymer bulk morphologies. In this process, polybutadiene formed spherical domains, which were selectively cross-linked. The PS/PMMA Janus micelles were obtained by redissolving in THF.<sup>[147]</sup> Depending on the bulk morphology (Scheme 1.6) of the triblock terpolymers used, cylindrical<sup>[148–150]</sup> or disc-like<sup>[151,152]</sup> Janus micelles can be produced in addition to spherical ones.<sup>[153]</sup> Alternatively, cylindrical Janus particles with the two faces being located perpendicular to the cylinder long axis can be produced using block-type molecular polymer brushes.<sup>[97]</sup> Janus micelles with poly(2-vinyl pyridine) (P2VP) as middle block could also be produced by cross-linking.<sup>[154,155]</sup> This cross-linking leads to the preservation of the compartmentalisation of the outer blocks after dissolution of the material.<sup>[156]</sup> Based on this polymer composition, amphiphilic Janus micelles could also be prepared. The PMMA surface of the PS/PMMA Janus particles was hydrolysed with potassium hydroxide in 1,4-dioxane. The resulting Janus micelles have a hydrophobic (PS) and a hydrophilic poly(methacrylic acid) part.<sup>[157]</sup> From this approach, further amphiphilic Janus micelles were realised.<sup>[158,159]</sup>



**Scheme 1.6.** Representation of the bulk morphologies formed by PS-*b*-PB-*b*-PMMA triblock terpolymers *via* film casting (top) and the architecture of the “Janus micelle” generated by cross-linking of the PB middle block followed by dissolution (bottom). Reproduced from Ref. <sup>[146]</sup> (Copyright 2008) with permission of the *Royal Society of Chemistry*.

Confinement self-assembly of PS-*b*-PB-*b*-PMMA (emulsion droplets) leads to prolate-ellipsoidal microparticles. These particles exhibit an internal lamellar *ll*-morphology, which allows Janus discs to be obtained. By altering the pore size of the *Shirasu* glass membrane with which the particles are produced, the shape, size and aspect ratio of the resulting Janus discs can be controlled. Subsequently, the PS parts were chemically modified to fix gold NPs.<sup>[160]</sup>

Janus micelles were also made by guided self-assembly of linear ABC triblock terpolymers in selective solvents as shown in Scheme 1.7. In this case, spherical MCMs consisting of a microphase-separated PS core with a defined number of PB patches and a soluble PMMA corona could be prepared. Subsequently, the PB patches were photo cross-linked. This allows permanent fixation of the phase-separated state, and dissolution in a solvent good for all blocks disassembles the MCMs into individual Janus particles.<sup>[159–162]</sup>



**Scheme 1.7.** Self-assembly of an ABC triblock terpolymer into MCMs, crosslinking of the middle block forming segment and subsequent disassembly into Janus particles. Reproduced from Ref. <sup>[161]</sup> (Copyright 2012) with permission of the *American Chemical Society*.

### 1.2.4 Application of Surface-Compartmentalized Micelles

The versatility of surface-compartmentalized micelles is reflected in the diversity of their applications. Due to the various possible combinations of polymer composition, tailor-made systems can therefore be used.

Micellar nanostructures have been established as a very efficient template for the incorporation of NPs. Here, the functional surface compartments not only act as ligands, they also prevent the agglomeration and *Ostwald* ripening of the embedded NPs due to the spatial separation (Figure 1.6).<sup>[33,131,132,142,153,162,163]</sup> Functional groups, e.g. by selective amidation of the PMMA block in SEM triblock terpolymers with *N,N*-dialkylethylenediamines, can be introduced in an efficient way to modify the corona. It was possible to tune the patch size and shape of patchy *w*CCMs using CDSA in THF by varying the block length ratio of the corona blocks or by selective solvent interactions. The functionalized patchy corona of the micelles was shown to allow the regio-selective incorporation of inorganic NPs.<sup>[33,34]</sup> These properties make it possible to implement these hybrid systems as heterogeneous catalysts.<sup>[35]</sup>

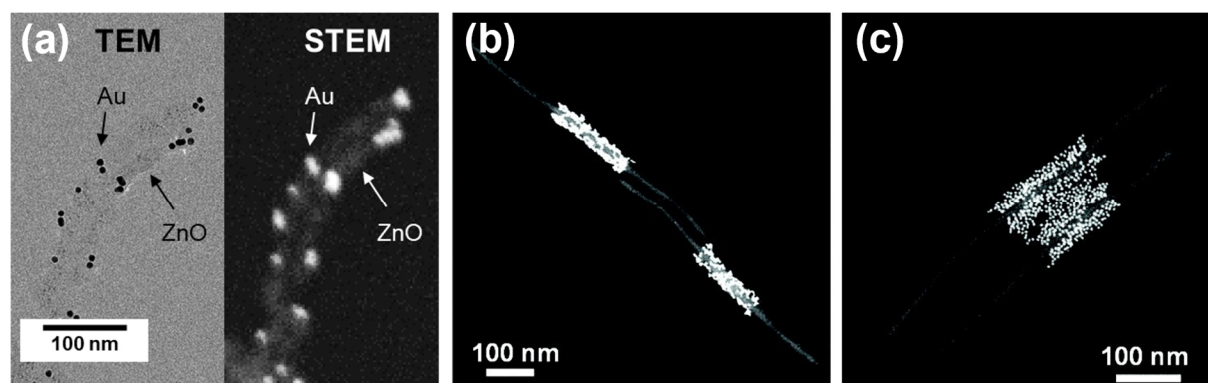


**Figure 1.6** (a) Bright-field (left) and high-angle annular dark-field scanning transmission electron microscopy (right) images showing a binary gold and zinc oxide NP loaded *w*CCM. Dark-field TEM images show block comicelles with the central block functionalized with gold NPs (b) and lead(II)sulfide quantum dots (c). (a) Reproduced from Ref. <sup>[34]</sup> (Copyright 2018) with permission of the *Royal Society of Chemistry* and (b, c) Reproduced from Ref. <sup>[131]</sup> (Copyright 2007) with permission of the *American Chemical Society*.

Complex hierarchical superstructures realized by means of self-assembly represent another facet of the broad applicability of surface-compartmentalized micelles. The micellar structures shown in Figure 1.7 require anisotropy or directional interactions to be formed, which is due to the shape and/or surface functionality of the initial building units.<sup>[164,165]</sup> For example, block comicelles are used as building blocks for the formation of 2D and 3D superstructures, further expanding the scope of complex micellar assemblies through hierarchical self-assembly. In this

context, hierarchical assemblies can be realised through various approaches. For example by coordination-driven co-assembly<sup>[166]</sup>, dialysis of amphiphilic block comicelles against selective solvents, enabling highly efficient side-by-side or end-to-end stacking,<sup>[167–169]</sup> or spatially confined hydrogen-bonding interactions<sup>[170,171]</sup>. MCMs can be obtained, for example, by self-assembly of PS-*b*-PB-*b*-PMMA triblock terpolymers.<sup>[161,172–174]</sup> *Zhu* and co-workers reported unimolecular Janus micelles in *N,N*-dimethylformamide based on a PS-*b*-P2VP-*b*-PEO triblock terpolymer. Here, the middle block was cross-linked by 1,4-dibromobutane. Increasing the concentration resulted in supermicelles with a hydrodynamic diameter of 50–115 nm.<sup>[155]</sup>

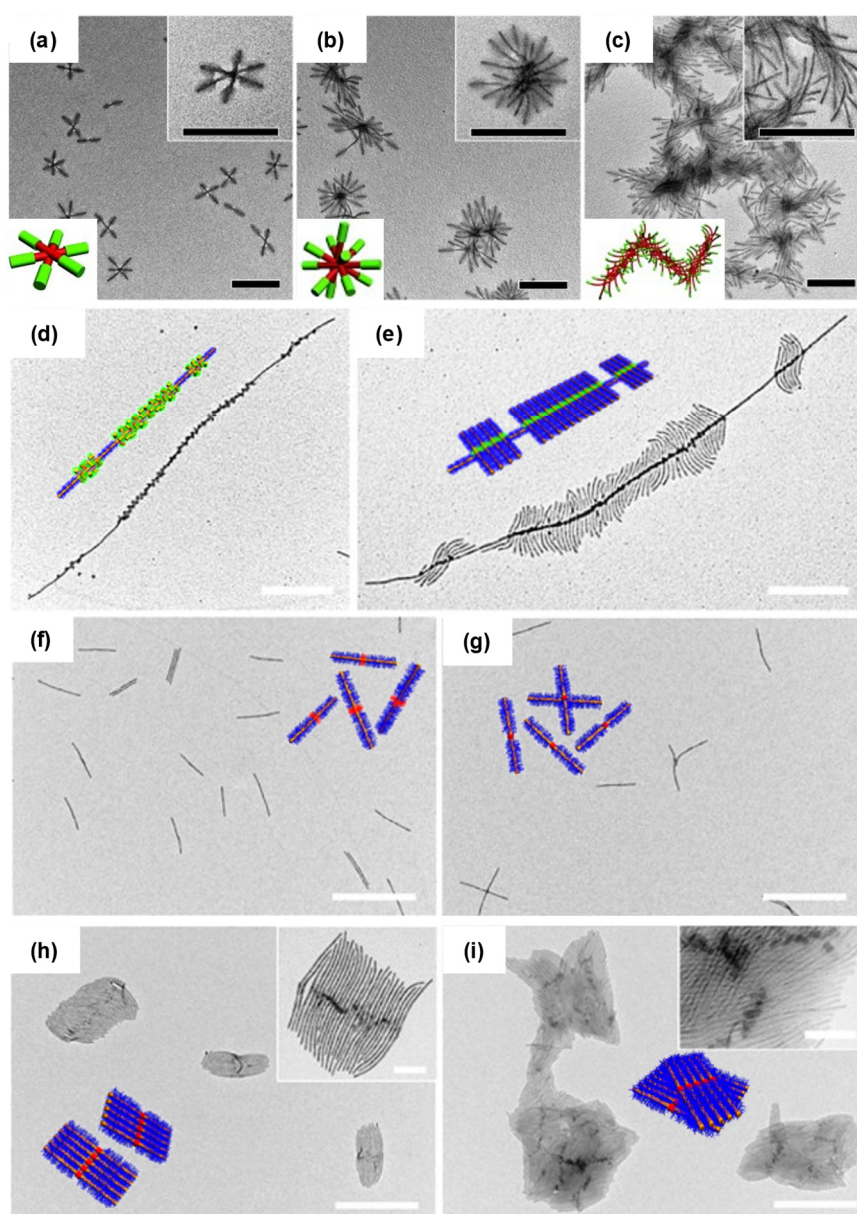


**Figure 1.7.** TEM micrographs with sketches of PFS-based hierarchical self-assemblies. (a - c) Supermicelles of amphiphilic cylindrical A-B-A triblock comicelles with different block lengths of A obtained by dialysis against *iso*-propanol (scale bar: 500 nm), (d) heptablock

composite “shish-kebab” supermicelles, (e) block fence-like “shish-kebab” supermicelles prepared by adding an additional BCP unimer to the previous “shish-kebab” structure (scale bars are 1  $\mu\text{m}$ ). A-B-A triblock comicelles in (f) *n*-hexane:iso-propanol = 1:4; (g) iso-propanol; (h) iso-propanol:methanol = 5:5 and (i) methanol (scale bars: 1  $\mu\text{m}$  and the insets are 200 nm). (a – c) Reproduced from Ref. [169] (Copyright 2012) with permission of *Wiley VCH Publications*, (d, e) Reproduced from Ref. [168] (Copyright 2016) with permission of *American Chemical Society* and (f – i) Reproduced from Ref. [171] (Copyright 2016) with permission of *American Chemical Society*.

Furthermore, surface-compartmentalized micelles show a unique interfacial activity (Figure 1.8a).<sup>[175–177]</sup> This is influenced by the adaptability of the respective corona-forming blocks. A special type of interface adjustment is exhibited by micelles with patchy PS/PMMA corona, in which the respective insoluble/soluble corona segment selectively collapses/swells. As a result, this behaviour leads to a kind of “*in situ* Janus” structure of the micelles at the interface. This property can be used for the stabilization of emulsions<sup>[159]</sup> or the compatibilization of polymer blends<sup>[173,178–182]</sup>, as shown in Figure 1.8b.<sup>[183]</sup>

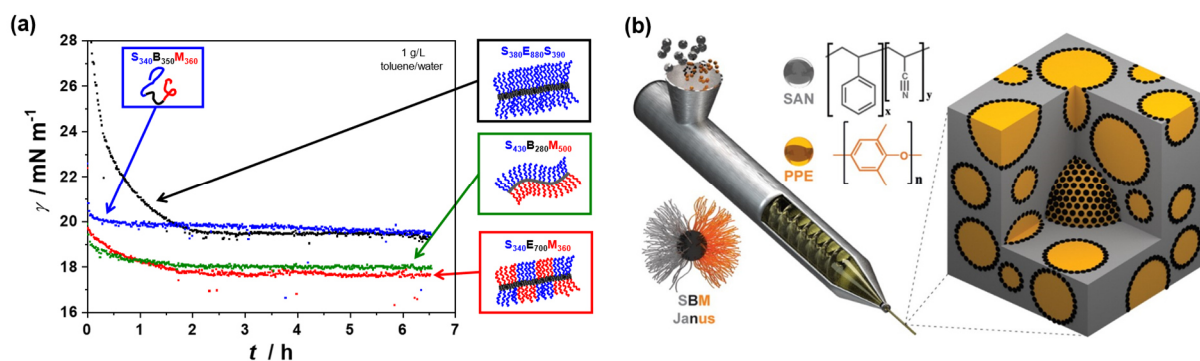


**Figure 1.8.** (a) Comparison of the interfacial tension measurements of 1  $\text{g}\cdot\text{L}^{-1}$  solutions containing SBM unimers (blue), SES *w*CCMs with a homogeneous PS corona (black), SBM-based Janus cylinders with opposing PS and PMMA faces (green) and SEM *w*CCMs with a patchy PS/PMMA corona (red) (subscripts correspond to average degrees of polymerization of the respective blocks). (b) PS/PMMA Janus particles used as compatibilizer in melt extrusion of a polymer blend. PS/PMMA Janus particles (black dots) compatibilize and stabilize poly(2,6-dimethyl-1,4-phenylene ether) droplets (yellow) within the poly(styrene-*co*-acrylonitrile) matrix (gray). (a) Reproduced from Ref. [175] (Copyright 2012) with permission of *Royal Society of Chemistry*, (b) Reproduced from Ref. [173] (Copyright 2014) with permission of *American Chemical Society*.

### 1.3. Objective of the Thesis

The CDSA of triblock terpolymers with a semi-crystalline PE middle block and incompatible end blocks of PS and either PMMA or poly(*N,N*-dialkylaminoethyl methacrylamides) (alkyl = Me, *i*Pr) has proven to be an excellent method for the preparation of functional patchy *w*CCMs. These micelles are distinguished for their excellent interfacial activity and can also be used as efficient templates for the incorporation of NPs. Thus, the aim of this doctoral thesis was to open up new applications for patchy *w*CCMs and for surface-compartmentalized CCMs in general, as well as to extend their functionality through implementing stimuli-responsive properties.

In a first study, supported gold NP loaded patchy *w*CCMs have been successfully applied in heterogeneous catalysis. However, a fundamental understanding on the parameters affecting the catalytic performance was still missing. Hence, one of the central objectives of this thesis was to systematically investigate the impact of micelle geometry (*w*CCM *vs.* *s*CCM), patch size and chemistry on the catalytic activity of these systems. The functional poly(*N,N*-dialkylaminoethyl methacrylamide) (PDxA) patches in the micelle corona, which have been utilized for NP incorporation, are chemically very similar to poly(*N,N*-dialkylaminoethyl methacrylate)s, showing a double-responsive (pH and temperature) solubility in water. This suggests that PDxA might also show a double-responsive solubility, depending on the alkyl substituents at the tertiary amino group. This in turn would add an additional functionality to the patchy *w*CCMs.

Another fundamental aspect of this work was the question whether the unique corona structure with alternating non-functional (neutral) PS and functional (amino groups) PDxA patches can be harnessed to generate hierarchical superstructures. As (supra)molecular self-assembly of small molecules, like benzene-1,3,5-tricarboxamides, has some similarities with CDSA with respect to the underlying self-assembly mechanism a combination of these two concepts was selected to develop a new approach toward hierarchical self-assemblies.

An aspect that has not been addressed up to now is the impact of confinement on CDSA. Besides, it has already been shown that confinement within emulsion droplets (organic solvent (toluene or chloroform) in water emulsions) exerts a significant impact on the self-assembly of amorphous block copolymers and, thus, on the morphologies of the obtained microparticles after the organic solvent has been removed by slow evaporation. Hence, CDSA of triblock terpolymers with semi-crystalline PE middle blocks in confinement might open access to new

types of microparticles with interesting internal morphologies and properties depending whether CDSA or microphase separation occurs first upon solvent evaporation.

Finally, the preparation of Janus-like  $w$ CCMs was aimed by the selection of suitable corona blocks. Theoretical works have shown that with sufficiently high incompatibility or the presence of additional driving forces for microphase separation in the corona, Janus micelles should be accessible. However, using CDSA, only patchy micelles could be realised so far. To this end the combination PS/PEO as corona blocks was selected, as PS and PEO are strongly incompatible and additional crystallisation of PEO within the corona could drive microphase separation toward a Janus-type structure.

## 1.4 Reference

- [1] M. Szwarc, *Nature* **1956**, *178*, 1168.
- [2] M. Szwarc, M. Levy, R. Milkovich, *J. Am. Chem. Soc.* **1956**, *78*, 2656.
- [3] S. Newman, *J. Appl. Polym. Sci.* **1962**, *6*, 15.
- [4] S. Krause, *J. Phys. Chem.* **1964**, *68*, 1948.
- [5] B. Lotz, A. J. Kovacs, G. A. Bassett, A. Keller, *Kolloid Z. Z. Polym.* **1966**, *209*, 115.
- [6] A. J. Kovacs, J. A. Manson, *Kolloid Z. Z. Polym.* **1966**, *214*, 1.
- [7] T. Vilgis, A. Halperin, *Macromolecules* **1991**, *24*, 2090.
- [8] J. Massey, K. N. Power, I. Manners, M. A. Winnik, *J. Am. Chem. Soc.* **1998**, *120*, 9533.
- [9] D. Richter, D. Schneiders, M. Monkenbusch, L. Willner, L. J. Fetters, J. S. Huang, M. Lin, K. Mortensen, B. Farago, *Macromolecules* **1997**, *30*, 1053.
- [10] A. Ramzi, M. Prager, D. Richter, V. Efstratiadis, N. Hadjichristidis, R. N. Young, J. B. Allgaier, *Macromolecules* **1997**, *30*, 7171.
- [11] E. K. Lin, A. P. Gast, *Macromolecules* **1996**, *29*, 4432.
- [12] J. A. Massey, K. Temple, L. Cao, Y. Rharbi, J. Raez, M. A. Winnik, I. Manners, *J. Am. Chem. Soc.* **2000**, *122*, 11577.
- [13] R. L. N. Hailes, A. M. Oliver, J. Gwyther, G. R. Whittell, I. Manners, *Chem. Soc. Rev.* **2016**, *45*, 5358.
- [14] U. Tritzler, S. Pearce, J. Gwyther, G. R. Whittell, I. Manners, *Macromolecules* **2017**, *50*, 3439.
- [15] W.-N. He, J.-T. Xu, *Prog. Polym. Sci.* **2012**, *37*, 1350.
- [16] S. Ganda, M. H. Stenzel, *Prog. Polym. Sci.* **2020**, *101*, 101195.
- [17] L. Cao, I. Manners, M. A. Winnik, *Macromolecules* **2002**, *35*, 8258.
- [18] F. Wurm, S. Hilf, H. Frey, *Chem. Eur. J.* **2009**, *15*, 9068.
- [19] G. Guerin, M. Cruz, Q. Yu, *Sci. Adv.* **2020**, *6*, eaaz7301.
- [20] A. van Du, H. Qiu, M. A. Winnik, G. R. Whittell, I. Manners, *Macromol. Chem. Phys.* **2016**, *217*, 1671.
- [21] T. Gädt, F. H. Schacher, N. McGrath, M. A. Winnik, I. Manners, *Macromolecules* **2011**, *44*, 3777.
- [22] T. Gädt, N. S. Jeong, G. Cambridge, M. A. Winnik, I. Manners, *Nat. Mater.* **2009**, *8*, 144.

- 
- [23] Y. Sha, M. A. Rahman, T. Zhu, Y. Cha, C. W. McAlister, C. Tang, *Chem. Sci.* **2019**, *10*, 9782.
- [24] Y. Sha, Y. Zhang, T. Zhu, S. Tan, Y. Cha, S. L. Craig, C. Tang, *Macromolecules* **2018**, *51*, 9131.
- [25] J. Schmelz, A. E. Schedl, C. Steinlein, I. Manners, H. Schmalz, *J. Am. Chem. Soc.* **2012**, *134*, 14217.
- [26] B. Fan, L. Liu, J.-H. Li, X.-X. Ke, J.-T. Xu, B.-Y. Du, Z.-Q. Fan, *Soft Matter* **2016**, *12*, 67.
- [27] H. Schmalz, J. Schmelz, M. Drechsler, J. Yuan, A. Walther, K. Schweimer, A. M. Mihut, *Macromolecules* **2008**, *41*, 3235.
- [28] J. Schmelz, M. Karg, T. Hellweg, H. Schmalz, *ACS Nano* **2011**, *5*, 9523.
- [29] T. Rudolph, M. von der Lhe, M. Hartlieb, S. Norsic, U. S. Schubert, C. Boisson, F. D'Agosto, F. H. Schacher, *ACS Nano* **2015**, *9*, 10085.
- [30] B. Fan, J.-Q. Xue, X.-S. Guo, X.-H. Cao, R.-Y. Wang, J.-T. Xu, B.-Y. Du, Z.-Q. Fan, *Macromolecules* **2018**, *51*, 7637.
- [31] S. Xu, C. Zhang, L. Li, S. Zheng, *Polymer* **2017**, *128*, 1.
- [32] B. Fan, R.-Y. Wang, X.-Y. Wang, J.-T. Xu, B.-Y. Du, Z.-Q. Fan, *Macromolecules* **2017**, *50*, 2006.
- [33] J. Schbel, M. Karg, D. Rosenbach, G. Krauss, A. Greiner, H. Schmalz, *Macromolecules* **2016**, *49*, 2761.
- [34] J. Schbel, C. Hils, A. Weckwerth, M. Schlenk, C. Bojer, M. C. A. Stuart, J. Brey, S. Frster, A. Greiner, M. Karg, H. Schmalz, *Nanoscale* **2018**, *10*, 18257.
- [35] J. Schbel, M. Burgard, C. Hils, R. Dersch, M. Dulle, K. Volk, M. Karg, A. Greiner, H. Schmalz, *Angew. Chem. Int. Ed.* **2017**, *56*, 405.
- [36] A. Radulescu, R. T. Mathers, G. W. Coates, D. Richter, L. J. Fetters, *Macromolecules* **2004**, *37*, 6962.
- [37] H. Xiong, C.-K. Chen, K. Lee, R. M. van Horn, Z. Liu, B. Ren, R. P. Quirk, E. L. Thomas, B. Lotz, R.-M. Ho, W.-B. Zhang, S. Z. D. Cheng, *Macromolecules* **2011**, *44*, 7758.
- [38] A. M. Mihut, A. Chiche, M. Drechsler, H. Schmalz, E. Di Cola, G. Krausch, M. Ballauff, *Soft Matter* **2009**, *5*, 208.
- [39] A. M. Mihut, M. Drechsler, M. Mller, M. Ballauff, *Macromol. Rapid Commun.* **2010**, *31*, 449.

- [40] E. Sevgen, M. Dolejsi, P. F. Nealey, J. A. Hubbell, J. J. de Pablo, *Macromolecules* **2018**, *51*, 9538.
- [41] C. E. Brubaker, D. Velluto, D. Demurtas, E. A. Phelps, J. A. Hubbell, *ACS Nano* **2015**, *9*, 6872.
- [42] Z. Coe, A. Weems, A. P. Dove, R. K. O'Reilly, *J. Vis. Exp.* **2019**, *20*, e59772.
- [43] M. C. Arno, M. Inam, Z. Coe, G. Cambridge, L. J. Macdougall, R. Keogh, A. P. Dove, R. K. O'Reilly, *J. Am. Chem. Soc.* **2017**, *139*, 16980.
- [44] Y. Cha, C. Jarrett-Wilkins, M. A. Rahman, T. Zhu, Y. Sha, I. Manners, C. Tang, *ACS Macro Lett.* **2019**, *8*, 835.
- [45] M. Inam, G. Cambridge, A. Pitto-Barry, Z. P. L. Laker, N. R. Wilson, R. T. Mathers, A. P. Dove, R. K. O'Reilly, *Chem. Sci.* **2017**, *8*, 4223.
- [46] N. Petzetakis, A. P. Dove, R. K. O'Reilly, *Chem. Sci.* **2011**, *2*, 955.
- [47] M. C. Arno, M. Inam, A. C. Weems, Z. Li, A. L. A. Binch, C. I. Platt, S. M. Richardson, J. A. Hoyland, A. P. Dove, R. K. O'Reilly, *Nat. Commun.* **2020**, *11*, 1420.
- [48] W. Yu, M. Inam, J. R. Jones, A. P. Dove, R. K. O'Reilly, *Polym. Chem.* **2017**, *8*, 5504.
- [49] Y. He, J.-C. Eloi, R. L. Harniman, R. M. Richardson, G. R. Whittell, R. T. Mathers, A. P. Dove, R. K. O'Reilly, I. Manners, *J. Am. Chem. Soc.* **2019**, *141*, 19088.
- [50] S. Ganda, C. K. Wong, M. H. Stenzel, *Macromolecules* **2021**, *54*, 6662.
- [51] Z. Li, A. K. Pearce, A. P. Dove, R. K. O'Reilly, *Polymers* **2021**, *13*, 2202.
- [52] J. R. Finnegan, X. He, S. T. G. Street, J. D. Garcia-Hernandez, D. W. Hayward, R. L. Harniman, R. M. Richardson, G. R. Whittell, I. Manners, *J. Am. Chem. Soc.* **2018**, *140*, 17127.
- [53] M. Lazzari, D. Scalarone, C. Vazquez-Vazquez, M. A. López-Quintela, *Macromol. Rapid Commun.* **2008**, *29*, 352.
- [54] X. Li, B. Jin, Y. Gao, D. W. Hayward, M. A. Winnik, Y. Luo, I. Manners, *Angew. Chem. Int. Ed.* **2016**, *55*, 11392.
- [55] H. Shaikh, X.-H. Jin, R. L. Harniman, R. M. Richardson, G. R. Whittell, I. Manners, *J. Am. Chem. Soc.* **2020**, *142*, 13469.
- [56] Y. Zhang, H. Shaikh, A. J. Sneyd, J. Tian, J. Xiao, A. Blackburn, A. Rao, R. H. Friend, I. Manners, *J. Am. Chem. Soc.* **2021**, *143*, 7032.
- [57] E. L. Kynaston, A. Nazemi, L. R. MacFarlane, G. R. Whittell, C. F. J. Faul, I. Manners, *Macromolecules* **2018**, *51*, 1002.
- [58] S. Shin, F. Menk, Y. Kim, J. Lim, K. Char, R. Zentel, T.-L. Choi, *J. Am. Chem. Soc.* **2018**, *140*, 6088.

- [59] Y.-J. Kim, C.-H. Cho, K. Paek, M. Jo, M. Park, N.-E. Lee, Y. Kim, B. J. Kim, E. Lee, *J. Am. Chem. Soc.* **2014**, *136*, 2767.
- [60] S. K. Patra, R. Ahmed, G. R. Whittell, D. J. Lunn, E. L. Dunphy, M. A. Winnik, I. Manners, *J. Am. Chem. Soc.* **2011**, *133*, 8842.
- [61] X. Li, P. J. Wolanin, L. R. MacFarlane, R. L. Harniman, J. Qian, O. E. C. Gould, T. G. Dane, J. Rudin, M. J. Cryan, T. Schmaltz, H. Frauenrath, M. A. Winnik, C. F. J. Faul, I. Manners, *Nat. Commun.* **2017**, *8*, 15909.
- [62] D. Tao, Y. Cui, X. Huang, G. Lu, I. Manners, M. A. Winnik, C. Feng, *J. Colloid Interface Sci.* **2020**, *560*, 50.
- [63] L. MacFarlane, C. Zhao, J. Cai, H. Qiu, I. Manners, *Chem. Sci.* **2021**, *12*, 4661.
- [64] X. Wang, G. Guerin, H. Wang, Y. Wang, I. Manners, M. A. Winnik, *Science* **2007**, *317*, 644.
- [65] J. B. Gilroy, T. Gädt, G. R. Whittell, L. Chabanne, J. M. Mitchels, R. M. Richardson, M. A. Winnik, I. Manners, *Nat. Chem.* **2010**, *2*, 566.
- [66] J. Qian, Y. Lu, A. Chia, M. Zhang, P. A. Rugar, N. Gunari, G. C. Walker, G. Cambridge, F. He, G. Guerin, I. Manners, M. A. Winnik, *ACS Nano* **2013**, *7*, 3754.
- [67] J. Qian, G. Guerin, Y. Lu, G. Cambridge, I. Manners, M. A. Winnik, *Angew. Chem. Int. Ed.* **2011**, *50*, 1622.
- [68] H. Qiu, Y. Gao, A. van Du, R. Harniman, M. A. Winnik, I. Manners, *J. Am. Chem. Soc.* **2015**, *137*, 2375.
- [69] X. He, Y. He, M.-S. Hsiao, R. L. Harniman, S. Pearce, M. A. Winnik, I. Manners, *J. Am. Chem. Soc.* **2017**, *139*, 9221.
- [70] X. He, M. S. Hsiao, C. E. Boott, R. L. Harniman, A. Nazemi, X. Li, M. A. Winnik, I. Manners, *Nat. Mater.* **2017**, *16*, 481.
- [71] A. Nazemi, X. He, L. R. MacFarlane, R. L. Harniman, M.-S. Hsiao, M. A. Winnik, C. F. J. Faul, I. Manners, *J. Am. Chem. Soc.* **2017**, *139*, 4409.
- [72] S. Pearce, X. He, M. S. Hsiao, R. L. Harniman, L. R. MacFarlane, I. Manners, *Macromolecules* **2019**, *52*, 6068.
- [73] H. Qiu, Y. Gao, C. E. Boott, O. E. C. Gould, R. L. Harniman, M. J. Miles, S. E. D. Webb, M. A. Winnik, I. Manners, *Science* **2016**, *352*, 697.
- [74] Z. M. Hudson, D. J. Lunn, M. A. Winnik, I. Manners, *Nat. Commun.* **2014**, *5*, 3372.
- [75] X.-H. Jin, M. B. Price, J. R. Finnegan, C. E. Boott, J. M. Richter, A. Rao, S. M. Menke, R. H. Friend, G. R. Whittell, I. Manners, *Science* **2018**, *360*, 897.
- [76] P. A. Rugar, L. Chabanne, M. A. Winnik, I. Manners, *Science* **2012**, *337*, 559.

- [77] J. Xu, H. Zhou, Q. Yu, G. Guerin, I. Manners, M. A. Winnik, *Chem. Sci.* **2019**, *10*, 2280.
- [78] C. E. Boott, J. Gwyther, R. L. Harniman, D. W. Hayward, I. Manners, *Nat. Chem.* **2017**, *9*, 785.
- [79] A. M. Oliver, J. Gwyther, C. E. Boott, S. Davis, S. Pearce, I. Manners, *J. Am. Chem. Soc.* **2018**, *140*, 18104.
- [80] J. Du, R. K. O'Reilly, *Chem. Soc. Rev.* **2011**, *40*, 2402.
- [81] J.-F. Lutz, A. Laschewsky, *Macromol. Chem. Phys.* **2005**, *206*, 813.
- [82] A. Laschewsky, *Curr. Opin. Colloid Interface Sci.* **2003**, *8*, 274.
- [83] T. I. Löbbling, O. Ikkala, A. H. Gröschel, A. H. E. Müller, *ACS Macro Lett.* **2016**, *5*, 1044.
- [84] B. Fang, A. Walther, A. Wolf, Y. Xu, J. Yuan, A. H. E. Müller, *Angew. Chem. Int. Ed.* **2009**, *48*, 2877.
- [85] S. Lee, S. Jang, K. Kim, J. Jeon, S.-S. Kim, B.-H. Sohn, *Chem. Commun.* **2016**, *52*, 9430.
- [86] A. Walther, A. H. Müller, *Chem. Commun.* **2009**, 1127.
- [87] W. Kong, W. Jiang, Y. Zhu, B. Li, *Langmuir* **2012**, *28*, 11714.
- [88] K. Kim, S. Jang, J. Jeon, D. Kang, B.-H. Sohn, *Langmuir* **2018**, *34*, 4634.
- [89] T.-L. Nghiem, R. Chakroun, N. Janoszka, C. Chen, K. Klein, C. K. Wong, A. H. Gröschel, *Macromol. Rapid Commun.* **2020**, *41*, 2000301.
- [90] K. Skrabania, H. V. Berlepsch, C. Böttcher, A. Laschewsky, *Macromolecules* **2010**, *43*, 271.
- [91] T. I. Löbbling, O. Borisov, J. S. Haataja, O. Ikkala, A. H. Gröschel, A. H. E. Müller, *Nat. Commun.* **2016**, *7*, 12097.
- [92] T.-L. Nghiem, T. I. Löbbling, A. H. Gröschel, *Polym. Chem.* **2018**, *9*, 1583.
- [93] A. O. Moughton, M. A. Hillmyer, T. P. Lodge, *Macromolecules* **2012**, *45*, 2.
- [94] L. Wang, J. Lin, *Soft Matter* **2011**, *7*, 3383.
- [95] A. H. Gröschel, A. H. E. Müller, *Nanoscale* **2015**, *7*, 11841.
- [96] C. K. Wong, X. Qiang, A. H. Müller, A. H. Gröschel, *Prog. Polym. Sci.* **2020**, *102*, 101211.
- [97] T. Pelras, C. S. Mahon, M. Müllner, *Angew. Chem. Int. Ed.* **2018**, *57*, 6982.
- [98] U. Nayanathara, S. S. Kermaniyan, G. K. Such, *Macromol. Rapid Commun.* **2020**, *41*, 2000298.
- [99] H. Dou, G. Liu, J. Dupont, L. Hong, *Soft Matter* **2010**, *6*, 4214.

- 
- [100] J. Dupont, G. Liu, K. I. Niihara, R. Kimoto, H. Jinnai, *Angew. Chem. Int. Ed.* **2009**, *48*, 6144.
- [101] E. Hoppenbrouwers, Z. Li, G. Liu, *Macromolecules* **2003**, *36*, 876.
- [102] J. Hu, G. Njikang, G. Liu, *Macromolecules* **2008**, *41*, 7993.
- [103] X. Liu, Y. Ding, J. Liu, S. Lin, Q. Zhuang, *Eur. Polym. J.* **2019**, *116*, 342.
- [104] G. Njikang, D. Han, J. Wang, G. Liu, *Macromolecules* **2008**, *41*, 9727.
- [105] W. Zhang, J. X. He, Q. Liu, G. Q. Ke, X. Dong, *AMR* **2014**, *1049-1050*, 137.
- [106] S.-W. Kuo, P.-H. Tung, C.-L. Lai, K.-U. Jeong, F.-C. Chang, *Macromol. Rapid Commun.* **2008**, *29*, 229.
- [107] S. W. Kuo, P. H. Tung, F. C. Chang, *Eur. Polym. J.* **2009**, *45*, 1924.
- [108] I. K. Voets, A. de Keizer, F. A. Leermakers, A. Debuigne, R. Jérôme, C. Detrembleur, M. A. Cohen Stuart, *Eur. Polym. J.* **2009**, *45*, 2913.
- [109] C. LoPresti, M. Massignani, C. Fernyhough, A. Blanazs, A. J. Ryan, J. Madsen, N. J. Warren, S. P. Armes, A. L. Lewis, S. Chirasatitsin, A. J. Engler, G. Battaglia, *ACS Nano* **2011**, *5*, 1775.
- [110] J. Hu, G. Liu, *Macromolecules* **2005**, *38*, 8058.
- [111] G. Srinivas, J. W. Pitera, *Nano Lett.* **2008**, *8*, 611.
- [112] R. Zheng, G. Liu, X. Yan, *J. Am. Chem. Soc.* **2005**, *127*, 15358.
- [113] D. A. Christian, A. Tian, W. G. Ellenbroek, I. Levental, K. Rajagopal, P. A. Janmey, A. J. Liu, T. Baumgart, D. E. Discher, *Nat. Mater.* **2009**, *8*, 843.
- [114] H. P. Hsu, W. Paul, K. Binder, *Macromol. Theory Simul.* **2007**, *16*, 660.
- [115] J. de Jong, G. ten Brinke, *Macromol. Theory Simul.* **2004**, *13*, 318.
- [116] R. Stepanyan, A. Subbotin, G. ten Brinke, *Macromolecules* **2002**, *35*, 5640.
- [117] P. E. Theodorakis, W. Paul, K. Binder, *Macromolecules* **2010**, *43*, 5137.
- [118] J. Schmelz, F. H. Schacher, H. Schmalz, *Soft Matter* **2013**, *9*, 2101.
- [119] S. Rosenfeldt, F. Lüdel, C. Schulreich, T. Hellweg, A. Radulescu, J. Schmelz, H. Schmalz, L. Harnau, *Phys. Chem. Chem. Phys.* **2012**, *14*, 12750.
- [120] H. Schmalz, J. Schmelz, M. Drechsler, J. Yuan, A. Walther, K. Schweimer, A. M. Mihut, *Macromolecules* **2008**, *41*, 3235.
- [121] J. Schmelz, H. Schmalz, *Polymer* **2012**, *53*, 4333.
- [122] A. M. Oliver, J. Gwyther, M. A. Winnik, I. Manners, *Macromolecules* **2018**, *51*, 222.
- [123] A. M. Oliver, R. J. Spontak, I. Manners, *Polym. Chem.* **2019**, *10*, 2559.
- [124] A. Nunns, G. R. Whittell, M. A. Winnik, I. Manners, *Macromolecules* **2014**, *47*, 8420.

- [125] J. R. Finnegan, D. J. Lunn, O. E. Gould, Z. M. Hudson, G. R. Whittell, M. A. Winnik, I. Manners, *J. Am. Chem. Soc.* **2014**, *136*, 13835.
- [126] M. Cruz, J. Xu, Q. Yu, G. Guerin, I. Manners, M. A. Winnik, *Macromol. Rapid Commun.* **2018**, *39*, 1.
- [127] J. Xu, H. Zhou, Q. Yu, I. Manners, M. A. Winnik, *J. Am. Chem. Soc.* **2018**, *140*, 2619.
- [128] C. E. Boott, R. F. Laine, P. Mahou, J. R. Finnegan, E. M. Leitao, S. E. Webb, C. F. Kaminski, I. Manners, *Chem. Eur. J.* **2015**, *21*, 18539.
- [129] J. C. Wittmann, A. M. Hodge, B. Lotz, *J. Polym. Sci. Polym. Phys. Ed.* **1983**, *21*, 2495.
- [130] J. C. Wittmann, B. Lotz, *J. Polym. Sci. Polym. Phys. Ed.* **1981**, *19*, 1837.
- [131] H. Wang, W. Lin, K. P. Fritz, G. D. Scholes, M. A. Winnik, I. Manners, *J. Am. Chem. Soc.* **2007**, *129*, 12924.
- [132] H. Wang, A. J. Patil, K. Liu, S. Petrov, S. Mann, M. A. Winnik, I. Manners, *Adv. Mater.* **2009**, *21*, 1805.
- [133] P. A. Rugar, G. Cambridge, M. A. Winnik, I. Manners, *J. Am. Chem. Soc.* **2011**, *133*, 16947.
- [134] A. Nazemi, C. E. Boott, D. J. Lunn, J. Gwyther, D. W. Hayward, R. M. Richardson, M. A. Winnik, I. Manners, *J. Am. Chem. Soc.* **2016**, *138*, 4484.
- [135] H. Qiu, G. Cambridge, M. A. Winnik, I. Manners, *J. Am. Chem. Soc.* **2013**, *135*, 12180.
- [136] S. Song, X. Liu, E. Nikbin, J. Y. Howe, Q. Yu, I. Manners, M. A. Winnik, *J. Am. Chem. Soc.* **2021**, *143*, 6266.
- [137] F. He, T. Gädt, I. Manners, M. A. Winnik, *J. Am. Chem. Soc.* **2011**, *133*, 9095.
- [138] S. T. Street, Y. He, X. H. Jin, L. Hodgson, P. Verkade, I. Manners, *Chem. Sci.* **2020**, *11*, 8394.
- [139] X. He, J. R. Finnegan, D. W. Hayward, L. R. MacFarlane, R. L. Harniman, I. Manners, *Macromolecules* **2020**, *53*, 10591.
- [140] J. Qian, X. Li, D. J. Lunn, J. Gwyther, Z. M. Hudson, E. Kynaston, P. A. Rugar, M. A. Winnik, I. Manners, *J. Am. Chem. Soc.* **2014**, *136*, 4121.
- [141] D. Tao, C. Feng, Y. Cui, X. Yang, I. Manners, M. A. Winnik, X. Huang, *J. Am. Chem. Soc.* **2017**, *139*, 7136.
- [142] D. Tao, Z. Wang, X. Huang, M. Tian, G. Lu, I. Manners, M. A. Winnik, C. Feng, *Angew. Chem. Int. Ed.* **2020**, *59*, 8232.
- [143] Z. M. Hudson, C. E. Boott, M. E. Robinson, P. A. Rugar, M. A. Winnik, I. Manners, *Nat. Chem.* **2014**, *6*, 893.

- [144] F. Wurm, A. F. Kilbinger, *Angew. Chem. Int. Ed.* **2009**, *48*, 8412.
- [145] A. Kirillova, C. Marschelke, A. Synytska, *ACS Appl. Mater. Interfaces* **2019**, *11*, 9643.
- [146] A. Walther, A. H. E. Müller, *Soft Matter* **2008**, *4*, 663.
- [147] R. Erhardt, A. Böker, H. Zettl, H. Kaya, W. Pyckhout-Hintzen, G. Krausch, V. Abetz, A. H. E. Müller, *Macromolecules* **2001**, *34*, 1069.
- [148] Liu, V. Abetz, A. H. E. Müller, *Macromolecules* **2003**, *36*, 7894.
- [149] A. Walther, M. Drechsler, S. Rosenfeldt, L. Harnau, M. Ballauff, V. Abetz, A. H. E. Müller, *J. Am. Chem. Soc.* **2009**, *131*, 4720.
- [150] A. Wolf, A. Walther, A. H. E. Müller, *Macromolecules* **2011**, *44*, 9221.
- [151] A. Walther, X. André, M. Drechsler, V. Abetz, A. H. E. Müller, *J. Am. Chem. Soc.* **2007**, *129*, 6187.
- [152] A. Walther, M. Drechsler, A. H. E. Müller, *Soft Matter* **2009**, *5*, 385.
- [153] A. Walther, A. H. E. Müller, *Chem. Rev.* **2013**, *113*, 5194.
- [154] R. Saito, A. Fujita, A. Ichimura, K. Ishizu, *J. Polym. Sci. A Polym. Chem.* **2000**, *38*, 2091.
- [155] L. Cheng, G. Hou, J. Miao, D. Chen, M. Jiang, L. Zhu, *Macromolecules* **2008**, *41*, 8159.
- [156] K. Watanabe, N. Kaizawa, B. J. Ree, T. Yamamoto, K. Tajima, T. Isono, T. Satoh, *Angew. Chem. Int. Ed.* **2021**, *60*, 18122.
- [157] R. Erhardt, M. Zhang, A. Böker, H. Zettl, C. Abetz, P. Frederik, G. Krausch, V. Abetz, A. H. E. Müller, *J. Am. Chem. Soc.* **2003**, *125*, 3260.
- [158] J. H. Schröder, M. Doroshenko, D. Pirner, M. E. Mauer, B. Förster, V. Boyko, B. Reck, K. J. Roschmann, A. H. Müller, S. Förster, *Polymer* **2016**, *106*, 208.
- [159] A. Walther, M. Hoffmann, A. H. E. Müller, *Angew. Chem. Int. Ed.* **2008**, *47*, 711.
- [160] X. Qiang, S. Franzka, G. Quintieri, X. Dai, C. K. Wong, A. H. Gröschel, *Angew. Chem. Int. Ed.*, DOI: 10.1002/anie.202105235.
- [161] A. H. Gröschel, A. Walther, T. I. Löbbling, J. Schmelz, A. Hanisch, H. Schmalz, A. H. E. Müller, *J. Am. Chem. Soc.* **2012**, *134*, 13850.
- [162] J. Wang, W. Li, J. Zhu, *Polymer* **2014**, *55*, 1079.
- [163] T. Zhou, B. Dong, H. Qi, S. Mei, C. Y. Li, *J. Polym. Sci. B Polym. Phys.* **2014**, *52*, 1620.
- [164] D. J. Lunn, J. R. Finnegan, I. Manners, *Chem. Sci.* **2015**, *6*, 3663.
- [165] S. C. Glotzer, M. J. Solomon, *Nat. Mater.* **2007**, *6*, 557.

- [166] D. J. Lunn, O. E. C. Gould, G. R. Whittell, D. P. Armstrong, K. P. Mineart, M. A. Winnik, R. J. Spontak, P. G. Pringle, I. Manners, *Nat. Commun.* **2016**, *7*, 12371.
- [167] H. Qiu, Z. M. Hudson, M. A. Winnik, I. Manners, *Science* **2015**, *347*, 1329.
- [168] X. Li, Y. Gao, C. E. Boott, D. W. Hayward, R. Harniman, G. R. Whittell, R. M. Richardson, M. A. Winnik, I. Manners, *J. Am. Chem. Soc.* **2016**, *138*, 4087.
- [169] H. Qiu, G. Russo, P. A. Rugar, L. Chabanne, M. A. Winnik, I. Manners, *Angew. Chem. Int. Ed.* **2012**, *51*, 11882.
- [170] X. Li, Y. Gao, C. E. Boott, M. A. Winnik, I. Manners, *Nat. Commun.* **2015**, *6*, 8127.
- [171] X. Li, Y. Gao, R. Harniman, M. Winnik, I. Manners, *J. Am. Chem. Soc.* **2016**, *138*, 12902.
- [172] A. H. Gröschel, T. I. Löbbling, P. D. Petrov, M. Müllner, C. Kuttner, F. Wieberger, A. H. E. Müller, *Angew. Chem. Int. Ed.* **2013**, *52*, 3602.
- [173] R. Bahrami, T. I. Löbbling, A. H. Gröschel, H. Schmalz, A. H. E. Müller, V. Altstädt, *ACS Nano* **2014**, *8*, 10048.
- [174] A. H. Gröschel, F. H. Schacher, H. Schmalz, O. V. Borisov, E. B. Zhulina, A. Walther, A. H. E. Müller, *Nat. Commun.* **2012**, *3*, 710.
- [175] J. Schmelz, D. Pirner, M. Krekhova, T. M. Ruhland, H. Schmalz, *Soft Matter* **2013**, *9*, 11173.
- [176] T. M. Ruhland, A. H. Gröschel, N. Ballard, T. S. Skelhon, A. Walther, A. H. E. Müller, S. A. F. Bon, *Langmuir* **2013**, *29*, 1388.
- [177] T. M. Ruhland, A. H. Gröschel, A. Walther, A. H. E. Müller, *Langmuir* **2011**, *27*, 9807.
- [178] T. Gegenhuber, M. Krekhova, J. Schöbel, A. H. Gröschel, H. Schmalz, *ACS Macro Lett.* **2016**, *5*, 306.
- [179] S. Bärwinkel, R. Bahrami, T. I. Löbbling, H. Schmalz, A. H. E. Müller, V. Altstädt, *Adv. Eng. Mater.* **2016**, *18*, 814.
- [180] R. Bahrami, T. I. Löbbling, H. Schmalz, A. H. Müller, V. Altstädt, *Polymer* **2017**, *109*, 229.
- [181] K. C. Bryson, T. I. Löbbling, A. H. E. Müller, T. P. Russell, R. C. Hayward, *Macromolecules* **2015**, *48*, 4220.
- [182] A. Walther, K. Matussek, A. H. E. Müller, *ACS Nano* **2008**, *2*, 1167.
- [183] Q. Yang, K. Loos, *Polym. Chem.* **2017**, *8*, 641.



## 2 Thesis Overview

This thesis consists of five publications, four have been published and one is submitted. The central aspect of this work, which was conducted in the framework of the *Collaborative Research Centre 840* (project A2), is the preparation, modification as well as application of crystalline-core micelles (CCM) with surface-compartmentalised corona. The triblock terpolymers used have a semicrystalline polyethylene (PE) middle block and incompatible end blocks consisting of polystyrene (PS), and either poly(methyl methacrylate) (PMMA), functional poly(*N,N*-dialkylaminoethyl methacrylamide) (PDxA) produced by post-polymerization amidation of the PMMA block, or poly(ethylene oxide) (PEO).

The use of CCMs with functional PDxA patches immobilised on a carrier fibre creates a heterogeneous catalyst system as nanoparticles can be efficiently immobilized with preservation of their high catalytically active surface area. In **chapter 3**, the influence of the template on the gold nanoparticle catalysed alcoholysis of silanes is investigated by varying the micelle geometry and chemistry of the functional PDxA patches.

CCMs with stimuli-responsive patches (e.g. pH, temperature) could open up further possibilities, for example in self-regulating catalytic reactions. This possibility is examined in **chapter 4**, where the responsive behaviour of PDxA homopolymers with different substitution patterns of the amide groups is analysed. The already mentioned post-polymerization amidation of PMMA is also applied heterogeneously, which enables the modification of surfaces.

**Chapter 5** deals with the assembly of defined hierarchical superstructures from aqueous medium, harnessing the unique patchy structure of the fibres described in chapter 3. Here, the functional, nanometre-sized patches are employed to assist nucleation of a benzene-1,3,5-tricarboxamide (BTA) in order to achieve a controlled growth of BTA fibres from the supporting patchy fibres.

The influence of confinement within emulsion droplets (toluene in water emulsions) on the crystallization-driven self-assembly (CDSA) of PS-*b*-PE-*b*-PMMA (SEM) triblock terpolymers and its influence on the internal morphology of microparticles obtained after solvent evaporation is addressed in **chapter 6**. The studies show that the morphology strongly depends on the preparation method.

Up to now, CDSA of triblock terpolymers with a PE middle block always yielded patchy micelles, whereby a Janus-type structure should also be feasible in case of a sufficiently strong incompatibility of the corona forming blocks. Hence in **chapter 7** CDSA of a PS-*b*-PE-*b*-PEO

triblock terpolymer is studied with the aim to produce Janus micelles. The triblock terpolymer not only features two highly incompatible end blocks (PS and PEO) but also an additional crystallizable block in the micelle corona (PEO). TEM analyses using different staining agents revealed the presence of a Janus-type microphase-separated corona. In addition, the interfacial activity of the Janus worm-like CCMs (*w*CCMs) at the toluene-water interface was investigated. These significantly reduced the interfacial tension at the toluene/water interface compared to patchy SEM *w*CCMs with comparable micelle lengths, which can be attributed to the amphiphilic nature of the PS/PEO corona.

A brief summary of the obtained results is given in chapter 2.1 – 2.5.

## 2.1 Influence of Patch Size and Chemistry on the Catalytic Activity of Patchy Hybrid Nonwovens

In this work, patchy hybrid nonwovens were produced by coaxial electrospinning and subsequent incorporation of preformed gold nanoparticles (AuNPs). PS was used as core (carrier fibre) and patchy spherical (*s*CCM) or worm-like (*w*CCM) crystalline-core micelles as shell (functional surface coating), respectively. The embedded AuNPs offer the possibility to apply these systems as supported heterogeneous catalysts according to the "tea bag"-principle. The influence of the patch-like surface structure on the activity of the AuNP loaded hybrid fibre mats was systematically studied for the catalytic alcoholysis of dimethylphenylsilane in *n*-butanol (*n*-BuOH), to gain insight into the impact of micelle geometry, patch size and chemistry on the catalytic performance.

In order to introduce suitable anchor groups for NP stabilisation a new synthesis method was developed, which allows for a quantitative amidation of the PMMA compartments of patchy micelles from different PS-*b*-PE-*b*-PMMA (SEM) triblock terpolymers. Quantitative conversion was achieved by activation of the employed *N,N*-dialkylaminoethylamines (alkyl = methyl, *iso*-propyl) with *n*-butyl lithium. The obtained functionalized PS-*b*-PE-*b*-PD<sub>x</sub>A (SED<sub>x</sub>A) triblock terpolymers showed comparable solubility and thermal properties to the SEM precursors. This enabled the production of well-defined patchy *w*CCMs and *s*CCMs *via* crystallization-driven self-assembly (CDSA) in THF and 1,4-dioxane, respectively (Figure 2.1). Tailoring the corona block lengths yielded micelles with symmetrical ( $d_{PS} \approx d_{PDx_A}$ ) and asymmetrical ( $d_{PS} > d_{PDx_A}$ ) widths ( $d$ ) of the corona patches.

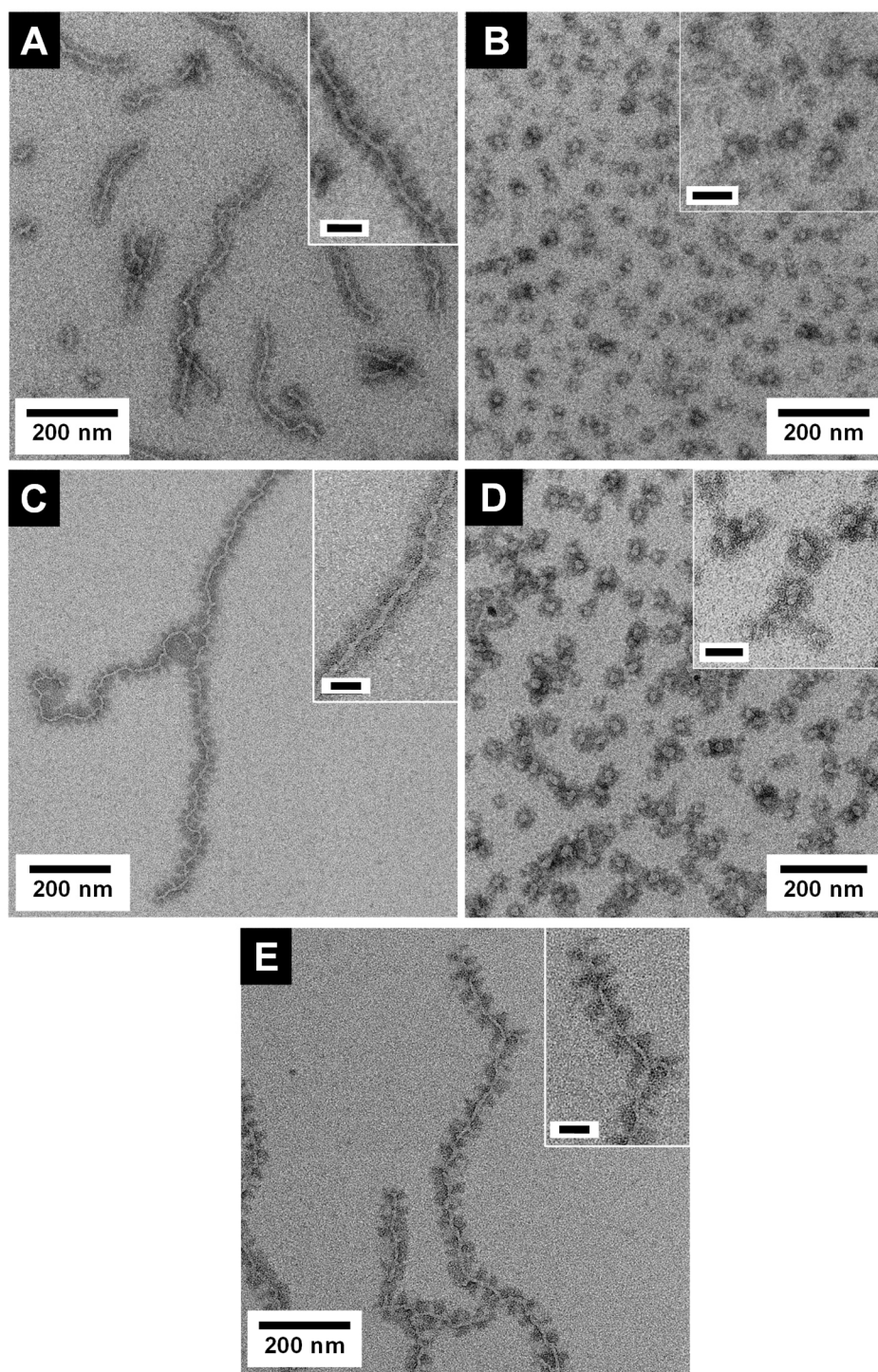


**Figure 2.1.** Transmission electron microscopy micrographs of different SEDxA CCMs.  $S_{28}E_{15}DiPA_{58}^{156}$  wCCMs (A) and sCCMs (B),  $S_{38}E_{21}DiPA_{41}^{181}$  wCCMs (C) and sCCMs (D), and  $S_{33}E_{17}DMA_{50}^{131}$  wCCMs (E); indices denote the weight fraction of the respective block and superscript gives the overall number average molecular weight in  $\text{kg}\cdot\text{mol}^{-1}$ . The PS domains were selectively stained with  $\text{RuO}_4$  and appear dark. Scale bars insets: 50 nm.

Patchy nonwovens (NWs) were produced by coaxial electrospinning (core: PS, shell: patchy-like s/wCCMs). Figure 2.2A shows a patchy nonwoven based on  $S_{33}E_{17}DMA_{50}^{131}$  wCCMs (s-SEDMA(w)), which was subsequently loaded with preformed, citrate-stabilized AuNPs by a

facile dipping process. Using scanning electron microscopy together with a back scattered electron (BSE) detector (Figure 2.2B) and small-angle X-ray scattering (SAXS, Figure 2.2C), the immobilization of the AuNPs in the NWs was investigated. The hybrid NWs showed a homogeneous loading with AuNPs, without any sign of significant agglomeration. The incorporated amount of NPs, which is relevant for the catalytic activity, was in the range of  $50 - 80 \mu\text{g}\cdot\text{cm}^{-2}$  determined by ICP-OES and UV-Vis.

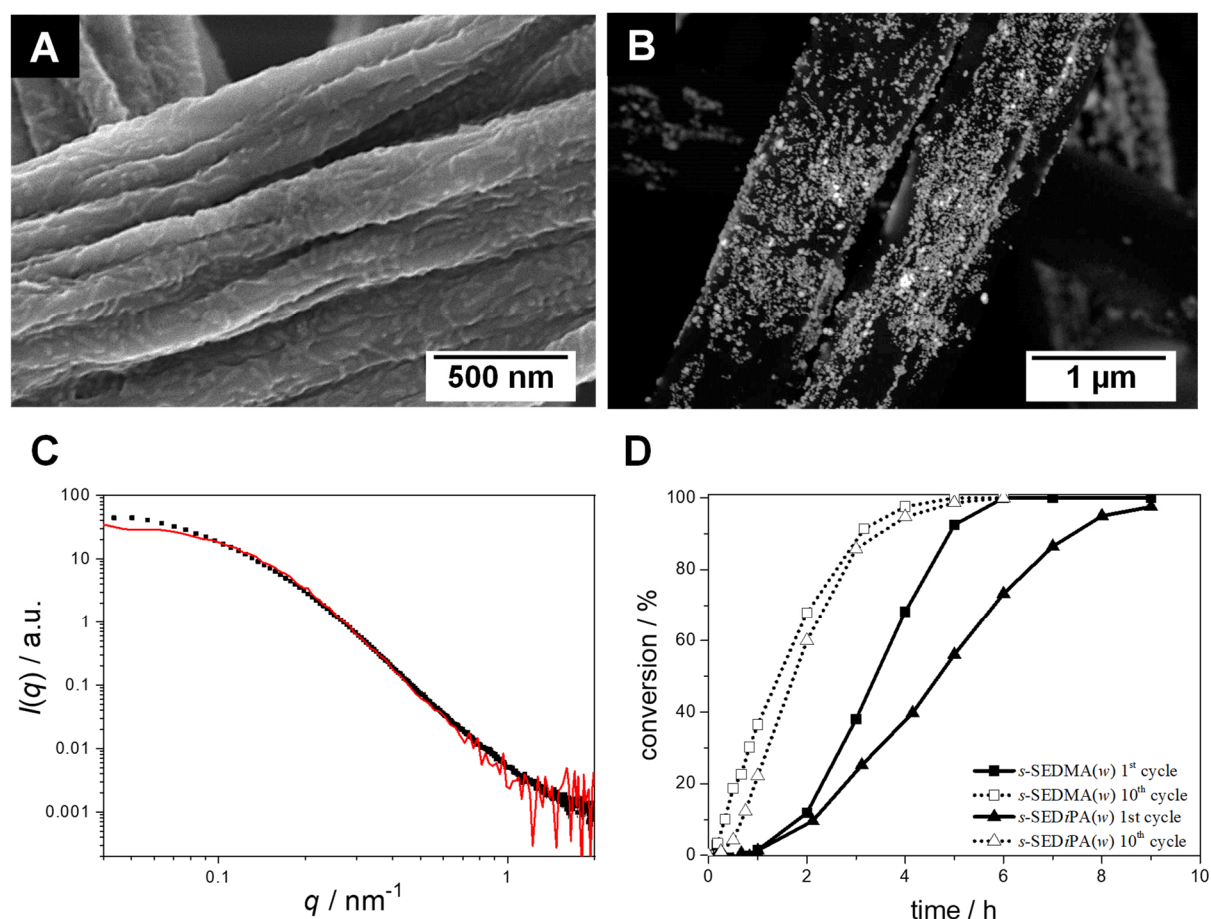


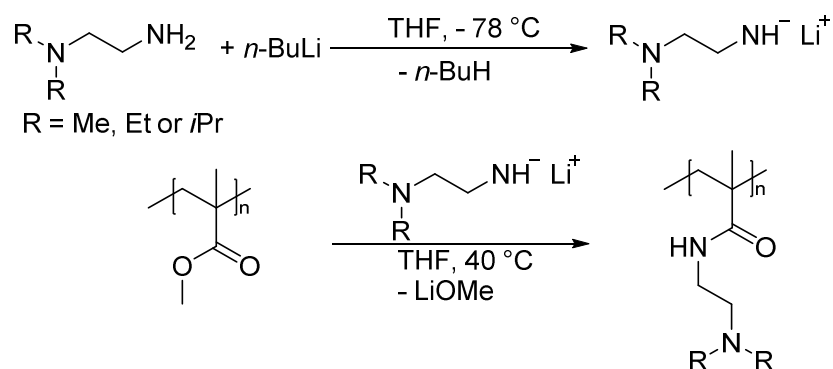
**Figure 2.2.** Scanning electron microscopy images of neat (A) and AuNP-loaded (B, BSE detector) patchy nonwovens based on  $\text{S}_{33}\text{E}_{17}\text{DMA}_{50}^{131}$  *w*CCMs (*s*-SEDMA(*w*)); the AuNPs in B) appear as bright dots. C) SAXS profiles of the AuNPs immobilized in the patchy nonwoven (filled squares) and of the corresponding used aqueous AuNP dispersion (red) before dipping. D) Comparison of conversion vs. time plots (1<sup>st</sup> and 10<sup>th</sup> cycles) for the catalytic alcoholysis of dimethylphenylsilane with hybrid NWs based on  $\text{S}_{28}\text{E}_{15}\text{DiPA}_{58}^{156}$  and  $\text{S}_{33}\text{E}_{17}\text{DMA}_{50}^{131}$  *w*CCMs as catalyst.

To study the catalytic activity of the produced hybrid NWs the alcoholysis of dimethylphenylsilane in *n*-BuOH was employed as model reaction. Reproducible quantitative conversion was observed even after 10 catalytic cycles, manifesting the excellent recyclability of the hybrid NWs. Because of the efficient stabilization of the NPs within the functional patchy hybrid NWs, a loss of catalytic activity can be successfully prevented. An influence of patch

chemistry (SEDMA *vs.* SEDiPA) was observed, reflected by a distinct induction phase and longer reaction times. This effect was clearly visible in the first catalysis cycles and was more pronounced for nonpolar DiPA patches, whereas all 10<sup>th</sup> catalysis cycles showed a comparable activity Figure 2.2D. This indicates that the swelling behaviour of the patches in the solvent (*n*-BuOH) and, thus, the accessibility of the NPs plays a major role in the first catalysis cycles, only. The studies with *s*CCMs indicate a similar dependency. Additionally, the rate constants of the catalytic alcoholysis were determined, assuming pseudo 1<sup>st</sup>-order kinetics with an induction phase.

## 2.2 Converting Poly(Methyl Methacrylate) into a Triple-Responsive Polymer

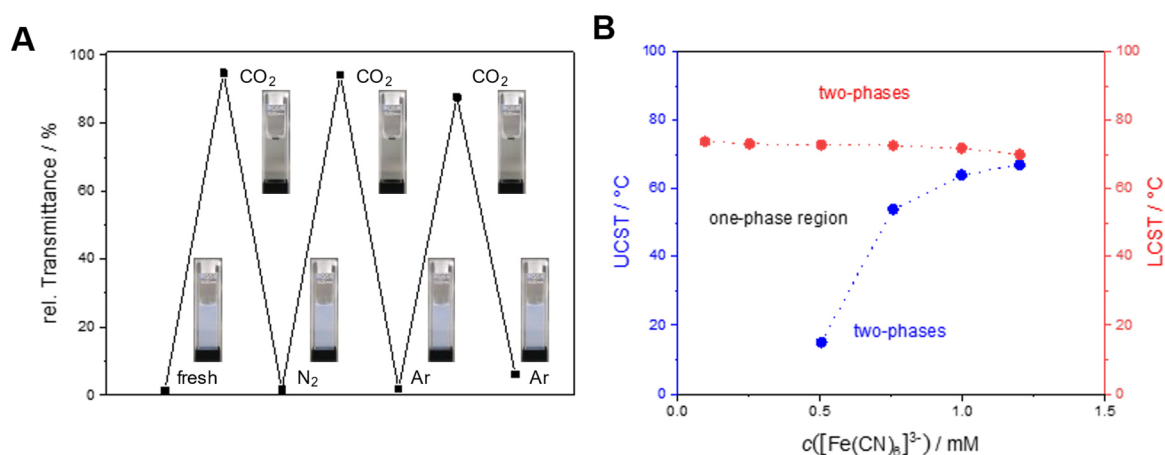
The aim of this work is to use the polymer analogues modification described in chapter 2.1 to transform PMMA into a stimuli-responsive polymer *via* amidation with activated *N,N*-dialkylethylenediamines (alkyl = methyl, ethyl, *iso*-propyl) according to Scheme 2.1. For example, the interfacial tension of functionalised patchy micelles could be controlled by external stimuli such as pH and/or temperature. This property also made it interesting for catalytic applications.



**Scheme 2.1.** Reaction scheme for polymer analogues modification of PMMA with activated *N,N*-dialkylethylenediamines.

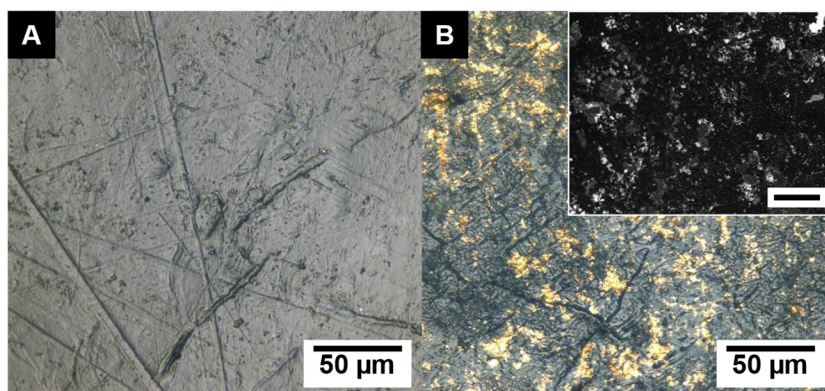
The polymers obtained show a distinct solubility behaviour in aqueous medium. While poly(*N,N*-diethylaminoethyl methacrylamide) (PDEA) and poly(*N,N*-di-*iso*-propyl-aminoethyl methacrylamide) (PDiPrA) show a temperature- and pH-responsive solubility, poly(*N,N*-dimethylaminoethyl methacrylamide) is soluble independent of pH and temperature. Compared to PDEA, the solubility of PDiPrA is shifted to lower pH values. PDEA shows a LCST (lower

critical solution temperature)-type solubility behaviour for  $\text{pH} \geq 8$ . The transition to the binary system (cloud point) can be controlled at room temperature through the pH value and for a fixed pH (in buffer solution) the cloud point decreases with increasing pH value. Additionally, the solubility of PDEA can be switched by addition (soluble) or release (insoluble) of carbon dioxide (Figure 2.3A). By a proper choice of pH, i.e. a certain fraction of the tertiary amino-groups need to be in the protonated state, both a LCST- and UCST (upper critical solution temperature)-type phase behaviour can be realised by the addition of trivalent hexacyanoferrate(III) ( $[\text{Fe}(\text{CN})_6]^{3-}$ ) counteranions (Figure 2.3B).



**Scheme 2.3.** A) UV-Vis measurements of PDEA<sub>210</sub> in pH 10 buffer at 55 °C ( $c = 1 \text{ g}\cdot\text{L}^{-1}$ ) upon subsequently bubbling CO<sub>2</sub>, N<sub>2</sub> or Ar through a cuvette. B) Tailoring the thermo-responsive solution behaviour of PDEA<sub>1030</sub> ( $c = 1 \text{ g}\cdot\text{L}^{-1}$ ) in the presence of trivalent  $[\text{Fe}(\text{CN})_6]^{3-}$  counterions in pH 8 buffer solutions. In the used notation PDEA<sub>x</sub> the index denotes the number average degree of polymerization.

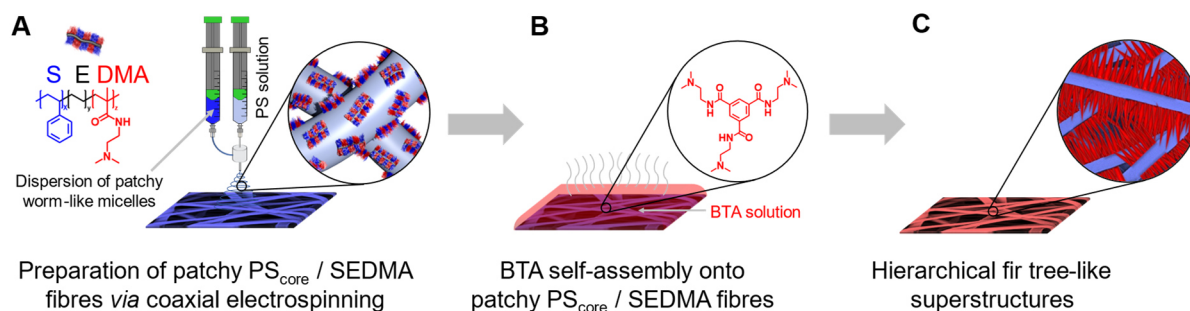
Furthermore, amidation can be conducted on a bulk PMMA disc with activated *N,N*-diethylethylenediamine (heterogenous amidation), enabling an easy surface modification. Because of the increase in polarity after amidation, the contact angle to water at 25 °C decreases from  $(93 \pm 2)^\circ$  to  $(49 \pm 5)^\circ$ . The diethylamino anchor groups of the amidated PMMA surface can also be used to fix preformed, citrate-stabilized AuNPs. After functionalisation and loading with AuNP, the decoration of the disc surface with AuNP is clearly visible. (Figure 2.4B).



**Figure 2.4.** Digital images of the surface of the PMMA disc before (A), and after heterogeneous amidation with subsequent immobilisation of AuNPs (B). The inset shows the corresponding scanning electron micrograph taken with a BSE detector (Au-rich regions appear bright, scale bar: 100  $\mu\text{m}$ ).

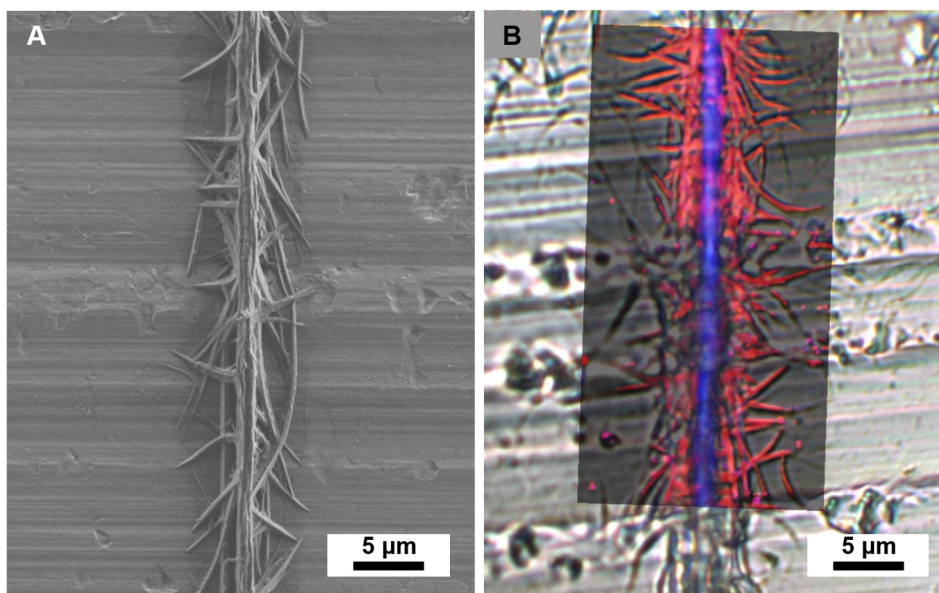
### 2.3 Hierarchical Superstructures by Combining Crystallization-Driven and Molecular Self-Assembly

This work demonstrates that the combination of two highly relevant self assembly concepts, CDSA and (supra)molecular self-assembly, provides access to well-defined complex hierarchical superstructures. Here, the unique corona structure of patchy  $w\text{CCMs}$  is utilized to induce and control the molecular self-assembly of a designed benzene-1,3,5-tricarboxamide (BTA). The patchy  $w\text{CCMs}$  bearing pendant, functional tertiary amino groups in one of the corona patches were prepared by CDSA of a SEDMA ( $\text{S}_{33}\text{E}_{17}\text{DMA}_{50}^{131}$ , indices denote the weight fraction of the respective block and superscript gives the overall number average molecular weight in  $\text{kg}\cdot\text{mol}^{-1}$ ) triblock terpolymer and immobilized on a supporting PS fibre by coaxial electrospinning (Scheme 2.2A). The obtained  $\text{PS}_{\text{core}} / \text{SEDMA}$  fibres (patchy fibres) were then immersed in an aqueous solution of  $N^1, N^3, N^5$ -tris[2-(dimethylamino)-ethyl]-1,3,5-benzenetricarboxamide (BTA-Methyl, Scheme 2.2B) to induce patch-mediated molecular self-assembly of BTA-Methyl to yield fir tree-like superstructures upon solvent evaporation (Scheme 2.2C).



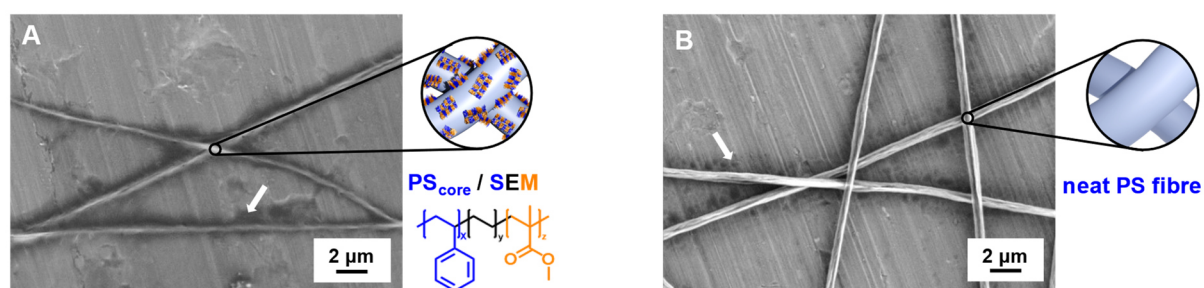
**Scheme 2.2.** Preparation of hierarchical fir tree-like superstructures starting from coaxial electrospun patchy PS<sub>core</sub> / SEDMA fibres (A) followed by immersion in an aqueous BTA-Methyl solution and evaporation to induce molecular self-assembly of BTA-methyl onto the patchy fibres (B). Resulting hierarchical fir tree-like superstructures after complete evaporation of the solvent.

Figure 2.5A shows a scanning electron microscopy image of the obtained fir tree-like superstructure. Here, the BTA-Methyl fibres (“needles”) grew away from the patchy polymer fibre core (“branch”) in an oriented manner. In addition, the BTA-Methyl fibres can be observed at different positions, indicating different starting points due to the randomly distributed wCCMs at the surface of the PS<sub>core</sub> / SEDMA fibre. In the respective Raman image of the formed superstructure (Figure 2.5B), the patchy PS<sub>core</sub> / SEDMA fibre (coloured in blue) and the BTA “needles (coloured in red) can be clearly distinguished, thus, confirming the fir tree-like structure.



**Figure 2.5.** A) Scanning electron micrograph of a hierarchical fir tree-like superstructure produced by molecular self-assembly of an aqueous BTA-Methyl solution (0.050 wt.%) onto patchy PS<sub>core</sub> / SEDMA fibres after solvent evaporation. B) Overlay of the spatially resolved component distribution from Raman imaging (blue: PS rich regions; red: BTA-Methyl rich regions) with the optical microscopy micrograph of the fir tree-like superstructure.

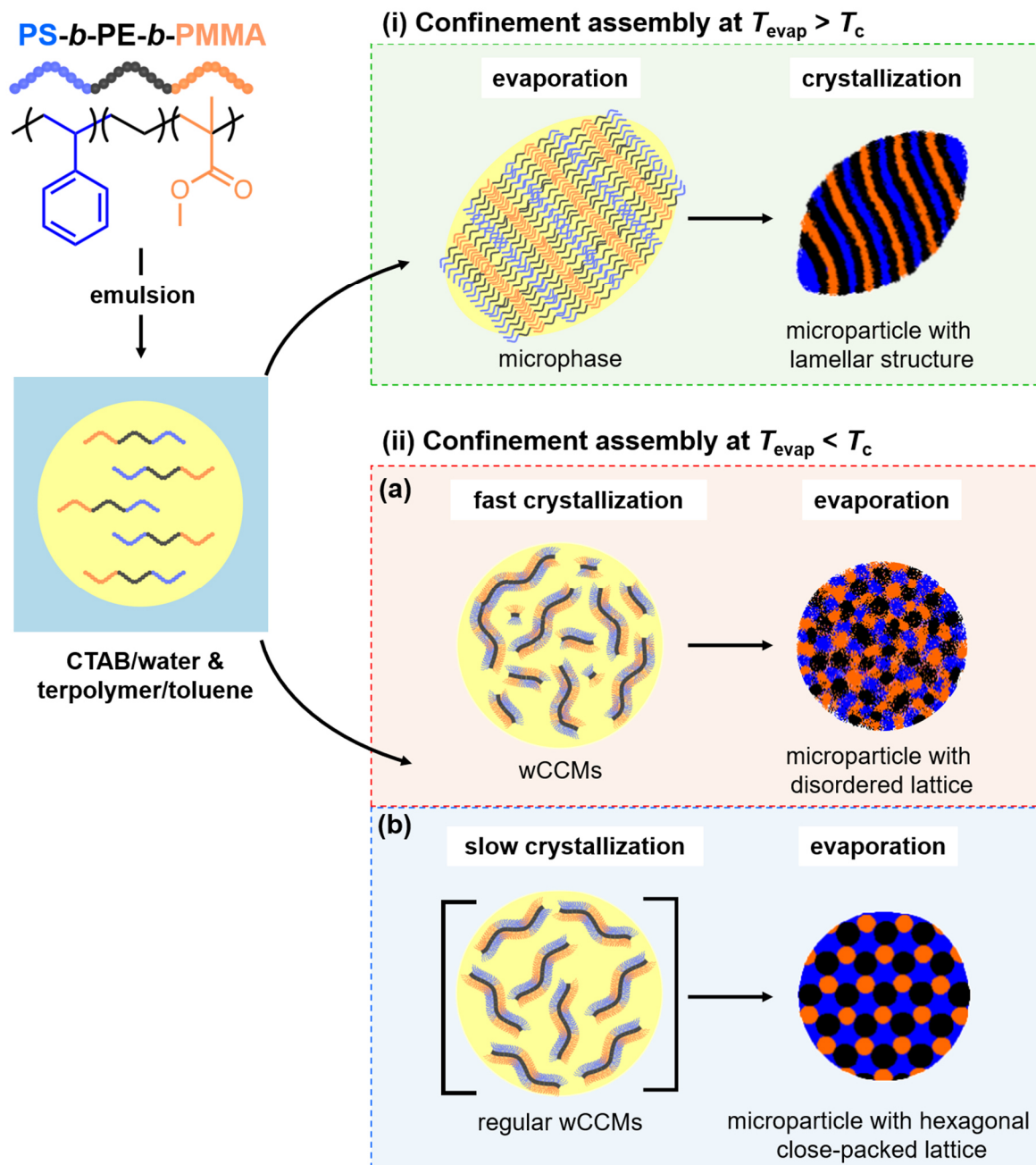
The key for the patch-mediated molecular self-assembly of the BTA from the polymer fibres is the chemical match between functional groups in the surface patches and the BTA peripheral groups that in turn controls the solubility and accessibility of the patch for the BTA. This is underlined by reference experiments with patchy fibres based on SEM *w*CCMs (Figure 2.6A), which feature only non-functional, hydrophobic PMMA patches, as well as with neat PS fibres (no surface patches, Figure 2.6B). These led to an accumulation of unstructured BTA methyl assemblies near the polymer fibre, i.e., no controlled molecular self-assembly to defined BTA fibres was observed.



**Figure 2.6.** Scanning electron images showing the absence of hierarchical superstructures. A) PS fibres with patchy SEM *w*CCMs (PS<sub>core</sub> / SEM) and B) neat PS fibres in the molecular self-assembly of BTA-Methyl. Unstructured BTA-Methyl assemblies formed upon drying (indicated by arrows).

## 2.4 Frustrated Microparticle Morphologies of a Semicrystalline Triblock Terpolymer in 3D Soft Confinement

In this publication, the (crystallization-driven) self-assembly of a SEM triblock terpolymer (S<sub>32</sub>E<sub>36</sub>M<sub>32</sub>)<sup>93</sup>, indices denote weight fraction of the blocks and superscript is the number average molecular weight in kg·mol<sup>-1</sup>) in the three-dimensional (3D) confinement of emulsion droplets was investigated as a route to the formation of functional microparticles. We found that the resulting morphology of the microparticles depends decisively on the temperature at which the toluene evaporates in the water/toluene emulsion (Scheme 2.3). At an evaporation temperature ( $T_{\text{evap}}$ ) of 80 °C above the crystallization temperature ( $T_c$ ) of the PE block (in bulk = 67 °C) a lamellar morphology is formed. In contrast, disordered structures were obtained when a dispersion of preformed short *w*CCMs was emulsified and evaporated at 30 °C. However, if the emulsions were cooled to a  $T_{\text{evap}}$  being close to the crystallization temperature of the PE block in solution ( $T_{c,\text{solution}}$ ) well-ordered hexagonal structures were obtained.



**Scheme 2.3.** Illustration of two different pathways for the 3D confinement self-assembly of  $S_{32}E_{36}M_{32}^{93}$ . Emulsification of  $S_{32}E_{36}M_{32}^{93}$  in toluene with CTAB/water followed by two evaporation/crystallization protocols: (i) Evaporation first (confinement assembly at  $T_{\text{evap}} > T_c$ ). (ii) Crystallization first (confinement assembly at  $T_{\text{evap}} < T_c$ ).

At  $T_{\text{evap}} > T_c$ , microphase separation occurs first and initially results in a lamella-lamella (*ll*) morphology with different orientations, where the molten PE lamellae are entrapped between the PS and PMMA lamellae. Upon cooling, the PE block crystallizes within this confinement and the morphology is kept. In addition to the axially aligned lamellae (Figure 2.7A), we have

also identified a number of other co-existing lamellae orientations that are more strongly influenced by the curved confinement (Figure 2.7B-D). This relatively selective process predominantly forms bud-like particles, especially at low concentrations.

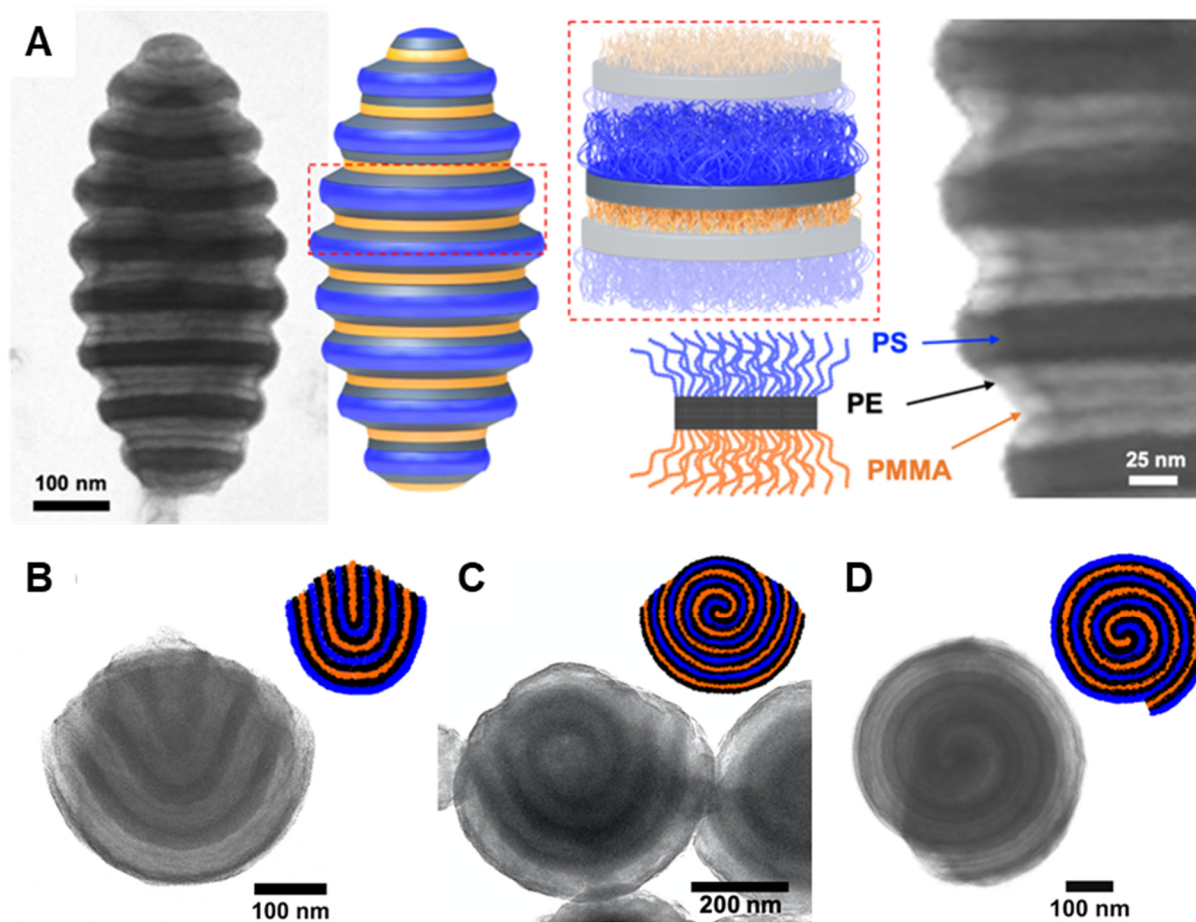


**Figure 2.7.** Different lamellar morphologies of S<sub>32</sub>E<sub>36</sub>M<sub>32</sub><sup>93</sup> (indices denote the weight fraction of the respective block and superscript gives the overall number average molecular weight in kg·mol<sup>-1</sup>) by evaporation at  $T_{\text{evap}} > T_c$ . (A) prolate ellipsoid microparticle with axially stacked lamellae of PS/PE/PMMA, (B) bud-like, (C) hemisphere/helix, and (D) spherocone morphology (RuO<sub>4</sub> was employed for selective staining of PS domains, which appears dark). Schematics clarifying the arrangement of polymer chains.

If evaporation takes place at significantly lower temperatures ( $T_{\text{evap}} \leq T_{c,\text{solution}}$ ), crystallization of the PE block from solution and, thus, CDSA to *w*CCMs occurs simultaneously to the evaporation of toluene (Figure 2.8). In this case, defined hexagonal structures can be realised. Thus, the confinement has an influence on the resulting morphology, since the forming *w*CCMs have to adapt to the conditions of the curved interface in the emulsion droplet. Presumably, the interfacial activity of the *w*CCMs, which gives them a pre-orientation at the water/toluene interface, also plays a role.

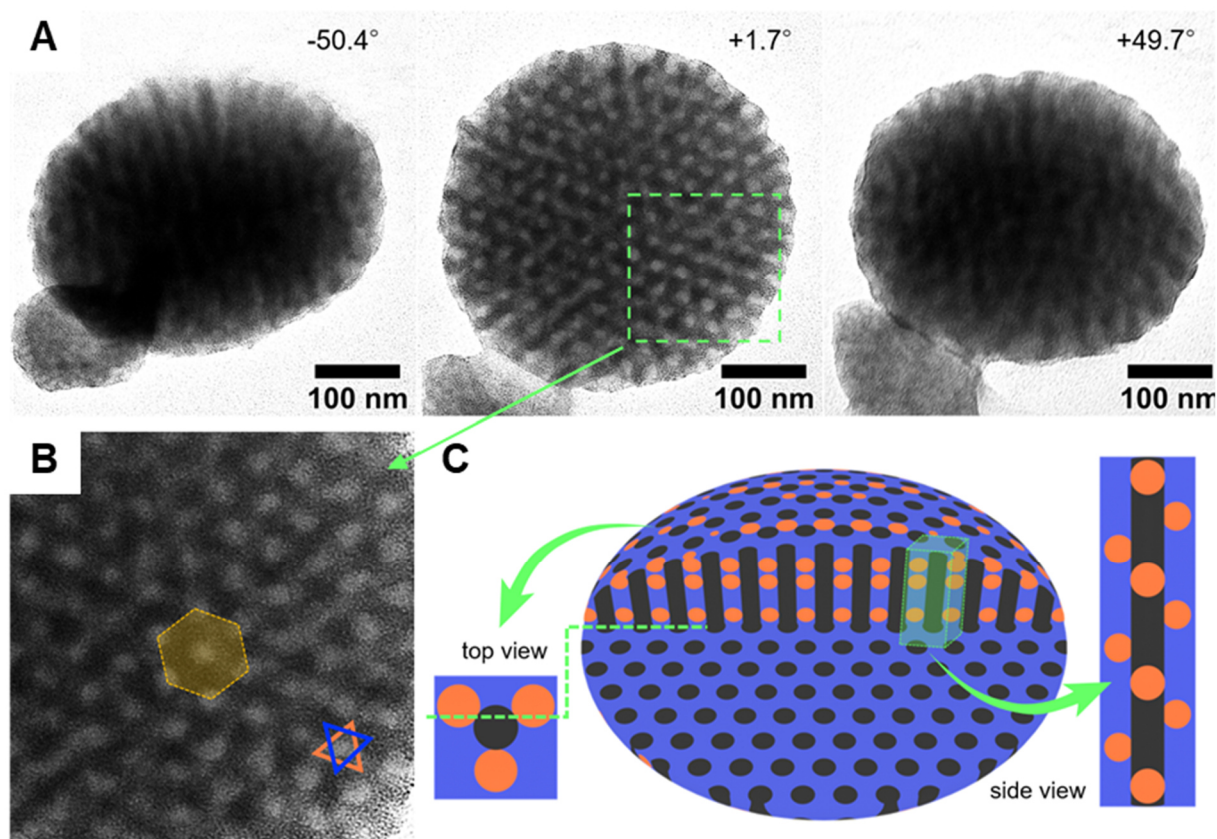


**Figure 2.8.** Hexagonally ordered  $S_{32}E_{36}M_{32}^{93}$  (indices denote the weight fraction of the respective block and superscript gives the overall number average molecular weight in  $\text{kg}\cdot\text{mol}^{-1}$ ) microparticles after cooling the emulsion from  $80\text{ }^{\circ}\text{C}$  to  $30\text{ }^{\circ}\text{C}$ , followed by simultaneous crystallization and evaporation at  $T_{\text{evap}} = 30\text{ }^{\circ}\text{C}$ . (A) TEM tilt series images, tilt angles are as marked in the images. (B) Close-up showing the three microphases of PS, PE and PMMA (PS domains appear dark due to  $\text{RuO}_4$  staining). (C) Schematic clarifying the packing of the blocks.

The frequency of these "frustrated" morphologies depends not only on the preparation route, but also on polymer concentration and evaporation rate. Overall, this study shows that the complex morphological behaviour of semi-crystalline block copolymers in 3D confinement can give rise to a range of microparticle morphologies from one single triblock terpolymer, including hexagonally packed cylinders with compartmentalized matrix, helical and double stair case morphologies, as well as spherocones

## 2.5 Janus or Patchy: Who Wins the Battle in Crystallization-Driven Self-Assembly of Double Crystalline Triblock Terpolymers?

This contribution addresses the question, whether *w*CCMs with a Janus-type microphase-separated corona are accessible *via* CDSA of triblock terpolymers with a crystallizable middle block. Up to now, only the formation of patchy *w*CCMs was reported, despite the fact that from a theoretical point of view Janus micelles should be possible for a sufficiently high incompatibility of the corona blocks or the presence of an additional driving force fostering the formation of a Janus structure. In this work a PS-*b*-PE-*b*-PEO ( $S_{280}E_{1350}EO_{670}$ , indices denote number average degrees of polymerization of the respective blocks) triblock terpolymer, containing two strongly incompatible corona-forming blocks (PS and PEO) was used. In addition, PEO has the ability to crystallize within the corona. The SEEO *w*CCMs were prepared by CDSA in toluene and the ability of the PEO corona block to crystallize was confirmed by micro-differential scanning calorimetry measurements in toluene. TEM was employed to characterize the type of microphase-separation in the corona, as TEM is the only method to unambiguously differentiate between a patchy or Janus-type structure. To this end, different staining methods were used to elucidate the corona structure. It was recognised that without staining and with OsO<sub>4</sub> only the PEO hemi-cylinder in the corona is visible. In contrast, if RuO<sub>4</sub> was used as staining agent (stains both PS and PEO), the entire width of the worm-like micelles (PE core plus PS and PEO hemi-corona) can be visualised. An assignment of the respective hemi-cylinders is possible due to the selective staining of PEO with OsO<sub>4</sub> and their different thicknesses (Figure 2.9).

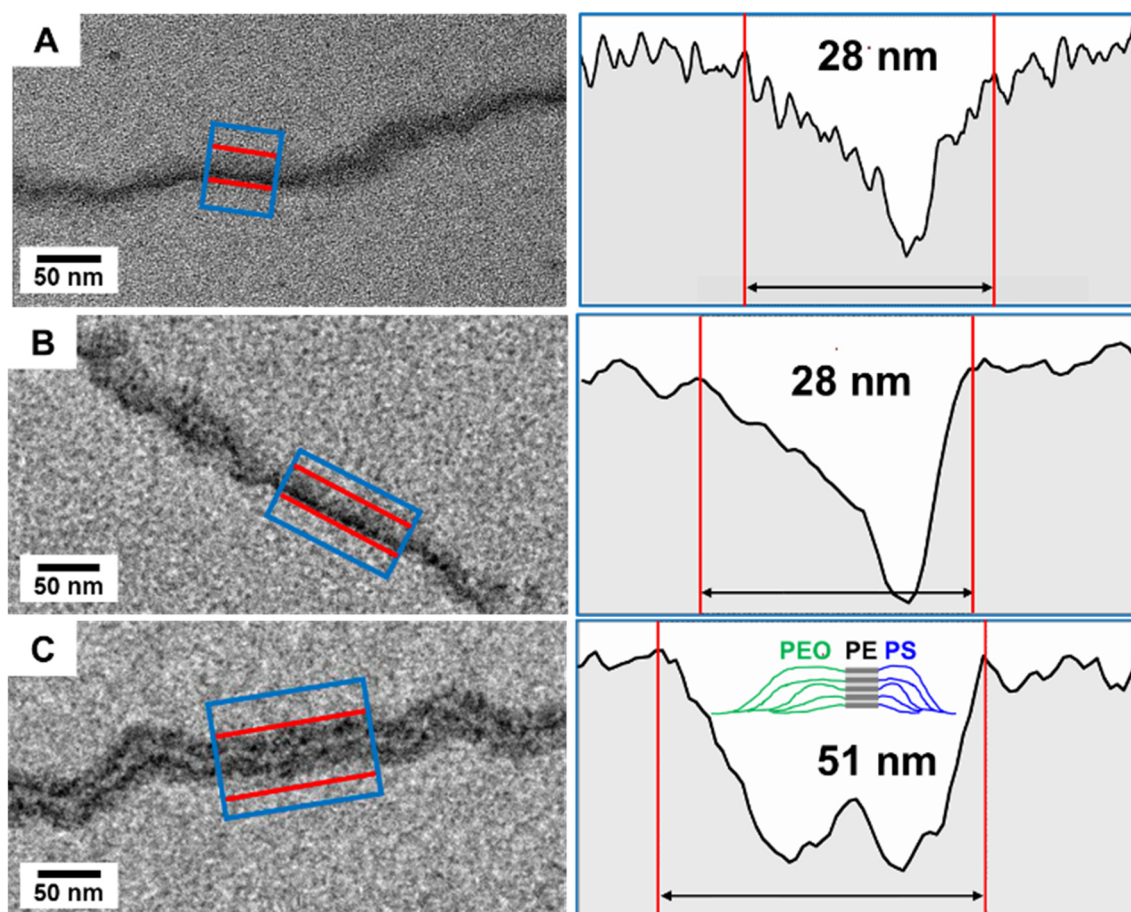


**Figure 2.9.** TEM micrographs (left) and corresponding grey scale analyses of the highlighted areas (right) for SEEEO Janus micelles: not stained (A), stained with OsO<sub>4</sub> (B), and RuO<sub>4</sub> (C) respectively.

In order to confirm the corona structure, the S<sub>280</sub>E<sub>1250</sub>EO<sub>670</sub> wCCMs were compared with patchy S<sub>330</sub>E<sub>1360</sub>M<sub>760</sub> (M = poly(methyl methacrylate) micelles, in which the corona blocks have comparable degrees of polymerization. The micelles were dialyzed against a selective solvent mixture for the PEO/PMMA corona blocks, resulting in the collapse of the PS chains in the corona. After staining (Figure 2.10), S<sub>330</sub>E<sub>1360</sub>M<sub>760</sub> wCCMs show spherical PS patches (RuO<sub>4</sub> staining), whereas a continuous PS phase is visible for S<sub>280</sub>E<sub>1350</sub>EO<sub>670</sub> (for both OsO<sub>4</sub> and RuO<sub>4</sub> staining). These results can only be explained by the presence of a Janus-type corona structure for SEEEO wCCMs, as otherwise a patchy structure would have been observed upon collapse of the PS chains in the corona.

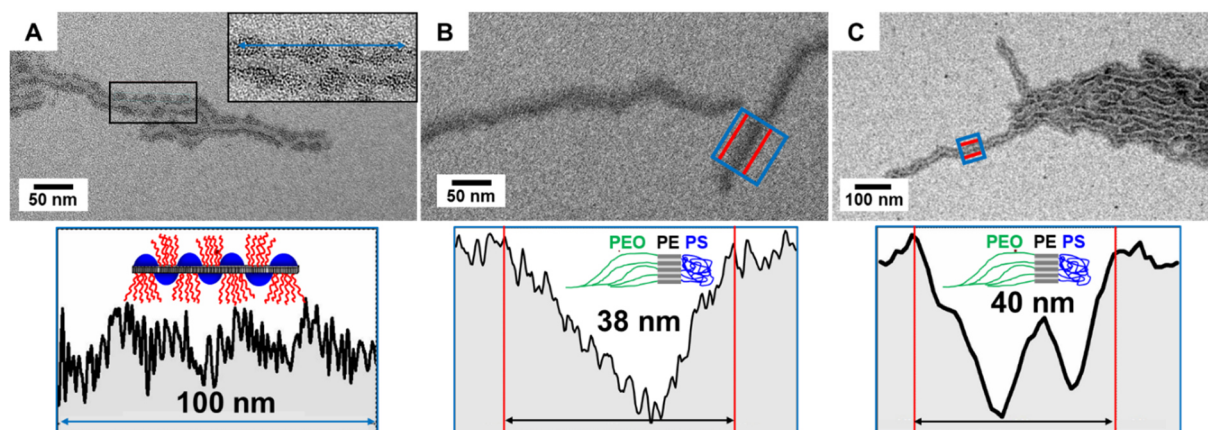


**Figure 2.10.** TEM micrographs (top) and corresponding grey scale analyses of the highlighted areas (bottom) for A) patchy  $S_{330}E_{1360}M_{760}$  micelles stained with  $RuO_4$ , and  $S_{280}E_{1250}EO_{670}$  Janus micelles stained with B)  $OsO_4$  and C)  $RuO_4$  respectively.

The prepared amphiphilic, worm-like Janus micelles with a PS/PEO corona show a significantly higher interfacial activity compared to patchy or Janus micelles with PS/PMMA corona, as revealed by pendant drop tensiometer measurements. Already at a very low concentration of  $c = 0.1 \text{ g}\cdot\text{L}^{-1}$  the SEEO Janus micelles reduce the quasi-equilibrium interfacial tension at the water/toluene interface to  $\gamma = 17.2 \pm 0.03 \text{ mN}\cdot\text{m}^{-1}$ , being significantly lower compared to the value reached by the patchy  $S_{330}E_{1360}M_{760}$  micelles ( $\gamma = 18.5 \pm 0.02 \text{ mN}\cdot\text{m}^{-1}$ ). This convincingly demonstrates the impact of the more amphiphilic nature of the PS/PEO corona on the interfacial activity of SEEO Janus  $wCCMs$ .

## 2.6 Individual Contributions to Joint Publications

The publications included in this thesis are a collaborative work of several researchers. The individual contributions of all (co-)authors are specified in this section.

Chapter 3 is published in *Nanoscale Adv.*, **2020**, 2, 438 – 452 under the title:

### **Influence of Patch Size and Chemistry on the Catalytic Activity of Patchy Hybrid Nonwovens**

by Christian Hils, Martin Dulle, Gabriel Sitaru, Stephan Gekle, Judith Schöbel, Andreas Frank, Markus Drechsler, Andreas Greiner and Holger Schmalz

I designed and conducted the main part of the experiments and analyses, including the amidation of the triblock terpolymers, self-assembly and synthesis of hybrid materials and

wrote the manuscript, unless stated otherwise in the following. Martin Dulle carried out SAXS experiments and wrote the corresponding section of the manuscript. Gabriel Sitaru did theoretical calculations on the catalytical activity. Stephan Gekle was involved in the theoretical calculations and wrote the respective part of the manuscript. Judith Schöbel contributed in discussions on *w*CCM preparation and catalysis, as well as preparation of the manuscript. Transmission electron microscopy investigations were performed by Markus Drechsler. Andreas Frank carried out scanning electron microscopy measurements and wrote the corresponding section of the manuscript. Andreas Greiner co-supervised the project. Holger Schmalz supervised the project, co-designed the experiments, and corrected the manuscript.

Chapter 4 is published in *Chem. Eur. J.*, **2020**, *26*, 5611 – 5614 under the title:

### **Converting Poly(Methyl Methacrylate) into a Triple-Responsive Polymer**

by Christian Hils, Emma Fuchs, Franziska Eger, Judith Schöbel and Holger Schmalz

I designed and conducted all experiments, did the main part of the analytics, and wrote the manuscript. Emma Fuchs and Franziska Eger were partly involved in the amidation of PMMA and did these experiments under my supervision. Judith Schöbel was involved in the early stage of the project and corrected the manuscript. Holger Schmalz supervised the project, co-designed the experiments, and corrected the manuscript.

Chapter 5 is published in *Angew. Chem. Int. Ed.*, (DOI: 10.1002/anie.202105787 (*Angew. Chem.*, DOI: 10.1002/ange.202105787) as “Hot Paper” under the title:

### **Hierarchical Superstructures by Combining Crystallization-Driven and Molecular Self-Assembly**

by Andreas Frank, Christian Hils, Melina Weber, Klaus Kreger, Holger Schmalz and Hans-Werner Schmidt

Andreas Frank and I contributed equally to this publication. We both designed and performed the experiments and analyses. Melina Weber conducted a part of the experiments under supervision of Andreas Frank and myself. Klaus Kreger was involved in scientific discussions and corrected the manuscript. Holger Schmalz co-designed the experiments, supervised the project, and corrected the manuscript. Hans-Werner Schmidt supervised the project and was involved in scientific discussions and manuscript correction.

Chapter 6 is published in *ASC Nano*, **2021**, *15*, 1111 – 1120 under the title:

**Frustrated Microparticle Morphologies of a Semicrystalline Triblock Terpolymer in 3D Soft Confinement**

by Xuezhi Dai, Xiaolian Qiang, Christian Hils, Holger Schmalz and André H. Gröschel

This publication is a cooperation of Physical Chemistry and Center for Nanointegration (CENIDE) at the University of Duisburg-Essen, Physical Chemistry and Center for Soft Nanoscience (SoN) at the University of Münster, and Macromolecular Chemistry II of the University of Bayreuth.

I co-authored this publication, did the synthesis of the triblock terpolymer, thermal characterization in bulk and solution. I was involved in the design of the experiments, scientific discussions and wrote a part of the manuscript. Xuezhi Dai and Xiaolian Qiang designed and conducted all confinement assembly experiments and wrote the main part of the manuscript. Holger Schmalz was involved in co-supervision of the project, in scientific discussions and corrected the manuscript. André H. Gröschel supervised the project and corrected the manuscript.

Chapter 7, submitted to *J. Am. Chem. Soc.* under the title:

**Janus or Patchy: Who Wins the Battle in Crystallization-Driven Self-Assembly of Double Crystalline Triblock Terpolymers?**

by Christian Hils, Joachim Schmelz, Markus Drechsler and Holger Schmalz

I designed and conducted all experiments, did the main part of the analytics, and wrote the manuscript. Joachim Schmelz was involved in analytics and did preliminary studies. Markus Drechsler performed TEM measurements. Holger Schmalz supervised the project, co-designed the experiments, and corrected the manuscript.

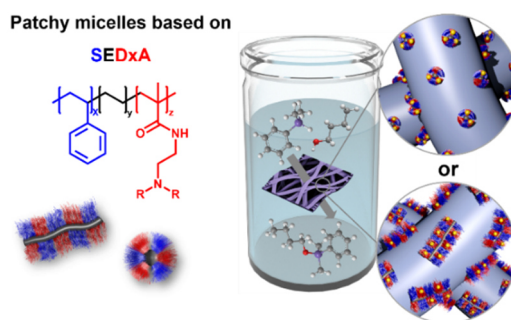
The review "*Patchy Micelles with a Crystalline Core: Self-Assembly Concepts, Properties, and Applications*" (Appendix) summarises the work on patchy micelles at our chair and puts it in context to current research activities in this field.



### 3 Influence of patch size and chemistry on the catalytic activity of patchy hybrid nonwovens

Christian Hils,<sup>a</sup> Martin Dulle,<sup>b</sup> Gabriel Sitaru,<sup>c</sup> Stephan Gekle,<sup>c</sup> Judith Schöbel,<sup>d</sup> Andreas Frank,<sup>e</sup> Markus Drechsler,<sup>f</sup> Andreas Greiner,<sup>a,g</sup> Holger Schmalz<sup>a,g,\*</sup>

- a) University of Bayreuth, Macromolecular Chemistry II, Universitätsstraße 30, 95440 Bayreuth, Germany
- b) Forschungszentrum Jülich GmbH, JCNS-1/ICS-1, Wilhelm-Johnen-Straße, 52428 Jülich, Germany
- c) University of Bayreuth, Biofluid Simulation and Modeling, Theoretische Physik VI, Universitätsstraße 30, 95440 Bayreuth, Germany
- d) University of Groningen, Macromolecular Chemistry & New Polymeric Materials, Zernike Institute for Advanced Materials, Nijenborgh 4, 9747 AG, Groningen, The Netherlands
- e) University of Bayreuth, Macromolecular Chemistry I, Universitätsstraße 30, 95440 Bayreuth, Germany
- f) University of Bayreuth, Bavarian Polymer Institute, Keylab Optical and Electron Microscopy, Universitätsstraße 30, 95440 Bayreuth, Germany
- g) University of Bayreuth, Bavarian Polymer Institute, Keylab Synthesis and Molecular Characterization, Universitätsstraße 30, 95440 Bayreuth, Germany



Published in: *Nanoscale Advances*, **2020**, 2, 438 – 452

Reprinted with permission from Royal Society of Chemistry.

## Abstract

In this work, we provide a detailed study on the influence of patch size and chemistry on the catalytic activity of patchy hybrid nonwovens in the gold nanoparticle (Au NP) catalysed alcoholysis of dimethylphenylsilane in *n*-butanol. The nonwovens were produced by coaxial electrospinning, employing a polystyrene solution as core and a dispersion of spherical or worm-like patchy micelles with functional, amino group-bearing patches (dimethyl and diisopropyl amino groups, anchor groups for Au NP) as shell. Subsequent loading by dipping into a dispersion of preformed Au NPs yields the patchy hybrid nonwovens. In terms of NP stabilization, *i.e.*, preventing agglomeration, worm-like micelles with poly(*N,N*-dimethylaminoethyl methacrylamide) (PDMA) patches are most efficient. Kinetic studies employing an extended 1<sup>st</sup> order kinetics model, which includes the observed induction periods, revealed a strong dependence on the accessibility of the Au NPs' surface to the reactants. The accessibility is controlled by the swellability of the functional patches in *n*-butanol, which depends on both patch chemistry and size. As a result, significantly longer induction ( $t_{ind}$ ) and reaction ( $t_R$ ) times were observed for the 1<sup>st</sup> catalysis cycles in comparison to the 10<sup>th</sup> cycles and nonwovens with more polar PDMA patches show a significantly lower  $t_R$  in the 1<sup>st</sup> catalysis cycle. Thus, the unique patchy surface structure allows to tailor the properties of this "tea-bag"-like catalyst system in terms of NP stabilization and catalytic performance, which resulted in a significant reduction of  $t_R$  to about 4 h for an optimized system.

## Introduction

Noble metal nanoparticles, and especially gold nanoparticles (Au NPs), are gaining increasing attention due to their excellent performance in heterogeneous catalysis, being ascribed to their extremely high specific surface area.<sup>1–5</sup> For decades, gold has been considered as poor catalyst since bulk gold is chemically inert. However, when gold is present in form of small particles with diameters in the nanometer-range it becomes surprisingly active.<sup>2,5</sup> First reports on the catalytic activity of Au NPs date back to the 1970s, describing the hydrogenation of alkenes and alkynes with supported Au NPs,<sup>6</sup> followed by the discovery that Au NPs show a high catalytic activity for CO oxidation even at temperatures below 0 °C in 1987.<sup>7</sup> Since then, a plethora of reactions catalysed by Au NPs have been identified, e.g. oxophilic activation of epoxides and carbonyl compounds, hydrosilylation reactions, hydrolysis/alcoholysis of silanes, hydrogenation reactions, reduction of aromatic nitro compounds and C-C coupling reactions.<sup>5</sup>

In general, an inherent problem involved in heterogeneous catalysis with NPs is their high specific surface area. On one hand, it is indispensable for a good catalytic performance, but on the other hand it makes the NPs prone to aggregation, which in turn will result in a decreased activity. Thus, efficient strategies have to be developed that can prevent NP agglomeration while preserving their excellent catalytic activity. One common way is the use of low molecular weight or polymeric ligands for NP stabilization. But one has to keep in mind that the ligands can influence the catalytic activity of the NPs as well as the selectivity and the ligands can fade away from the NP surface with time, resulting in a destabilization and, thus, agglomeration.<sup>8,9</sup> Moreover, the complete separation of ligand-stabilized NPs after catalysis is rather difficult, leading to a limited recyclability of the NPs.<sup>10</sup> One strategy to overcome these issues is the immobilization of NPs on a solid inorganic support, like (porous) metal oxides and silica,<sup>11–15</sup> nanotubes and -rods,<sup>16–18</sup> or two-dimensional layered materials like graphene or graphitic carbon nitride<sup>19–21</sup>. An interesting approach is the use of magnetic iron oxide NPs as support, facilitating an easy recovery of the catalyst by applying a magnetic field.<sup>22</sup> In addition, metal organic frameworks (MOFs) have been employed as versatile hosts for metal NPs.<sup>23–25</sup> Next to these examples polymeric supports, like nanocellulose,<sup>26</sup> micro- or nanoporous polymers,<sup>27–31</sup> microgels,<sup>32,33</sup> polyelectrolyte brushes,<sup>34–36</sup> dendrimers and unimolecular micelles,<sup>37,38</sup> as well as polymer micelles,<sup>39–44</sup> are highly attractive for NP stabilization, as their properties can be easily tailored to the demands of a specific catalytic application (NP stabilization, selectivity, responsivity). In a different approach, polymer nanofibers produced by electrospinning<sup>45,46</sup> or polyelectrolyte brushes<sup>47</sup> can be used as sacrificial support for NPs, which can be removed by

subsequent calcination. Here, sintering of the NPs occurs during calcination, resulting in porous, mesostructured catalysts that can be easily removed from the reaction media, allowing a good reusability/recyclability. However, due to the sintering of the NPs the catalytically active surface area is partially reduced.

Crystallization-driven self-assembly (CDSA) is increasingly gaining importance for the production of defined cylindrical micelles with tailored functionality for NP stabilization.<sup>48</sup> This field was pioneered by the inspiring work of Manners and Winnik on the CDSA of diblock copolymers with a crystallizable poly(ferrocenyl dimethylsilane) (PFS) block.<sup>49</sup> In analogy to living polymerizations, CDSA can be conducted in a living manner, using small micellar fragments as seeds for the addition of unimers (molecularly dissolved block copolymers bearing a crystallizable block).<sup>50,51</sup> This seeded-growth protocol paves the way to a precise length control of cylindrical micelles and to a variety of different micellar architectures, like patchy micelles and block comicelles (in analogy to BCPs),<sup>52–55</sup> branched and platelet-like micelles,<sup>56</sup> and hierarchical self-assemblies.<sup>57–59</sup> In addition to PFS-containing BCPs, a variety of other semi-crystalline polymers were reported to undergo CDSA, e.g. polyethylene (PE),<sup>60,61</sup> poly(*L*-lactide),<sup>62,63</sup> poly(3-hexylthiophene),<sup>64</sup> oligo(*p*-phenylenevinylene),<sup>65</sup> polycarbonates,<sup>66</sup> or poly( $\epsilon$ -caprolactone)<sup>67</sup>.

We have recently shown that Au NP-loaded patchy nonwovens with functional, nanometer-sized patches at the nonwoven's surface are efficient, “tea-bag”-like catalyst systems.<sup>68</sup> The patchy nonwovens were prepared by combining coaxial electrospinning<sup>46,69</sup> as a versatile “*top-down*” method with CDSA (“*bottom-up*” approach), employing a polystyrene (PS) solution as core and a dispersion of functional, patchy worm-like crystalline-core micelles (*wCCMs*) as shell (Fig. 3.1). The patchy *wCCMs* were produced by CDSA and consist of a semi-crystalline polyethylene (PE) core and a corona made of alternating nanometer-sized PS and functional, amino group-containing patches. To this end, the poly(methyl methacrylate) (PMMA)-block of a polystyrene-*block*-polyethylene-*block*-poly(methyl methacrylate) (PS-*b*-PE-*b*-PMMA) triblock terpolymer was functionalized by post-polymerization amidation with *N,N*-diisopropylethylenediamine (DiPA) at 130 °C in DMSO.<sup>44</sup> The patchy nonwovens were loaded with catalytically active Au NPs *via* a simple dipping process and showed excellent performance and reusability in the catalytic alcoholysis of dimethylphenylsilane with *n*-butanol. However, due to the comparably harsh conditions used for the amidation of the PS-*b*-PE-*b*-PMMA triblock terpolymer a significant fraction of imide units (amide/imide  $\approx$  50/50) was formed, leading to a limited solubility of the functionalized triblock terpolymer in THF, the solvent employed for CDSA. Thus, the degree of functionalization of the amidated patches

could not be increased above  $f \approx 55\%$ , as for higher degrees of functionalization the amidated patches were insoluble in THF and CDSA to defined  $w$ CCMs was not possible. However, with respect to the efficient stabilization of Au NPs a higher degree of functionalization would be beneficial. In the meantime, we have developed a more efficient amidation method, which will be used in this study. In this approach, the amine is activated with *n*-butyllithium, allowing an almost quantitative amidation without the formation of undesired imide units.<sup>43</sup>

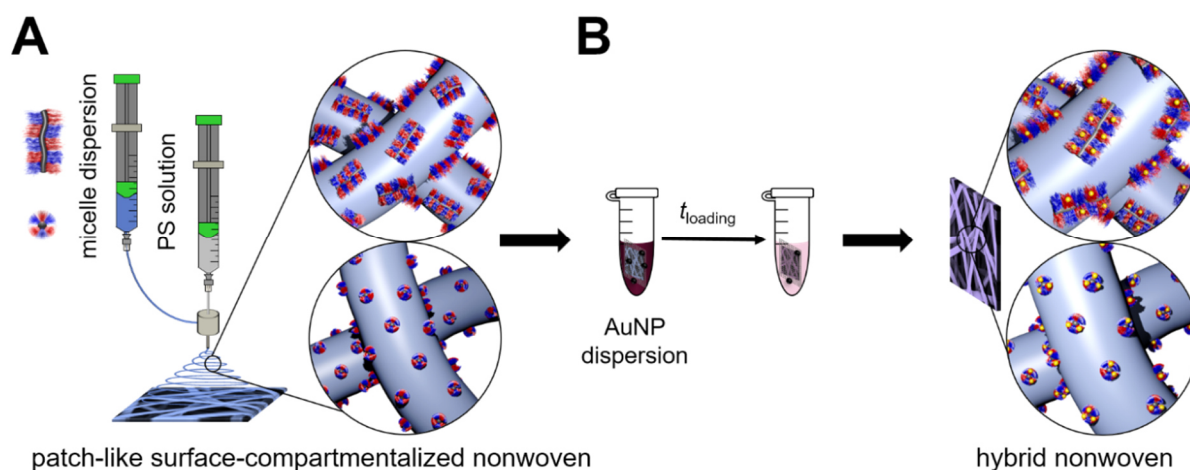


**Fig. 3.1.** Preparation of catalytically active hybrid nonwovens: A) Functional, patch-like surface-compartmentalized nonwovens are produced by coaxial electrospinning of PS as core (grey) and patchy  $w$ CCMs or  $s$ CCMs as shell (blue), followed by loading with preformed citrate-stabilized Au NPs by a simple ligand exchange (dipping process, B).

Here, we present a comprehensive study on the influence of micelle geometry as well as patch size and chemistry on the catalytic activity of Au NP-loaded patchy nonwovens, prepared by coaxial electrospinning and subsequent loading with Au NPs *via* a facile dipping process (Fig. 3.1). Patchy micelles with different shapes (worm-like, spherical), employed as shell in coaxial electrospinning, were prepared by CDSA of polystyrene-*block*-polyethylene-*block*-poly(*N,N*-dialkylaminoethyl methacrylamide) (SEDxA) triblock terpolymers in THF for  $w$ CCMs and dioxane for  $s$ CCMs (spherical crystalline-core micelles),<sup>60</sup> respectively. The chemistry/polarity of the amidated patches was tuned by using *N,N*-diisopropylethylenediamine and *N,N*-dimethylethylenediamine for post-polymerization amidation of PS-*b*-PE-*b*-PMMA triblock terpolymers, whereby the size of the patches was altered by using PS-*b*-PE-*b*-PMMA triblock terpolymers with different PS and PMMA weight fractions. The morphology of the neat and Au NP-loaded patchy nonwovens was studied by scanning electron microscopy (SEM) and small-angle X-ray scattering (SAXS). As this study focuses on the influence of the patchy surface structure of the support on the catalytic activity of the embedded Au NPs we

have chosen the alcoholysis of dimethylphenylsilane with *n*-butanol as established model reaction. This allows comparison to our previous results and to literature data.<sup>68,70</sup>

## Experimental

### Materials

All chemicals were used as received unless otherwise noted. Deionized water (filtered through a Millipore Milli-Q Plus system, QPAK® 2 purification cartridge, conductivity: 18.2 MΩ·cm), tetrachloroauric(III) acid trihydrate (HAuCl<sub>4</sub> · 3 H<sub>2</sub>O, 99.99%, Alfa Aesar), sodium borohydride (NaBH<sub>4</sub>, ≥ 96%, Fluka), trisodium citrate dihydrate (99% for analytical purposes, Grüssing), dimethylphenylsilane (≥ 97%, TCI Europe), *n*-butanol (99.9%, anhydrous, Alfa Aesar), undecane (≥ 99%, Sigma-Aldrich), *n*-butyllithium (2.5 mol·L<sup>-1</sup> in hexane, Acros Organics), *n*-pentane (purified by distillation prior to use), deuterated chloroform (CDCl<sub>3</sub>, 99.8%, Deutero), calcium hydride (CaH<sub>2</sub>, Merck), *N,N*-dimethylethylenediamine (DMEDA, ≥ 98%, Sigma-Aldrich, dried over CaH<sub>2</sub> and purified by distillation), *N,N*-diisopropylethylenediamine (DiPEDA, 97%, Acros Organics, dried over CaH<sub>2</sub> and purified by distillation), dry ice, hydrochloric acid (37 wt% in water, VWR), nitric acid (> 65 wt% in water, Sigma-Aldrich), ruthenium(III) chloride hydrate (ReagentPlus®, Sigma-Aldrich), sodium hypochlorite solution (NaOCl, 10 – 15 wt% in water, Sigma-Aldrich), *N,N*-dimethylformamide (DMF, 99%, Acros Organics), tetrahydrofuran (THF, ≥ 99.9%, Sigma-Aldrich, dried by successive distillation over CaH<sub>2</sub> and potassium and stored under nitrogen until use), acetone (99.9%, Acros Organics), dioxane (p.a., AppliChem) and polystyrene (synthesized by anionic polymerization in THF,  $M_n = 1.8 \cdot 10^6$  g·mol<sup>-1</sup>,  $D = 1.08$ ). Special care was taken for handling CaH<sub>2</sub>, as it strongly reacts with alcohols and water under formation of hydrogen.

### Synthesis of citrate-stabilized Au NPs

The citrate-stabilized Au NPs were prepared according to the procedure reported by *Schaal et al.*<sup>71</sup> To 100 mL of an aqueous HAuCl<sub>4</sub> solution ( $c = 0.50 \cdot 10^{-3}$  mol·L<sup>-1</sup>) 9 mL of a NaBH<sub>4</sub> solution in water ( $c = 4.85 \cdot 10^{-2}$  mol·L<sup>-1</sup>) were added dropwise followed by stirring for 5 min. The reaction mixture changed colour from yellow to red, indicating the formation of Au NPs. Subsequently, 5 mL of an aqueous sodium citrate solution ( $c = 0.05$  mol·L<sup>-1</sup>) were added and the mixture was stirred for another 5 min. Au NPs ( $c_{Au} = 0.50 \cdot 10^{-3}$  mol·L<sup>-1</sup>, determined by inductively coupled plasma-optical emission spectrometry (ICP-OES)) with a mean diameter

of  $D_{\text{TEM}} = 9.5 \pm 2.4$  nm, as determined by transmission electron microscopy (TEM), were obtained (Fig. S3.1A,B). The Au NP dispersion showed a localized surface plasmon resonance at  $\lambda_{\text{max}} = 529$  nm (Fig. S3.1C).

### Synthesis of the PS-*b*-PE-*b*-PMMA triblock terpolymers

The PS-*b*-PE-*b*-PMMA triblock terpolymers were synthesized by a combination of living anionic polymerization and catalytic hydrogenation, as published elsewhere.<sup>60</sup> The composition of the employed PS-*b*-PE-*b*-PMMA triblock terpolymers is S<sub>40</sub>E<sub>21</sub>M<sub>39</sub><sup>108</sup> and S<sub>48</sub>E<sub>27</sub>M<sub>25</sub><sup>141</sup>. In this notation, the subscripts describe the mass fraction of the corresponding block in wt% and the superscript denotes the overall number average molecular weight in kg·mol<sup>-1</sup>. The number-average molecular weight in kg·mol<sup>-1</sup> was determined by a combination of MALDI-ToF MS (matrix assisted laser desorption ionization – time of flight mass spectrometry) and <sup>1</sup>H NMR (nuclear magnetic resonance) spectroscopy.

### Synthesis of SEDxA triblock terpolymers

For the post-polymerization modification of the PS-*b*-PE-*b*-PMMA triblock terpolymers, the PMMA block was amidated with the corresponding *N,N*-dialkylethylenediamine (DMEDA, DiPEDA) under an inert argon atmosphere, as published elsewhere.<sup>43</sup> The amidation resulted in quantitative functionalization of the PMMA block, as determined by <sup>1</sup>H NMR and FT-IR (Fourier transform-infrared) spectroscopy (Fig. S3.2 and S3.3). The following polystyrene-*block*-polyethylene-*block*-poly(*N,N*-dialkylaminoethyl methacrylamide) (SEDxA) triblock terpolymers were prepared: S<sub>28</sub>E<sub>15</sub>DiPA<sub>58</sub><sup>156</sup> (*s*-SEDiPA), S<sub>48</sub>E<sub>21</sub>DiPA<sub>41</sub><sup>181</sup> (*as*-SEDiPA) and S<sub>33</sub>E<sub>17</sub>DMA<sub>50</sub><sup>132</sup> (*s*-SEDMA).

### Formation of patchy micelles<sup>60</sup>

The functional, patchy *s*CCMs of the amidated SEDxA triblock terpolymers were prepared by dissolving the triblock terpolymers in dioxane ( $c = 10$  g·L<sup>-1</sup>) at 95 °C for 30 min, followed by cooling to room temperature. The patchy *w*CCMs were prepared by crystallization-driven self-assembly (CDSA) of the amidated SEDxA triblock terpolymers in THF. To this end, the triblock terpolymers were dissolved in THF ( $c = 10$  g·L<sup>-1</sup>) at 65 °C for 30 min and subsequently cooled to the crystallization temperature ( $T_c$ , Table S3.1 and Fig. S3.4) of the polyethylene middle block, using a thermostated shaker unit (HLC-MKR 13, Ditabis). The self-assembly process was allowed to proceed for 24 h at a shaking rate of 200 rpm.

### Preparation of patchy nonwovens by coaxial electrospinning

For the preparation of patchy nonwovens by coaxial electrospinning different solutions were prepared. For the core a 7 wt% PS ( $M_n = 1.8 \cdot 10^6 \text{ g} \cdot \text{mol}^{-1}$ ) solution in DMF and for the shell dispersions of SEDxA sCCMs or wCCMs in dioxane or THF ( $c = 10 \text{ g} \cdot \text{L}^{-1}$ ), respectively, were employed. The fibres were spun on a rotating disk collector ( $D = 20 \text{ cm}$ , 800 rpm) placed at a distance of 5 cm from the coaxial needle (COAX\_2DISP sealed coaxial needles, LINARI NanoTech,  $d_{\text{core}} = 0.51 \text{ mm}$  and  $d_{\text{shell}} = 1.37 \text{ mm}$ ) at a temperature of 20.8 °C and a relative humidity of ca. 30%. For electrospinning, a high voltage of 11.4 kV at the needle and -1.0 kV at the collector were applied. The feed rate of the PS core solution was  $1.2 \text{ mL} \cdot \text{h}^{-1}$  and for the micellar shell dispersion  $1.0 \text{ mL} \cdot \text{h}^{-1}$ .

### Loading of patchy nonwovens with citrate-stabilized Au NPs (dipping process)

For each system, the loading of the nonwovens was done in an Eppendorf vial by dipping a piece of nonwoven (surface area:  $S = 1 \text{ cm}^2$ , thickness:  $d \approx 400 \text{ }\mu\text{m}$ ) fixed in a cage made of stainless-steel mesh (1.4432 V4A/316L, mesh size: 400 mesh, wire thickness: 30  $\mu\text{m}$ ) into 1 mL of an aqueous, citrate-stabilized Au NP dispersion ( $c_{\text{Au}} = 0.50 \cdot 10^{-3} \text{ mol} \cdot \text{L}^{-1}$ ,  $D_{\text{TEM}} = 9.5 \pm 2.4 \text{ nm}$ ) for 24 h. After incorporation of the Au NPs, the nonwovens were subsequently washed with a sodium citrate solution ( $c = 5 \cdot 10^{-3} \text{ mol} \cdot \text{L}^{-1}$ ) and water (2 x 5 mL each). The hybrid nonwovens were dried in a vacuum oven (< 5 mbar, 40 °C) for 15 h. The amount of Au in the patchy nonwovens was determined by inductively coupled plasma-optical emission spectrometry (ICP-OES, triple determination) and UV-Vis measurements (for details see electronic supplementary information (ESI), eqn (S3.1) and Fig. S3.5) from the respective Au contents of the dispersions before and after loading (difference method).

### Catalytic alcoholysis of dimethylphenylsilane

In a typical synthesis, 32 mg of dimethylphenylsilane (0.23 mmol) and 36.7 mg of undecane (0.23 mmol, internal standard for gas chromatography) were dissolved in 4 g of dry *n*-butanol, as published elsewhere.<sup>68</sup> An Au NP-loaded nonwoven ( $S = 1 \text{ cm}^2$ ,  $d \approx 400 \text{ }\mu\text{m}$ , pre-swollen for 24 h in pure *n*-butanol) was placed in the reaction solution. The reaction was shaken at 400 rpm (Heidolph Multi Reax Shaker) for 24 h and aliquots of 10  $\mu\text{L}$  of the reaction solution were taken after different periods of time for kinetic studies. The aliquots were diluted with 1 mL of acetone for gas chromatography measurements. This procedure was repeated 9 times using the same hybrid nonwoven and a freshly prepared reaction mixture, whereby kinetics were followed for the 1<sup>st</sup> and 10<sup>th</sup> cycles only. Before reuse, the Au NP nonwovens were

washed with *n*-butanol and dried by placing on a piece of filter paper. The determination of conversion ( $x_p$ ) via gas chromatography was based on the ratio of the integrals of reactant (dimethylphenylsilane) to internal standard (undecane, 0.23 mmol) and was referenced to the respective zero measurement.

### Instruments

*Nuclear Magnetic Resonance (NMR) Spectroscopy.* The amidated SEDxA triblock terpolymers were characterized by  $^1\text{H}$  NMR spectroscopy (Bruker Ultrashield 300 spectrometer) using  $\text{CDCl}_3$  as solvent. The signal assignment was supported by simulations with the NMR software *MestReNova*.

*Gas Chromatography (GC).* The GC measurements were performed on a Shimadzu GC Plus 2010, equipped with an autosampler (AOC 20i) and a Zebron ZB-5ms column (Phenomenex,  $L = 30$  m,  $ID = 0.25$  mm,  $df = 25$   $\mu\text{m}$ , 5% polysilarylene + 95% polydimethylsiloxane; temperature range: 60 to 325/350  $^\circ\text{C}$ ). The start temperature was set to 50  $^\circ\text{C}$  and kept constant for 2 min. Subsequently, the column was heated to 300  $^\circ\text{C}$  at 15  $\text{K}\cdot\text{min}^{-1}$  and kept at 300  $^\circ\text{C}$  for 5 min. The overall measurement time was 23 min and nitrogen was used as carrier gas (purity: 5.0, 1.6  $\text{mL}\cdot\text{h}^{-1}$ ). The following retention times ( $R_t$ ) were observed:  $R_t(\text{dimethylphenylsilane}) = 6.5$  min,  $R_t(\text{undecane}) = 8.4$  min and  $R_t(\text{butoxydimethylphenylsilane}) = 10.6$  min (Fig. S3.6).

*Asymmetric Flow Field-Flow Fractionation (AF4).* The AF4 measurement of the AuNP dispersion ( $c_{\text{Au}} = 0.50 \cdot 10^{-3}$   $\text{mol}\cdot\text{L}^{-1}$ ,  $D_{\text{TEM}} = 9.5 \pm 2.4$  nm) was performed on an AF2000 Multi Flow Series system from Postnova Analytics, connected to an UV-Vis detector (SPD-20A prominence; Postnova Analytics) operated at  $\lambda = 530$  nm (absorbance maximum of Au NPs (localized surface plasmon resonance, LSPR)) and a DLS detector (Zetasizer Nano-S; Malvern) for signal detection. The flow channel was equipped with a 350  $\mu\text{m}$  spacer and a 10 kDa membrane (regenerated cellulose). Deionized water (Millipore Milli-Q Plus system, QPAK® 2 purification cartridge, conductivity: 18.2  $\text{M}\Omega\cdot\text{cm}$ , filtered through a 100 nm membrane) was used as eluent, employing a detector flow of 0.5  $\text{mL}\cdot\text{min}^{-1}$  and a linear cross flow profile (from 2  $\text{mL}\cdot\text{min}^{-1}$  to 0  $\text{mL}\cdot\text{min}^{-1}$  over 60 min) for separation.

*Inductively Coupled Plasma-Optical Emission Spectrometry (ICP-OES).* ICP-OES was measured on a VARIAN Vista-Pro (40 MHz, argon plasma) equipped with an ASX-510 autosampler, Echelle polychromator, argon humidifier and an ACCD semiconductor detector (calibration to respective sample matrix with a single gold standard (1000  $\text{mg}\cdot\text{L}^{-1}$ , Merck) and

drift correction). The aqueous Au NP dispersions were evaporated at 60 °C, the solid residue was dissolved in 1.5 mL *aqua regia*, and 0.5 mL of the solution obtained was diluted to 10 mL with deionized water (Millipore Milli-Q Plus system, QPAK® 2 purification cartridge, conductivity: 18.2 MΩ·cm). Due to the strong oxidizing and corrosive properties of *aqua regia* and its decomposition into toxic gases special care has to be taken when handling *aqua regia*.

*Micro Differential Scanning Calorimetry (μDSC)*. The measurements were performed on a SETARAM Micro DSC III using sealed measuring cells ("batch cells",  $V = 1$  mL) filled with approx. 0.7 mL of micelle dispersion ( $c = 10$  g·L<sup>-1</sup> in THF). A scanning rate of 0.5 K·min<sup>-1</sup> was employed, and pure THF was used as reference.

*Fourier Transform-Infrared (FT-IR) Spectroscopy*. The FT-IR spectra were recorded with a Digilab Excalibur 3000 FTIR instrument equipped with an ATR unit (diamond) at a resolution of 4 cm<sup>-1</sup>.

*Ultraviolet-Visible (UV-Vis) Spectroscopy*. The UV-Vis measurements were conducted with a JASCO V 630 spectrophotometer (wavelength accuracy: ± 0.7 nm) using a quartz glass cuvette ( $D = 10$  mm). A halogen lamp was used as the light source and the sample holder was a JASCO ETCS 761.

*Transmission Electron Microscopy (TEM)*. The TEM measurements were carried out with a ZEISS / LEO EM922 Omega and a JEOL JEM-2200FS field emission energy filtering transmission electron microscope (FE-EFTEM), both operated at an acceleration voltage of 200 kV. Zero-loss filtered micrographs ( $\Delta E \approx 0$  eV) were taken with a CCD camera system (Ultrascan 1000, Gatan) in case of the ZEISS Omega and a bottom mounted CMOS camera system (OneView, Gatan) for the JEOL JEM-2200FS, respectively. The images were processed with a digital image processing software (DM 1.9 and DM 3.3, Gatan). For TEM analysis of the triblock terpolymer micelle dispersions ( $w$ CCMs,  $s$ CCMs), the samples were diluted to a concentration of  $c = 0.1$  g·L<sup>-1</sup> and stirred for 30 min at room temperature. Subsequently, 10 μL of the respective dispersion was applied to a carbon-coated copper grid and residual solvent was removed by blotting with a filter paper followed by drying of the coated copper grid in a vacuum oven (24 h, 2 mbar, room temperature). For selective staining of PS, the samples were treated for 11 min with RuO<sub>4</sub> vapor, which was formed *in situ* from RuCl<sub>3</sub> hydrate and NaOCl. After staining, the samples were stored for at least 1 h in a fume hood to ensure that any not reacted RuO<sub>4</sub> was completely removed. The average  $w$ CCM lengths and patch sizes of the triblock terpolymer micelles as well as the average size of the Au NPs were determined by measuring at least 100 micelles/NPs using the software *ImageJ* (Fig. S3.7).<sup>72</sup>

*Scanning Electron Microscopy (SEM).* The SEM measurements on samples sputter coated with platinum were performed on a Zeiss 1530 with field emission cathode at an acceleration voltage of 1-10 kV (detectors: back scattered electron (BSE), secondary electrons (SE2) and Inlens SE). The samples were applied to a conductive adhesive carrier mounted on an aluminium plate, fixed with an aluminium adhesive strip and coated with a thin platinum layer ( $d \approx 1.3$  nm, Cressington 208HR high resolution sputter coater with MTM-20 thickness controller). The average diameter of the fibres was determined by measuring at least 100 fibres using the software *ImageJ*.<sup>72</sup>

For SEM measurements on the uncoated patchy nonwovens based on *s*-SEDiPA *w*CCMs (NW\_*s*-SEDiPA(*w*)) a FEI Quanta FEG 250 scanning electron microscope (Thermo Fisher Scientific) equipped with a field emission gun was used. The measurements were conducted under high vacuum at an acceleration voltage of 2 kV by utilizing the beam deceleration mode. This mode is used to measure samples with a very low accelerating voltage. Here, an additional negative voltage (stage bias, -4 kV) was applied to the stage and, thus, to the sample. This influences the primary electron beam and the signal electrons (secondary and back scattered electrons) coming from the sample. The primary beam is decelerated before reaching the sample and the signal electrons are accelerated toward the detector (centric back scattering electron detector).

*Small Angle X-Ray Scattering (SAXS).* The scattering patterns were recorded with the SAXS system “Ganesha-Air” from (SAXSLAB/XENOCs). The X-ray source of this laboratory based system is a D2-MetalJet (Excillum) with a liquid metal anode operating at 70 kV and 3.57 mA with Ga- $K_{\alpha}$  radiation (wavelength  $\lambda = 0.13414$  nm), providing a very brilliant and a very small beam ( $< 100$   $\mu\text{m}$ ). The beam was slightly focused with a focal length of 55 cm, using a specially made X-ray optics (Xenocs) to provide a very small and intense beam at the sample position. Two pairs of scatterless slits were used to adjust the beam size depending on the detector distance. The data were acquired with a position-sensitive detector (PILATUS 300K, Dectris). Different detector positions were used to cover the range of scattering vectors between 0.04 and 5.0  $\text{nm}^{-1}$ . The measurements were performed at room temperature in 1 mm glass capillaries (Hilgenberg, code 4007610, Germany) or directly on the nonwovens. The circularly averaged data were normalized to the incident beam, sample thickness and measurement time before subtracting the background, which was water for the NP dispersion and the neat (unloaded) patchy nonwoven for the hybrid nonwovens, respectively.

*Dynamic Light Scattering (DLS).* DLS measurements were performed on an ALV DLS/SLS-SP 5022F compact goniometer system with an ALV 5000/E cross-correlator at a scattering

angle of  $\theta = 90^\circ$  and 23 °C, using a HeNe laser (max. 35 mW,  $\lambda = 632.8$  nm) as the light source. The time-dependent scattering intensity was monitored with an APD (avalanche photodiode)-based pseudo cross correlation system. All samples were filtered through 0.45  $\mu\text{m}$  PTFE syringe filters (BGB Analytik) and filled into NMR tubes (VWR, 5 mm outer diameter) for measurement. For each sample at least 3 measurements were averaged. The data were evaluated using the ALV Correlator software (version V.3.0.0.17 10/2002) and the implemented ALV regularized fit option (g2(t), CONTIN-analysis).

## Results and discussion

Table 1 summarizes the molecular characteristics of the employed SEDxA triblock terpolymers, which were prepared by post-polymerization amidation of the PMMA block of the corresponding PS-*b*-PE-*b*-PMMA triblock terpolymers using *N,N*-dimethylethylenediamine and *N,N*-diisopropylethylenediamine, respectively.<sup>43</sup> Quantitative functionalization of the obtained SEDMA (polystyrene-*block*-polyethylene-*block*-poly(*N,N*-dimethylaminoethyl methacrylamide)) and SEDiPA (polystyrene-*block*-polyethylene-*block*-poly(*N,N*-diisopropylaminoethyl methacrylamide)) triblock terpolymers was confirmed by <sup>1</sup>H NMR (nuclear magnetic resonance) and FT-IR (Fourier transform-infrared) spectroscopy (Fig. S3.2 and S3.3). The polarity of the amidated PDxA block was tuned by employing different amines for functionalization, whereas the patch sizes in the corona of the self-assembled crystalline-core micelles (CCMs) were altered using PS/PDxA blocks of different lengths. Consequently, triblock terpolymers with comparable block lengths of the PS and PDxA corona blocks are termed symmetric, *i.e.*, *s*-SEDiPA and *s*-SEDMA, and the triblock terpolymer with unequal block lengths is termed asymmetric, *i.e.*, *as*-SEDiPA.

**Table 3.1.** Characteristics of the employed SEDxA triblock terpolymers and micellar dispersions.

sample code	composition <sup>a</sup>	block length PS/PDxA	PDxA corona [wt%]	$R_h$ ( <i>s</i> CCMs) <sup>b</sup> [nm]	$l$ ( <i>w</i> CCMs) <sup>c</sup> [nm]	patch size PS/PDxA <sup>c</sup> [nm]
<i>s</i> -SEDiPA	S <sub>28</sub> E <sub>15</sub> DiPA <sub>58</sub> <sup>156</sup>	420/430	67	31.4 ± 0.3	260 ± 100	12 ± 2/10 ± 3
<i>as</i> -SEDiPA	S <sub>38</sub> E <sub>21</sub> DiPA <sub>41</sub> <sup>181</sup>	660/350	52	35.8 ± 0.3	480 ± 240	18 ± 4/9 ± 2
<i>s</i> -SEDMA	S <sub>33</sub> E <sub>17</sub> DMA <sub>50</sub> <sup>131</sup>	420/430	60	-	510 ± 310	18 ± 5/17 ± 5

<sup>a</sup> subscripts denote the content of the respective polymer block in wt%, superscript denotes the number-average molecular weight in kg·mol<sup>-1</sup> determined by a combination of MALDI-ToF MS (matrix assisted laser desorption ionization – time of flight mass spectrometry) and <sup>1</sup>H NMR. <sup>b</sup> hydrodynamic radii of the *s*CCMs determined by DLS. <sup>c</sup> average sizes ± standard deviation as determined by TEM image analysis of at least 100 micelles/patches.

The patchy CCMs with different shapes (worm-like, spherical) were obtained by CDSA of the functionalized triblock terpolymers.<sup>60</sup> First, the triblock terpolymers were dissolved above the melting point ( $T_m$ ) of the polyethylene (PE) middle block using a selective (non-)solvent for the PE block, then cooled down to the respective crystallization temperature ( $T_c$ ) and, finally, crystallized at  $T_c$  for 24 h. Worm-like CCMs (*w*CCMs) are formed when a good solvent for the PE middle block (THF) is chosen, whereas a bad solvent for the PE block (1,4-dioxane) leads to the formation of spherical CCMs (*s*CCMs). The employed crystallization temperatures and respective  $\mu$ DSC (micro-differential scanning calorimetry) traces are given in the electronic supplementary information (ESI, Table S3.1, Fig. S3.4).

The transmission electron microscopy (TEM) micrographs shown in Fig. 3.2 as well as dynamic light scattering (DLS) results (Table 3.1, Fig. S3.8) prove the successful formation of both micelle shapes, *i.e.*, patchy *w*CCMs and *s*CCMs. The *s*CCMs exhibit apparent hydrodynamic radii of  $R_h \approx 31 - 37$  nm and the *w*CCMs show average lengths of  $l \approx 260 - 510$  nm. Selective staining of the PS block with RuO<sub>4</sub> reveals the patchy structure of the corona for both micelle shapes. However, the patchy corona of the *s*CCMs is less defined compared to the well-ordered corona of the *w*CCMs, which shows an almost alternating arrangement of the PS (dark) and PDxA (bright) patches (Fig. 3.2). This is in agreement to our previous results on the corona structure of patchy PS-*b*-PE-*b*-PMMA triblock terpolymer micelles.<sup>60</sup> The size of the corona patches varies with the block length of the PS and PDxA corona blocks (Table 3.1), *i.e.*, the width of both corona patches is similar for a symmetric composition of the corona in terms of PS and PDxA block lengths ( $\approx 18$  nm for *s*-SEDMA and

$\approx 11$  nm for *s*-SEDiPA *w*CCMs, respectively), but shows a significant difference for an asymmetric block length ratio ( $\approx 18$  nm for PS and  $\approx 9$  nm for PDiPA in case of *as*-SEDiPA *w*CCMs).

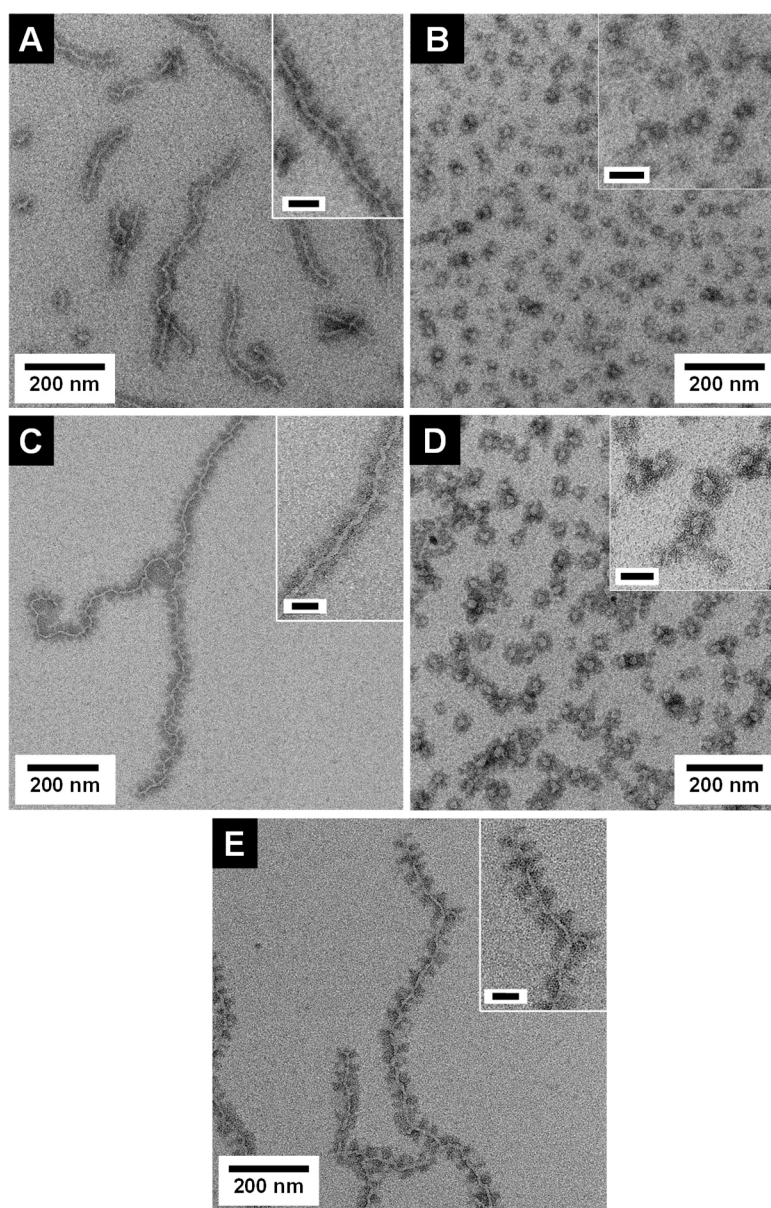


**Fig. 3.2.** TEM micrographs of  $S_{28}E_{15}DiPA_{58}^{156}$  *w*CCMs (A, *s*-SEDiPA(*w*)) and *s*CCMs (B, *s*-SEDiPA(*s*)),  $S_{38}E_{21}DiPA_{41}^{181}$  *w*CCMs (C, *as*-SEDiPA(*w*)) and *s*CCMs (D, *as*-SEDiPA(*s*)) and  $S_{33}E_{17}DMA_{50}^{131}$  *w*CCMs (E, *s*-SEDMA(*w*)). The PS domains were selectively stained with  $RuO_4$  and appear dark. The inset in D) shows at higher resolution  $RuO_2$  nanoparticles formed by the reaction of the PS units with  $RuO_4$  (oxidative cleavage of the phenyl rings). Scale bars in the insets are 50 nm.

The functional patchy micelles were then used in a coaxial electrospinning process to generate nonwovens with a patch-like surface structure (Fig. 3.1A), employing a PS solution ( $M_n = 1.8 \cdot 10^6$  g $\cdot$ mol $^{-1}$ ,  $c = 7$  wt% in DMF) as core-forming material and a dispersion of the patchy micelles as shell ( $c = 10$  g $\cdot$ L $^{-1}$  in THF (*w*CCMs) or dioxane (*s*CCMs)). The patchy

nonwovens are termed according to the micelle type employed as shell material, *i.e.*, NW\_*s*-SEDiPA(*w*) stands for a nonwoven with *s*-SEDiPA *w*CCMs on the surface. The resulting fibres show a uniform thickness of  $1.27 \pm 0.15 \mu\text{m}$  and a homogeneous coating of the surface with the functionalized CCMs (Fig. 3.3A-C, 3.8A, S3.9), as revealed by scanning electron microscopy (SEM). This is promoted by the PS patches of the micelles, which adsorb at the surface of the PS nonwoven. The characteristic shape of the *s*CCMs (Fig. 3.3A, S3.9B) as well as *w*CCMs (Fig. 3.3B, 3.8A, S3.9A) was preserved after electrospinning, as indicated by spherical and elongated structures observable on the fibres' surface. In order to exclude any effect arising from the sample preparation for SEM, *i.e.*, coating with a thin Pt layer ( $d \approx 1.3 \text{ nm}$ ), we have measured one uncoated patchy nonwoven based on *s*-SEDiPA *w*CCMs (NW\_*s*-SEDiPA(*w*), Fig. 3.3C). Here, the so-called beam deceleration mode was employed (for details see experimental section) and again worm-like structures arising from the decoration of the PS fibres with *w*CCMs are visible, showing that coating with Pt has no impact on the observed fibre morphology.

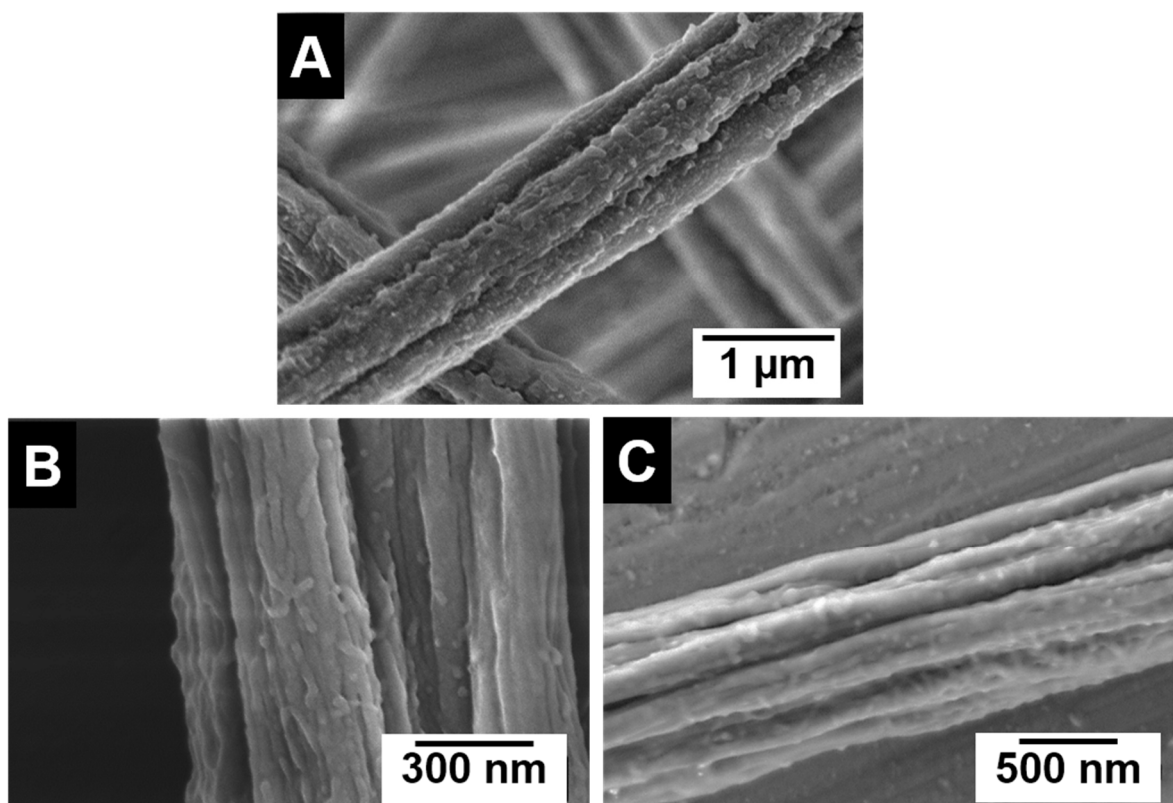


**Fig. 3.3.** SEM micrographs of patchy nonwovens based on *s*-SEDiPA *s*CCMs (A; NW\_*s*-SEDiPA(*s*)) and *w*CCMs (B,C; NW\_*s*-SEDiPA(*w*)). The SEM image in C) was acquired on an uncoated sample of NW\_*s*-SEDiPA(*w*), employing the beam deceleration mode (for details see experimental section).

In the next step, Au NP-containing hybrid nonwovens were produced *via* a facile ligand exchange process (Fig. 3.1B), *i.e.*, the patchy nonwovens (surface area:  $S = 1 \text{ cm}^2$ , thickness:  $d \approx 400 \text{ }\mu\text{m}$ ) were dipped in an aqueous dispersion of preformed, citrate-stabilized Au NPs for 24 h and subsequently washed with sodium citrate solution and water to remove unbound Au NPs. The employed Au NPs showed a rather broad size distribution with a number average diameter of  $D_{\text{TEM}} = 9.5 \pm 2.4 \text{ nm}$ , as determined by TEM (Fig. S3.1A,B). This was also confirmed by asymmetric flow field-flow fractionation (AF4), revealing a tailing of the size distribution toward larger particle sizes (Fig. S3.1D). The obtained average diameter of gyration of  $D_g = 17.9 \pm 2 \text{ nm}$  agrees with the size determined by TEM ( $D_{\text{TEM}} = 9.5 \pm 2.4 \text{ nm}$ ), taking the rather broad size distribution and the fact that light scattering overestimates the content of larger particles (scattering intensity is proportional to  $D^6$ ) into account. It is noted that we intentionally did not aim for the production of narrowly distributed Au NPs, as for catalytic applications a simple and fast NP synthesis is preferred.

The successful incorporation of Au NPs within the functional surface of the patchy nonwovens could be easily followed by the discoloration of the Au NP dispersion and the resulting purple colour of the produced hybrid nonwovens. The strong binding of the Au NPs within the functional surface patches can be attributed to a replacement of the citrate ligands by the multidentate, amino-group containing patches (gain in entropy by release of citrate molecules). Electrostatic interactions with the amino groups ( $\text{p}K_a \approx 7$ ) in the functional patches can be neglected as the Au NP dispersion shows a pH of 8 and under these conditions the amino groups are uncharged.<sup>68</sup> The Au content of the hybrid nonwovens was determined from the respective Au content of the Au NP dispersions after loading, as determined by UV-Vis (ultraviolet-visible) spectroscopy. Here, the Au content of the initial Au NP dispersion determined by ICP-OES (inductively coupled plasma-optical emission spectrometry) was used as reference (difference method). A detailed description of this method is given in the ESI (Fig. S3.5). The Au contents of the hybrid nonwovens and the overall surface area ( $S_{\text{AuNP}}$ ) of the embedded Au NPs, as determined from the respective Au content and the average diameter of  $D_{\text{TEM}} = 9.5 \pm 2.4 \text{ nm}$ , are given in Table 2. The Au NP-loaded hybrid nonwovens are termed according to the employed patchy nonwoven template, *i.e.*, NW\_*s*-SEDiPA(*w*)/Au stands for a patchy NW\_*s*-SEDiPA(*w*) nonwoven loaded with Au NPs.

**Table 3.2.** Au content and overall surface area of embedded Au NPs in the hybrid nonwovens.

hybrid nonwoven	$m_{\text{Au, calibration}}^{\text{a, b}}$ [ $\mu\text{g}\cdot\text{cm}^{-2}$ ]	$m_{\text{Au, UV-Vis 400nm}}^{\text{a, c}}$ [ $\mu\text{g}\cdot\text{cm}^{-2}$ ]	$S_{\text{AuNP}}^{\text{d}}$ [ $\text{m}^2$ ]
NW <sub>s</sub> -SEDiPA(s)/Au	69	70	$(2.29 \pm 0.58)\cdot 10^{-3}$
NW <sub>s</sub> -SEDiPA(w)/Au	52	57	$(1.86 \pm 0.47)\cdot 10^{-3}$
NW <sub>as</sub> -SEDiPA(s)/Au	77	77	$(2.52 \pm 0.64)\cdot 10^{-3}$
NW <sub>as</sub> -SEDiPA(w)/Au	82	82	$(2.68 \pm 0.68)\cdot 10^{-3}$
NW <sub>s</sub> -SEDMA(w)/Au	76	77	$(2.52 \pm 0.64)\cdot 10^{-3}$

<sup>a</sup> relative to the area of the nonwoven ( $S = 1 \text{ cm}^2$ ) under assumption of an equal thickness ( $d \approx 400 \mu\text{m}$ ). <sup>b</sup> the amount of Au in the dispersions was calculated according to Fig. S3.5, using a calibration based on the employed Au NP dispersion. <sup>c</sup> determined from the absorbance at  $\lambda = 400 \text{ nm}$  according to eqn (S3.1). <sup>d</sup> Overall surface area of the embedded Au NPs calculated from the NP diameter obtained by TEM ( $D_{\text{TEM}} = 9.5 \pm 2.4 \text{ nm}$ ) and the Au content in the hybrid nonwovens ( $m_{\text{Au, UV-Vis 400nm}}$ ), assuming a perfect spherical shape (eqn (S3.7 – S3.10)). Given errors were calculated based on error propagation (eqn S3.11).

An important issue in heterogeneous catalysis with supported NPs is the efficient immobilization and stabilization of the NPs in order to avoid agglomeration and, thus, a loss in catalytically active surface area, while preserving the catalytic activity of the NPs. The latter might be strongly influenced by the type of stabilizing ligands, *i.e.*, their binding strength to the Au NPs' surface. Accordingly, the performance of the patchy nonwovens as support for the efficient stabilization of Au NPs was analysed by SEM and SAXS (small-angle X-ray scattering), and the catalytic activity of the immobilized NPs was probed employing the alcoholysis of dimethylphenylsilane. In the following, the impact of the micelle morphology and patch size as well as patch chemistry will be discussed in detail.

### Effect of micelle morphology and patch size

SEM coupled with a backscattered electron (BSE) detector confirms the homogeneous loading of the patchy nonwovens based on spherical and worm-like *s*-SEDiPA CCMs with Au NPs (Fig. 3.4A,B). NP agglomerates, which would be discernible as large, bright appearing domains, are hardly detectable. The absence of larger NP agglomerates is also supported by the SAXS results shown in Fig. 3.4C (NW\_*s*-SEDiPA(*w*)/Au) and 3.4D (NW\_*s*-SEDiPA(*s*)/Au), which compare the scattering profiles of the Au NPs within the hybrid nonwovens (open triangles) with that of the Au NP dispersion (coloured in red) used in the loading process. The scattering profiles of the embedded Au NPs were determined by subtracting the scattering intensity of the Au NP-loaded hybrid nonwovens from that of the corresponding neat nonwovens, as described in our previous work.<sup>68</sup> For both hybrid nonwovens, the scattering profile of the embedded Au NPs is similar to that of the neat Au NP dispersion for scattering vectors  $q > 0.1 \text{ nm}^{-1}$ . Only for smaller  $q$ -values, the scattering profiles do not reach a plateau but show a slight increase with decreasing  $q$ -values. This might point to a weak, partial agglomeration of the incorporated Au NPs or to an additional structure factor contribution due to the close vicinity of the embedded Au NPs in the corona of the patchy micelles located at the nonwovens' surface.

We have also studied whether agglomeration or a loss of the embedded Au NPs might occur during catalysis. For the hybrid nonwoven based on *s*-SEDiPA *w*CCMs (Fig. 3.4C, NW\_*s*-SEDiPA(*w*)/Au) the scattering profiles prior to (open triangles) and after 10 catalysis cycles (dotted profile) are nearly identical, *i.e.*, neither a loss of Au NPs (scattering intensity would decrease) nor a significant agglomeration (steeper increase of scattering intensity for low  $q$ -values would be expected) take place during catalysis. In contrast, for the hybrid nonwoven based on *s*-SEDiPA *s*CCMs (Fig. 3.4D, NW\_*s*-SEDiPA(*s*)/Au) a significantly lower scattering intensity and a pronounced plateau for low  $q$ -values were observed after 10 catalysis cycles. This points to a partial loss of larger Au NPs during catalysis, revealing that patchy nonwovens based on spherical *s*-SEDiPA CCMs are less efficient in NP stabilization with respect to *s*-SEDiPA *w*CCMs. This might be attributed to the less defined patchy corona of the *s*CCMs (Fig. 3.2).

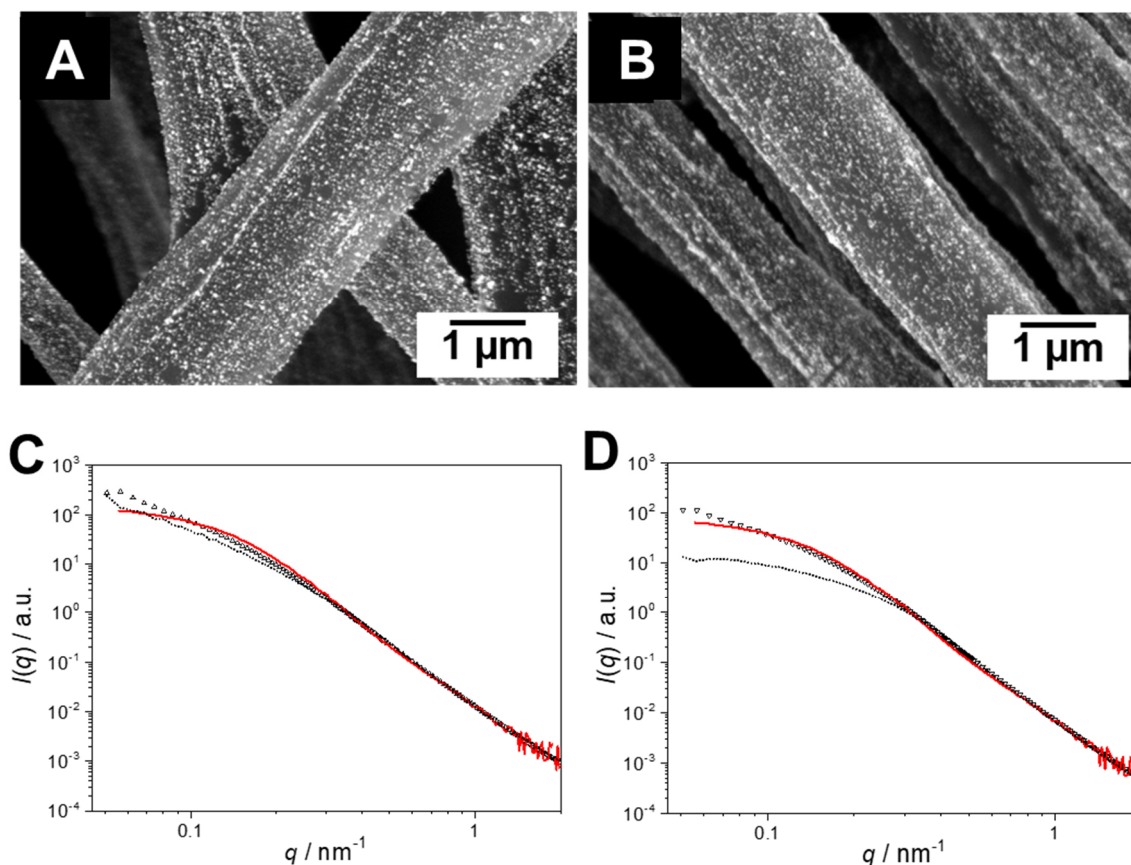


**Fig. 3.4.** SEM micrographs of Au NP-loaded patchy nonwovens based on *s*-SEDiPA *w*CCMs (A, NW\_*s*-SEDiPA(*w*)/Au) and *s*CCMs (B, NW\_*s*-SEDiPA(*s*)/Au), analysed with a BSE detector; the Au NPs appear as bright dots. SAXS profiles of the Au NPs immobilized in patchy nonwovens based on *s*-SEDiPA *w*CCMs (C, NW\_*s*-SEDiPA(*w*)/Au) and *s*CCMs (D, NW\_*s*-SEDiPA(*s*)/Au), prior to (open triangles) and after 10 catalysis cycles (dotted profiles). The SAXS profile of the corresponding aqueous Au NP dispersion employed for the dipping process is shown in red and was shifted vertically to match the scattering intensity of the Au NPs in the respective hybrid nonwovens in the high *q*-range to facilitate comparison.

Fig. 3.5 displays the scattering profiles of the embedded Au NPs for hybrid nonwovens based on spherical (NW\_*as*-SEDiPA(*s*)/Au, filled squares) and worm-like (NW\_*as*-SEDiPA(*w*)/Au, open triangles) *as*-SEDiPA CCMs, which exhibit a highly asymmetric corona, *i.e.*, different PS and PDiPA patch sizes (Table 3.1). Here, the scattering intensity for NW\_*as*-SEDiPA(*w*)/Au shows only a comparably weak increase for low *q*-values and tends to form a plateau, unlike the behaviour of NW\_*s*-SEDiPA(*w*)/Au (symmetric corona). Moreover, the scattering profile of the embedded Au NPs is now almost identical to that of the Au NPs in the initial Au NP dispersion (red profile). This points to a more efficient stabilization of the Au NPs embedded within the asymmetric patchy corona of *as*-SEDiPA *w*CCMs against agglomeration. Again, for the NW\_*as*-SEDiPA(*s*)/Au hybrid nonwoven a steeper increase in scattering intensity for low *q*-values is observed, which points to a partial agglomeration and

underpins the conclusion that patchy *s*CCMs are less efficient in NP stabilization compared to *w*CCMs. The enhanced stabilization of Au NPs against agglomeration for *as*-SEDiPA *w*CCMs might be attributed to the slightly smaller size of the functional PDiPA patches ( $9 \pm 2$  nm for *as*-SEDiPA(*w*),  $10 \pm 3$  nm for *s*-SEDiPA(*w*)) in combination with the increased size of the PS patches ( $18 \pm 4$  nm for *as*-SEDiPA(*w*),  $12 \pm 2$  nm for *s*-SEDiPA(*w*)), which separate the PDiPA patches from each other (Table 3.1). Accordingly, there is less space for the Au NPs in the PDiPA patches and the spatial separation of the PDiPA patches by the PS patches is stronger, leading to a reduced possibility to form NP agglomerates.

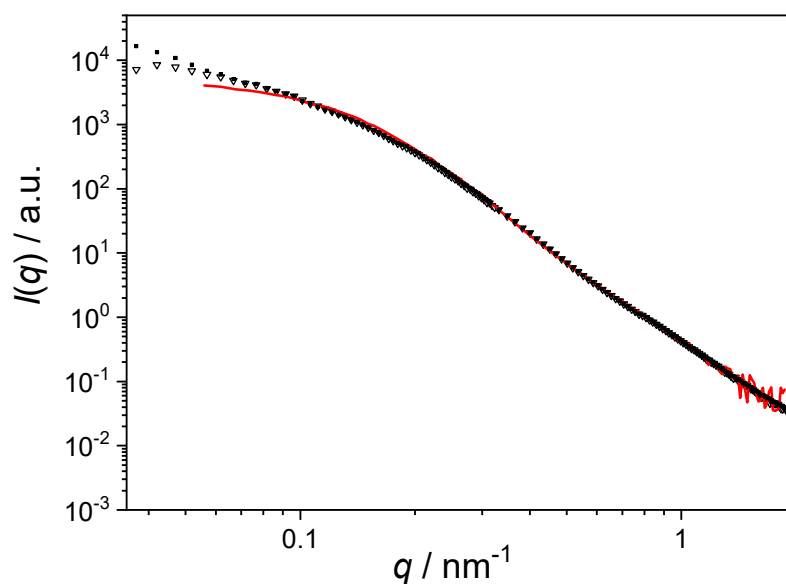


**Fig. 3.5.** SAXS profiles of the Au NPs immobilized in patchy nonwovens based on *as*-SEDiPA *w*CCMs (NW\_*as*-SEDiPA(*w*)/Au, open triangles) and *s*CCMs (NW\_*as*-SEDiPA(*s*)/Au, filled squares). The SAXS profile of the corresponding aqueous Au NP dispersion employed for the dipping process is shown in red and was shifted vertically to match the scattering intensity of the Au NPs in the respective hybrid nonwovens in the high *q*-range to facilitate comparison.

Next, we studied the impact of micelle shape and patch size on the catalytic activity of the patchy hybrid nonwovens, employing the alcoholysis of dimethylphenylsilane in *n*-butanol (*n*-BuOH) as established model reaction (Fig. 3.6A).<sup>68</sup> We ran 10 consecutive cycles and the kinetics were followed for the 1<sup>st</sup> and 10<sup>th</sup> cycles in order to address the effect of swelling of the PDxA patches in *n*-BuOH on the catalytic performance and to probe the reusability of our catalyst system. Detailed information on the Au content of the nonwovens are given in Table 3.2, the used molar ratio of Au to dimethylphenylsilane and other kinetic parameters are summarized in Table 3.3.

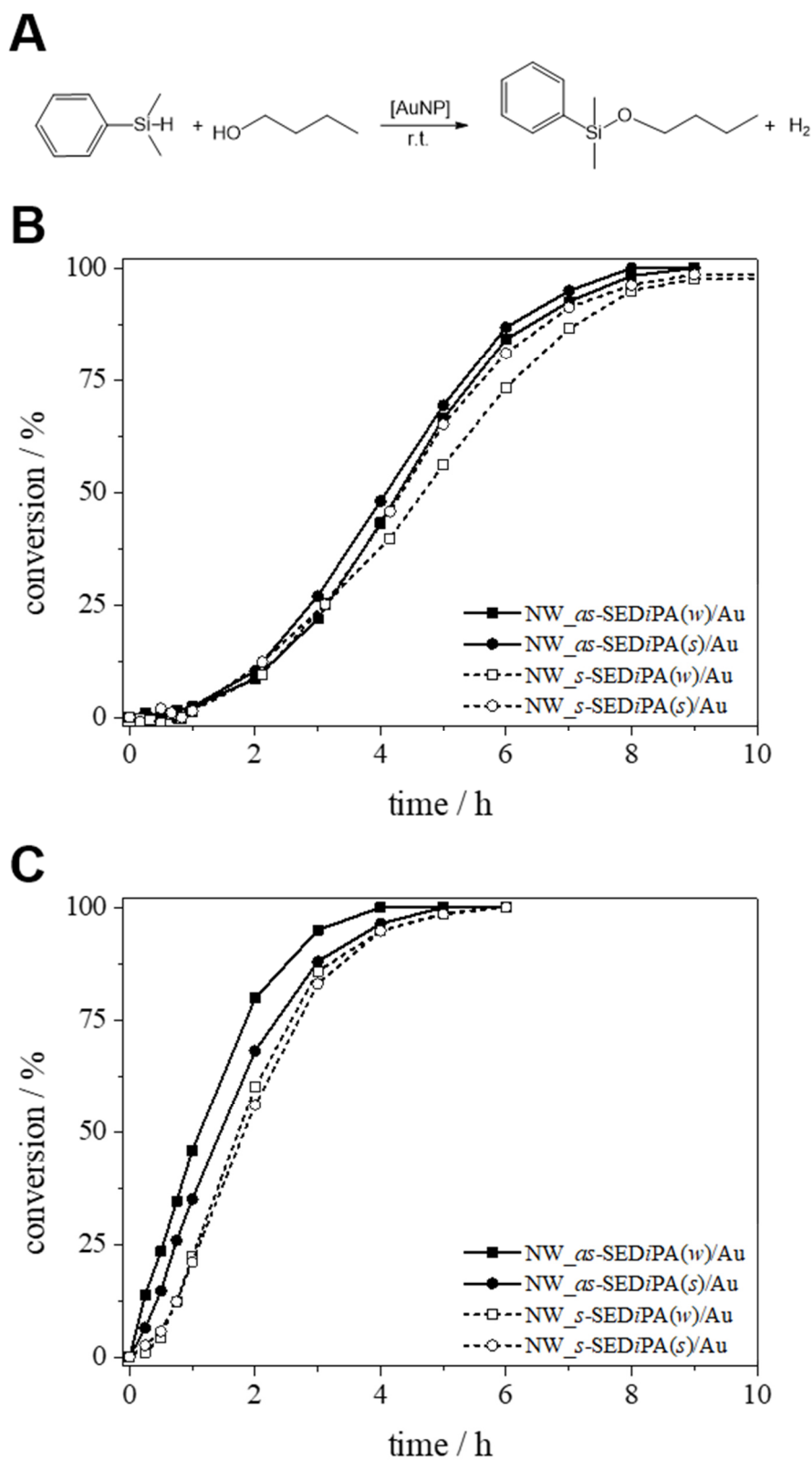


**Fig. 3.6.** A) Au NP-catalysed alcoholysis of dimethylphenylsilane in *n*-BuOH. Corresponding conversion vs. time plots employing different Au NP-loaded patchy nonwovens based on *s*- and *as*-SEDiPA CCMs as catalyst (B, 1<sup>st</sup> cycles; C, 10<sup>th</sup> cycles).

**Table 3.3.** Kinetic parameters for the 10<sup>th</sup> cycles of the catalytic alcoholysis of dimethylphenylsilane in *n*-BuOH, obtained using our extended pseudo 1<sup>st</sup> order kinetics model given in eqn (3.5).

hybrid nonwovens	Au <sup>a</sup> mol-%	$k_{app}$ <sup>b</sup> [h <sup>-1</sup> ]	$r$ [h <sup>-1</sup> ]	$t_{ind}$ <sup>c</sup> [min]	$t_R$ <sup>d</sup> [h]	$k$ <sup>e</sup> [L·m <sup>2</sup> ·mol <sup>-1</sup> ·s <sup>-1</sup> ]
NW_ <i>s</i> -SEDiPA( <i>s</i> )/Au	0.15	1.77 ± 0.10	0.29 ± 0.02	21	5.29	(1.97 ± 0.51)·10 <sup>-2</sup>
NW_ <i>s</i> -SEDiPA( <i>w</i> )/Au	0.12	1.54 ± 0.11	0.38 ± 0.05	20	5.25	(2.10 ± 0.55)·10 <sup>-2</sup>
NW_ <i>as</i> -SEDiPA( <i>s</i> )/Au	0.17	1.18 ± 0.10	0.79 ± 0.15	16	5.16	(1.19 ± 0.31)·10 <sup>-2</sup>
NW_ <i>as</i> -SEDiPA( <i>w</i> )/Au	0.18	1.27 ± 0.11	1.43 ± 0.38	11	4.32	(1.20 ± 0.32)·10 <sup>-2</sup>
NW_ <i>s</i> -SEDMA( <i>w</i> )/Au	0.17	1.55 ± 0.26	0.54 ± 0.16	17	4.68	(1.56 ± 0.47)·10 <sup>-2</sup>

<sup>a</sup> relative to dimethylphenylsilane (0.23 mmol). <sup>b</sup> apparent rate constant ( $k_{app}$ ) and accessibility rate ( $r$ ) determined according to eqn (3.5). <sup>c</sup> time at 3% conversion was taken as induction time ( $t_{ind}$ ) and calculated using eqn (3.5). <sup>d</sup> reaction time ( $t_R$ ) at 99% conversion, calculated using eqn (3.5). <sup>e</sup> rate constant normalized to the overall surface area of the embedded Au NPs ( $S_{AuNP}$ , Table 3.2) and the concentration of *n*-BuOH ( $c_{n-BuOH} = 10.93 \text{ mol}\cdot\text{L}^{-1}$ ), given errors were calculated based on error propagation (eqn S3.12).

Fig. 3.6B shows the conversion *vs.* time ( $x_p/t$ ) plots of the 1<sup>st</sup> catalysis cycles for hybrid nonwovens based on *s*- and *as*-SEDiPA CCMs. Irrespective of the micelle morphology and patch sizes of the CCMs employed for surface decoration, the hybrid nonwovens showed an induction time of  $t_{ind} \approx 1$  h. Full conversion is reached in about 8 - 9 h for all hybrid nonwovens, while the *s*-SEDiPA based systems show slightly longer reaction times. The latter might be attributed to the higher PDiPA content in the corona of the *s*-SEDiPA micelles in combination with a higher PDiPA block length (Table 3.1), resulting in a slightly higher diffusion barrier for the reactants in the swollen PDiPA patches with respect to *as*-SEDiPA based hybrid nonwovens. However, one has to take the slightly different Au contents of the hybrid nonwovens into account (Table 3.2). This point will be addressed in detail later on in the discussion of the kinetics of the 10<sup>th</sup> catalysis cycles. Interestingly, the induction times are significantly decreased for the 10<sup>th</sup> catalysis cycles ( $t_{ind} \approx 10 - 20$  min, Table 3.3) and, in addition, full conversion is already reached in about 4 - 6 h. This shows that the higher induction and reaction times observed in the 1<sup>st</sup> catalysis cycles are most likely related to an initial period, where the PDiPA patches swell in *n*-BuOH and, thus, enable the reactants to access the embedded Au NPs. This is also in contrast to our previous work, where we have

observed that the 1<sup>st</sup> and 10<sup>th</sup> catalysis cycles were almost identical with comparable induction times.<sup>68</sup> This discrepancy can be attributed to the different degrees of functionalization ( $f$ ) of the PDiPA blocks ( $f = 55\%$  vs. quantitative functionalization in this study) and the fact that the previously employed amidation method resulted in about 50 mol% imide units, which show only limited solubility in  $n$ -BuOH. Hence, the swelling of the PDiPA patches clearly affects the accessibility of the catalytically active Au NP surface and, as a consequence, the duration of the induction period and the overall reaction time.

In order to get a deeper insight into the kinetics of the reaction and, hence, the influence of micelle shape and patch size, we have evaluated the kinetics of the 10<sup>th</sup> catalysis cycles. We have purposely chosen the 10<sup>th</sup> catalysis cycles to rule out the effect of initial swelling from the dry state, manifested by the long induction times observed for the 1<sup>st</sup> catalysis cycles. Despite the large excess of  $n$ -BuOH compared to silane, Fig. S3.10 shows that a classical pseudo 1<sup>st</sup> order kinetics model cannot reproduce the experimental data over the full time range. We therefore developed a theoretical model, which extends the classical pseudo 1<sup>st</sup> order kinetics with an additional induction period to address the influence of patch swelling. We consider the reaction of dimethylphenylsilane (reactant  $E$ ) with  $n$ -BuOH, which acts as both solvent and reactant, employing the rate law

$$\frac{d[E]}{dt} = -\kappa(t)[E][n\text{-BuOH}]. \quad (3.1)$$

In order to model the induction period, *i.e.*, the swelling of the patches, the two reactants (dimethylphenylsilane and  $n$ -BuOH) are considered to become available for the embedded catalytically active Au NPs with a certain accessibility rate  $r$ . The specialty of our model is that the reaction rate  $\kappa(t)$  is increasing over time according to

$$\kappa(t) = \kappa_0(1 - e^{-rt}), \quad (3.2)$$

representing the slowly increasing availability of the reactants over the time  $t$ . The accessibility rate  $r$  is a measure how quickly this process occurs.

Replacing (3.2) in (3.1) yields the rate law for our model

$$\frac{d[E]}{dt} = -k_{app}(1 - e^{-rt})[E], \quad (3.3)$$

where  $k_{app} = \kappa_0[n\text{-BuOH}]$  is the apparent rate constant. Separating variables and integrating eqn (3.3) leads to

$$-\int_{[E]_0}^{[E]} \frac{1}{[E']} d[E'] = \int_0^t k_{app}(1 - e^{-rt'}) dt' \quad (3.4)$$

The natural logarithm form of the power law expression is finally obtained as

$$-\ln \frac{[E]}{[E]_0} = k_{app} \left( \frac{e^{-rt}}{r} + t \right) - \frac{k_{app}}{r}. \quad (3.5)$$

We note that for immediate availability of the reactants, *i.e.*,  $r \rightarrow \infty$ , the classic equation describing the kinetics of a pseudo 1<sup>st</sup> order reaction (eqn (S3.5)) is recovered from eqn (3.5).

Accordingly, the experimental data were fitted with eqn (3.5) to yield the apparent rate constants ( $k_{app}$ ) and the accessibility rates ( $r$ ) (Fig. 3.7, S3.11). To facilitate comparison between the different catalyst systems the apparent rate constants were normalized to the concentration of *n*-BuOH ( $c_{n\text{-BuOH}} = 10.93 \text{ mol}\cdot\text{L}^{-1}$ ) and the overall surface area ( $S_{\text{AuNP}}$ ) of the embedded Au NPs, yielding the rate constants  $k$  for the Au NP-catalysed alcoholysis of dimethylphenylsilane (eqn (S3.6), Table 3.3). Using the obtained values for  $k_{app}$  and  $r$ , the corresponding induction times ( $t_{ind}$ ) and overall reaction times ( $t_R$ ) can be calculated from eqn (3.5) and are also given in Table 3.3.

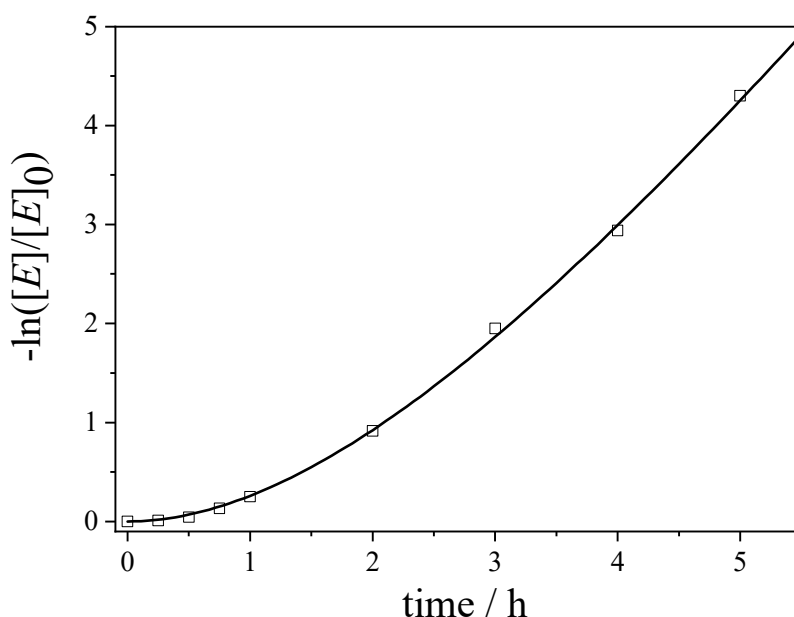


**Fig. 3.7.** Kinetics plot for the 10<sup>th</sup> cycle of the catalytic alcoholysis of dimethylphenylsilane with an Au NP-loaded patchy nonwoven based on *s*-SEDiPA wCCMs (NW\_*s*-SEDiPA(*w*)/Au) as catalyst (squares: experimental data, line: fit according to our extended pseudo 1<sup>st</sup> order kinetics model in eqn (3.5)).

The normalized rate constants ( $k$ ) are in a comparable range for the different hybrid nonwovens based on *s*-SEDiPA and *as*-SEDiPA CCMs (Table 3.3). Similar results were obtained by using the classical 1<sup>st</sup> order kinetics model for the determination of the reaction rate constants (eqn (S3.5), Fig. S3.10, Table S3.2), although in this case only the second half of the observation period, where the plot exhibits a constant slope, can be fitted by the classical model. Interestingly, the accessibility parameters ( $r$ ) for the *as*-SEDiPA based hybrid nonwovens are higher with respect to that of the *s*-SEDiPA based ones. A possible explanation

is the lower steric demand of the PDiPA patches in the *as*-SEDiPA CCMs (lower PDiPA block length and content in the corona, Table 3.1). This is also reflected in the shorter induction and reaction times observed for the *as*-SEDiPA based hybrid nonwovens, despite the slightly lower normalized rate constants compared to *s*-SEDiPA based nonwovens. Altogether, the induction ( $t_{\text{ind}} \approx 10 - 20$  min) and reaction times ( $t_{\text{R}} \approx 4 - 5$  h) for the 10<sup>th</sup> catalysis cycles (Table 3.3) are significantly shorter in comparison to the 1<sup>st</sup> catalysis cycles ( $t_{\text{ind}} \approx 1$  h,  $t_{\text{R}} \approx 8 - 9$  h, as estimated from the  $x_{\text{p}}/t$  plots in Fig. 3.6B), showing again the importance of patch swelling in *n*-BuOH for the reaction kinetics. With respect to our previous work a significant reduction of the reaction time from about 7 to 4.3 h could be achieved for the NW\_*as*-SEDiPA(*w*)/Au hybrid nonwoven.<sup>68</sup>

### Effect of patch chemistry

To further study the effect of patch swelling on the catalytic activity of the hybrid nonwovens, we altered the patch chemistry (PDMA *vs.* PDiPA) and compared nonwovens decorated with *s*-SEDiPA (Fig. 3.3B,C) and *s*-SEDMA (Fig. 3.8A) *w*CCMs. If there is any effect of patch chemistry on the reaction kinetics, this effect should be largest for the CCMs with the highest weight fraction of PDxA units in the corona, *i.e.*, *s*-SEDMA and *s*-SEDiPA (Table 3.1). The PDMA patches are more hydrophilic compared to PDiPA and, consequently, are expected to swell faster and to a greater extend in *n*-BuOH.

The SEM image acquired with a BSE detector again shows nicely dispersed, bright appearing Au NPs at the surface of the respective NW\_*s*-SEDMA(*w*)/Au hybrid nonwoven (Fig. 3.8B). The SAXS profile of the embedded Au NPs (Fig. 3.8C, filled squares) shows no sign of agglomeration, in contrast to the weak, partial agglomeration observed for the *s*-SEDiPA (Fig. 3.4C,D) and *as*-SEDiPA (Fig. 3.5) based hybrid nonwovens. The scattering profile is almost identical to that of the Au NPs in the initial NP dispersion (Fig 3.8C, red profile) and the scattering intensity runs into a well-defined plateau for low *q*-values. This shows that nonwovens decorated with *s*-SEDMA *w*CCMs are best suited for Au NP stabilization and efficiently hinder the formation of NP agglomerates.

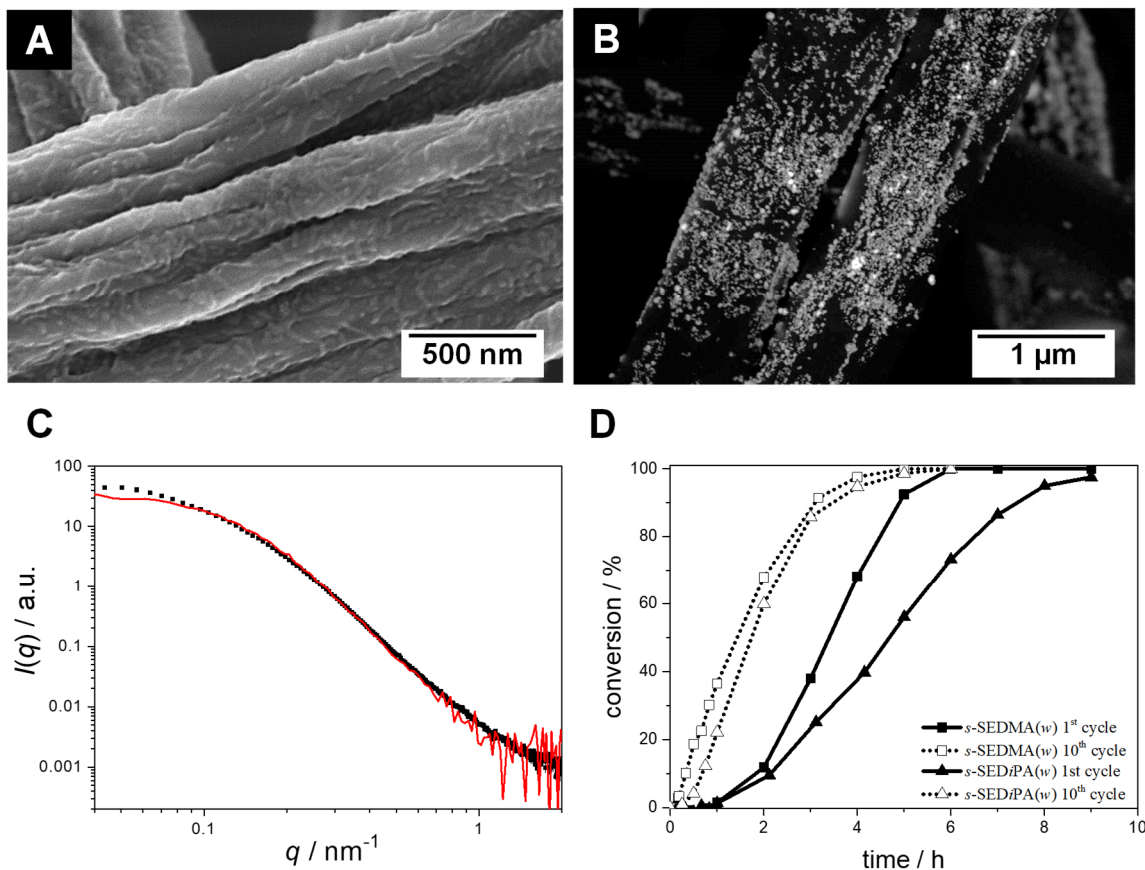


**Fig. 3.8.** SEM micrographs of neat (A) and Au NP-loaded (B, BSE detector) patchy nonwovens based on *s*-SEDMA(*w*) (NW\_*s*-SEDMA(*w*)/Au); the Au NPs in B) appear as bright dots. C) SAXS profiles of the Au NPs immobilized in the patchy nonwoven (filled squares) and of the corresponding aqueous Au NP dispersion employed for the dipping process (red). D) Comparison of conversion vs. time plots (1<sup>st</sup> and 10<sup>th</sup> cycles) for the catalytic alcoholysis of dimethylphenylsilane with Au NP-loaded patchy nonwovens based on *s*-SEDiPA (NW\_*s*-SEDiPA(*w*)/Au) and *s*-SEDMA (NW\_*s*-SEDMA(*w*)/Au) wCCMs as catalyst.

Fig. 3.8D compares the  $x_p/t$ -plots for the 1<sup>st</sup> and 10<sup>th</sup> cycles of the catalytic alcoholysis of dimethylphenylsilane with NW\_*s*-SEDiPA(*w*)/Au and NW\_*s*-SEDMA(*w*)/Au, respectively. The most obvious difference can be observed in the 1<sup>st</sup> catalysis cycles. The induction times are comparable ( $t_{\text{ind}} \approx 1$  h), but the overall reaction time is significantly lower for the *s*-SEDMA(*w*) based hybrid nonwoven (about 6 h compared to 9 h for NW\_*s*-SEDiPA(*w*)/Au). In addition, for the 10<sup>th</sup> cycles the accessibility parameter ( $r$ ) is higher and the induction ( $t_{\text{ind}}$ ) as well as overall reaction time ( $t_{\text{R}}$ ) are lower for the *s*-SEDMA(*w*) decorated hybrid nonwoven (Table 3.3). This clearly underlines the influence of patch swelling on the reaction kinetics and supports our assumption that the increased hydrophilicity of the PDMA patches results in a better swelling of the patches in *n*-BuOH (higher accessibility parameter) and, thus, leads to reduced induction and reaction times.

In summary, concerning the efficiency for Au NP stabilization patchy *w*CCMs are more efficient compared to *s*CCMs and the *s*-SEDMA(*w*) based nonwoven showed the best performance, *i.e.*, no hints for NP agglomeration could be detected by SEM and SAXS. However, the shortest induction and reaction times for the 10<sup>th</sup> cycle of the Au NP-catalyzed alcoholysis of dimethylphenylsilane were observed for the *as*-SEDiPA(*w*) based hybrid nonwoven. Accordingly, the interplay of micelle shape, patch size and chemistry influences the stabilization and catalytic activity of the embedded Au NPs. PDMA patches are more efficient for NP stabilization, which might be attributed to a stronger interaction with the NPs' surface (less steric hindrance of methyl groups compared to *iso*-propyl groups). But in contrast, a stronger interaction with the NPs' surface could lead to reduced reaction rate constants (Table 3.3: NW\_*s*-SEDMA(*w*)/Au shows a slightly lower normalized rate constant (*k*) compared to NW\_*s*-SEDiPA(*w*)/Au). Next to these parameters, also the accessibility parameter (*r*) has to be taken into account, which describes the rate at which the reactants (dimethylphenylsilane and *n*-BuOH) become available for the embedded Au NPs. This parameter is largest for NW\_*as*-SEDiPA(*w*)/Au and results in the shortest observed induction and reaction times, despite the lower normalized rate constant in comparison to *s*-SEDMA(*w*) and *s*-SEDiPA(*w*) based hybrid nonwovens (Table 3.3).

The reaction times for full conversion and the rate constants strongly depend on the Au content and the Au NP size, *i.e.*, the total Au NP surface area. This makes a comparison to other studies difficult, as mostly only reaction times are given and the rate constants are not normalized to the overall Au NP surface area. Nevertheless, the reported reaction times for the Au NP-catalysed alcoholysis of dimethylphenylsilane with *n*-BuOH at room temperature are in the range of the reaction times found in this study ( $t_R \approx 4 - 5$  h) or even higher (Table S3.3).<sup>70,73,74</sup> Shorter reaction times at full conversion were only reported for Au NPs supported on nanoasized hydroxyapatite (Au/HAP<sub>nano</sub>) and were attributed to the high adsorption capacity of the support, which increases locally the concentration of dimethylphenylsilane at the surface of Au/HAP<sub>nano</sub>.<sup>75</sup> However, the employed Au NPs ( $D = 3$  nm) were significantly smaller compared to the Au NPs used in this study ( $D_{TEM} = 9.5 \pm 2.4$  nm), which results in an increased catalytically active surface area.

## Conclusions

The studied electrospun patchy nonwovens are efficient supports for the stabilization of Au NPs against agglomeration and the corresponding hybrid nonwovens with embedded Au NPs exhibit a high activity and reusability in the catalytic alcoholysis of dimethylphenylsilane. Utilizing an extended pseudo 1<sup>st</sup> order kinetics model revealed that the catalytic activity is influenced by the patch size and chemistry (PDMA vs. PDiPA patches), which determine the accessibility of the reactants to the surface of the embedded Au NPs. This is also manifested by the observation of longer induction and reaction times in the 1<sup>st</sup> catalysis cycles in comparison to that of the 10<sup>th</sup> cycles. This allows to tailor the properties of the patchy hybrid nonwovens in terms of NP stabilization and catalytic performance. Compared to heterogeneous catalysis with Au NPs that are stabilized by particulate supports (MOFs, metal oxides, 2D materials) our “tea-bag”-like catalyst system can be simply dipped in the reaction mixture and pulled out after catalysis without the need of filtration or centrifugation to separate the catalyst. Electrospinning as a top-down approach can be easily upscaled and the synthesis of the PS-*b*-PE-*b*-PMMA precursor triblock terpolymers (catalytic hydrogenation of polystyrene-*block*-polybutadiene-*block*-poly(methyl methacrylate) triblock terpolymers produced by living anionic polymerization (also commercially available from Arkema)) can be conducted on a kg scale. In addition, the functional, amino group-containing patches are not only efficient stabilizers for Au NPs, but can also be employed for the incorporation of other metal (Ag, Pd) or transition metal oxide (CuO, ZnO) NPs. This opens the way for a variety of applications in heterogeneous catalysis, which will be addressed in future studies. Moreover, the facile loading of the patchy nonwovens by a simple dipping process and the efficient stabilization of the embedded NPs might be also utilized for water purification.

*Electronic Supplementary Information (ESI) available:* Characterization of the AuNP dispersion (TEM, DLS, AF4), the SEDxA triblock terpolymers (<sup>1</sup>H NMR, FT-IR,  $\mu$ DSC, DLS and TEM), nonwovens based on *as*-SEDiPA *s*- and *w*CCMs (SEM) and details on determination of the Au content in the patchy nonwovens and on treatment of kinetics data. This is available free of charge via the Internet at <http://pubs.rsc.org>.

## Acknowledgements

This work was supported by the German Research Foundation through the Collaborative Research Centre SFB 840 (projects A2, A12 and B8) and the Bavarian State Ministry of the Environment and Consumer Protection (TNT01NaT-72524). We thank S. Agarwal for assistance with coaxial electrospinning and H.-W. Schmidt for discussion and support on SEM measurements. We appreciate support of the Keylab Mesoscale Characterization: Scattering Techniques (S. Rosenfeldt) of the Bavarian Polymer Institute (BPI) for conducting some of the SAXS experiments, Carmen Kunert for SEM and TEM and Rika Schneider for AF4 measurements. C.H. acknowledges support by the Graduate School of the University of Bayreuth. G.S. acknowledges support from the Biological Physics program of the Elite Network of Bavaria and S.G. thanks the Volkswagen Foundation. We appreciate support through the computational resources provided by the Bavarian Polymer Institute.

## References

- 1 A. Alshammari and V. N. Kalevaru, in *Catalytic Application of Nano-Gold Catalysts*, ed. N. K. Mishra, InTech, 2016.
- 2 M. Haruta, *Chem. Rec.*, 2003, **3**, 75–87.
- 3 S. Nishimura and K. Ebitani, *ChemCatChem*, 2016, **8**, 2303–2316.
- 4 C. Burda, X. Chen, R. Narayanan and M. A. El-Sayed, *Chem. Rev.*, 2005, **105**, 1025–1102.
- 5 M. Stratakis and H. Garcia, *Chem. Rev.*, 2012, **112**, 4469–4506.
- 6 G. C. Bond, P. A. Sermon, G. Webb, D. A. Buchanan and P. B. Wells, *J. Chem. Soc., Chem. Commun.*, 1973, 444–445.
- 7 M. Haruta, T. Kobayashi, H. Sano and N. Yamada, *Chem. Lett.*, 1987, **16**, 405–408.
- 8 L. M. Rossi, J. L. Fiorio, M. A. S. Garcia and C. P. Ferraz, *Dalton Trans.*, 2018, **47**, 5889–5915.
- 9 S. Kunz, *Top. Catal.*, 2016, **59**, 1671–1685.
- 10 Á. Molnár and A. Papp, *Coord. Chem. Rev.*, 2017, **349**, 1–65.
- 11 A. Cao, R. Lu and G. Veser, *Phys. Chem. Chem. Phys.*, 2010, **12**, 13499–13510.
- 12 M. Davidson, Y. Ji, G. J. Leong, N. C. Kovach, B. G. Trewyn and R. M. Richards, *ACS Appl. Nano Mater.*, 2018, **1**, 4386–4400.
- 13 I. Ro, J. Resasco and P. Christopher, *ACS Catal.*, 2018, **8**, 7368–7387.
- 14 Y. Wang, H. Arandiyani, J. Scott, A. Bagheri, H. Dai and R. Amal, *J. Mater. Chem. A*, 2017, **5**, 8825–8846.
- 15 G. Zhan and H. C. Zeng, *Coord. Chem. Rev.*, 2016, **320–321**, 181–192.
- 16 M. Massaro, C. G. Colletti, G. Lazzara, S. Milioto, R. Noto and S. Riela, *J. Mater. Chem. A*, 2017, **5**, 13276–13293.
- 17 J. Yuan, H. Schmalz, Y. Xu, N. Miyajima, M. Drechsler, M. W. Möller, F. Schacher and A. H. E. Müller, *Adv. Mater.*, 2008, **20**, 947–952.
- 18 J. John, E. Gravel, A. Hagège, H. Li, T. Gacoin and E. Doris, *Angew. Chem. Int. Ed.*, 2011, **50**, 7533–7536.
- 19 Y. Gong, M. Li, H. Li and Y. Wang, *Green Chem.*, 2015, **17**, 715–736.
- 20 A. Kumar and Q. Xu, *ChemNanoMat*, 2018, **4**, 28–40.

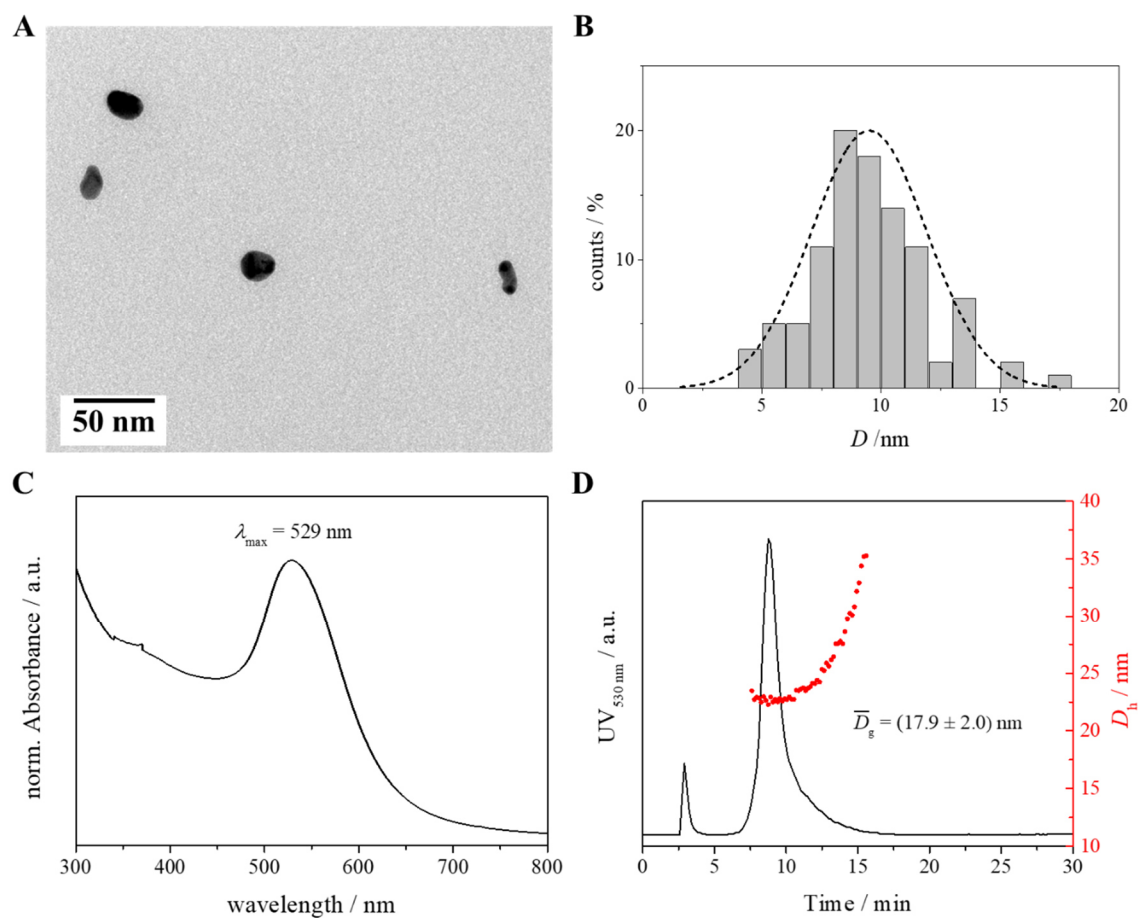
- 21 S. Navalon, A. Dhakshinamoorthy, M. Alvaro and H. Garcia, *Coord. Chem. Rev.*, 2016, **312**, 99–148.
- 22 R. K. Sharma, S. Dutta, S. Sharma, R. Zboril, R. S. Varma and M. B. Gawande, *Green Chem.*, 2016, **18**, 3184–3209.
- 23 H. R. Moon, D.-W. Lim and M. P. Suh, *Chem. Soc. Rev.*, 2013, **42**, 1807–1824.
- 24 C. R. Kim, T. Uemura and S. Kitagawa, *Chem. Soc. Rev.*, 2016, **45**, 3828–3845.
- 25 A. Dhakshinamoorthy, A. M. Asiri and H. Garcia, *ACS Catal.*, 2017, **7**, 2896–2919.
- 26 M. Kaushik and A. Moores, *Green Chem.*, 2016, **18**, 622–637.
- 27 M. Rose, *ChemCatChem*, 2014, **122**, 1166–1182.
- 28 J. Artz, *ChemCatChem*, 2018, **10**, 1753–1771.
- 29 S. Bhattacharyya, D. Samanta, S. Roy, V. P. Haveri Radhakantha and T. K. Maji, *ACS Appl. Mater. Interfaces*, 2019, **11**, 5455–5461.
- 30 J. He, S. Razzaque, S. Jin, I. Hussain and B. Tan, *ACS Appl. Nano Mater.*, 2019, **2**, 546–553.
- 31 S. K. Dey, D. Dietrich, S. Wegner, B. Gil-Hernández, S. S. Harmalkar, N. de Sousa Amadeu and C. Janiak, *ChemistrySelect*, 2018, **3**, 1365–1370.
- 32 Z. H. Farooqi, S. R. Khan and R. Begum, *Mater. Sci. Technol.*, 2017, **33**, 129–137.
- 33 R. Roa, S. Angioletti-Uberti, Y. Lu, J. Dzubiella, F. Piazza and M. Ballauff, *Z. Phys. Chem.*, 2018, **232**, 773–803.
- 34 Y. Lu and M. Ballauff, *Prog. Polym. Sci.*, 2016, **59**, 86–104.
- 35 P. Hervés, M. Pérez-Lorenzo, L. M. Liz-Marzán, J. Dzubiella, Y. Lu and M. Ballauff, *Chem. Soc. Rev.*, 2012, **41**, 5577–5587.
- 36 M. Müllner and A. H.E. Müller, *Polymer*, 2016, **98**, 389–401.
- 37 X. Fan, Z. Li and X. J. Loh, *Polym. Chem.*, 2016, **7**, 5898–5919.
- 38 R. Ye, A. V. Zhukhovitskiy, C. V. Deraedt, F. D. Toste and G. A. Somorjai, *Acc. Chem. Res.*, 2017, **50**, 1894–1901.
- 39 T. Rudolph, M. von der Lühe, M. Hartlieb, S. Norsic, U. S. Schubert, C. Boisson, F. D'Agosto and F. H. Schacher, *ACS Nano*, 2015, **9**, 10085–10098.
- 40 S. H. Jo, H. W. Kim, M. Song, N. J. Je, S.-H. Oh, B.-Y. Chang, J. Yoon, J. H. Kim, B. Chung and S. I. Yoo, *ACS Appl. Mater. Interfaces*, 2015, **7**, 18778–18785.

- 41 F. H. Schacher, P. A. Rugar and I. Manners, *Angew. Chem. Int. Ed.*, 2012, **51**, 7898–7921.
- 42 E. M. Sulman, V. G. Matveeva, M. G. Sulman, G. N. Demidenko, P. M. Valetsky, B. Stein, T. Mates and L. M. Bronstein, *J. Catal.*, 2009, **262**, 150–158.
- 43 J. Schöbel, C. Hils, A. Weckwerth, M. Schlenk, C. Bojer, M. C. A. Stuart, J. Breu, S. Förster, A. Greiner, M. Karg and H. Schmalz, *Nanoscale*, 2018, **10**, 18257–18268.
- 44 J. Schöbel, M. Karg, D. Rosenbach, G. Krauss, A. Greiner and H. Schmalz, *Macromolecules*, 2016, **49**, 2761–2771.
- 45 C.-L. Zhang and S.-H. Yu, *Chem. Soc. Rev.*, 2014, **43**, 4423–4448.
- 46 S. Agarwal, A. Greiner and J. H. Wendorff, *Prog. Polym. Sci.*, 2013, **38**, 963–991.
- 47 C. Bojer, K. Ament, H. Schmalz, J. Breu and T. Lunkenbein, *CrystEngComm*, 2019, **21**, 4840–4850.
- 48 U. Tritschler, S. Pearce, J. Gwyther, G. R. Whittell and I. Manners, *Macromolecules*, 2017, **50**, 3439–3463.
- 49 R. L. N. Hailes, A. M. Oliver, J. Gwyther, G. R. Whittell and I. Manners, *Chem. Soc. Rev.*, 2016, **45**, 5358–5407.
- 50 X. Wang, G. Guerin, H. Wang, Y. Wang, I. Manners and M. A. Winnik, *Science*, 2007, **317**, 644–647.
- 51 J. B. Gilroy, T. Gädt, G. R. Whittell, L. Chabanne, J. M. Mitchels, R. M. Richardson, M. A. Winnik and I. Manners, *Nat. Chem.*, 2010, **2**, 566–570.
- 52 P. A. Rugar, L. Chabanne, M. A. Winnik and I. Manners, *Science*, 2012, **337**, 559–562.
- 53 T. Gädt, N. S. Jeong, G. Cambridge, M. A. Winnik and I. Manners, *Nat. Mater.*, 2009, **8**, 144–150.
- 54 J. Xu, H. Zhou, Q. Yu, G. Guerin, I. Manners and M. A. Winnik, *Chem. Sci.*, 2019, **10**, 2280–2284.
- 55 A. M. Oliver, R. J. Spontak and I. Manners, *Polym. Chem.*, 2019, **43**, 3577.
- 56 Z. M. Hudson, C. E. Boott, M. E. Robinson, P. A. Rugar, M. A. Winnik and I. Manners, *Nat. Chem.*, 2014, **6**, 893–898.
- 57 H. Qiu, Z. M. Hudson, M. A. Winnik and I. Manners, *Science*, 2015, **347**, 1329–1332.
- 58 X. Li, Y. Gao, C. E. Boott, M. A. Winnik and I. Manners, *Nat. Commun.*, 2015, **6**, 8127.

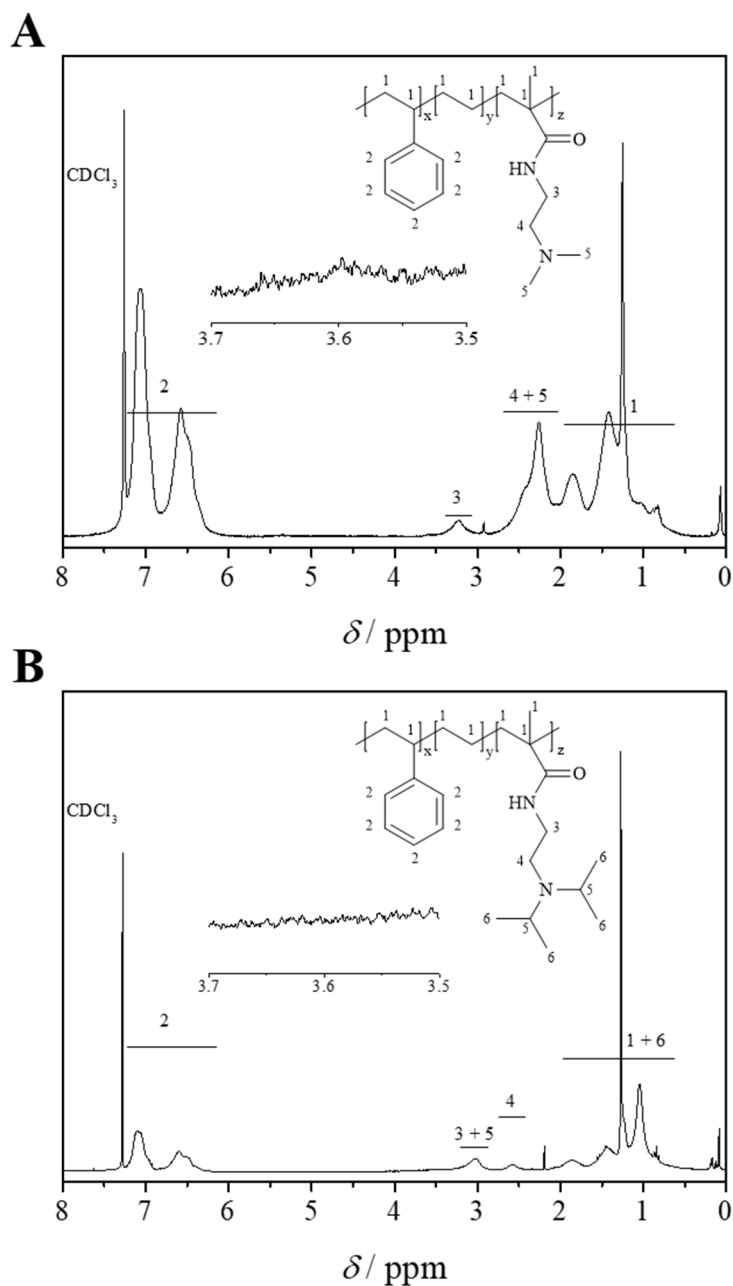
- 59 H. Dou, M. Li, Y. Qiao, R. Harniman, X. Li, C. E. Boott, S. Mann and I. Manners, *Nat. Commun.*, 2017, **8**, 426.
- 60 J. Schmelz, M. Karg, T. Hellweg and H. Schmalz, *ACS Nano*, 2011, **5**, 9523–9534.
- 61 B. Fan, L. Liu, J.-H. Li, X.-X. Ke, J.-T. Xu, B.-Y. Du and Z.-Q. Fan, *Soft Matter*, 2016, **12**, 67–76.
- 62 W. Yu, M. Inam, J. R. Jones, A. P. Dove and R. K. O'Reilly, *Polym. Chem.*, 2017, **8**, 5504–5512.
- 63 M. Inam, G. Cambridge, A. Pitto-Barry, Z. P. L. Laker, N. R. Wilson, R. T. Mathers, A. P. Dove and R. K. O'Reilly, *Chem. Sci.*, 2017, **8**, 4223–4230.
- 64 X. Li, P. J. Wolanin, L. R. MacFarlane, R. L. Harniman, J. Qian, O. E. C. Gould, T. G. Dane, J. Rudin, M. J. Cryan, T. Schmaltz, H. Frauenrath, M. A. Winnik, C. F. J. Faul and I. Manners, *Nat. Commun.*, 2017, **8**, 15909.
- 65 D. Tao, C. Feng, Y. Cui, X. Yang, I. Manners, M. A. Winnik and X. Huang, *J. Am. Chem. Soc.*, 2017, **139**, 7136–7139.
- 66 J. R. Finnegan, X. He, S. T. G. Street, J. D. Garcia-Hernandez, D. W. Hayward, R. L. Harniman, R. M. Richardson, G. R. Whittell and I. Manners, *J. Am. Chem. Soc.*, 2018, **140**, 17127–17140.
- 67 M. C. Arno, M. Inam, Z. Coe, G. Cambridge, L. J. Macdougall, R. Keogh, A. P. Dove and R. K. O'Reilly, *J. Am. Chem. Soc.*, 2017, **139**, 16980–16985.
- 68 J. Schöbel, M. Burgard, C. Hils, R. Dersch, M. Dulle, K. Volk, M. Karg, A. Greiner and H. Schmalz, *Angew. Chem. Int. Ed.*, 2017, **56**, 405–408.
- 69 A. Greiner and J. H. Wendorff, *Angew. Chem. Int. Ed.*, 2007, **46**, 5670–5703.
- 70 F. Mitschang, H. Schmalz, S. Agarwal and A. Greiner, *Angew. Chem. Int. Ed.*, 2014, **53**, 4972–4975.
- 71 P. A. Schaal and U. Simon, *Beilstein J. Nanotechnol.*, 2013, **4**, 336–344.
- 72 W. S. Rasband, *ImageJ*, U. S. National Institutes of Health, Bethesda, Maryland, USA, 1997–2018.
- 73 P. Raffa, C. Evangelisti, G. Vitulli and P. Salvadori, *Tetrahedron Lett.*, 2008, **49**, 3221–3224.
- 74 T. Taguchi, K. Isozaki and K. Miki, *Adv. Mater.*, 2012, **24**, 6462–6467.

- 75 T. Mitsudome, Y. Yamamoto, A. Noujima, T. Mizugaki, K. Jitsukawa and K. Kaneda, *Chem. Eur. J.*, 2013, **19**, 14398–14402.

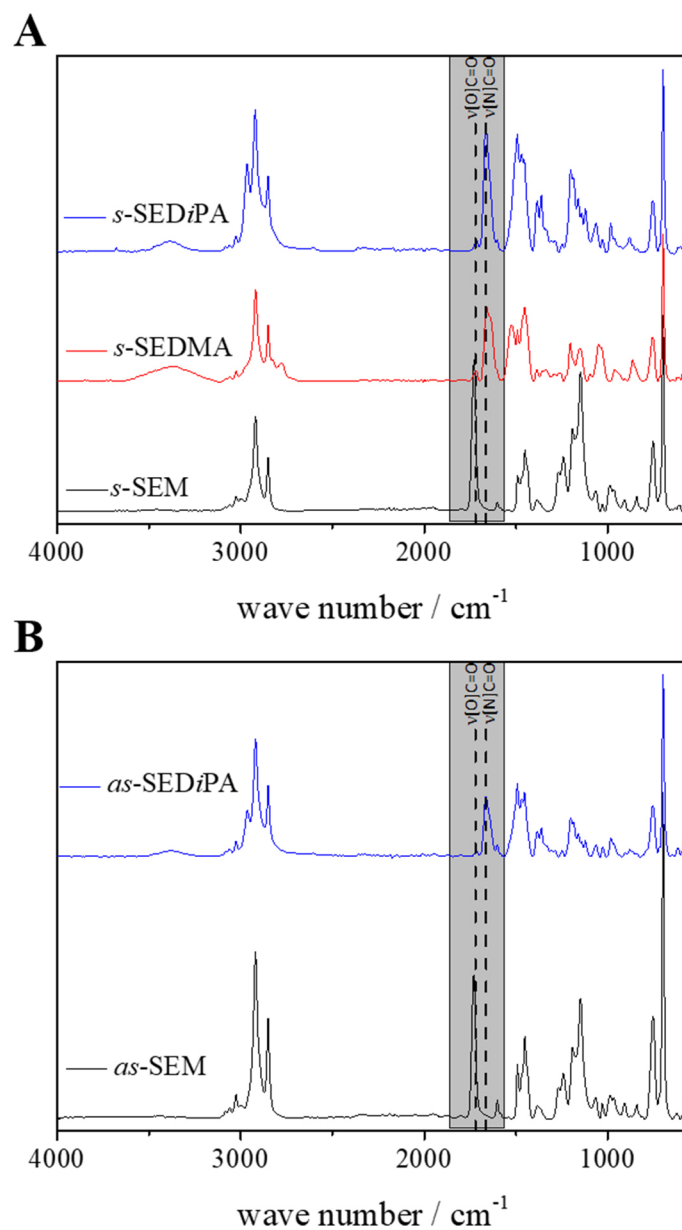
## Electronic Supplementary Information



**Fig. S3.1.** Characterization of the employed aqueous, citrate-stabilized Au NP dispersion. A) TEM micrograph, B) size distribution with  $D_{\text{TEM}} = 9.5 \pm 2.4$  nm, C) UV-Vis spectrum and D) AF4 measurement revealing a diameter of gyration of  $D_g = 17.9 \pm 2$  nm, using the relation  $D_g/D_h = 0.775$  for solid spheres.



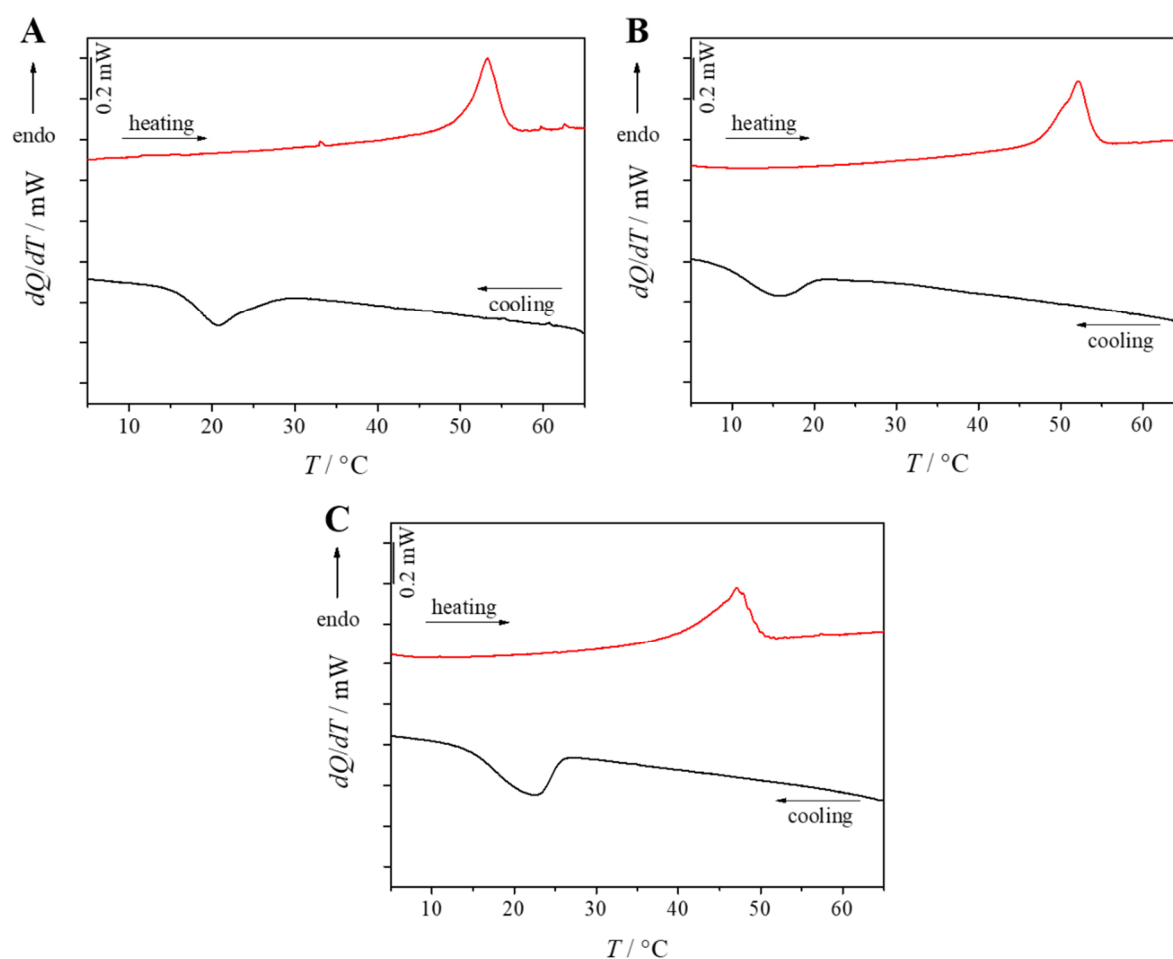
**Fig. S3.2.**  $^1\text{H}$  NMR spectra of A) *s*-SEDMA ( $\text{S}_{33}\text{E}_{17}\text{DMA}_{50}^{131}$ ) and B) *s*-SEDiPA ( $\text{S}_{28}\text{E}_{15}\text{DiPA}_{58}^{156}$ ) measured in  $\text{CDCl}_3$ . Quantitative conversion in the polymer analogous amidation of the corresponding PS-*b*-PE-*b*-PMMA triblock terpolymer precursor is proven by the absence of methyl ester protons, which would be expected to appear at  $\delta = 3.6$  ppm.



**Fig. S3.3.** FT-IR spectra of A) symmetric and B) asymmetric triblock terpolymers. In the FT-IR spectra of the amidated triblock terpolymers the carbonyl stretching vibration ( $\nu[\text{O}]\text{C}=\text{O}$ ) of the methyl ester units of the PS-*b*-PE-*b*-PMMA triblock terpolymer precursor (black spectra) is hardly detectable, confirming a nearly complete conversion.

**Table S3.1.** Thermal properties of the amidated triblock terpolymers determined by  $\mu$ DSC.\*

triblock terpolymer	$T_c$ [ $^{\circ}\text{C}$ ]	$T_m$ [ $^{\circ}\text{C}$ ]
<i>s</i> -SEDiPA	15	52
<i>as</i> -SEDiPA	22	47
<i>s</i> -SEDMA	21	53

\*  $c = 10 \text{ g}\cdot\text{L}^{-1}$  in THF, scanning rate  $0.5 \text{ K}\cdot\text{min}^{-1}$ .**Fig. S3.4.**  $\mu$ DSC heating (red) and cooling (black) traces ( $c = 10 \text{ g}\cdot\text{L}^{-1}$  in THF, scanning rate  $0.5 \text{ K}\cdot\text{min}^{-1}$ ). A) *s*-SEDMA ( $\text{S}_{33}\text{E}_{17}\text{DMA}_{50}^{131}$ ), B) *s*-SEDiPA ( $\text{S}_{28}\text{E}_{15}\text{DiPA}_{58}^{156}$ ) and C) *as*-SEDiPA ( $\text{S}_{38}\text{E}_{21}\text{DiPA}_{41}^{181}$ ).

**UV-Vis Measurements.** The initial concentration of the Au NP dispersion was determined by ICP-OES measurements ( $c_{\text{Au}} = 0.50 \cdot 10^{-3} \text{ mol} \cdot \text{L}^{-1}$ ). Furthermore, the concentration of elemental gold ( $[\text{Au}]$ ) can be determined directly from the measured UV-Vis spectrum according to eqn (S3.1), using the absorbance of the Au NP dispersions at a wavelength of  $\lambda = 400 \text{ nm}$  ( $A_{400}$ ).<sup>1</sup> The Au content in  $[\mu\text{g}]$  ( $m_{\text{Au, UV-Vis } 400\text{nm}}$ ) is then calculated from the respective volume of the dispersion and the molar mass of Au ( $M_{\text{Au}} = 196.97 \text{ g} \cdot \text{mol}^{-1}$ ). In addition, a calibration based on the employed Au NP dispersion was constructed by plotting the absorbance at  $\lambda = 400 \text{ nm}$  vs. the Au content (in  $[\mu\text{g}]$ ) of the dispersions with different dilutions (Fig. S3.5). For both methods the amount of embedded gold in the hybrid nonwovens was calculated from the respective Au contents of the dispersions before and after loading (difference method).

$$[\text{Au}] = \frac{A_{400} \cdot f \cdot 1.25 \cdot 10^{-4} \text{ mol} \cdot \text{L}^{-1}}{0.3} \cdot 100 \quad (\text{S3.1})$$

The dilution factor  $f$  indicates the dilution of the measured dispersion.<sup>1</sup>

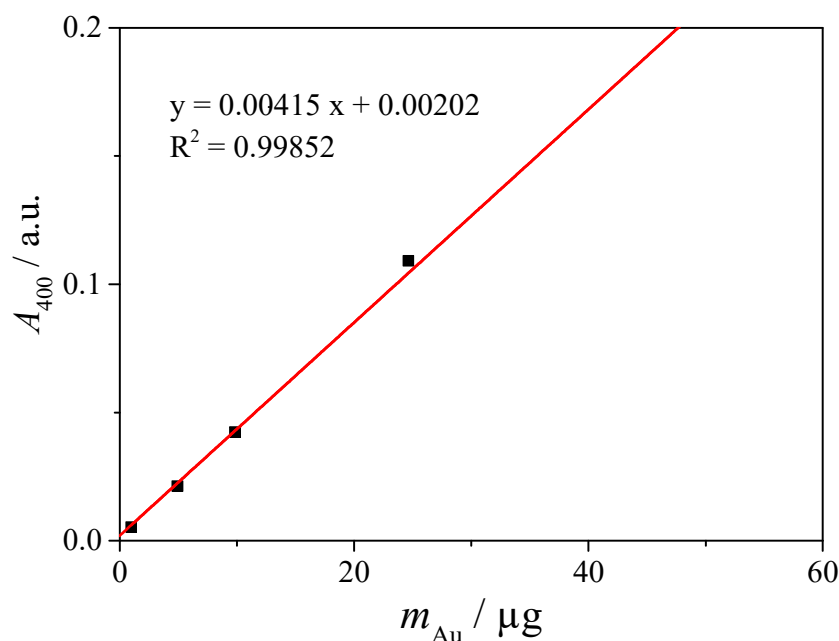


**Fig. S3.5.** Calibration line for the determination of the gold content from the absorbance of the employed aqueous Au NP dispersion at  $\lambda = 400 \text{ nm}$ .

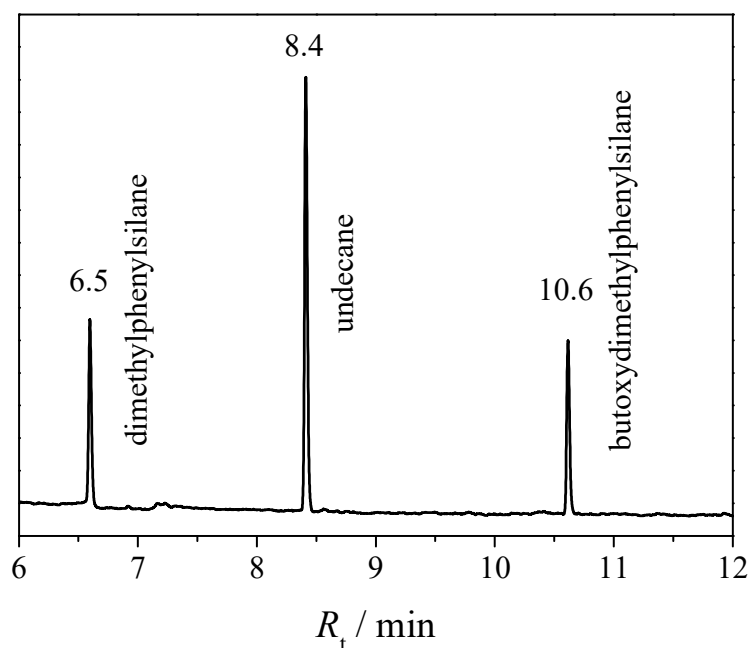


**Fig. S3.6.** Representative GC spectrum for the sample taken after 4h in the catalytic alcoholysis of dimethylphenylsilane with NW\_s-SEDMA(w)/Au. The assignment of the GC signals was proven by GC-MS (gas chromatography coupled with mass spectrometry) in our previous report.<sup>2</sup>

**Determination of patch sizes and average micelle lengths by TEM.** The determination of the patch size (red for the amidated and blue for the PS patches) was done with *ImageJ* using the tool “straight line” after setting the scalebar (Fig. S3.7). The mean average and standard deviation were calculated from 100 patches. The mean length and standard deviation of the worm-like micelles was calculated using the tool “segmented line” (green), evaluating 100 worm-like micelles.

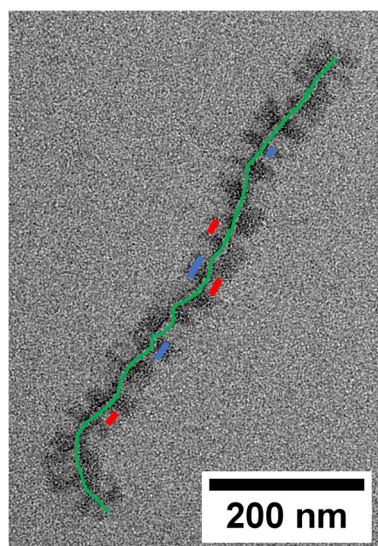


**Fig. S3.7.** Determination of patch size (PS: blue; PDxA: red) and length (green) of the worm-like micelles using the software *ImageJ*.

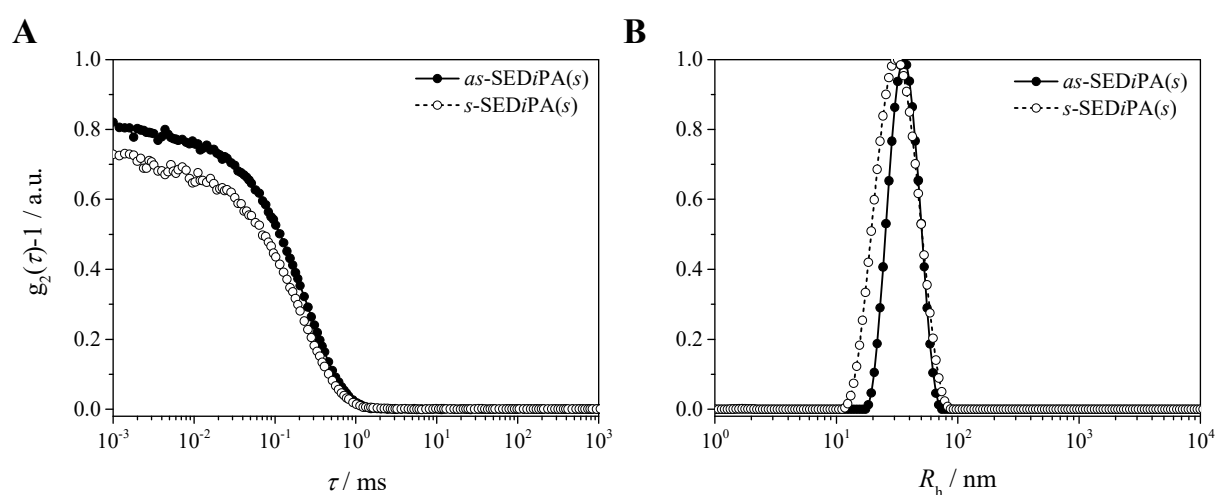


**Fig. S3.8.** DLS measurements of the *s*CCMs ( $c = 0.1 \text{ g}\cdot\text{L}^{-1}$ , dioxane) at a scattering angle of  $\theta = 90^\circ$ . A) Auto-correlation functions and B) unweighted hydrodynamic radii distributions (CONTIN analysis,  $R_h(\textit{s}\text{-SEDiPA}(\textit{s})) = 31.4 \pm 0.3 \text{ nm}$  and  $R_h(\textit{as}\text{-SEDiPA}(\textit{s})) = 35.8 \pm 0.3 \text{ nm}$ ).

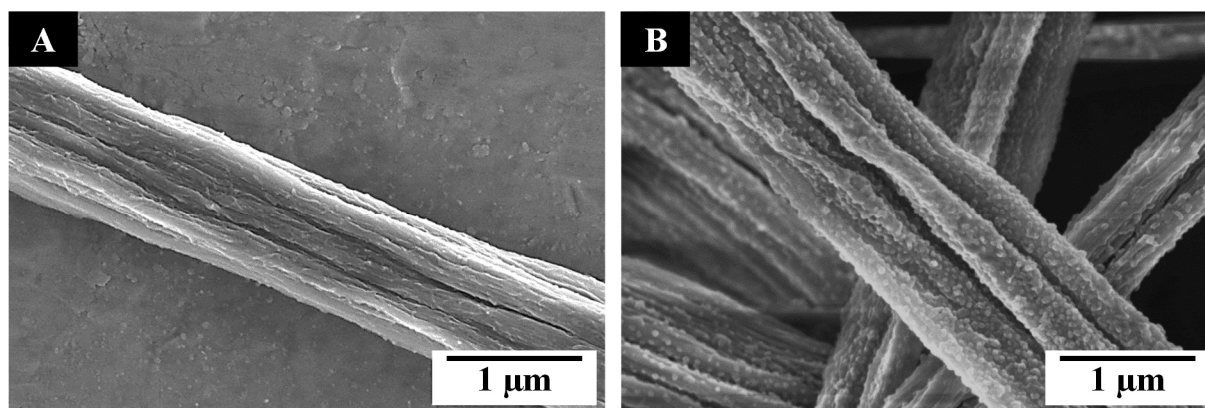


**Fig. S3.9.** SEM micrographs of patchy nonwovens. A) NW<sub>as</sub>-SEDiPA(w), B) NW<sub>as</sub>-SEDiPA(s).

**Evaluation of the reaction kinetics according to the classical pseudo 1<sup>st</sup> order kinetics model.** Due to the large excess of *n*-butanol (*n*-BuOH) compared to silane, a pseudo 1<sup>st</sup> order kinetics can be assumed. Consequently, the apparent reaction rate constants ( $k_{app}$ ) can be calculated from the slope in the linear range of the corresponding 1<sup>st</sup> order kinetics plot as follows (Fig. S3.10):

$$-\frac{d[E]}{dt} = k \cdot [E] \cdot [n\text{-BuOH}] \quad (\text{S3.2})$$

with  $[E] = [\text{silane}]$

introducing  $k_{app, classical} = k \cdot [n\text{-BuOH}] \quad (\text{S3.3})$

results in  $-\frac{d[E]}{dt} = k_{app, classical} \cdot [E] \quad (\text{S3.4})$

integration gives  $-\ln\left(\frac{[E]}{[E]_0}\right) = k_{app, classical} \cdot t \quad (\text{S3.5})$

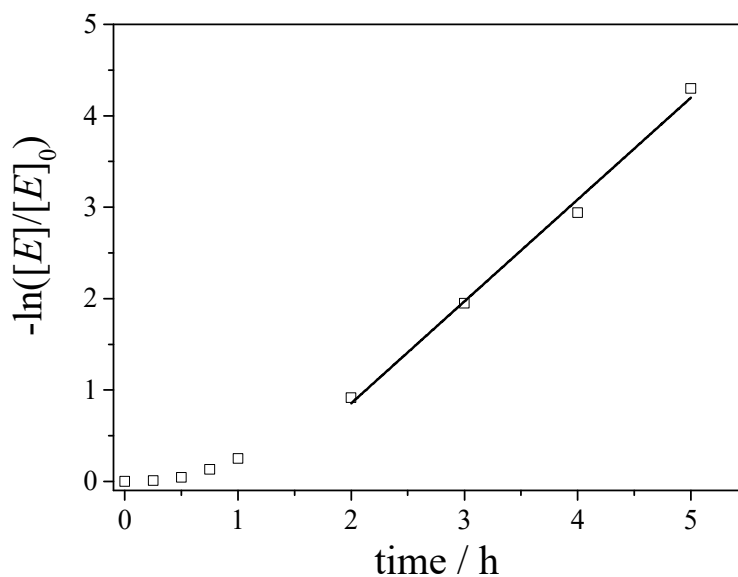


**Fig. S3.10.** Kinetics plot for the catalytic alcoholysis of dimethylphenylsilane with the Au NP-loaded patchy nonwoven NW<sub>S</sub>-SEDiPA(w)/Au, showing the determination of the apparent rate constants ( $k_{app, classical}$ ) according to the classical 1<sup>st</sup> order kinetics model (squares: experimental data, line: linear fit according to eqn (S3.5)). An accurate fit is possible only for the second half of the observation period, where the plot shows a constant slope.

The reaction rate constants  $k$ , normalized to the concentration of *n*-butanol ( $[n\text{-BuOH}] = 10.93 \text{ mol}\cdot\text{L}^{-1}$ ) and the overall surface area of the embedded Au NPs ( $S_{NP, total}$ ), were determined from eqn (S3.6). The total NP surface area ( $S_{NP, total}$ , eqn (S3.7 – S3.10)) was calculated on the basis of the Au NP's mean diameter ( $D_{TEM} = 9.5 \pm 2.4 \text{ nm}$ ), the Au content in the hybrid nonwovens ( $m_{Au, UV\text{-}Vis 400nm}$ , Table 3.2) and the density of Au ( $\rho_{Au} = 19.32 \text{ g}\cdot\text{cm}^{-3}$ ). The errors for  $S_{NP, total}$  (eqn S3.11) and  $k$  (eqn S3.12) were calculated based on error propagation.

$$k = \frac{k_{app}}{[n\text{-BuOH}] \cdot S_{NP, total}} \quad (\text{S3.6})$$

with 
$$S_{NP, total} = S_{NP, single} \cdot N_{NP} \quad (\text{S3.7})$$

where 
$$S_{NP, single} = \pi \cdot D_{TEM}^2 \quad (\text{S3.8})$$

and 
$$N_{NP} = \frac{m_{NP}}{\frac{4}{3} \cdot \pi \cdot \left(\frac{D_{TEM}}{2}\right)^3 \cdot \rho_{Au}} \quad (\text{S3.9})$$

leads to 
$$S_{NP, total} = \frac{6 \cdot m_{NP}}{\rho_{Au}} \cdot \frac{1}{D_{TEM}} \quad (\text{S3.10})$$

with 
$$\Delta S_{NP,total} = \sqrt{\left(-\frac{6 \cdot m_{NP}}{\rho_{Au}} \cdot \frac{1}{(D_{TEM})^2}\right)^2 \cdot (\Delta D_{TEM})^2}$$
 (S3.11)

and 
$$\Delta k = \sqrt{\left(\frac{1}{[n\text{-BuOH}] \cdot S_{NP,total}}\right)^2 \cdot (\Delta k_{app})^2 + \left(-\frac{k_{app}}{[n\text{-BuOH}] \cdot (S_{NP,total})^2}\right)^2 \cdot (\Delta S_{NP,total})^2}$$
 (S3.12)

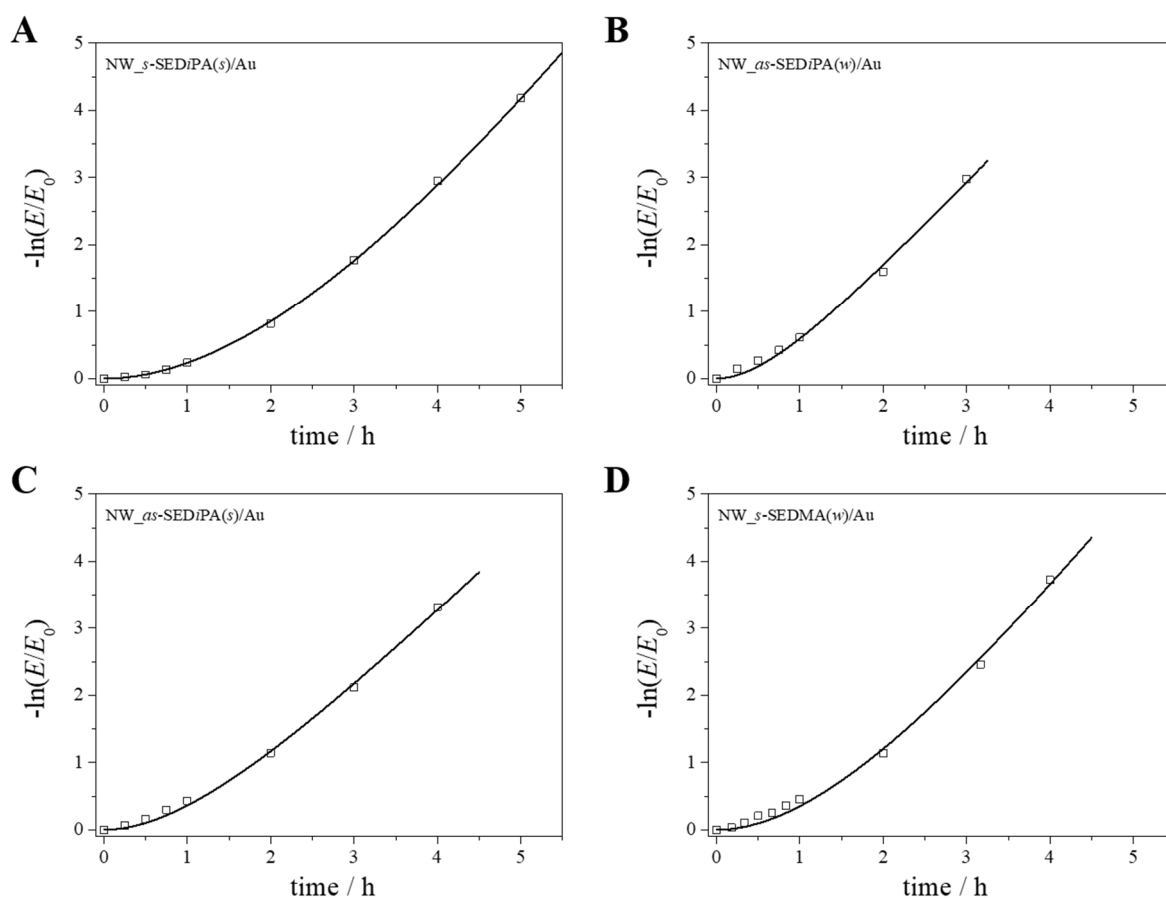


**Fig. S3.11.** Kinetics plot for the catalytic alcoholysis of dimethylphenylsilane with Au NP-loaded patchy nonwovens (squares: experimental data, line: fit according to our extended pseudo 1<sup>st</sup> order kinetics model (eqn (3.5)).

**Table S3.2.** Comparison of the apparent rate constants ( $k_{app}$ ) and the corresponding normalized rate constants ( $k$ ), determined using the classical and the extended 1<sup>st</sup> order kinetics model, respectively.

hybrid nonwovens	$k_{app}$ <sup>a</sup> [h <sup>-1</sup> ]	$k$ <sup>b</sup> [L·m <sup>-2</sup> ·mol <sup>-1</sup> ·s <sup>-1</sup> ]	$k_{app, classical}$ <sup>c</sup> [h <sup>-1</sup> ]	$k_{classical}$ <sup>b</sup> [L·m <sup>-2</sup> ·mol <sup>-1</sup> ·s <sup>-1</sup> ]
NW_ <i>s</i> -SEDiPA( <i>s</i> )/Au	1.77 ± 0.10	(1.97 ± 0.51)·10 <sup>-2</sup>	1.21 ± 0.02	(1.34 ± 0.34)·10 <sup>-2</sup>
NW_ <i>s</i> -SEDiPA( <i>w</i> )/Au	1.54 ± 0.11	(2.10 ± 0.55)·10 <sup>-2</sup>	1.11 ± 0.06	(1.52 ± 0.39)·10 <sup>-2</sup>
NW_ <i>as</i> -SEDiPA( <i>s</i> )/Au	1.18 ± 0.10	(1.19 ± 0.31)·10 <sup>-2</sup>	1.09 ± 0.06	(1.10 ± 0.28)·10 <sup>-2</sup>
NW_ <i>as</i> -SEDiPA( <i>w</i> )/Au	1.27 ± 0.11	(1.20 ± 0.32)·10 <sup>-2</sup>	1.18 ± 0.11	(1.12 ± 0.30)·10 <sup>-2</sup>
NW_ <i>s</i> -SEDMA( <i>w</i> )/Au	1.55 ± 0.26	(1.56 ± 0.47)·10 <sup>-2</sup>	1.28 ± 0.11	(1.30 ± 0.34)·10 <sup>-2</sup>

<sup>a</sup> determined according to eqn (3.5) (extended 1<sup>st</sup> order kinetics model). <sup>b</sup> rate constant normalized to the surface of the embedded Au NPs ( $S_{AuNP}$ , Table 3.2) and the concentration of *n*-BuOH ( $c_{n-BuOH} = 10.93 \text{ mol}\cdot\text{L}^{-1}$ ). <sup>c</sup> calculated using the classical 1<sup>st</sup> order kinetics model (eqn (S3.5), Fig. S3.10).

**Table S3.3.** Comparison of the obtained kinetic parameters for the alcoholysis of dimethylphenylsilane with *n*-BuOH with literature data.

catalyst	Au [mol-%]	<sup>d</sup> $D$ <sup>e</sup> [nm]	time [h]	temp. [°C]	$x_p$ <sup>f</sup> [%]	recyclability	Reference
NW_SEDxA( <i>w</i> )/Au	0.18	9.5	4-5	25	>99	>99% 10 cycles	this work
Au NP-loaded nonwoven	patchy 0.1	11	7	25	>99	>99% 10 cycles	2
Au-containing nanotubes	PPX 6.6	9.5	26	25	>99	>99% 18 cycles	3
Au/Al <sub>2</sub> O <sub>3</sub>	20	3-5	3	100	99	n/a	4
10Dod-Au NP array <sup>a</sup>	0.02	9	1	25	83	95% 3 cycles	5
Au/HAP <sub>nano</sub> <sup>b</sup>	0.05	3	0.33	25	>99	>99% 3 cycles	6
PSSH@Au NP <sup>c</sup>	0.06	15-24	5	25	>99	n/a	7

<sup>a</sup> dodecanethiol self-assembled-monolayer-capped Au NPs. <sup>b</sup> nanohydroxyapatite-supported Au NPs. <sup>c</sup> with toluene as co-solvent. <sup>d</sup> relative to silane. <sup>e</sup> average diameter of Au NPs. <sup>f</sup> conversion.

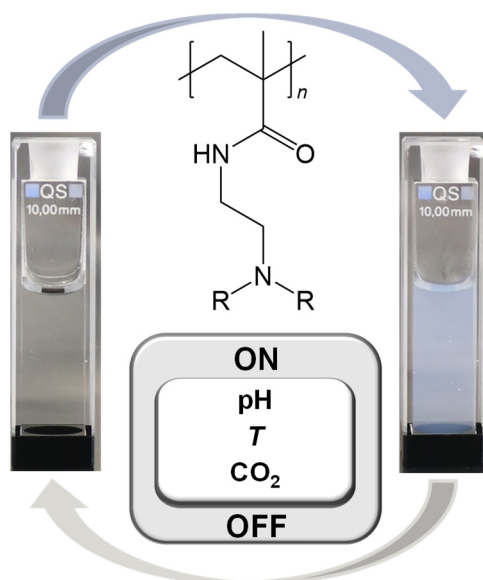
## References

- 1 T. Hendel, M. Wuthschick, F. Kettemann, A. Birnbaum, K. Rademann, J. Polte, *Anal. Chem.*, 2014, **86**, 11115–11124.
- 2 Schöbel, J.; Burgard, M.; Hils, C.; Dersch, R.; Dulle, M.; Volk, K.; Karg, M.; Greiner, A.; Schmalz, H. *Angew. Chem. Int. Ed.* **2017**, *56*, 405–408.
- 3 Mitschang, F.; Schmalz, H.; Agarwal, S.; Greiner, A. *Angew. Chem. Int. Ed.* **2014**, *53*, 4972–4975.
- 4 Raffa, P.; Evangelisti, C.; Vitulli, G.; Salvadori, P. *Tetrahedron Lett.* **2008**, *49*, 3221–3224.
- 5 Taguchi, T.; Isozaki, K.; Miki, K. *Adv. Mater.* **2012**, *24*, 6462–6467
- 6 Mitsudome, T.; Yamamoto, Y.; Noujima, A.; Mizugaki, T.; Jitsukawa, K.; Kaneda, K. *Chem. Eur. J.* **2013**, *19*, 14398–14402.
- 7 Kronawitt, J.; Fan, Z.; Schöttle, M.; Agarwal, S.; Greiner, A. *ChemNanoMat* **2019**, *5*, 181–186.

## 4 Converting poly(methyl methacrylate) into a triple-responsive polymer

Christian Hils,<sup>[a]</sup> Emma Fuchs,<sup>[a]</sup> Franziska Eger,<sup>[a]</sup> Judith Schöbel,<sup>[b]</sup> and Holger Schmalz<sup>[a],[c]\*</sup>

- a) University of Bayreuth, Macromolecular Chemistry II, Universitätsstraße 30, 95440 Bayreuth, Germany
- b) University of Groningen, Macromolecular Chemistry & New Polymeric Materials, Zernike Institute for Advanced Materials, Nijenborgh 4, 9747 AG, Groningen, The Netherlands
- c) University of Bayreuth, Bavarian Polymer Institute, Keylab Synthesis and Molecular Characterization, Universitätsstraße 30, 95440 Bayreuth, Germany



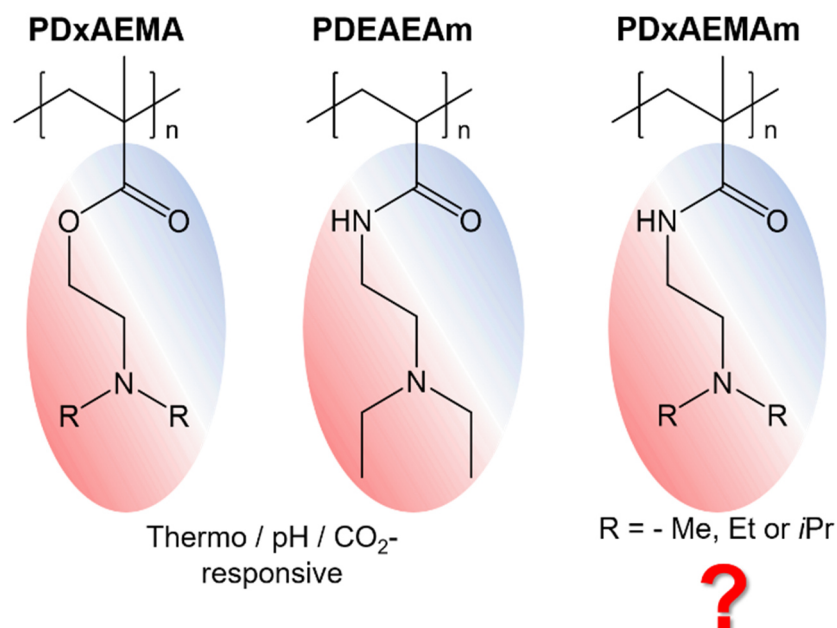
Published in: *Chem. Eur. J.*, 2020, 26, 5611 – 5614

Reprinted with permission from Wiley VCH Publications.

## Abstract

Multi-responsive polymers that can respond to several external stimuli are promising materials for a manifold of applications. Here, we present a facile method for the synthesis of triple-responsive (pH, temperature, CO<sub>2</sub>) poly(*N,N*-diethylaminoethyl methacrylamide) *via* a post-polymerization amidation of poly(methyl methacrylate) (PMMA). Combined with trivalent counterions ([Fe(CN)<sub>6</sub>]<sup>3-</sup>) both an UCST and LSCT-type (upper/lower critical solution temperature) phase behaviour can be realized at pH 8 and 9. PMMA and PMMA-based block copolymers are readily accessible by living anionic and controlled radical polymerization techniques, which opens access to various responsive polymer architectures based on the developed functionalization method. This method can also be applied on melt-processed bulk PMMA samples to introduce functional, responsive moieties at the PMMA surface.

Stimuli-responsive or "smart" polymers, which can change their physicochemical properties (e.g. solubility) upon applying an external stimulus (pH, temperature, light, magnetic fields, CO<sub>2</sub>, etc.), are highly attractive and intensively studied materials due to the wide range of applications, like responsive micelles and micro/nano-gels for biomedical applications, switchable membranes and coatings, smart actuators, or CO<sub>2</sub> sensing.<sup>[1,2,3]</sup> The most prominent examples of multi-responsive polymers are based on methacrylate or acrylamide-type monomers with pendant *N,N*-dialkylamino groups (alkyl = methyl, ethyl, *iso*-propyl, Scheme 4.1), which are commonly prepared by controlled radical polymerization techniques.<sup>[2-5,6,7-9]</sup> In contrast, there are considerably less reports on living anionic polymerization, e.g. of *N,N*-dimethylaminoethyl methacrylate (DMAEMA),<sup>[10]</sup> despite the fact that anionic polymerization is still the best suited method to prepare well-defined, complex block copolymer architectures of high molecular weight on a large scale.<sup>[11]</sup> Especially, when soft blocks based on polydienes (polybutadiene, polyisoprene) are required to allow for a dynamic rearrangement of micellar nanostructures or a later fixation of the structures by crosslinking, anionic polymerization is the method of choice. However, the high requirements on monomer purity for anionic polymerization makes the purification of polar, high boiling monomers like DMAEMA complex and time consuming. To overcome these limitations we made use of an efficient post-polymerization modification to convert poly(methyl methacrylate) (PMMA), which is easily accessible by living anionic as well as controlled radical polymerization techniques, into a triple-responsive polymer, being responsive to pH, temperature and CO<sub>2</sub>. This was realized by amidation of PMMA with different preactivated *N,N*-dialkylethylenediamines to yield the corresponding poly(*N,N*-dialkylaminoethyl methacrylamide)s (alkyl = methyl, ethyl, *iso*-propyl; PDxAEMAm), which were studied with respect to their responsive solution behaviour. This concept was also applied for the surface functionalization of a bulk PMMA sample.



**Scheme 4.1.** Comparison of the chemical structure of well-known triple-responsive (pH, T, CO<sub>2</sub>) polymers with poly(*N,N*-dialkylaminoethyl methacrylamide)s investigated in this study.

The amidation of PMMA with *N,N*-dialkylethylenediamines was conducted according to our previously published method for the post-polymerization functionalization of polystyrene-*block*-polyethylene-*block*-poly(methyl methacrylate) triblock terpolymers (Figure 4.1A, details on used materials and synthesis protocols are given in the Supporting Information).<sup>[12]</sup> Due to the prior activation of the amines with *n*-butyllithium, quantitative functionalization can be reached in less than 1h, irrespective of the steric demand of the used amine (Figure S4.1, S4.2, Table S4.1), as verified by <sup>1</sup>H-NMR and FT-IR studies. In addition, there are no signs of a broadening of the molecular weight distribution by size exclusion chromatography (Figure S4.3), showing that amidation proceeds without significant side reactions. A quantitative conversion of the methyl ester groups of PMMA is indispensable in order to avoid hydrolysis to methacrylic acid at elevated temperatures and high pH values, which will cause a significant shift of the cloud point to higher temperatures with time.<sup>[8]</sup> This is manifested by the disappearance of the LCST-type phase behaviour (LCST = lower critical solution temperature) of an intentionally prepared poly(methyl methacrylate-*co*-*N,N*-diethylaminoethyl methacrylamide) copolymer (P(MMA<sub>31</sub>-*co*-DEAEAM<sub>179</sub>), subscripts correspond to the degree of polymerization) already after 9 consecutive heating/cooling cycles in pH = 10 buffer solution (Figure S4).

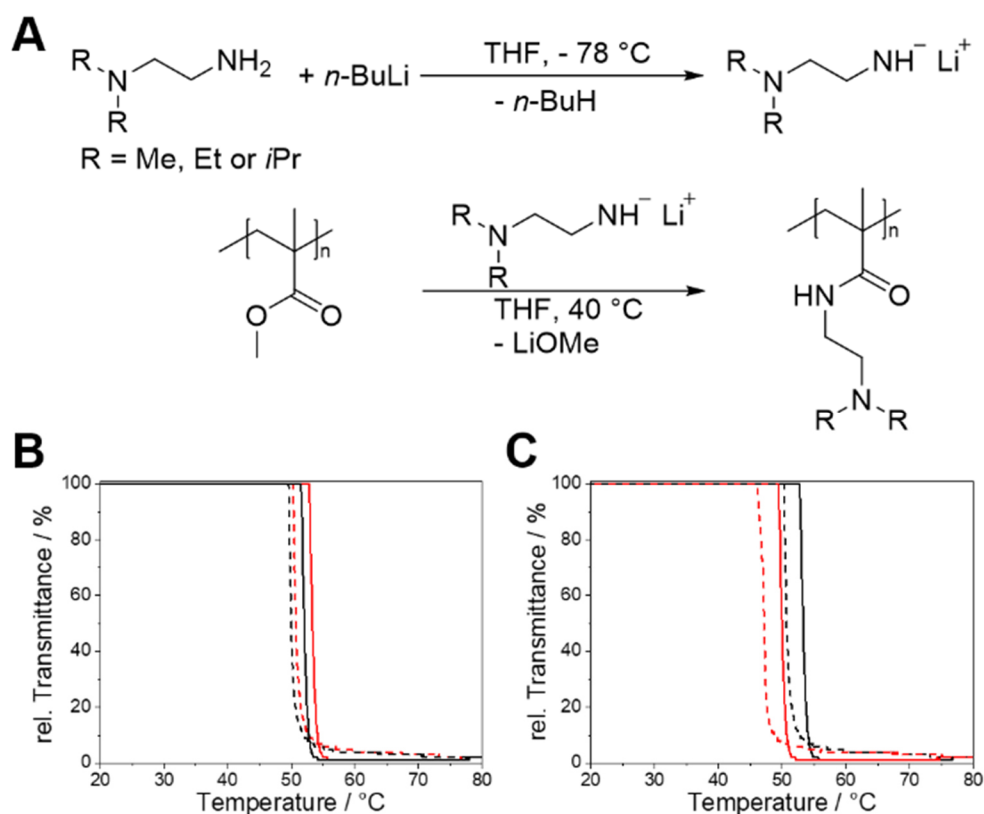


**Figure 4.1.** A) Reaction scheme for the amidation of PMMA with *N,N*-dialkyl-ethylenediamines. B) Temperature-dependent transmittance of PDEAEMAm<sub>210</sub> ( $M_n = 3.9 \cdot 10^4 \text{ g} \cdot \text{mol}^{-1}$ , 1<sup>st</sup> cycle: red, 9<sup>th</sup> cycle: black) and C) comparison with PDEAEMAm<sub>1030</sub> ( $M_n = 1.9 \cdot 10^5 \text{ g} \cdot \text{mol}^{-1}$ , red trace) in pH = 9 buffer. Heating traces are depicted as solid and cooling traces as dashed lines, respectively ( $c = 1 \text{ g} \cdot \text{L}^{-1}$ ).

The synthesized poly(*N,N*-dimethylaminoethyl methacrylamide) (PDMAEMAm<sub>210</sub>) is neither responsive to pH nor to temperature, as confirmed by turbidity measurements at varying pH (Figure S4.5A). In contrast, poly(*N,N*-diethylaminoethyl methacrylamide) (PDEAEMAm<sub>210</sub>, Figure 4.1B) and poly(*N,N*-diisopropylaminoethyl methacrylamide) (PDiPAEMAm<sub>210</sub>, Figure S4.5B) exhibit a LCST-type phase behaviour at pH = 8. However, only PDEAEMAm<sub>210</sub> shows a narrow hysteresis ( $\Delta T_{\text{CP}} \approx 3 \text{ K}$ ), whereas for PDiPAEMAm<sub>210</sub> the phase transitions upon heating and cooling are comparably broad with a large hysteresis ( $\Delta T_{\text{CP}} \approx 24 \text{ K}$ ). The cloud point ( $T_{\text{CP}}$ ) of PDEAEMAm<sub>210</sub> changes only marginally after 9 consecutive heating/cooling cycles in pH = 9 buffer solution (1<sup>st</sup> cycle:  $T_{\text{CP}} = 53\text{ }^\circ\text{C}$ , 9<sup>th</sup> cycle:  $T_{\text{CP}} = 52\text{ }^\circ\text{C}$ , Figure 4.1B), revealing the excellent hydrolytic stability of PDEAEMAm<sub>210</sub>. There is a concentration dependence of the cloud point, which leads to a pronounced shift of  $T_{\text{CP}}$  by ca. 20 °C to lower values with increasing concentration ( $c = 0.05\text{--}2 \text{ g} \cdot \text{L}^{-1}$ , Figure S4.5C). This is expected as we move along the binodal which has a minimum in the LCST.

Figure 4.1C reveals an influence of the molecular weight on the cloud point, as the  $T_{CP}$  of PDEAEMAm<sub>1030</sub> is about 5 °C lower compared to that of PDEAEMAm<sub>210</sub>. This indicates that PDEAEMAm acts as an LCST polymer of class I, *i.e.*, the cloud point decreases with increasing molecular weight.<sup>[13]</sup>

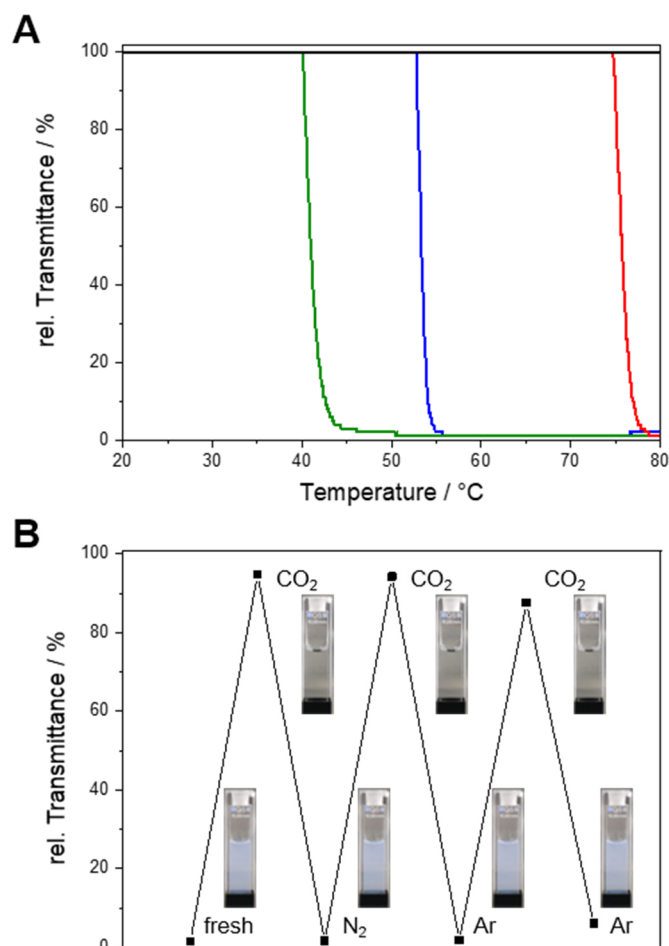


**Figure 4.2.** A) Temperature-dependent transmittance of PDEAEMAm<sub>210</sub> in buffer solutions of different pH ( $c = 1 \text{ g}\cdot\text{L}^{-1}$ , pH = 7 black, pH = 8 red, pH = 9 blue and pH = 10 green). B) Change in transmittance of PDEAEMAm<sub>210</sub> in pH = 10 buffer at 55 °C ( $c = 1 \text{ g}\cdot\text{L}^{-1}$ ) upon bubbling CO<sub>2</sub>, N<sub>2</sub> or Ar through a cuvette.

Turbidity measurements were conducted in buffer solutions of different pH (Figure 4.2A, Table S4.2) to further study the potential multi-responsivity of PDEAEMAm. PDEAEMAm is soluble over the entire temperature range for  $\text{pH} \leq 7$ , whereas for  $8 < \text{pH} < 10$  the cloud point shifts from  $T_{CP} = 72 \text{ °C}$  at  $\text{pH} = 8$  to  $T_{CP} = 37 \text{ °C}$  at  $\text{pH} = 10$ . This matches well with the measured  $\text{p}K_a$  value of 7.1 (Figure S4.6), *i.e.*, an LCST-type phase behaviour is only observed for pH values at which less than 50% of the pendant tertiary amino groups are protonated. This is consistent with studies on the chemically similar poly(*N,N*-diethylaminoethyl

methacrylate).<sup>[4,9]</sup> The pH-dependence of the cloud point can be harnessed for a reversible, CO<sub>2</sub>-induced phase transition (Figure 4.2B). Bubbling CO<sub>2</sub> through a turbid solution of PDEAEMAm<sub>210</sub> in pH = 10 buffer at 55 °C, *i.e.*, above the  $T_{CP}$  of 37 °C at pH = 10, results in a complete dissolution of the polymer. This is caused by a decrease in solution pH by the dissolved CO<sub>2</sub> (chemical equilibrium with carbonic acid) and consequently by the protonation of the pendant diethylamino groups as proven by <sup>1</sup>H-NMR (Figure S4.7). Subsequent bubbling of nitrogen or argon in order to remove the dissolved CO<sub>2</sub> results again in a turbid solution. This process can be repeated several times, proving the reversibility of the CO<sub>2</sub>-induced solubility switching.

In comparison to the respective methacrylate-based poly(*N,N*-dialkylaminoethyl methacrylate)s the replacement of the ester linkage by an amide linkage in poly(*N,N*-dialkylaminoethyl methacrylamide)s leads to an increase in polarity and, thus, to an increased solubility. This is manifested by the fact that poly(*N,N*-dimethylaminoethyl methacrylate) (PDMAEMA) shows a pH-dependent LCST-type phase behaviour for pH ≥ 7,<sup>[4,8]</sup> whereas PDMAEMAm is completely soluble irrespective of temperature and pH (Figure S4.5A; Table S4.2, S4.3). A similar behaviour is found for the diethyl derivatives. PDEAEMA shows an LCST-type phase behaviour at pH = 6 – 7 and is hardly soluble for pH ≥ 8.<sup>[9]</sup> In contrast, PDEAEMAm exhibits a temperature-dependent solubility for pH ≥ 8. This is in line with the lower  $pK_a$  value observed for PDEAEMA ( $pK_a = 6.6$ )<sup>[9]</sup> with respect to that of PDEAEMAm ( $pK_a = 7.1$ , Figure S4.6). In analogy to poly(*N,N*-diethylaminoethyl acrylamide) (PDEAEAm) the synthesized PDEAEMAm also shows a triple-responsive behaviour, being responsive to pH, temperature and CO<sub>2</sub>.<sup>[5,7]</sup> However, introducing a methyl group in  $\alpha$ -position leads to a slightly increased hydrophobicity and a resulting shift of the critical pH at which an LCST-type phase behaviour is observed from pH = 8.5 for PDEAEAm to pH = 8 for PDEAEMAm, respectively (Table S4.2).

In addition to the pH-dependent LCST-type phase behaviour an UCST-type (UCST = upper critical solution temperature) phase behaviour can be induced by the addition of small quantities of a trivalent counterion. This is realized by the addition of K<sub>3</sub>[Fe(CN)<sub>6</sub>] to the respective solutions of PDEAEMAm<sub>1030</sub> ( $c = 1 \text{ g}\cdot\text{L}^{-1}$ ) in buffers of pH 6 - 10 (Figure 4.3A, Figure S4.8). For pH 8 and 9 both an UCST- and LCST-type phase behaviour is observed, whereas for pH < 8 and pH > 9 only an UCST- or LCST-behaviour can be detected, respectively. This can be explained by the lack of protonated (charged) repeating units for pH > 9, as electrostatic interactions between the positively charged polymer and the trivalent

$[\text{Fe}(\text{CN})_6]^{3-}$  counterions are responsible for the UCST-type phase separation.<sup>[14]</sup> Consequently, at  $\text{pH} < 8$  the polymer chain is highly charged ( $\text{p}K_a = 7.1$ ) which leads to a vanishing of the LCST. In analogy to studies on linear and star-shaped PDMAEMA the UCST-type cloud point increases with the  $[\text{Fe}(\text{CN})_6]^{3-}$  concentration, whereas the LCST-type cloud point is not affected (Figure 4.3B). However, the UCST-type phase transitions for PDEAEMAm<sub>1030</sub> are more sensitive to the  $[\text{Fe}(\text{CN})_6]^{3-}$  concentration and the UCST coincides with the LCST-type cloud point already at  $c([\text{Fe}(\text{CN})_6]^{3-}) = 1.25 \text{ mM}$ .

The post-polymerization amidation of PMMA can even be conducted in bulk, allowing the direct heterogeneous amidation of melt-processed PMMA parts. The successful amidation of the surface of a PMMA disc with *N,N*-diethylethylenediamine was proven by FT-IR spectroscopy, revealing the presence of the characteristic amide band at  $\approx 1650 \text{ cm}^{-1}$  (Figure S4.9). Due to the increase in polarity the contact angle to water at  $25 \text{ }^\circ\text{C}$  decreases from  $(93 \pm 2)^\circ$  to  $(49 \pm 5)^\circ$  after amidation (Table S4). The responsivity of the amidated PMMA surface can be used for a temperature-induced switching of the contact angle. Employing a  $\text{pH} = 10$  buffer solution a shift of the contact angle from  $(48 \pm 6)^\circ$  to  $(77 \pm 1)^\circ$  can be induced by a temperature increase to  $55 \text{ }^\circ\text{C}$ , as under these conditions the PDEAEMAm units become insoluble ( $T_{\text{CP}} = 37 \text{ }^\circ\text{C}$  at  $\text{pH} = 10$ ). Moreover, the diethylamino anchor groups at the PMMA surface can be utilized to bind preformed, citrate-stabilized gold nanoparticles (Au NPs,  $D = 9.5 \pm 2.4 \text{ nm}$ ). After functionalization and loading with Au NPs the decoration of the PMMA surface with Au NPs is clearly visible in the digital photograph as well as the scanning electron microscopy (SEM) image acquired with a back-scattered electron (BSE) detector (Figure 4.4).

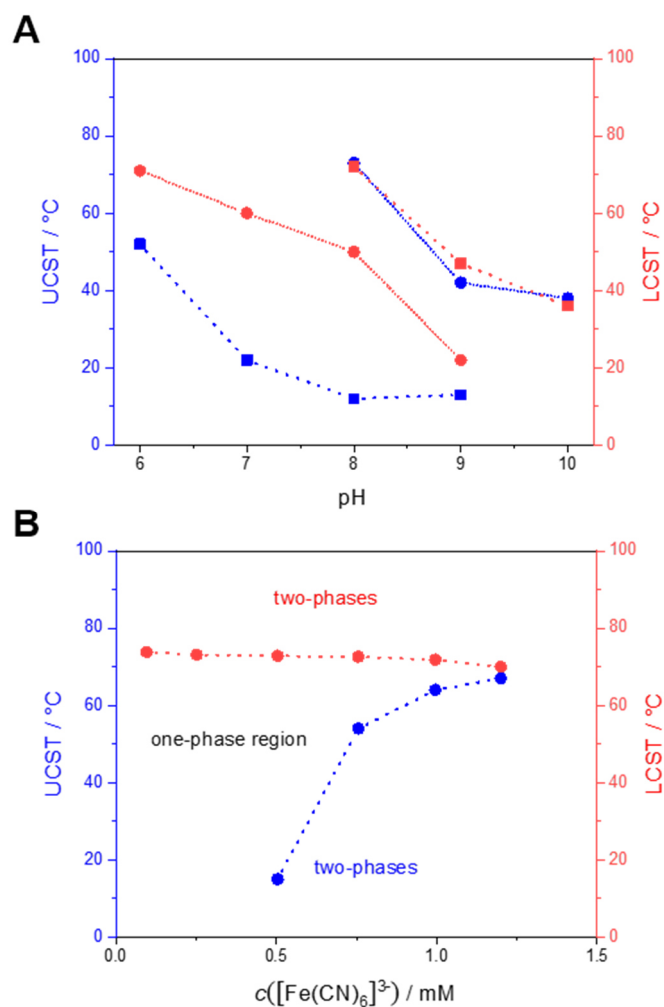


**Figure 4.3.** Tailoring the thermo-responsive solution behaviour of PDEAEMAM<sub>1030</sub> ( $c = 1 \text{ g}\cdot\text{L}^{-1}$ ) in the presence of trivalent  $[\text{Fe}(\text{CN})_6]^{3-}$  counterions. A) UCST- and LCST-type phase transitions in dependence of pH for two different  $\text{K}_3[\text{Fe}(\text{CN})_6]$  concentrations ( $c = 0.5 \text{ mM}$  (squares),  $c = 0.75 \text{ mM}$  (circles) and B) in dependence of  $\text{K}_3[\text{Fe}(\text{CN})_6]$  concentration in pH = 8 buffer solutions.

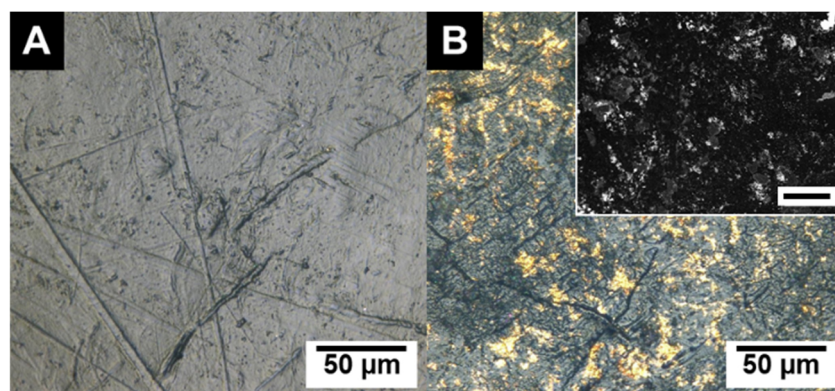


**Figure 4.4.** Digital photographs of the surface of the PMMA disc employed for heterogeneous amidation (A) and of the surface of the PMMA disc after amidation and successive loading with Au NPs (B). The inset shows the corresponding SEM image acquired with a BSE detector (Au NP rich regions appear bright, scale bar inset =  $100 \mu\text{m}$ ).

In conclusion, we have shown that PMMA can be converted to a triple-responsive (pH, temperature, CO<sub>2</sub>) polymer by a fast and quantitative post-polymerization amidation with *N,N*-diethylethylenediamine. This opens access to a variety of responsive polymer architectures, like defined (multi)block copolymers,<sup>[12]</sup> as PMMA is easily accessible via controlled radical as well as living anionic polymerization. The excellent efficiency of this functionalization reaction also allows a direct heterogeneous amidation of the surface of melt-processed PMMA parts, which can be harnessed for a temperature-induced switching of the surface hydrophilicity or the binding of metal nanoparticles, *e.g.* for catalytic purposes. Hence, we believe that the herein established method will find broad application in the synthesis of responsive and/or functional materials that might find application in responsive gels, actuators, or catalysis.

### **Acknowledgements**

This work was supported by the German Research Foundation (SFB 840, project A2). We acknowledge Prof. Andreas Greiner and Prof. Seema Agarwal for helpful discussions on heterogeneous amidation and thermo-responsive polymers, respectively. We thank Rika Schneider for SEC, Carmen Kunert for SEM and Lukas Weber for preparative work. C. Hils acknowledges support by the Graduate School of the University of Bayreuth.

**Keywords:** Polymer analogous modification • multi-responsive polymers • temperature responsive • pH responsive • switchable surface hydrophilicity

## References

- [1] a) M. A. C. Stuart, W. T. S. Huck, J. Genzer, M. Müller, C. Ober, M. Stamm, G. B. Sukhorukov, I. Szleifer, V. V. Tsukruk, M. Urban et al., *Nature Mater.* **2010**, *9*, 101; b) S. Guo, H. Zhang, X. Lu, H. Xiao, Y. Zhao, *J. Mater. Chem. C* **2019**, *7*, 4049; c) M. F. Cunningham, P. G. Jessop, *Macromolecules* **2019**, *52*, 6801; d) M. Wei, Y. Gao, X. Li, M. J. Serpe, *Polym. Chem.* **2017**, *8*, 127; e) L. Hu, Y. Wan, Q. Zhang, M. J. Serpe, *Adv. Funct. Mater.* **2019**, *6*, 1903471; f) H. Ko, A. Javey, *Acc. Chem. Res.* **2017**, *50*, 691; g) S.-J. Jeon, A. W. Hauser, R. C. Hayward, *Acc. Chem. Res.* **2017**, *50*, 161; h) X. Hu, Y. Zhang, Z. Xie, X. Jing, A. Bellotti, Z. Gu, *Biomacromolecules* **2017**, *18*, 649; i) Z.-Q. Cao, G.-J. Wang, *Chem. Rec.* **2016**, *16*, 1398.
- [2] P. Schattling, F. D. Jochum, P. Theato, *Polym. Chem.* **2014**, *5*, 25.
- [3] J. Madsen, S. P. Armes, *Soft Matter* **2012**, *8*, 592.
- [4] T. Thavanesan, C. Herbert, F. A. Plamper, *Langmuir* **2014**, *30*, 5609.
- [5] Z. Song, K. Wang, C. Gao, S. Wang, W. Zhang, *Macromolecules* **2016**, *49*, 162.
- [6] a) J. Lee, K. H. Ku, C. H. Park, Y. J. Lee, H. Yun, B. J. Kim, *ACS Nano* **2019**, *13*, 4230; b) G. Moad, *Polym. Chem.* **2017**, *8*, 177.
- [7] K. Wang, Z. Song, C. Liu, W. Zhang, *Polym. Chem.* **2016**, *7*, 3423.
- [8] F. A. Plamper, M. Ruppel, A. Schmalz, O. Borisov, M. Ballauff, A. H. E. Müller, *Macromolecules* **2007**, *40*, 8361.
- [9] A. Schmalz, M. Hanisch, H. Schmalz, A. H. E. Müller, *Polymer* **2010**, *51*, 1213.
- [10] a) I. Dewald, J. Gensel, E. Betthausen, O. V. Borisov, A. H. E. Müller, F. H. Schacher, A. Fery, *ACS Nano* **2016**, *10*, 5180; b) A. Hanisch, H. Schmalz, A. H. E. Müller, *Macromolecules* **2012**, *45*, 8300; c) F. Schacher, T. Rudolph, F. Wieberger, M. Ulbricht, A. H. E. Müller, *ACS Appl. Mater. Interfaces* **2009**, *1*, 1492; d) X. Wang, M. A. Winnik, I. Manners, *Macromolecules* **2005**, *38*, 1928; e) T. Lunkenbein, M. Kamperman, Z. Li, C. Bojer, M. Drechsler, S. Förster, U. Wiesner, A. H. E. Müller, J. Breu, *J. Am. Chem. Soc.* **2012**, *134*, 12685.
- [11] a) G. Polymeropoulos, G. Zapsas, K. Ntetsikas, P. Bilalis, Y. Gnanou, N. Hadjichristidis, *Macromolecules* **2017**, *50*, 1253; b) R. Bahrami, T. I. Löbbling, A. H. Gröschel, H. Schmalz, A. H. E. Müller, V. Altstädt, *ACS Nano* **2014**, *8*, 10048.
- [12] J. Schöbel, C. Hils, A. Weckwerth, M. Schlenk, C. Bojer, M. C. A. Stuart, J. Breu, S. Förster, A. Greiner, M. Karg et al., *Nanoscale* **2018**, *10*, 18257.

- [13] F. Meeussen, E. Nies, H. Berghmans, S. Verbrugghe, E. Goethals, F. Du Prez, *Polymer* **2000**, *41*, 8597.
- [14] F. A. Plamper, A. Schmalz, M. Ballauff, A. H. E. Müller, *J. Am. Chem. Soc.* **2007**, *129*, 14538.

## Supporting Information

### General Procedures

**Materials.** All chemicals were used as received unless otherwise specified. Deionized water (filtered through a Millipore Milli-Q Plus system, QPAK® 2, conductivity: 18.2 MΩ·cm), poly(methyl methacrylate) (PMMA, Acros Organics,  $M_w = 3.5 \cdot 10^4$  g·mol<sup>-1</sup> (PMMA<sub>210</sub>) and  $M_w = 1.2 \cdot 10^5$  g·mol<sup>-1</sup> (PMMA<sub>1030</sub>)), *n*-butyllithium (*n*-BuLi, 2.5M in hexane, Acros Organics), *n*-pentane (technical grade, purified by distillation prior to use), deuterated chloroform (CDCl<sub>3</sub>, 99.8%, Deutero), calcium hydride (CaH<sub>2</sub>, Merck), *N,N*-dimethylethylenediamine (DMEDA, ≥ 98%, Sigma-Aldrich), *N,N*-diethylethylenediamine (DEEDA, 99%, Acros Organics), *N,N*-diisopropylethylenediamine (DiPEDA, 97%, Acros Organics), dry ice, hydrochloric acid (37 wt% in water, VWR), tetrahydrofuran (THF, ≥ 99.9%, Sigma-Aldrich), acetone (99.9%, Acros Organics), buffer solutions (VWR, AVS Titrinorm (pH = 6 – 9) and Merck, Certipur (pH = 10)), potassium hexacyanoferrate(III) (K<sub>3</sub>[Fe(CN)<sub>6</sub>], ReagentPlus®, ~99%, Sigma-Aldrich), diethyl ether (Et<sub>2</sub>O, technical grade, purified by distillation prior to use), tetrachloroauric(III) acid trihydrate (HAuCl<sub>4</sub> · 3 H<sub>2</sub>O, 99.99%, Alfa Aesar), sodium borohydride (NaBH<sub>4</sub>, ≥ 96%, Fluka), and trisodium citrate dihydrate (99% for analytical purposes, Grüssing).

**Purification of chemicals.** The used PMMAs were dissolved in THF and precipitated from MeOH in order to obtain a fine powder (PMMA<sub>210</sub>:  $M_n = 2.1 \cdot 10^4$  g·mol<sup>-1</sup>,  $\bar{D} = 1.50$ ; PMMA<sub>1030</sub>:  $M_n = 1.0 \cdot 10^5$  g·mol<sup>-1</sup>,  $\bar{D} = 1.17$ ; SEC-MALLS combination; subscript denotes the degree of polymerization). *N,N*-dialkylethylenediamines were dried over CaH<sub>2</sub> and purified by distillation (stored under argon until use). THF was dried by successive distillation over CaH<sub>2</sub> and potassium (stored under nitrogen until use).

**Nuclear Magnetic Resonance (NMR) spectroscopy.** The polymers were characterized by <sup>1</sup>H-NMR spectroscopy (Bruker Ultrashield 300 spectrometer) using CDCl<sub>3</sub> as solvent. The signal assignment was supported by simulations with the NMR software *MestReNova*.

**Fourier Transform-Infrared Spectroscopy (FT-IR).** The FT-IR spectra were recorded with a Digilab Excalibur 3000 FT-IR instrument equipped with an ATR unit (diamond) at a resolution of 4 cm<sup>-1</sup> (16 scans).

**Size Exclusion Chromatography (SEC).** HFIP-SEC was performed on an instrument equipped with three PSS-PFG gel columns (particle size = 7  $\mu\text{m}$ ) with porosity range from 100 – 300  $\text{\AA}$  (PSS, Mainz, Germany) together with a refractive index detector (Gynkotek). HFIP (hexafluoroisopropanol, HPLC grade, Appollo Scientific Limited) with potassium trifluoroacetate (98%, Sigma-Aldrich, 4.8 g in 600 mL HFIP) was used as eluant at a flow rate of 0.5  $\text{mL}\cdot\text{min}^{-1}$ , employing toluene (HPLC grade, Sigma-Aldrich) as internal standard. The calibration was done with narrowly distributed poly(methyl methacrylate) (PMMA) homopolymers (PSS calibration kit). The samples were dissolved in HFIP with potassium trifluoroacetate and filtered through a 0.22  $\mu\text{m}$  PTFE filter before analysis. An injection volume of 20  $\mu\text{L}$  was used for the measurements and the SEC columns were maintained at room temperature. The molar masses reported for the amidated PMMA samples are given in reference to PMMA standards.

The SEC-MALLS (THF) measurements for PMMA ( $dn/dc = 0.087 \text{ mL}\cdot\text{g}^{-1}$ ) were performed on an instrument having three PSS-SDV gel columns (particle size = 5  $\mu\text{m}$ ) with porosity range from  $10^3$  to  $10^5$   $\text{\AA}$  (PSS, Mainz, Germany) together with a refractive index detector (Agilent, G1362A 1200 Series) as concentration detector and a multi-angle laser light scattering detector (MALLS) with eighteen different angles (Wyatt Technology, Dawn EOS). THF (99.9%, Fisher Scientific) was used as eluent at a flow rate of 0.8  $\text{mL}\cdot\text{min}^{-1}$ . The normalization and determination of the inter detector delay as well as the detector constants were done with a narrowly distributed polystyrene standard (PSS, Mainz, Germany). An injection volume of 20  $\mu\text{L}$  was used and the measurements were carried out at room temperature.

**Turbidity measurements.** Freshly prepared polymer solutions ( $c = 1 \text{ g}\cdot\text{L}^{-1}$ ) in the corresponding media were analysed with a Crystal16 multiple reactor system (Technobis Crystallization Systems, screw cap vials) or an UV-Vis spectrophotometer (JASCO V 630, wavelength accuracy:  $\pm 0.7 \text{ nm}$ ; quartz glass cuvettes ( $D = 10 \text{ mm}$ ); halogen lamp as light source and a JASCO ETCS 761 sample holder) at a wavelength of  $\lambda = 645 \text{ nm}$  and a scanning rate of 1.0  $\text{K}\cdot\text{min}^{-1}$ . The cloud points ( $T_{\text{CP}}$ ) were calculated from the intersection of the tangents at the onset of turbidity.

**Scanning Electron Microscopy (SEM).** The SEM measurements were performed on a Zeiss 1530 with field emission cathode at an acceleration voltage of 10 kV using a back-scattering electron (BSE) detector. The samples were applied to a conductive adhesive carrier mounted on an aluminium plate and fixed with an aluminium adhesive strip.

**Optical Microscope (OM).** The measurements were performed on a Keyence VHX-100.

**Contact Angle (CA) measurements.** The CA measurements were performed employing a DS25 from Krüss. The CA was determined with the software “*Advanced Drop Shape Analysis*” (version 1.3.1.0) and the method “*Ellipse Tangent Sessile Drop*” using a droplet volume of  $V = 5 \mu\text{L}$  (deionized water or pH = 10 buffer solution). For the measurements at 55 °C a Mettler FP82 hot stage (FP80 Central Processor) was used.

## Synthesis Procedures

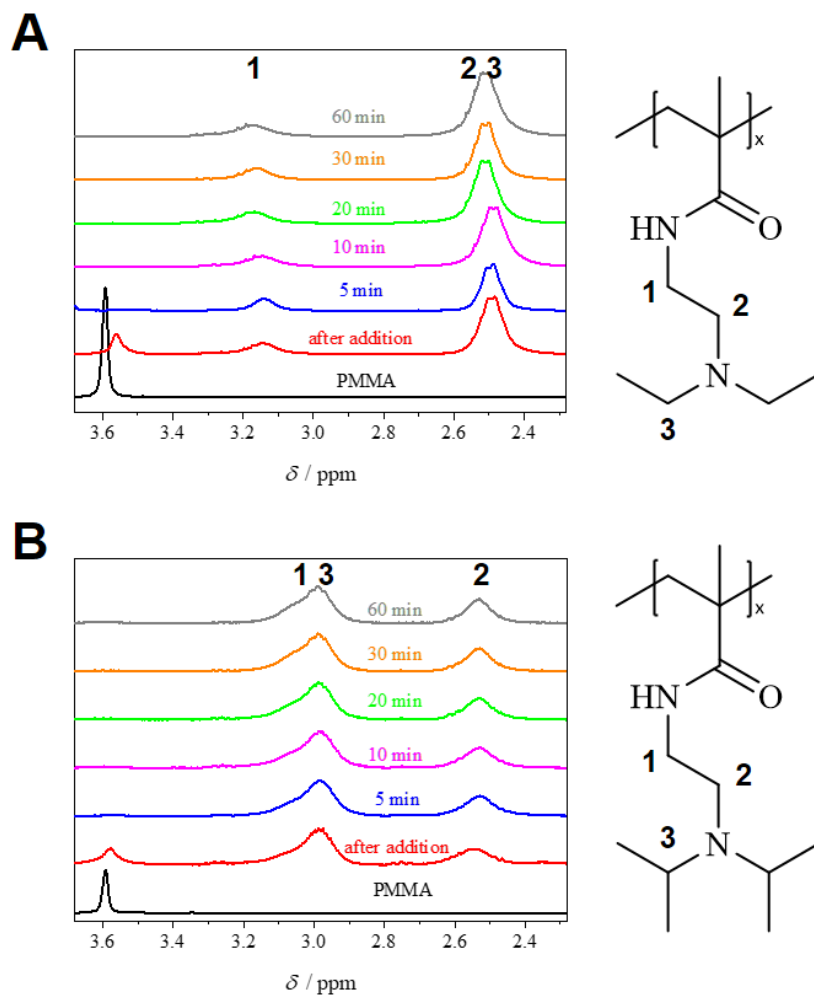
**Synthesis of citrate-stabilized gold nanoparticles (Au NPs).** Citrate-stabilized Au NPs were prepared according to the method reported by *Schaal et al.*<sup>[1]</sup> To 100 mL of an aqueous  $\text{HAuCl}_4$  solution ( $c = 0.50 \cdot 10^{-3} \text{ mol} \cdot \text{L}^{-1}$ ) 9 mL of a  $\text{NaBH}_4$  solution in water ( $c = 4.85 \cdot 10^{-2} \text{ mol} \cdot \text{L}^{-1}$ ) were added dropwise followed by stirring for 5 min. The reaction mixture changed colour from yellow to red, indicating the formation of Au NPs. Subsequently, 5 mL of an aqueous sodium citrate solution ( $c = 0.05 \text{ mol} \cdot \text{L}^{-1}$ ) were added and the mixture was stirred for another 5 min. Au NPs with a mean diameter of  $D_{\text{TEM}} = 9.5 \pm 2.4 \text{ nm}$ , as determined by transmission electron microscopy (TEM), were obtained.

**Synthesis of PDxAEMAm.** The post-polymerization amidation of PMMA with the corresponding *N,N*-dialkylethylenediamines (DMEDA, DEEDA and DiPEDA) was conducted under an inert argon atmosphere.<sup>[2]</sup> The amines were dissolved in THF ( $c = 0.25 - 1 \text{ mol} \cdot \text{L}^{-1}$ ) and the solution was cooled to -78 °C (acetone/dry ice) before *n*-BuLi (1 eq. with respect to amine) was added. After 30 min the cooling bath was removed and the activated amines were transferred to a solution of PMMA in THF ( $c = 10 \text{ g} \cdot \text{L}^{-1}$ ), followed by heating to 40 °C and stirring for 4 h. The reaction was quenched with 2 mL of deionized water. After precipitation from *n*-pentane, the polymers were filtered and dried in vacuum. The amidation resulted in quantitative functionalization of PMMA, as confirmed by <sup>1</sup>H-NMR and FT-IR spectroscopy (Figure S4.1, S4.2). The following poly(*N,N*-dialkylaminoethyl methacrylamide)s (PDxAEMAm) were prepared: PDMAEMAm<sub>210</sub>, P(MMA<sub>31-co</sub>-DEAEMAm<sub>179</sub>), PDEAEMAm<sub>210</sub>, PDEAEMAm<sub>1030</sub>, and PDiPAEMAm<sub>210</sub> (subscripts correspond to the degree of polymerization).

**Heterogeneous amidation and loading with Au NPs.** First, the PMMA disc (Plexiglas<sup>®</sup> 7N, Röhm GmbH:  $M_n = 5.9 \cdot 10^4 \text{ g} \cdot \text{mol}^{-1}$ ,  $D = 1.67$ ;  $9 \times 8 \times 1 \text{ mm}^3$ , 0.13 g, 1 eq.) was washed with Et<sub>2</sub>O and deionized water and dried in vacuo. *N,N*-Diethylethylenediamine (360  $\mu\text{L}$ , 2 eq.) was dissolved in 10 mL Et<sub>2</sub>O and cooled to -78 °C (acetone/dry ice) before *n*-BuLi (1.04 mL, 2 eq.) was added. After 10 min the PMMA disc was added followed by stirring for another 5 min. Subsequently, the yellowish reaction mixture was heated to 25 °C and stirred for 15 h. The reaction was quenched by adding 2 mL deionized water and the amidated PMMA disc was washed with deionized water and dried in vacuo.

For the loading with Au NPs, a piece of the amidated PMMA disc ( $7 \times 4 \times 1 \text{ mm}^3$ ) was added to a mixture of 1 mL deionized water and 0.5 mL of an aqueous, citrate-stabilized AuNP dispersion ( $c = 0.5 \cdot 10^{-3} \text{ mol} \cdot \text{L}^{-1}$ ) and shaken for 15 h at 25 °C (400 rpm, thermal shaker HLC MKR-13, Ditabis). Afterwards, the disc was washed with a sodium citrate solution (2 x 5 mL;  $c = 0.05 \text{ mol} \cdot \text{L}^{-1}$ ) and deionized water (2 x 5 mL).

## Characterization

Kinetics of the amidation of PMMA, as studied by  $^1\text{H-NMR}$ 

**Figure S4.1.** Kinetics of the amidation of PMMA with DEEDA (A) and DiPEDA (B) studied by  $^1\text{H-NMR}$  in  $\text{CDCl}_3$ . The signal at  $\delta = 3.6$  ppm can be assigned to the methoxy protons of the ester units of PMMA.

Kinetics of the amidation of PMMA, as studied by FT-IR spectroscopy

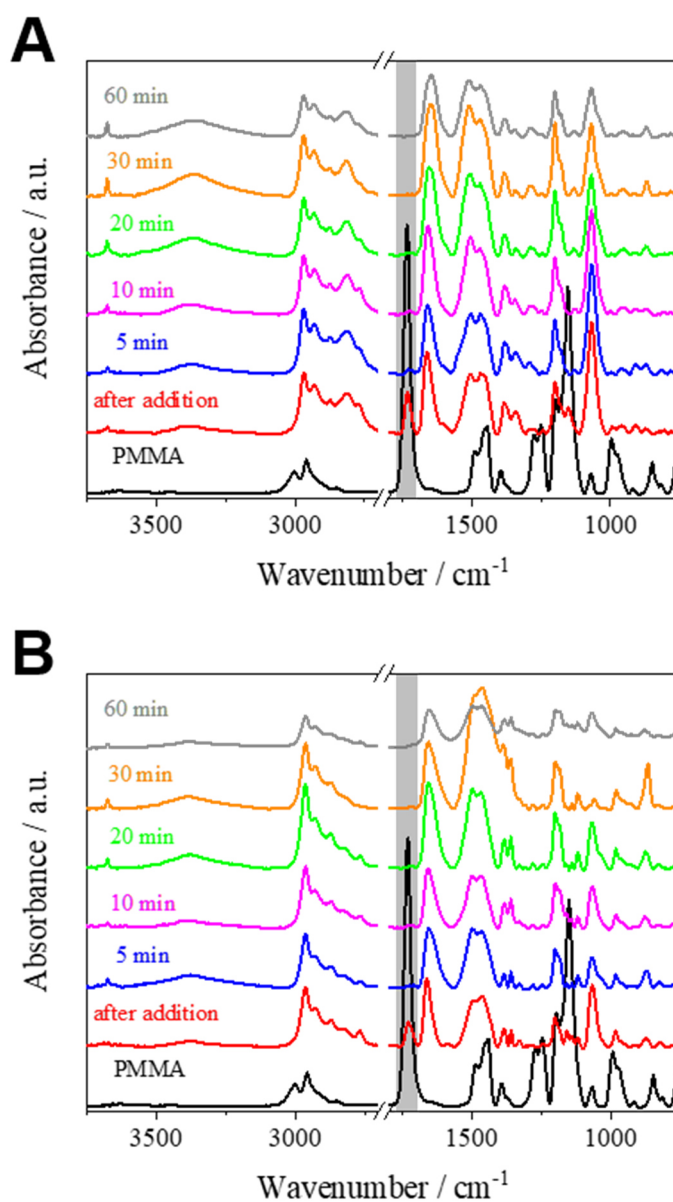


**Figure S4.2.** Kinetics of the amidation of PMMA with DEEDA (A) and DiPEDA (B) studied by FT-IR spectroscopy. The progress of the reaction can be monitored by the decrease of the PMMA ester band at  $\nu \approx 1730 \text{ cm}^{-1}$  (marked in grey) and the corresponding appearance/increase of the amide band at  $\nu \approx 1650 \text{ cm}^{-1}$ , respectively.

Overview of the synthesized polymers using PMMA<sub>210</sub> and PMMA<sub>1030</sub> as precursor

**Table S4.1.** Overview of the synthesized polymers using PMMA<sub>210</sub> and PMMA<sub>1030</sub> as precursor.

Polymer	eq. amine	degree of amidation / % <sup>[a]</sup>	$M_n$ / g·mol <sup>-1</sup> <sup>[b]</sup>
PDEAEMAm <sub>210</sub> <sup>[c]</sup>	2	≥ 99	39 000
PDEAEMAm <sub>1030</sub> <sup>[c]</sup>	2	≥ 99	190 000
P(MMA <sub>31</sub> - <i>co</i> -DEAEMAm <sub>179</sub> ) <sup>[d]</sup>	1.7	85	36 000
PD <i>i</i> PAEMAm <sub>210</sub> <sup>[e]</sup>	2	≥ 99	44 600

[a] with respect to converted methyl ester units of PMMA (-O-CH<sub>3</sub>,  $\delta$  = 3.6 ppm), as determined by <sup>1</sup>H-NMR, [b] calculated using the degree of polymerization of the precursor PMMA (determined by SEC-MALLS) and the respective degree of amidation (determined by <sup>1</sup>H-NMR), [c] poly(diethylaminoethyl methacrylamide), [d] poly(methyl methacrylate-*co*-diethylaminoethyl methacrylamide), [e] poly(di*is*opropylaminoethyl methacrylamide).

HFIP-SEC

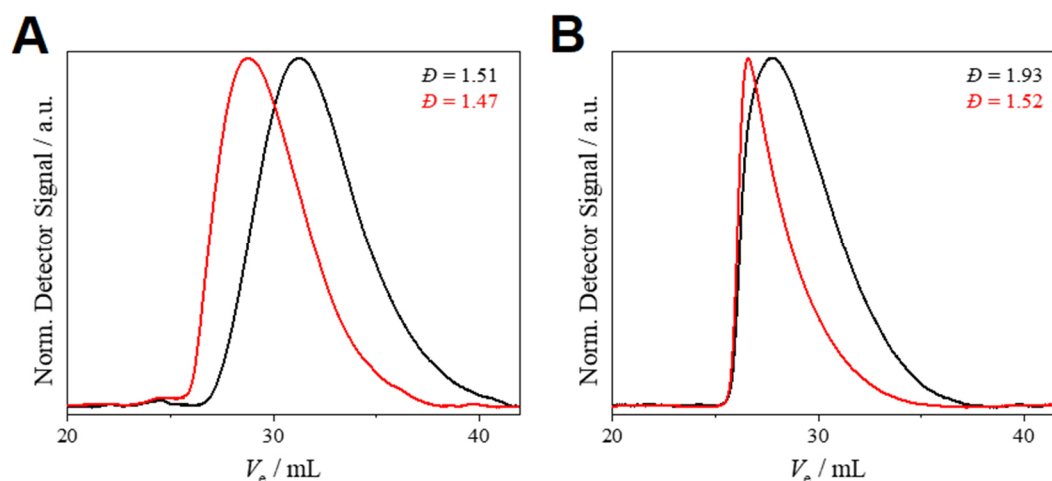


**Figure S4.3.** HFIP-SEC of A) PMMA<sub>210</sub> (black), PDEAEMAm<sub>210</sub> (red) and B) PMMA<sub>1030</sub> (black), PDEAEMAm<sub>1030</sub> (red). The asymmetric shape of the SEC trace of PDEAEMAm<sub>1030</sub> is due to the fact that the molecular weight is close to the molecular weight cut-off of the employed columns. Nevertheless, it shows that no by-products of lower molecular weight were formed during amidation.

## Temperature-dependent transmittance

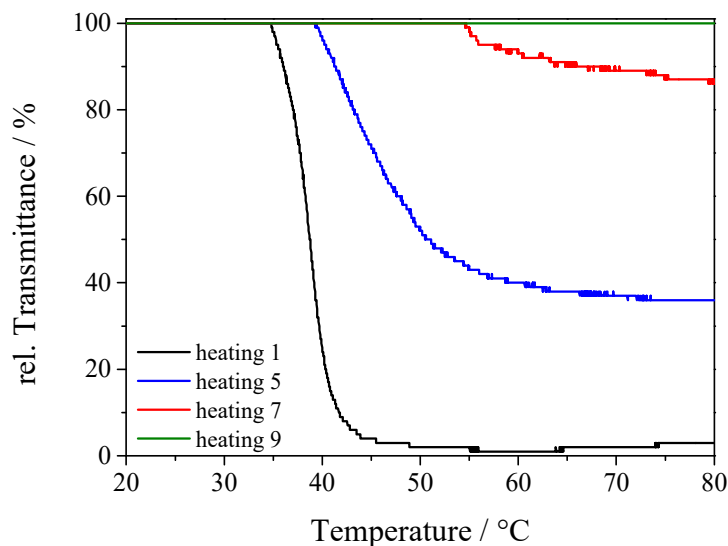


**Figure S4.4.** Temperature-dependent transmittance of P(MMA<sub>31</sub>-co-DEAEMAm<sub>179</sub>) in pH = 10 buffer solution ( $c = 1 \text{ g}\cdot\text{L}^{-1}$ ).

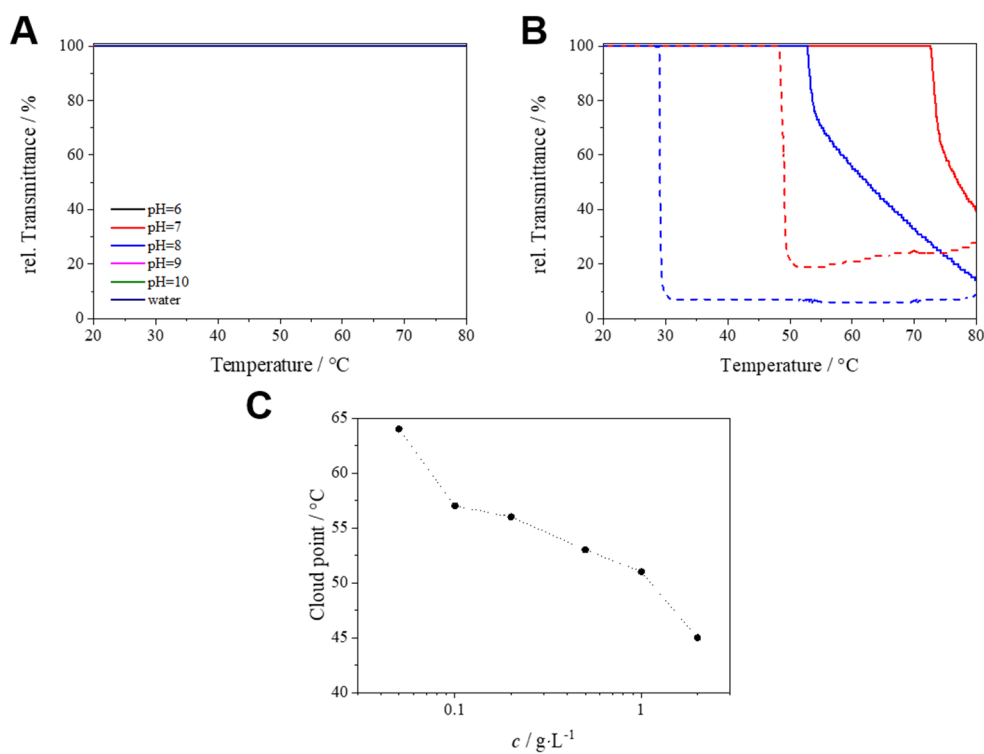


**Figure S4.5.** Temperature-dependent transmittance of A) PDMAEMAm<sub>210</sub> ( $c = 1 \text{ g}\cdot\text{L}^{-1}$ ) in buffer solutions of different pH as indicated, B) PDiPAEMAm<sub>210</sub> ( $c = 1 \text{ g}\cdot\text{L}^{-1}$ ) in pH = 7 (red traces) and pH = 8 (blue traces) buffer solutions (solid lines represent heating and dashed lines

cooling traces, respectively) and C) concentration-dependent cloud points of PDEAEMAm<sub>210</sub> in pH = 9 buffer solution.

Determination of  $pK_a$  for PDEAEMAm<sub>210</sub>

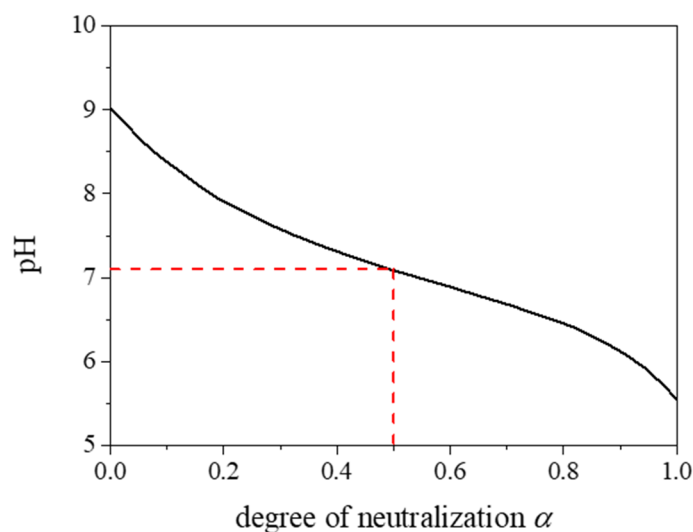


**Figure S4.6.** Titration curve of PDEAEMAm<sub>210</sub> ( $c = 1 \text{ g}\cdot\text{L}^{-1}$ ) in deionized water with 0.1N HCl.

<sup>1</sup>H NMR studies on PDEAEMAm<sub>210</sub>/impact of dissolved CO<sub>2</sub>

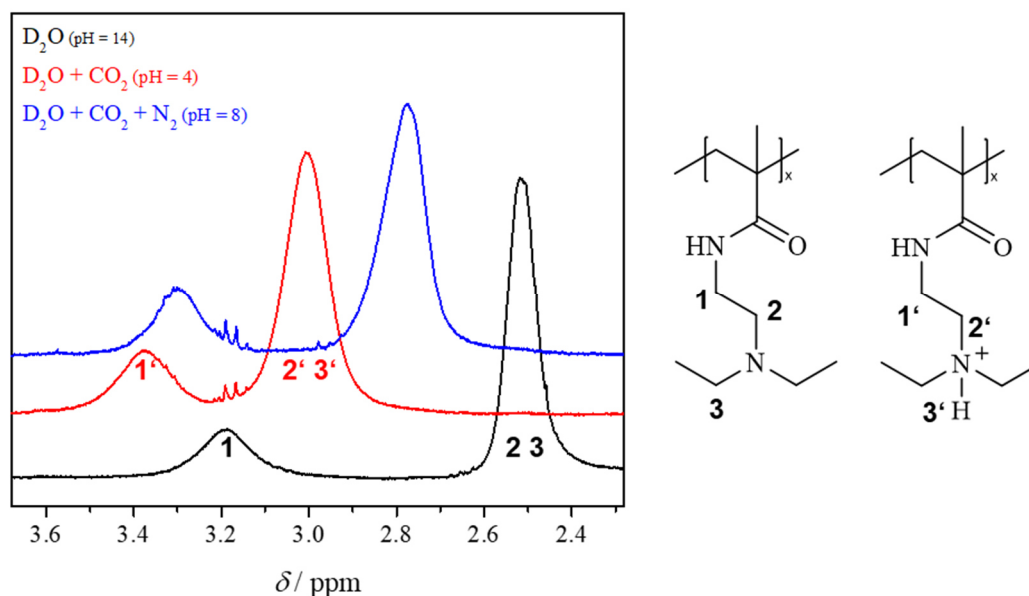


**Figure S4.7.** <sup>1</sup>H NMR spectra of PDEAEMAm<sub>210</sub> ( $c = 10 \text{ g}\cdot\text{L}^{-1}$ ) in D<sub>2</sub>O directly after dissolution (black), after bubbling of CO<sub>2</sub> through the solution (red) and after bubbling of nitrogen to remove most of the dissolved CO<sub>2</sub> (blue). Due to protonation of the pendant amino groups the respective signals are reversibly shifted downfield.

## Comparison of cloud points

**Table S4.2.** Comparison of cloud points for (meth)acryl amide-based polymers.

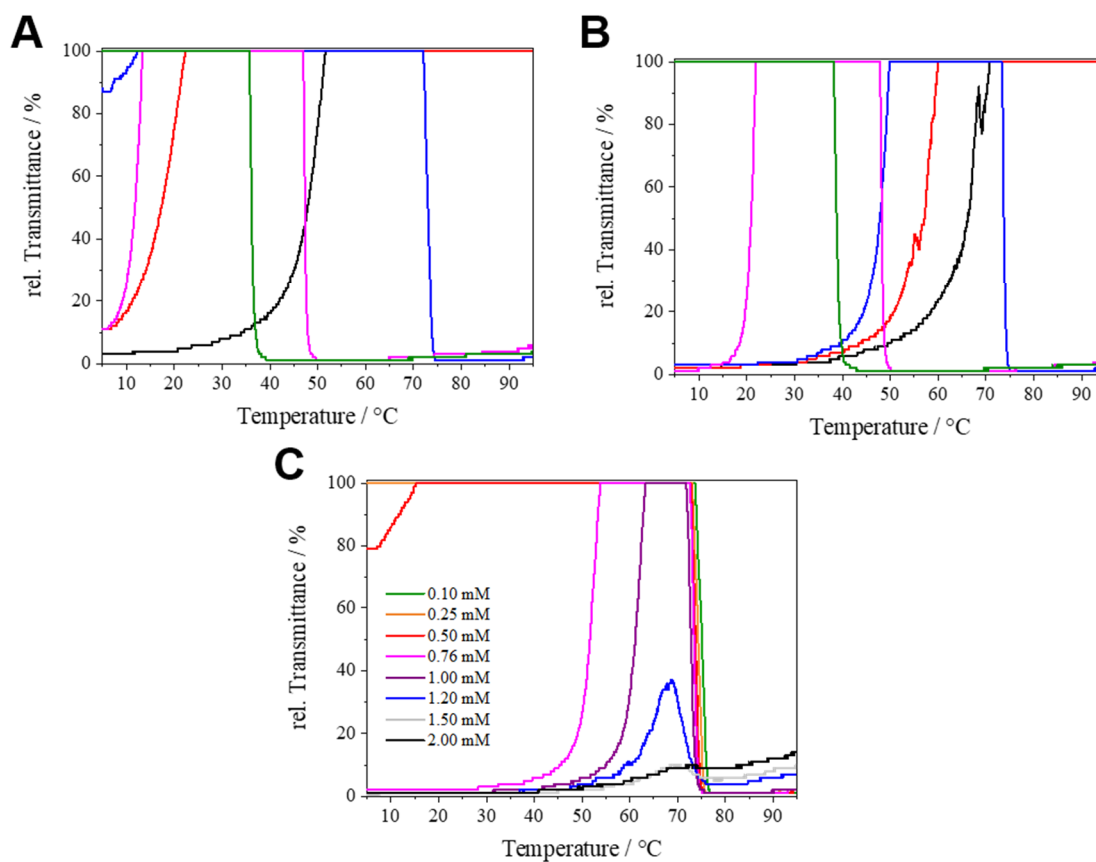
polymer	$c / \text{g}\cdot\text{L}^{-1}$	pH	$T_{\text{CP}}^{[\text{a}]}/\text{°C}$	Reference
PDMAEMAm <sub>210</sub>	1	6-10	soluble	
	1	6	soluble	
	1	7	soluble	
	1	8	72	
	0.05	9	64	
	0.1	9	57	
	0.2	9	56	this work
	0.5	9	54	
PDEAEMAm <sub>210</sub>	1	9	53	
	2	9	45	
	1	10	37	
	1	9	49	
PDEAEMAm <sub>1030</sub>	1	9	49	
	1	7	73	
PDiPAEMAm <sub>210</sub>	1	8	53	
	1	14	soluble	
PDMAEAm <sub>144</sub> <sup>[b]</sup>	1	14	soluble	
	0.5	8	soluble	
	0.5	8.5	50.2	3
PDEAEAm <sub>130</sub> <sup>[c]</sup>	0.5	11	33.1	
	0.5	13	31.5	
	0.5	14	27.5	

[a]  $\lambda = 645$  nm for PDxAEMAm<sub>210</sub>,  $\lambda = 500$  nm for PDMAEAm<sub>144</sub> and PDEAEAm<sub>130</sub>, [b] poly(**d**imethylaminoethyl acrylamide), [c] poly(**d**iethylaminoethyl acrylamide).

**Table S4.3.** Comparison of cloud points for methacrylate-based polymers.

polymer	$c / \text{g}\cdot\text{L}^{-1}$	pH	$T_{\text{CP},523 \text{ nm}} / \text{°C}$	Reference
PDEAEMA <sub>109</sub>	1	6	70	4
	[a]	7	40	
		7	76	
PDMAEMA <sub>108</sub>	1	8	53	5
	[a]	9	42.3	
		10	38.7	

[a] poly(**diethylaminoethyl methacrylate**), [b] poly(**dimethylaminoethyl methacrylate**).

Temperature-dependent transmittance – switching the solubility behaviour with  $K_3[Fe(CN)_6]$ 

**Figure S4.8.** Temperature-dependent transmittance of PDEAEMAm<sub>1030</sub> ( $c = 1$  g·L<sup>-1</sup>) in the presence of  $[Fe(CN)_6]^{3-}$  counterions in buffer solutions of different pH (pH = 6 (black), 7 (red), 8 (blue), 9 (magenta) and 10 (green)) with A)  $c([Fe(CN)_6]^{3-}) = 0.50$  mM and B)  $c([Fe(CN)_6]^{3-}) = 0.75$  mM. C) Dependence on  $[Fe(CN)_6]^{3-}$  concentration in pH = 8 buffer solution.

## Heterogeneous amidation

FT-IR spectra

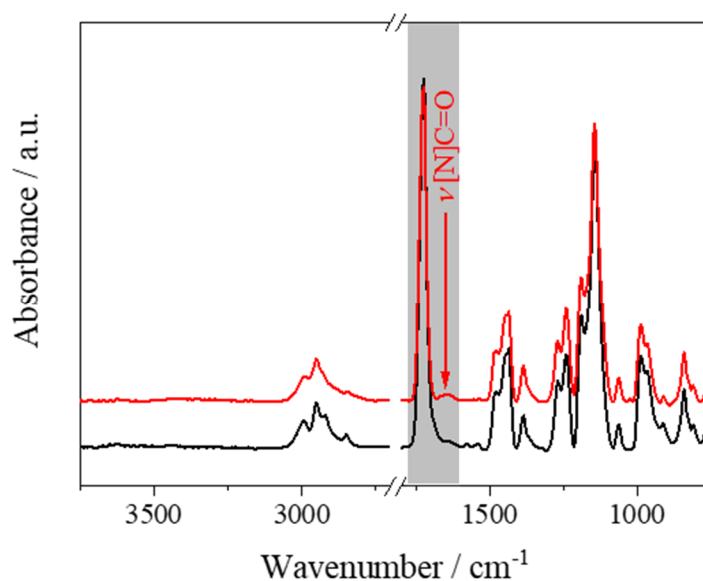


**Figure S4.9.** FT-IR spectra of a PMMA disc before (black) and after (red) heterogeneous amidation.

Contact angle

**Table S4.4.** Overview of the contact angle measurements before and after heterogeneous amidation.

sample	media	temperature / °C	contact angle / °
PMMA disc	deionized water	25	93 ± 2
	deionized water	55	83 ± 3
	pH 10 buffer	25	89 ± 4
	pH 10 buffer	55	75 ± 4
amidated PMMA disc	deionized water	25	49 ± 5
	pH 10 buffer	25	48 ± 6
	pH 10 buffer	55	77 ± 1

## References

- [1] P. A. Schaal, U. Simon, *Beilstein J. Nanotechnol.*, 2013, *4*, 336–344.
- [2] J. Schöbel, C. Hils, A. Weckwerth, M. Schlenk, C. Bojer, M. C. A. Stuart, J. Brey, S. Förster, A. Greiner, M. Karg, H. Schmalz. *Nanoscale* **2018**, *10*, 18257–18268.
- [3] Z. Song, K. Wang, C. Gao, S. Wang, W. Zhang. *Macromolecules* **2016**, *49*, 162–171.
- [4] A. Schmalz, M. Hanisch, H. Schmalz, A. H. E. Müller. *Polymer* **2010**, *51*, 1213–1217.
- [5] F. A. Plamper, M. Ruppel, A. Schmalz, O. Borisov, M. Ballauff, A. H. E. Müller. *Macromolecules* **2007**, *40*, 8361–8366.

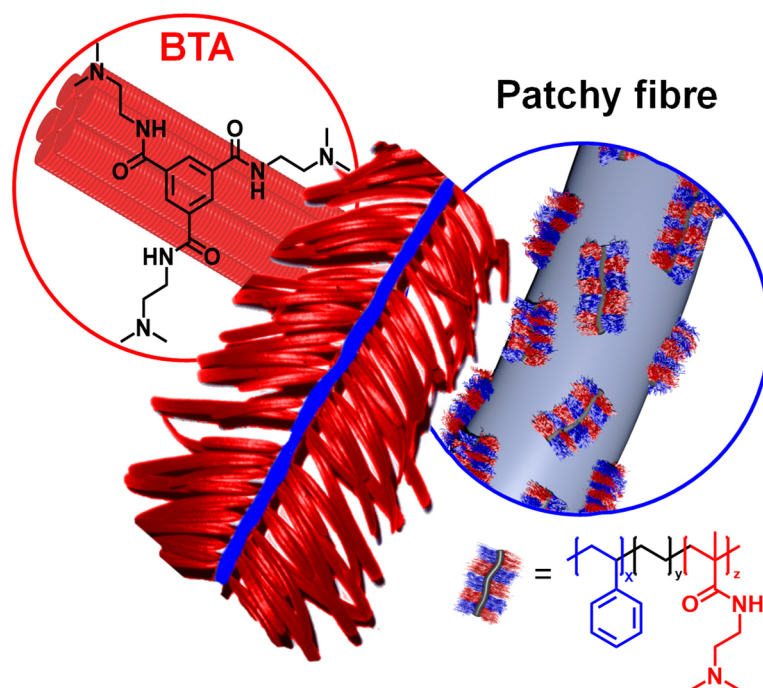
## 5 Hierarchical superstructures by combining crystallization-driven and molecular self-assembly

Andreas Frank,<sup>[a] +</sup> Christian Hils,<sup>[b] +</sup> Melina Weber,<sup>[a]</sup> Klaus Kreger,<sup>[a]</sup> Holger Schmalz<sup>[b]\*</sup> and Hans-Werner Schmidt<sup>[a]\*</sup>

[a] Macromolecular Chemistry I, University of Bayreuth and Bavarian Polymer Institute, Universitätsstraße 30, 95447 Bayreuth (Germany)

[b] Macromolecular Chemistry II, University of Bayreuth and Bavarian Polymer Institute, Keylab Synthesis and Molecular Characterization, Universitätsstraße 30, 95447 Bayreuth (Germany)

[+] These authors contributed equally to this work.



Published in: *Angew. Chem. Int. Ed.*, DOI: 10.1002/anie.202105787

Reprinted with permission from Wiley VCH Publications.

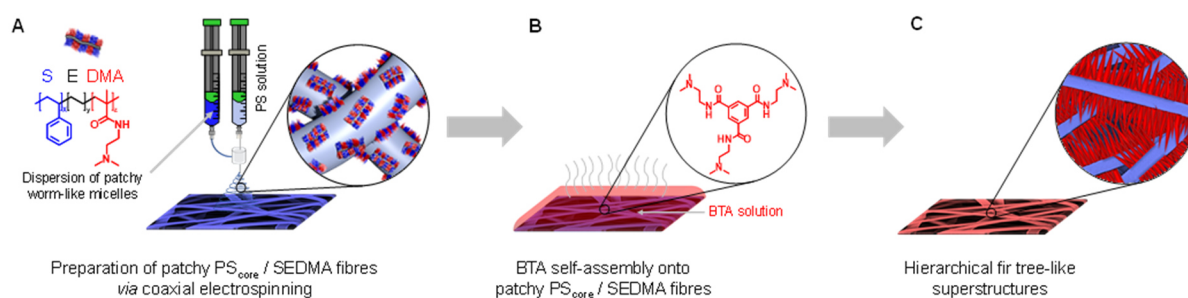
## Abstract

Combining the unique corona structure of worm-like patchy micelles immobilized on a polymer fibre with the molecular self-assembly of 1,3,5-benzenetricarboxamides (BTAs) leads to hierarchical superstructures with a fir tree-like morphology. For this purpose, worm-like patchy micelles bearing pendant, functional tertiary amino groups in one of the corona patches were prepared by crystallization-driven self-assembly and immobilized on a supporting polystyrene fibre by coaxial electrospinning. The obtained patchy fibres were then immersed in an aqueous solution of a tertiary amino-functionalized BTA to induce patch-mediated molecular self-assembly to well-defined fir-tree like superstructures upon solvent evaporation. Interestingly, defined superstructures are obtained only if the pendant functional groups in the surface patches match with the peripheral substituents of the BTA, which is attributed to a local increase in BTA concentration at the polymer fibres' surface.

Hierarchical self-assembly represents an intriguing approach to realize complex superstructures at the nano- and mesoscale in nature. Although artificial molecular and macromolecular self-assembly concepts have already proven to pave the way to more complex assemblies, the outstanding control over shape, dimension and functionality found in nature is still far from being achieved. The guided hierarchical self-assembly of amorphous block copolymers in solution has shown to represent a facile way to tailor-made multicompartments structures.<sup>[1]</sup> However, particularly for one- (1D) and two- (2D) dimensional structures, the precise control over size and size-distribution is difficult to achieve. Here, the introduction of a crystallizable block, which adds an additional and strong driving force for micelle formation, can be harnessed to solve these issues in a process termed crystallization-driven self-assembly (CDSA). Especially, the discovery of living CDSA,<sup>[2]</sup> which closely resembles the features of living polymerization processes with respect to control over size and size distribution, has given access to a multitude of complex and hierarchical micellar assemblies of controlled shape and size, like for example patchy and block comicelles, branched and scarf-like micelles, colloidosomes and multidimensional superstructures.<sup>[3]</sup> A closely related concept to CDSA is supramolecular polymerization, that is the self-assembly of small molecules *via* directed and reversible secondary interactions, which we denote as molecular self-assembly in the following.<sup>[4]</sup> Similarly, molecular self-assembly processes allow for the fabrication of defined nanostructures and superstructures.<sup>[5]</sup> In particular, control over the self-assembly process and in turn on the objects' dimensions can be achieved with living supramolecular polymerization,<sup>[6]</sup> which can be realized for instance by a seed-initiated growth approach. The combination of a precise "top-down" coating technique such as coaxial electrospinning<sup>[7]</sup> with CDSA, a typical "bottom-up" approach, was recently employed in our group to construct patchy hybrid nonwovens with excellent performance in heterogeneous catalysis.<sup>[8]</sup> Utilizing a similar strategy for the immobilization of 1,3,5-benzenetricarboxamide (BTA) seeds onto electrospun fibres yielded mesostructured nonwovens with a penguin downy feather-like morphology by an *in-situ* growth of supramolecular BTA fibres from the electrospun seed fibres.<sup>[9]</sup> However, with this approach the control over the seed density on the electrospun fibres is limited.

In this communication we show that hierarchical fir tree-like superstructures can be generated by the combination of two self-assembly concepts, that is crystallization-driven self-assembly and molecular self-assembly (Scheme 5.1). Our conceptual approach to these defined superstructures comprises A) the preparation of patchy PS<sub>core</sub> / SEDMA fibres by coaxial electrospinning of polystyrene (PS) and patchy worm-like polystyrene-*block*-polyethylene-

*block*-poly(*N,N*-dimethylaminoethyl methacrylamide) (SEDMA) triblock terpolymer micelles, B) the immersion of this patchy fibres into an aqueous  $N^1, N^3, N^5$ -tris[2-(dimethylamino)-ethyl]-1,3,5-benzenetricarboxamide (BTA-Methyl) solution and C) the controlled molecular self-assembly of BTA-Methyl to highly defined hierarchical superstructures upon solvent evaporation. In the resulting fir tree-like superstructures the PS<sub>core</sub> / SEDMA fibres form the core, from which supramolecular BTA-Methyl fibres (“needles”) have grown away from the surface in a well-controlled fashion.



**Scheme 5.1.** Formation of hierarchical fir tree-like superstructures. A) Coaxial electrospinning of a polystyrene (PS) solution and a dispersion of patchy worm-like polystyrene-*block*-polyethylene-*block*-poly(*N,N*-dimethylaminoethyl methacrylamide) (SEDMA) triblock terpolymer micelles to prepare patchy PS<sub>core</sub> / SEDMA fibres. B) Immersion of the patchy PS<sub>core</sub> / SEDMA fibres into an aqueous  $N^1, N^3, N^5$ -tris[2-(dimethylamino)-ethyl]-1,3,5-benzenetricarboxamide (BTA-Methyl) solution and subsequent evaporation induced molecular self-assembly of BTA-Methyl onto the patchy fibres. C) Final hierarchical fir tree-like superstructures after complete solvent evaporation.

The PS<sub>core</sub> / SEDMA fibres with functional surface patches were prepared by immobilizing patchy worm-like SEDMA micelles on top of PS fibres by coaxial electrospinning, employing a PS solution (7 wt.% in DMF;  $M_n = 1.8 \cdot 10^6 \text{ g} \cdot \text{mol}^{-1}$ ) as core and a dispersion of patchy worm-like SEDMA micelles ( $c = 10 \text{ g} \cdot \text{L}^{-1}$  in THF) as shell, respectively (Scheme 5.1A). The dispersion of the patchy worm-like SEDMA micelles was prepared *via* CDSA, as previously reported, whereby the PS patches provide compatibility with the supporting PS fibre and the PDMA patches the functionality.<sup>[10]</sup> Experimental details and the molecular characteristics of the employed triblock terpolymers are described in the supporting information. Exemplarily, a TEM image of the patchy worm-like SEDMA micelles is depicted in Figure S1. Here, the semi-crystalline PE block forms the core and the micellar corona consists of alternating, nanometre-sized PS ( $18 \pm 5 \text{ nm}$ ) and PDMA ( $17 \pm 5 \text{ nm}$ ) patches (Table S1). Figure 5.1A shows a scanning electron microscope image of a patchy PS<sub>core</sub> / SEDMA polymer fibre, where the worm-like SEDMA micelles on top of the supporting PS fibre can be clearly distinguished.

As building block for the molecular self-assembly (Scheme 5.1B) BTA-Methyl was selected featuring peripheral tertiary *N,N*-dimethylaminoethyl substituents,<sup>[11]</sup> which match the pendant functional groups in the PDMA patches of the SEDMA micelles. BTA-Methyl is highly water soluble up to a concentration of 15 wt.%<sup>[11]</sup> and exhibits no temperature-induced formation of supramolecular structures at a concentration of 2 wt.%, as demonstrated by temperature-dependent turbidity measurements and micro-differential scanning calorimetry (Figure S5.2, S5.3). Only upon solvent evaporation, apparently a threshold concentration is reached, where homogeneous nucleation results in the formation of randomly distributed supramolecular BTA-Methyl fibres with a broad length distribution (Figure 5.1B). The final deposited fibre density correlates with the initially used concentration of BTA-Methyl (Figure S5.4). In an analogous manner, also the PDMA block of the SEDMA triblock terpolymer shows complete solubility in water over a broad temperature range.<sup>[12]</sup>

Remarkably, immersion of the patchy PS<sub>core</sub> / SEDMA fibres into a BTA-Methyl solution of only 0.05 wt.% followed by solvent evaporation (Scheme 5.1B, C) resulted in highly defined hierarchical fir tree-like superstructures as shown in Figure 5.1C. Moreover, the BTA-Methyl fibres grow away from the patchy polymer fibre in an oriented manner and can be observed at different positions, which indicates different starting points due to the randomly distributed worm-like micelles at the surface of the PS<sub>core</sub> / SEDMA fibre. This is confirmed by Raman imaging, which allows to distinguish between the patchy PS<sub>core</sub> / SEDMA fibre and the BTA fibres. The Raman spectra of the corresponding neat compounds can be found in Figure S5.5. Figure 5.1D shows an overlay of the optical microscopy image of the fir tree-like superstructure and the spatially resolved component distribution from Raman imaging (PS is depicted in blue and BTA-Methyl in red) clearly demonstrating that the BTA-Methyl fibres are directly attached onto the patchy PS<sub>core</sub> / SEDMA fibre. Furthermore, Raman imaging allows to probe the alignment of the BTA-Methyl units, since the spectra differ depending on their orientation with respect to the polarization of the laser (horizontally polarized). Most of the BTA-Methyl units show a perpendicular stacking to the PS fibre (Figure S5.6).

These results indicate that the patchy surface of the fibres is able to initiate the molecular self-assembly of BTA-Methyl. As PDMA is amorphous and well soluble in water, the PDMA patches are highly swollen and, accordingly, the pendant tertiary *N,N*-dimethylaminoethyl groups are not expected to show any structural order. This makes a heterogeneous nucleation of BTA-Methyl due to an epitaxial match highly unlikely. Hence, the nucleation effect might be attributed to an accumulation (local increase in concentration) of BTA-Methyl in the PDMA

patches at the fibres' surface promoted by the chemical match of peripheral groups of BTA-Methyl and pendant tertiary amino-groups in the PDMA patches.

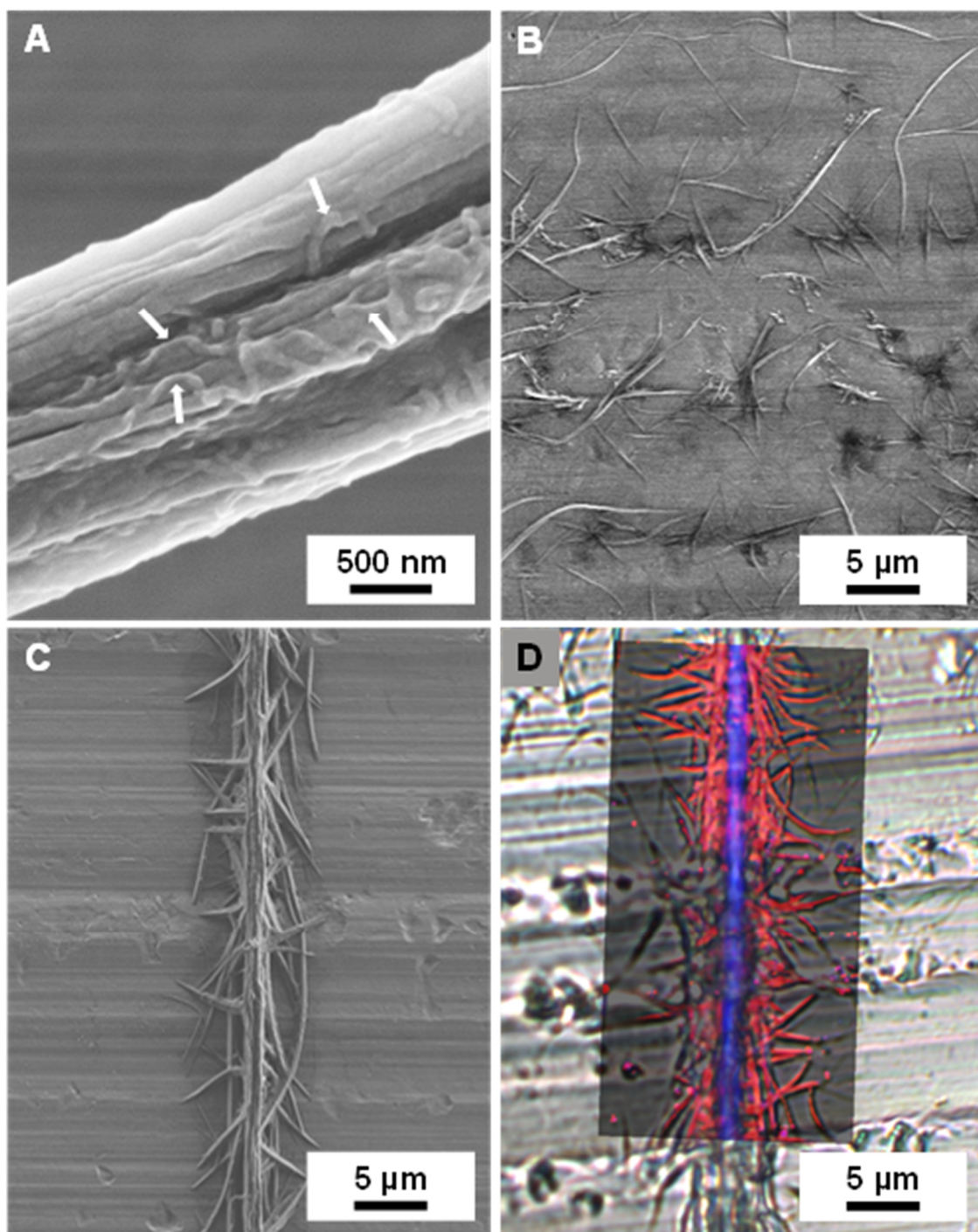


**Figure 5.1.** Scanning electron micrographs of A) a patchy PS<sub>core</sub> / SEDMA fibre, the arrows indicate the patchy worm-like micelles on top of the supporting PS<sub>core</sub> fibre; B) uncontrolled supramolecular BTA assemblies prepared upon solvent evaporation from a 0.050 wt.% aqueous solution on aluminium foil; C) hierarchical fir tree-like superstructure prepared by molecular self-assembly of a 0.050 wt.% aqueous BTA-Methyl solution onto patchy PS<sub>core</sub> / SEDMA fibres after solvent evaporation. D) Overlay of the spatially resolved component distribution from Raman imaging (PS rich regions are coloured in blue and BTA-Methyl rich in red, respectively) with the optical microscopy image of the fir tree-like superstructure.

To get a closer insight into the superstructure formation *via* molecular self-assembly of BTA-Methyl mediated by the functional PDMA patches at the surface of PS<sub>core</sub> / SEDMA fibres, electrospun polymer fibres with immobilized, non-functional patchy micelles (PS<sub>core</sub> / SEM) and neat PS fibres were prepared and used as reference (Figure 5.2). Here, SEM denotes patchy worm-like micelles prepared by CDSA of a polystyrene-*block*-polyethylene-*block*-poly(methyl methacrylate) triblock terpolymer. Replacing the functional hydrophilic PDMA patches by hydrophobic poly(methyl methacrylate) (PMMA) patches in the micellar corona, led predominantly to an accumulation of unstructured BTA-Methyl assemblies near the polymer fibre, which is attributed to a drying effect (Figure 5.2A). In a similar manner, neat PS fibres also resulted in non-defined BTA structures near the polymer fibres, however to a slightly lesser extent (Figure 5.2B). This clearly demonstrates that neither a neat PS fibre nor patchy SEM micelles on top of the supporting PS fibre are sufficient to initiate the molecular self-assembly of BTA-Methyl, underlining the necessity of a chemical match of the pendant tertiary amino-groups in the micellar patches and the peripheral groups of BTA-Methyl. Consequently, two decisive factors might be extracted from these observations: i) The patches need to be soluble in the solvent (here water) used for the molecular self-assembly of BTA-Methyl as otherwise they would not be accessible and ii) hydrogen-bonding and dipole interactions between the pendant tertiary-amino groups in the functional PDMA patches and the peripheral substituents of BTA-Methyl most likely result in a local increase of the BTA-Methyl concentration within the PDMA patches. The latter in turn might facilitate the formation of nuclei and, thus, a patch-mediated molecular self-assembly of BTA-Methyl from the surface of the patchy PS<sub>core</sub> / SEDMA fibres.

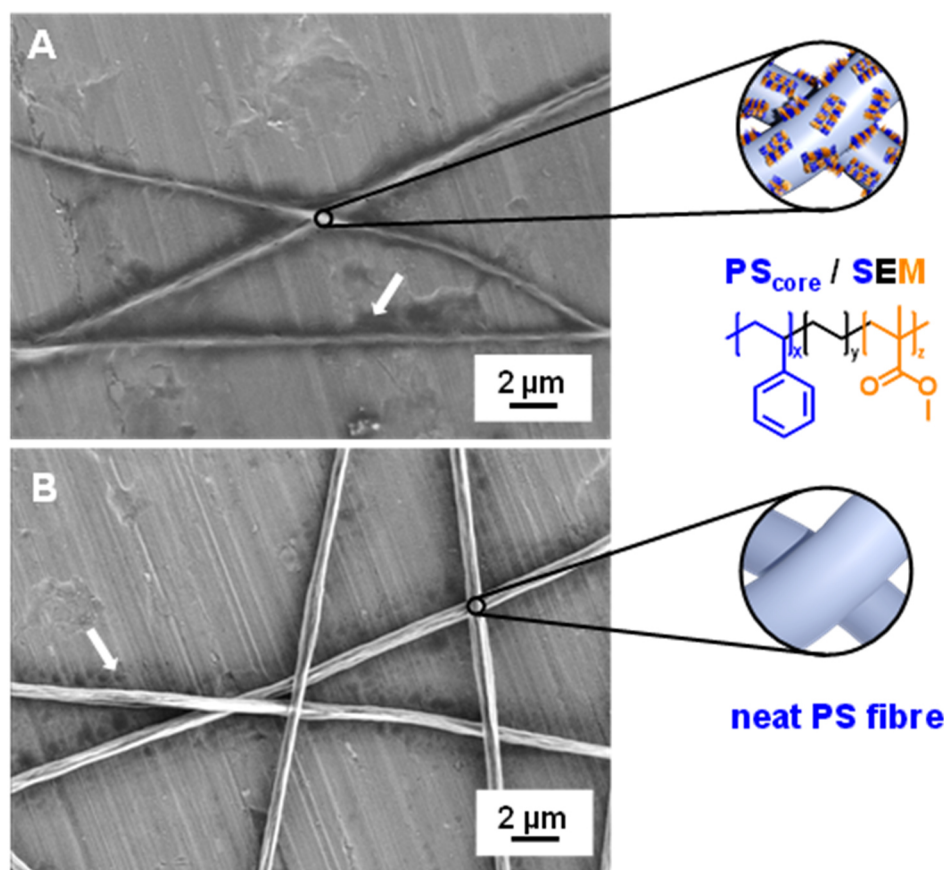


**Figure 5.2.** Scanning electron micrographs showing the absence of hierarchical superstructures for reference experiments employing A) PS fibres with patchy worm-like micelles of polystyrene-*block*-polyethylene-*block*-poly(methyl methacrylate) (PS<sub>core</sub> / SEM) and B) neat PS fibres without patches in the molecular self-assembly of BTA-Methyl. The arrows indicate unstructured BTA-Methyl assemblies formed upon drying.

To support our assumption that the PDMA patches locally increase the concentration of BTA-Methyl and, thus, induce controlled self-assembly, the concentration of the BTA-Methyl solution was systematically varied (Figure 5.3). For a low BTA-Methyl concentration of only  $c = 0.025$  wt.% in water, no molecular self-assembly at the patchy PS<sub>core</sub> / SEDMA fibres was observed (Figure 5.3A). Up to an initial concentration of  $c = 0.100$  wt.%, very defined superstructures by patch-mediated molecular self-assembly were obtained (Figure 5.3B, C). However, a further increase in concentration to  $c = 0.250$  wt.% led to highly dense, less ordered supramolecular BTA-Methyl fibres instead of well-defined hierarchical superstructures (Figure 5.3D). For the self-assembly of neat BTA-Methyl upon solvent evaporation, the formation of ordered structures was only observed from aqueous solutions with a concentration higher than  $c = 0.250$  wt.% (Figure S5.4). At this concentration, homogenous nucleation is favoured resulting in star-shaped assemblies, where several fibres emanate from one central starting point. Consequently, there is a competition between the patch-mediated molecular self-assembly and homogenous BTA-Methyl nucleation. At low concentrations, that is well below

the concentration where self-assembly is observed for neat BTA-Methyl solutions, the patch-mediated self-assembly dominates and is driven by the local increase in BTA-Methyl concentration in the PDMA patches allowing the formation of BTA-Methyl nuclei. In contrast, at higher concentrations the homogenous nucleation of BTA-Methyl to randomly distributed supramolecular fibres is favoured and control over the formed superstructure is lost.

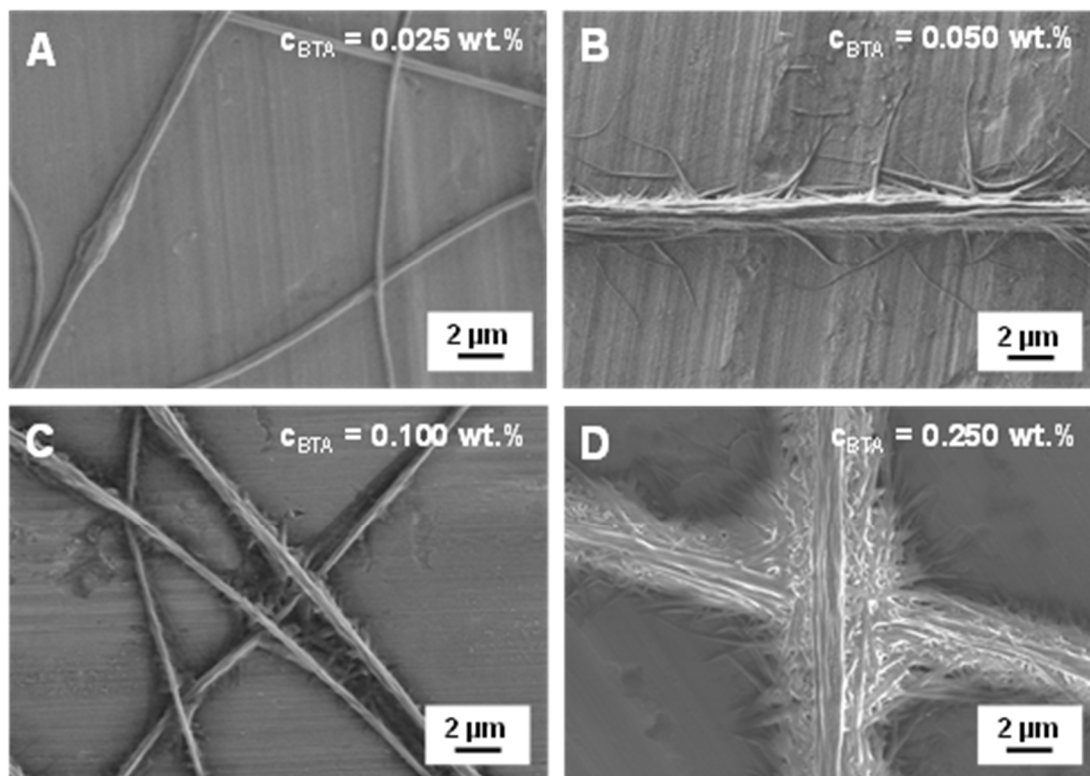


**Figure 5.3.** Scanning electron micrographs of hierarchical superstructures prepared by employing a A) 0.025 wt.%, B) 0.050 wt.%, C) 0.100 wt.% and D) 0.250 wt.% aqueous BTA-Methyl solution for molecular self-assembly onto patchy PS<sub>core</sub> / SEDMA fibres.

In conclusion, this work shows that polymer fibres with tailored functional surface patches can induce the molecular self-assembly of a designed 1,3,5-benzenetricarboxamide (BTA) into well-defined hierarchical fir tree-like superstructures. The key for the patch-mediated molecular self-assembly of the BTA from the polymer fibres is the chemical match of the functional groups in the surface patches and the BTA peripheral groups that in turn controls the solubility and accessibility of the patch for the BTA. These results open the opportunity to construct a large variety of complex hierarchical superstructures, as the chemistry of the polymer patches and the BTA peripheral groups can be easily tuned to transfer this concept to other functional components and solvent systems. Thus, the design criteria comprise the chemical match, the solvent as well as the BTA concentration. This might stimulate further research on the fabrication of functional hierarchical superstructures for (nano)particle

separation and immobilization with potential applications in filtration and heterogeneous catalysis.

### Acknowledgements

This work was supported by the German Research Foundation (DFG) in the framework of the Collaborative Research Centre SFB840, projects A2 and B8. We thank Prof. Andreas Greiner for help with coaxial electrospinning. We acknowledge the Keylab Electron and Optical Microscopy of the Bavarian Polymer Institute (University of Bayreuth) for providing access to the electron microscopy facilities and for support during measurements. A. F. thanks the Elite Study Program *Macromolecular Science* within the Elite Network of Bavaria (ENB) for support. A. F. and C. H. acknowledge support by the Graduate School of the University of Bayreuth.

### Conflict of Interest

The authors declare no conflict of interest.

**Keywords:** patchy polymer fibres • crystallization-driven self-assembly • molecular self-assembly • hierarchical superstructures • supramolecular structures

### References

- [1] a) F. H. Schacher, P. A. Rugar, I. Manners, *Angew. Chem., Int. Ed.* **2012**, *51*, 7898; *Angew. Chem.* **2012**, *124*, 8020; b) A. H. Gröschel, A. Walther, T. I. Löblich, F. H. Schacher, H. Schmalz, A. H. E. Müller, *Nature* **2013**, *503*, 247; c) J. C. Brendel, F. H. Schacher, *Chem. Asian J.* **2018**, *13*, 230; d) A. H. Gröschel, A. H. E. Müller, *Nanoscale* **2015**, *7*, 11841; e) D. J. Lunn, J. R. Finnegan, I. Manners, *Chem. Sci.* **2015**, *6*, 3663; f) U. Tritschler, S. Pearce, J. Gwyther, G. R. Whittell, I. Manners, *Macromolecules* **2017**, *50*, 3439; g) A. O. Moughton, M. A. Hillmyer, T. P. Lodge, *Macromolecules* **2012**, *45*, 2.
- [2] a) X. Wang, G. Guerin, H. Wang, Y. Wang, I. Manners, M. A. Winnik, *Science* **2007**, *317*, 644; b) J. B. Gilroy, T. Gädt, G. R. Whittell, L. Chabanne, J. M. Mitchels, R. M. Richardson, M. A. Winnik, I. Manners, *Nat. Chem.* **2010**, *2*, 566; c) S. Ganda, M. H. Stenzel, *Prog. Polym. Sci.* **2020**, *101*, 101195.

- [3] a) L. MacFarlane, C. Zhao, J. Cai, H. Qiu, I. Manners, *Chem. Sci.* **2021**, *12*, 4661; b) J. Schmelz, M. Karg, T. Hellweg, H. Schmalz, *ACS Nano* **2011**, *5*, 9523; c) J. Schmelz, A. E. Schedl, C. Steinlein, I. Manners, H. Schmalz, *J. Am. Chem. Soc.* **2012**, *134*, 14217; d) H. Qiu, Z. M. Hudson, M. A. Winnik, I. Manners, *Science* **2015**, *347*, 1329; e) T. Gädt, N. S. Jeong, G. Cambridge, M. A. Winnik, I. Manners, *Nat. Mater.* **2009**, *8*, 144; f) H. Dou, M. Li, Y. Qiao, R. Harniman, X. Li, C. E. Boott, S. Mann, I. Manners, *Nat. Commun.* **2017**, *8*, 426; g) O. E. C. Gould, H. Qiu, D. J. Lunn, J. Rowden, R. L. Harniman, Z. M. Hudson, M. A. Winnik, M. J. Miles, I. Manners, *Nat. Commun.* **2015**, *6*, 10009.
- [4] a) L. Brunsveld, B. J. Folmer, E. W. Meijer, R. P. Sijbesma, *Chem. Rev.* **2001**, *101*, 4071; b) T. F. A. de Greef, M. M. J. Smulders, M. Wolffs, Schenning, Albert P. H. J., R. P. Sijbesma, E. W. Meijer, *Chem. Rev.* **2009**, *109*, 5687.
- [5] a) T. Aida, E. W. Meijer, S. I. Stupp, *Science* **2012**, *335*, 813; b) T. Aida, E. W. Meijer, *Isr. J. Chem.* **2020**, *60*, 33; c) F. V. Gruschwitz, T. Klein, S. Catrouillet, J. C. Brendel, *Chem. Commun.* **2020**, *56*, 5079; d) K. Liu, Y. Kang, Z. Wang, X. Zhang, *Adv. Mater.* **2013**, *25*, 5530; e) D. Spitzer, L. L. Rodrigues, D. Straßburger, M. Mezger, P. Besenius, *Angew. Chem., Int. Ed.* **2017**, *56*, 15461; *Angew. Chem.* **2017**, *129*, 15664; f) B. N. S. Thota, X. Lou, D. Bochicchio, T. F. E. Paffen, R. P. M. Lafleur, J. L. J. van Dongen, S. Ehrmann, R. Haag, G. M. Pavan, A. R. A. Palmans, E. W. Meijer, *Angew. Chem., Int. Ed.* **2018**, *57*, 6843; *Angew. Chem.* **2018**, *130*, 6959; g) S.-P. Wang, W. Lin, X. Wang, T.-Y. Cen, H. Xie, J. Huang, B.-Y. Zhu, Z. Zhang, A. Song, J. Hao, J. Wu, S. Li, *Nat. Commun.* **2019**, *10*, 1399.
- [6] a) J. Matern, Y. Dorca, L. Sánchez, G. Fernández, *Angew. Chem., Int. Ed.* **2019**, *58*, 16730; *Angew. Chem.* **2019**, *131*, 16884; b) M. Wehner, F. Würthner, *Nat. Rev. Chem.* **2020**, *4*, 38; c) E. Weyandt, M. F. J. Mabesoone, L. N. J. de Windt, E. W. Meijer, A. R. A. Palmans, G. Vantomme, *Org. Mater.* **2020**, *02*, 129; d) S. Ogi, K. Sugiyasu, S. Manna, S. Samitsu, M. Takeuchi, *Nat. Chem.* **2014**, *6*, 188; e) K. Zhang, M. C.-L. Yeung, S. Y.-L. Leung, V. W.-W. Yam, *Proc. Natl. Acad. Sci.* **2017**, *114*, 11844; f) A. Singh, J. P. Joseph, D. Gupta, I. Sarkar, A. Pal, *Chem. Commun.* **2018**, *54*, 10730.
- [7] a) S. Agarwal, A. Greiner, J. H. Wendorff, *Prog. Polym. Sci.* **2013**, *38*, 963; b) A. Greiner, J. H. Wendorff, *Angew. Chem., Int. Ed.* **2007**, *46*, 5670; *Angew. Chem.* **2007**, *119*, 5770.
- [8] a) J. Schöbel, M. Burgard, C. Hils, R. Dersch, M. Dulle, K. Volk, M. Karg, A. Greiner, H. Schmalz, *Angew. Chem., Int. Ed.* **2017**, *56*, 405; *Angew. Chem.* **2017**, *129*, 416; b) C. Hils, M. Dulle, G. Sitaru, S. Gekle, J. Schöbel, A. Frank, M. Drechsler, A. Greiner, H. Schmalz, *Nanoscale Adv.* **2020**, *2*, 438.

- [9] M. Burgard, D. Weiss, K. Kreger, H. Schmalz, S. Agarwal, H.-W. Schmidt, A. Greiner, *Adv. Funct. Mater.* **2019**, *29*, 1903166.
- [10] J. Schöbel, C. Hils, A. Weckwerth, M. Schlenk, C. Bojer, M. C. A. Stuart, J. Breu, S. Förster, A. Greiner, M. Karg, H. Schmalz, *Nanoscale* **2018**, *10*, 18257.
- [11] A. Frank, A. Bernet, K. Kreger, H.-W. Schmidt, *Soft Matter* **2020**, *16*, 4564.
- [12] C. Hils, E. Fuchs, F. Eger, J. Schöbel, H. Schmalz, *Chem. - Eur. J.* **2020**, *26*, 5611.

## Supporting Information

### Experimental Procedures

**Materials.** All chemicals were used as received unless otherwise noted. *N,N*-dimethylformamide (DMF, 99%, Acros Organics), tetrahydrofuran (THF,  $\geq 99.9\%$ , VWR). Polystyrene (PS) was synthesized by anionic polymerization in THF at  $-80\text{ }^{\circ}\text{C}$  using *sec*-butyllithium as initiator ( $M_n = 1.8 \cdot 10^6\text{ g}\cdot\text{mol}^{-1}$ ,  $D = 1.08$ ).

**Synthesis of *N*<sup>1</sup>,*N*<sup>3</sup>,*N*<sup>5</sup>-tris[2-(dimethylamino)-ethyl]-1,3,5-benzenetricarboxamide (BTA-Methyl).** BTA-Methyl was synthesized as described previously.<sup>[1]</sup> Briefly, trimesic acid trimethyl ester was dispersed in *N,N*-dimethylethylenediamine under an argon atmosphere. The mixture was heated to  $125\text{ }^{\circ}\text{C}$ , stirred overnight and subsequently allowed to cool down to room temperature. The resulting mixture was dispersed in acetone and heated until an almost clear solution was obtained. The hot solution was filtrated using a sintered glass funnel filter. The solvent was removed and the product was dried in a vacuum oven at  $50\text{ }^{\circ}\text{C}$  over night, yielding a white powder.

**Synthesis of triblock terpolymers.** Polystyrene-*block*-polyethylene-*block*-poly(methyl methacrylate) ( $S_{40}E_{21}M_{39}^{108}$ ) was synthesized by a combination of living anionic polymerization and catalytic hydrogenation, as described elsewhere.<sup>[2]</sup> Polystyrene-*block*-polyethylene-*block*-poly(*N,N*-dimethylaminoethyl methacrylamide) ( $S_{33}E_{17}DMA_{50}^{132}$ ) was prepared *via* post-polymerization functionalization of the poly(methyl methacrylate) (PMMA) block of  $S_{40}E_{21}M_{39}^{108}$ .<sup>[3,4]</sup> In the used triblock terpolymer notation the subscripts describe the mass fraction of the corresponding block in wt.% and the superscript denotes the overall number average molecular weight ( $M_n$ ) in  $\text{kg}\cdot\text{mol}^{-1}$ .  $M_n$  was determined by a combination of MALDI-ToF MS (matrix-assisted laser desorption/ionization – time of flight mass spectrometry) and  $^1\text{H}$  NMR (nuclear magnetic resonance) spectroscopy, employing the absolute  $M_n$  of the polystyrene precursor from MALDI-ToF for  $^1\text{H}$  NMR signal calibration.

**Formation of patchy worm-like triblock terpolymer micelles.** The patchy worm-like micelles were prepared by crystallization-driven self-assembly (CDSA) of the triblock terpolymers  $S_{40}E_{21}M_{39}^{108}$  and  $S_{33}E_{17}DMA_{50}^{132}$  in THF according to our previous work.<sup>[2,3]</sup> The polymers were dissolved in THF ( $c = 10\text{ g}\cdot\text{L}^{-1}$ ) at  $65\text{ }^{\circ}\text{C}$  for 0.5 h using a thermostated shaker unit (HCL-

MKR 13, Ditabis). The self-assembly process occurred by subsequently cooling to the crystallization temperature ( $T_c$ ) of the polyethylene middle block (**Table S5.1**). The process was allowed to proceed for 24 h with 200 rpm resulting in the respective patchy worm-like micelle dispersions.

**Table S5.1.** Properties of the used patchy worm-like micelles.

Triblock terpolymer <sup>[a]</sup>	$T_c$ [°C] <sup>[b]</sup>	patch size [nm] <sup>[c]</sup>		length of micelles [nm] <sup>[c]</sup>	Ref.
		S	M / DMA		
S <sub>40</sub> E <sub>21</sub> M <sub>39</sub> <sup>108</sup>	20	13 ± 4	13 ± 4	520 ± 140	[2,5]
S <sub>33</sub> E <sub>17</sub> DMA <sub>50</sub> <sup>132</sup>	21	18 ± 5	17 ± 5	510 ± 310	[3]

<sup>[a]</sup> Subscripts describe the mass fraction of the corresponding block in wt.% and the superscript denotes the overall molecular weight in  $\text{kg}\cdot\text{mol}^{-1}$ . <sup>[b]</sup> crystallization temperature of the PE block,  $c = 10 \text{ g}\cdot\text{L}^{-1}$  in THF.

<sup>[c]</sup> Average sizes  $\pm$  standard deviation as determined by TEM image analysis of at least 100 micelles/patches.

**Electrospinning.** Preparation of patchy polymer fibres  $PS_{\text{core}} / \text{SEM}$  and  $PS_{\text{core}} / \text{SEDMA}$ . Patchy polymer fibres were produced by coaxial electrospinning, according to our previous work.<sup>[3,6]</sup> To this end, a 7 wt.% polystyrene ( $PS_{\text{core}}$ ) ( $M_n = 1.8 \cdot 10^6 \text{ g}\cdot\text{mol}^{-1}$ ) solution in DMF was used as core and for the shell dispersions of patchy worm-like SEM or SEDMA micelles in THF ( $c = 10 \text{ g}\cdot\text{L}^{-1}$ ) were employed. The fibres were spun on a collector placed at a distance of 20 cm from the coaxial needle (COAX\_2DISP sealed coaxial needles, LINARI NanoTech,  $d_{\text{core}} = 0.51 \text{ mm}$  and  $d_{\text{shell}} = 1.37 \text{ mm}$ ) at a temperature of 20.8 °C and a relative humidity of ca. 30%. For electrospinning, a high voltage of 11.4 kV at the needle and -1.0 kV at the collector were applied. The feed rate of the  $PS_{\text{core}}$  solution was  $1.2 \text{ mL}\cdot\text{h}^{-1}$  and for the micellar dispersions  $1.0 \text{ mL}\cdot\text{h}^{-1}$ . Neat polystyrene fibres were prepared as reference material in the same manner but without using the micellar dispersions.

***Self-assembly of aqueous BTA-Methyl solutions upon solvent evaporation onto aluminium foil.*** 25  $\mu\text{L}$  of an aqueous BTA-Methyl solution with concentrations ranging from 0.025 to 1.000 wt.% were dropped onto aluminium foil and the solvent was allowed to evaporate at ambient conditions. After solvent evaporation, turbid films were obtained and investigated by scanning electron microscopy.

***Self-assembly of aqueous BTA-Methyl solutions onto patchy polymer fibres.*** The PS<sub>core</sub> / SEDMA and PS<sub>core</sub> / SEM fibres as well as the neat PS fibres on aluminium foil were immersed into BTA-Methyl solutions (varying in concentration ranging from 0.025 wt.% to 0.250 wt.% with a pH value from 7 to 11, respectively) for a fixed time of 30 s and allowed to dry at ambient conditions for complete solvent evaporation.

## Methods

***Scanning electron microscopy.*** For scanning electron microscopy measurements, a FEI Quanta FEG 250 scanning electron microscope (Thermo Fisher Scientific) equipped with a field emission gun was used. The untreated samples, i.e. without applying a sputter coating, were measured in the beam deceleration mode (only Figure 5.1A, 5.1C and 5.3B) or in the low vacuum mode. Measurements in the beam deceleration mode were conducted under high vacuum at an acceleration voltage of 6 kV. This mode was used to image surfaces at high magnification with a concentric back scattered (CBS) electron detector, which is insensitive to sample charging. Here, an additional negative voltage (bias, -4 kV) was applied to the stage. In this way, the primary electrons were decelerated to 2 kV when reaching the sample and interacted electrons were accelerated toward the CBS detector. The samples measured in the low vacuum mode (water pressure of 40 Pa in the sample chamber) were mounted on a sample holder using an adhesive graphite pad and were investigated with an acceleration voltage of 3 kV with a large-field (gaseous secondary electron) detector (LFD) for topographical details.

***Transmission electron microscopy.*** The morphology of triblock terpolymer worm-like micelles were analysed by elastic bright-field transmission electron microscopy (TEM) on a Zeiss 922 Omega EFTEM (Zeiss NTS GmbH, Oberkochen, Germany). Zero-loss filtered images were recorded digitally on a bottom mounted CCD camera system (Ultrascan 1000, Gatan) at an acceleration voltage of 200 kV. The micrographs were processed with the digital imaging processing system of Gatan (Digital Micrograph 3.9 for GMS 1.4). The samples were

diluted to  $c = 0.1 \text{ g}\cdot\text{L}^{-1}$  and a droplet was placed onto a carbon coated copper grid. The residual solvent was immediately blotted by filter paper, dried in a vacuum oven (20 mbar, room temperature) and stained with  $\text{RuO}_4$  vapor (selective staining of PS). The average length and patch size were determined by measuring at least 100 micelles/patches using the software ImageJ.<sup>[7]</sup>

**Raman imaging.** A WITec alpha 300 RA+ imaging system, equipped with a UHTS 300 spectrometer and a back-illuminated Andor Newton 970 EMCCD camera, was employed for confocal Raman imaging. The measurements were conducted at an excitation wavelength of  $\lambda = 532 \text{ nm}$ , using a laser power of 4 mW and an integration time of  $0.6 \text{ s}\cdot\text{pixel}^{-1}$  (100x objective,  $\text{NA} = 0.9$ , step size  $100 \text{ nm}\cdot\text{pixel}^{-1}$ , software WITec Control FIVE 5.3). All spectra were subjected to a cosmic ray removal routine and baseline correction. The spatial distribution of PS and BTA-Methyl was determined using the tool “true component analysis” in the WITec Project FIVE 5.3 software.

**Crystallization system Crystal16.** Temperature-dependent turbidity measurements of aqueous BTA-Methyl solutions were determined optically for eight concentrations in parallel at a wavelength of  $\lambda = 645 \text{ nm}$  using the crystallization system Crystal16 (Technobis Crystallization Systems). Concentrations of 0.05, 0.10, 0.25, 0.50, 0.75, 1.00, 1.50 and 2.00 wt.% of BTA-Methyl in water were prepared at room temperature. The transmittance at  $\lambda = 645 \text{ nm}$  of each sample was recorded for two cycles in the range of 5 to 90 °C. Each cycle consists of a heating and cooling step with a scanning rate of  $0.5 \text{ K}\cdot\text{min}^{-1}$ .

**Micro-differential scanning calorimetry.** Micro-differential scanning calorimetry measurements were performed on a SETARAM Micro DSC III using sealed measuring cells (“batch cells”,  $V = 1 \text{ mL}$ , stainless steel) filled with about 0.7 mL of aqueous solution of the BTA-Methyl at a concentration of  $c = 0.05$  or 2.00 wt.%. The measurements were carried out applying a heating and cooling rate of  $0.5 \text{ K}\cdot\text{min}^{-1}$ . The reference cell was filled with an equal amount of water.

## Supporting Figures

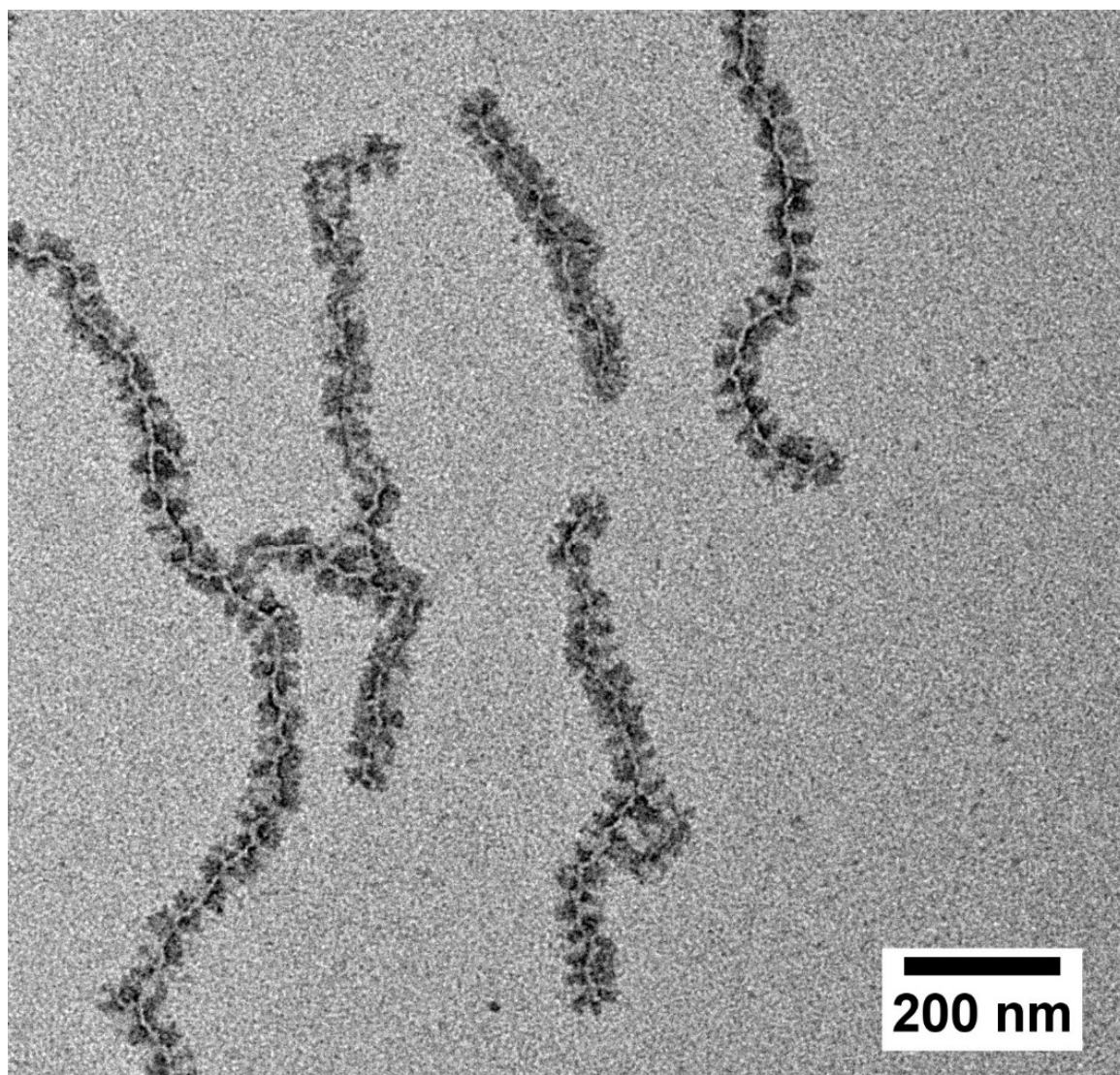


**Figure 5.S1.** TEM micrograph of patchy worm-like  $S_{33}E_{17}DMA_{50}^{132}$  micelles ( $c = 0.1 \text{ g}\cdot\text{L}^{-1}$  in THF). The micelles are composed of polyethylene (PE) as crystalline core and almost alternating corona patches of polystyrene (PS) and poly(*N,N*-dimethylaminoethyl methacrylamide) (PDMA). The polystyrene block was selectively stained with  $\text{RuO}_4$  and appears dark.

Temperature-dependent turbidity measurement of aqueous BTA-Methyl solution. Exemplarily, both heating and cooling cycles and the recorded transmittance for BTA-Methyl with a concentration of  $c = 2.0$  wt.% are shown in **Figure S5.2**. During heating and cooling all measured samples show a constant transmittance of 100% indicating that the BTA-Methyl remains dissolved during the measurements.

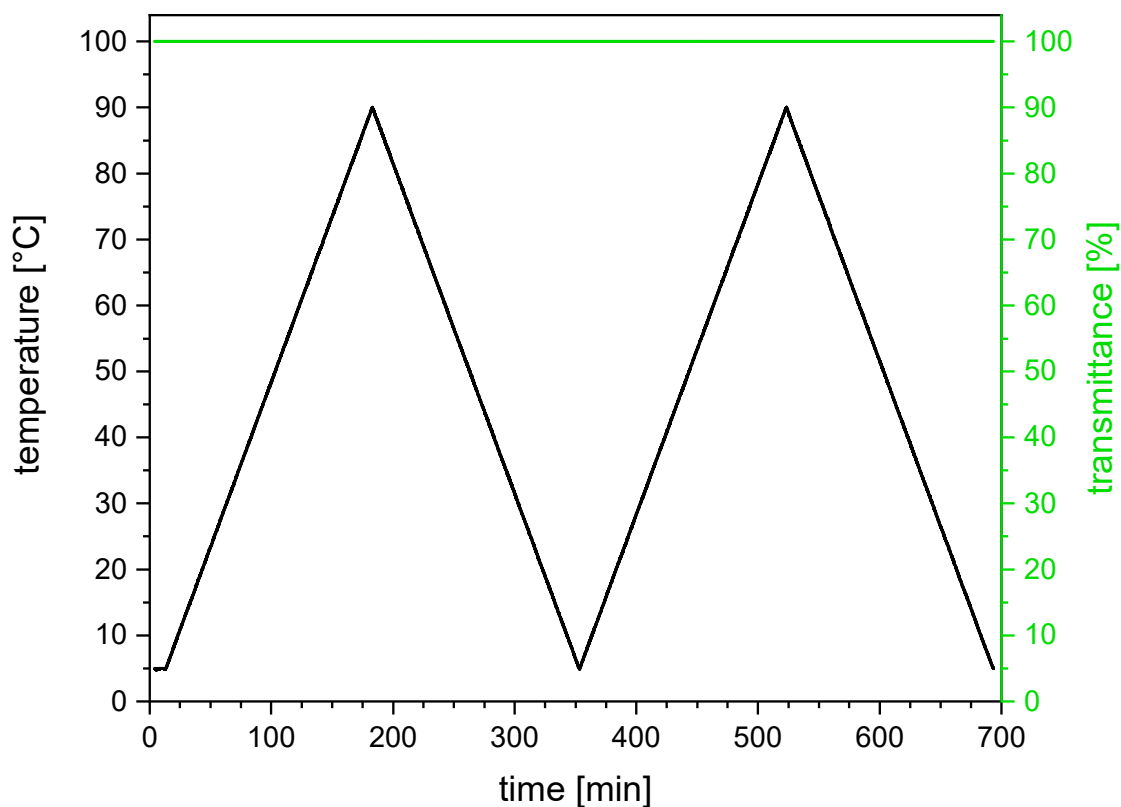


**Figure S5.2.** Temperature-dependent transmittance of a 2.00 wt.% aqueous BTA-Methyl solution upon subsequent heating and cooling cycles at a scanning rate of  $0.5 \text{ K} \cdot \text{min}^{-1}$ .

Exemplarily, the 2<sup>nd</sup> heating and 2<sup>nd</sup> cooling traces for the aqueous BTA-Methyl solution with a concentration of  $c = 2.00$  wt.% is shown in **Figure S5.3**. The same behaviour is observed for the 0.05 wt.% BTA-Methyl solution.

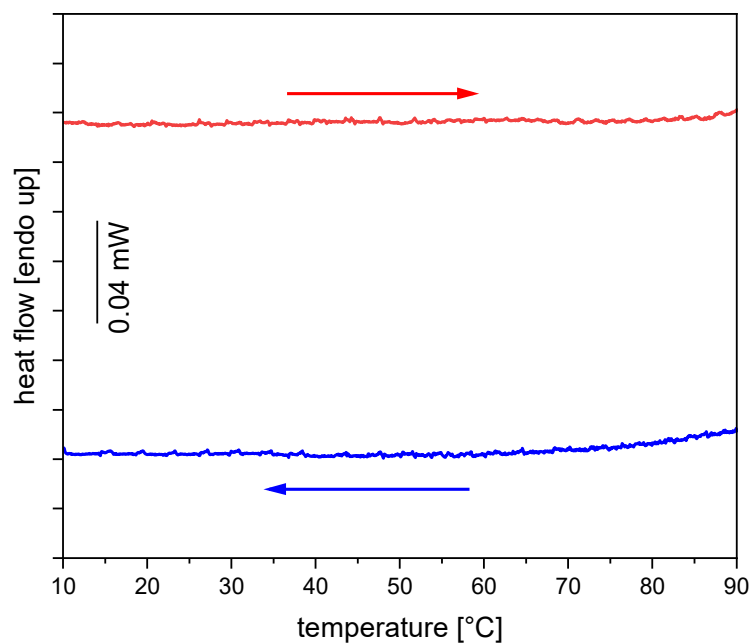


**Figure S5.3.** Micro-differential scanning calorimetry measurement of BTA-Methyl in water with a concentration of 2.00 wt.% at a scanning rate of  $0.5 \text{ K} \cdot \text{min}^{-1}$ .

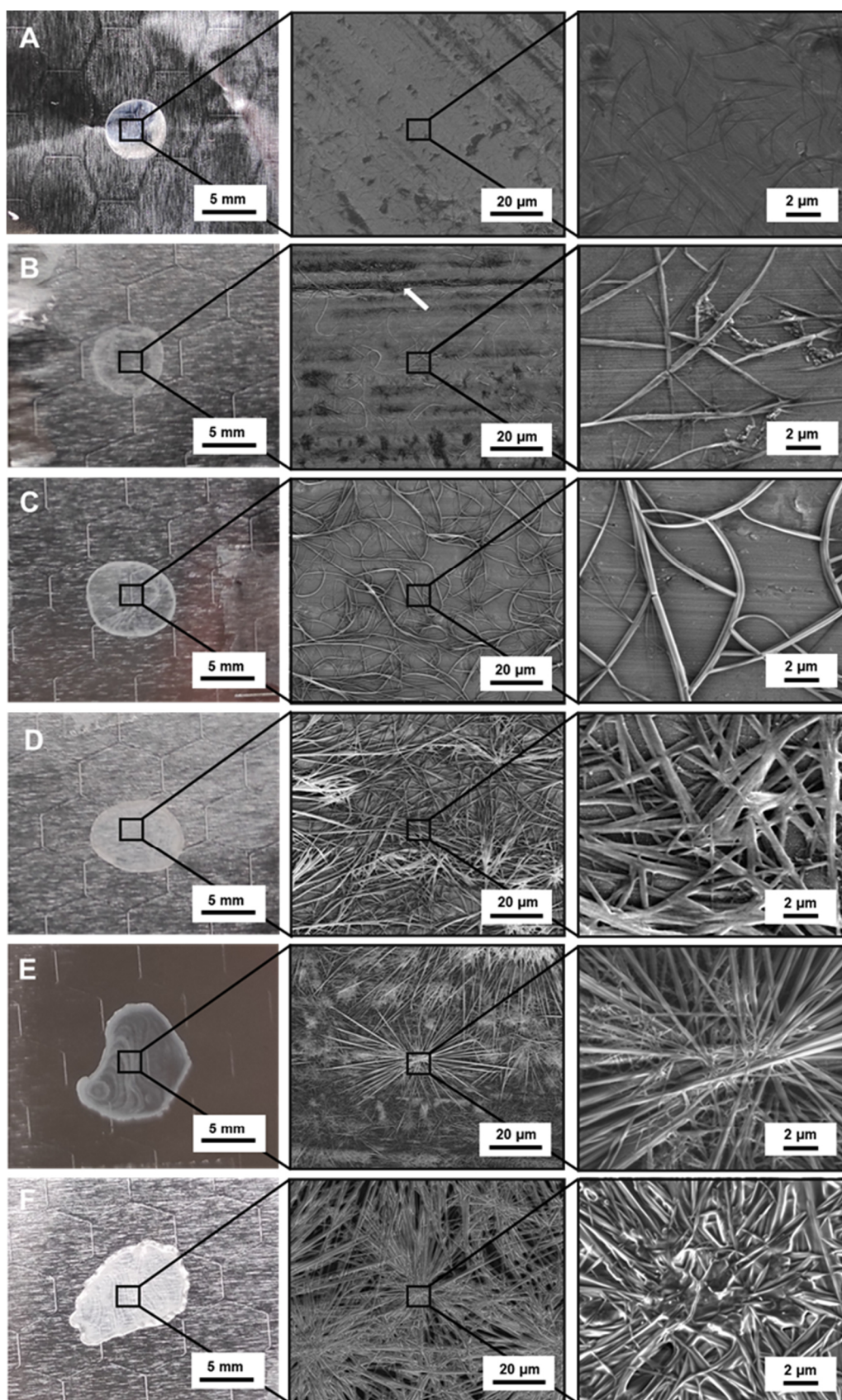


**Figure S5.4.** Optical (left) and scanning electron (middle and right with higher magnification) micrographs of the supramolecular fibres of BTA-Methyl prepared upon solvent evaporation from an A) 0.025 wt.% B) 0.050 wt.%, C) 0.100 wt.%, D) 0.250 wt.%, E) 0.500 wt.% and F) 1.000 wt.% aqueous solution onto aluminium foil.

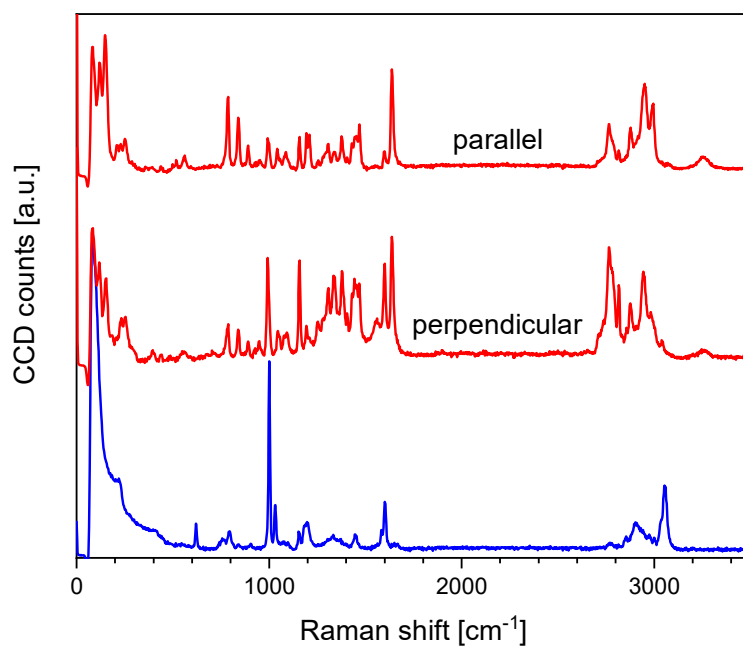


**Figure S5.5.** Raman measurements of polystyrene (blue) and a BTA-Methyl fibre (red) for polarization of the laser parallel and perpendicular to the self-assembled BTA-Methyl fibre long axis.

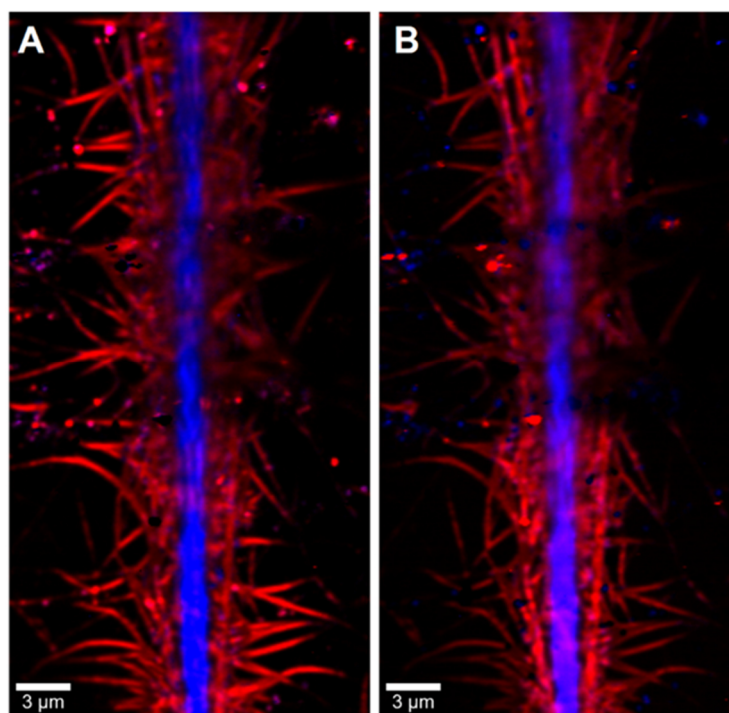


**Figure S5.6.** Spatially resolved component distribution from Raman imaging (horizontal polarization of the laser, PS rich regions are coloured in blue and BTA-Methyl rich in red), employing the Raman spectra of PS and BTA-Methyl for parallel and perpendicular orientation with respect to the laser polarization (Figure S5) in the true component analysis. As the Raman spectra of BTA-Methyl fibres depend on their orientation with respect to the laser polarization it is possible to extract the fraction of BTA-Methyl fibres being oriented parallel (A) and perpendicular (B) with respect to the laser, thus appearing more intense in the respective image.

## References

- [1] A. Frank, A. Bernet, K. Kreger, H.-W. Schmidt, *Soft Matter* **2020**, *16*, 4564.
- [2] J. Schmelz, M. Karg, T. Hellweg, H. Schmalz, *ACS Nano* **2011**, *5*, 9523.
- [3] C. Hils, M. Dulle, G. Sitaru, S. Gekle, J. Schöbel, A. Frank, M. Drechsler, A. Greiner, H. Schmalz, *Nanoscale Adv.* **2020**, *2*, 438.
- [4] J. Schöbel, C. Hils, A. Weckwerth, M. Schlenk, C. Bojer, M. C. A. Stuart, J. Breu, S. Förster, A. Greiner, M. Karg, H. Schmalz, *Nanoscale* **2018**, *10*, 18257.
- [5] J. Schmelz, D. Pirner, M. Krekhova, T. M. Ruhland, H. Schmalz, *Soft Matter* **2013**, *9*, 11173.
- [6] J. Schöbel, M. Burgard, C. Hils, R. Dersch, M. Dulle, K. Volk, M. Karg, A. Greiner, H. Schmalz, *Angew. Chem., Int. Ed.* **2017**, *56*, 405; *Angew. Chem.* **2017**, *129*, 416.
- [7] W.S., Rasband, ImageJ, U. S. National Institutes of Health, Bethesda, Maryland, USA, "<https://imagej.nih.gov/ij/>, 1997-2018".

## 6 Frustrated Microparticle Morphologies of a Semicrystalline Triblock Terpolymer in 3D Soft Confinement

Xuezhi Dai,<sup>1</sup> Xiaolian Qiang,<sup>2,3</sup> Christian Hils,<sup>4</sup> Holger Schmalz,<sup>4,5,\*</sup> and André H. Gröschel<sup>2,3,6,\*</sup>

<sup>1</sup> Physical Chemistry and Center for Nanointegration Duisburg-Essen (CENIDE), University of Duisburg-Essen, 47057 Duisburg, Germany

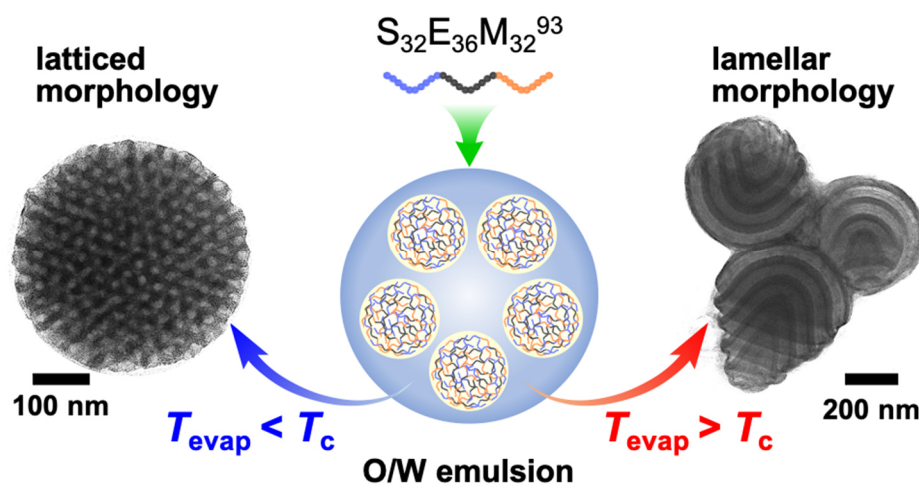
<sup>2</sup> Physical Chemistry, University of Münster, 48149 Münster, Germany

<sup>3</sup> Center for Soft Nanoscience (SoN), University of Münster, 48149 Münster, Germany

<sup>4</sup> Macromolecular Chemistry II, University of Bayreuth, 95440 Bayreuth, Germany

<sup>5</sup> Bavarian Polymer Institute, Universität Bayreuth, 95440 Bayreuth, Germany

<sup>6</sup> Center for Nanotechnology (CeNTech), University of Münster, 48149 Münster, Germany



Published in: *ACS Nano*, 2021, 15, 1111 – 1120

Reprinted with permission from ACS Publications.

## Abstract

Self-assembly of block copolymers (BCPs) in three-dimensional (3D) confinement of emulsion droplets has emerged as versatile route for the formation of functional micro- and nanoparticles. While the self-assembly of amorphous coil-coil BCPs is fairly well documented, less is known about the behaviour of crystalline-coil BCPs. Here, we demonstrate that confining a linear ABC triblock terpolymer with a crystallizable middle block in oil-in-water (O/W) emulsions results in a range of microparticles with frustrated inner structure originating from the conflict between crystallization and curved interfaces. Polystyrene-*block*-polyethylene-*block*-poly(methyl methacrylate) (PS-*b*-PE-*b*-PMMA, S<sub>32</sub>E<sub>36</sub>M<sub>32</sub><sup>93</sup>) in toluene droplets was subjected to different preparation protocols. If evaporation was performed well above the bulk crystallization temperature of the PE block ( $T_{\text{evap}} > T_c$ ), S<sub>32</sub>E<sub>36</sub>M<sub>32</sub><sup>93</sup> first microphase-separated into microparticles with lamella morphology followed by crystallization into a variety of frustrated morphologies (*e.g.*, bud-like, double staircase, spherocone). By evaporating at significantly lower temperatures that allow the PE block to crystallize from solution ( $T_{\text{evap}} < T_c$ ), S<sub>32</sub>E<sub>36</sub>M<sub>32</sub><sup>93</sup> underwent crystallization driven self-assembly into patchy crystalline-core micelles (CCMs), followed by confinement assembly into lenticular microparticles with compartmentalized hexagonal cylinder lattices. The frequency of these frustrated morphologies depends on polymer concentration and the evaporation protocol. These results provide a preliminary understanding of the morphological behaviour of semicrystalline block copolymers in 3D soft confinement and may provide alternative routes to structure multicompartment microparticles from a broader range of polymer properties

**KEYWORDS:** 3D confinement, block copolymers, crystallization, microparticles, microphase separation

## Introduction

Block copolymers (BCPs) have become an important part in nanotechnology and materials science due to their designable molecular structure and their ability to form precise nanostructures. So far, BCP nanostructures have predominantly been investigated in bulk (or melt), at interfaces and in dilute solution, which has brought about functional nanomaterials with promising application in, for instance, nanomedicine,<sup>1</sup> catalytic chemistry,<sup>2</sup> and optoelectronics.<sup>3–5</sup>

More recently, microphase separation of BCPs in the three-dimensional (3D) soft confinement of evaporating emulsion droplets has been adopted to create multicompart ment microparticles<sup>6–14</sup> and nanoparticles thereof.<sup>15–18</sup> While the morphology of amorphous BCPs in bulk mainly depends on the volume fraction of the blocks ( $\phi$ ), number of blocks (AB, ABC, ...) and their enthalpic interactions ( $\chi N$ ,  $\chi$  is the Flory Huggins interaction parameter and  $N$  the number of repeating units),<sup>19–22</sup> in 3D confinement the morphology is further controlled by the degree of confinement ( $D/L_0$ ; with drop diameter  $D$  and periodicity  $L_0$ ),<sup>23</sup> evaporation rate,<sup>24</sup> and the interfacial tension between blocks and the surfactant/water interface.<sup>25–27</sup> Many of these parameters have been investigated for amorphous coil-coil BCPs. The confining barrier of spherical droplets has a structure directing effect on the inner morphology of the microparticles, *i.e.*, BCPs develop frustrated microphases if  $D \approx L_0$ <sup>23</sup> or lamellae have a concentric orientation due to preferential interactions with the surfactant/water interface.<sup>28–30</sup> By lowering the contribution of interfacial tension (*e.g.*, by using surfactant mixtures),<sup>31</sup> the combination of enthalpic repulsion between blocks and their entropic relaxation may also dominate over the confining barrier leading to elliptic microparticles with axially stacked lamellae or strongly shape-anisotropic microparticle (*e.g.*, discs).<sup>25,32</sup>

Besides these external conditions, more evidence emerges that also the packing behaviour of the polymer chains themselves can become strong enough to overcome the confining geometry and thereby influence the final microparticle shape and morphology. For instance, densely grafted diblock polymer brushes<sup>33</sup> with relatively rigid backbones rapidly form dense packings. This packing has led to frustrated microparticles with pronounced surface features (terraces)<sup>34</sup> and highly anisotropic ellipsoids with photonic properties under strong confinement conditions<sup>35</sup> (in weak confinement polymer brushes remain photonic but microparticles are spherical).<sup>36</sup> Similarly, poly(ionic liquid)s with highly charged backbones were shown to form axially striped nanoparticles with only 50 nm diameter due to the liquid-crystalline-like

packing order in confinement.<sup>37</sup> Polypeptides with helical packing self-assembled into microparticles with 3D spiral morphology showing enantiomeric sorting.<sup>38</sup> We recently also showed that the shape and morphology of microparticles can be altered by directly introducing liquid-crystalline molecules into BCP morphologies *via* hydrogen bonding, whose tendency for dense packing caused chains to reorganize into frustrated morphologies in confinement.<sup>39</sup>

Despite these intriguing examples of internal ordering on microparticle shape, semicrystalline BCPs as the most obvious choice for dense and rigid chain packing have not been studied in 3D soft confinement of emulsion droplets.<sup>40</sup> Semicrystalline BCPs contain at least one crystallizable block (crystalline-coil BCPs)<sup>41</sup> and their morphological behaviour is known to exhibit distinct differences compared to coil-coil BCPs. The crystallization of BCPs into rigid structures is typically incompatible with curved substrates<sup>42</sup> resulting in frustrated morphologies. For the confinement assembly of semicrystalline BCPs, two limiting cases of structure formation need to be considered depending on the relation between the evaporation temperature of solvent ( $T_{\text{evap}}$ ) and the crystallization temperature of the crystallizable block ( $T_c$ ). In case of  $T_{\text{evap}} > T_c$ , the BCP morphology may form first inside the microparticle followed by crystallization, which is likely to relate to crystallization modes in bulk, *i.e.*, confined, templated, and breakout.<sup>43–51</sup> However, in case of  $T_{\text{evap}} < T_c$ , nucleation and growth of crystalline-core cylinders,<sup>52</sup> ribbons,<sup>53</sup> or platelets<sup>54</sup> may occur first due to crystallization-driven self-assembly (CDSA) in solution,<sup>55–67</sup> followed by confinement assembly of these preformed nanoparticles. To control the formation of microparticles from semicrystalline BCPs, it would therefore be important to develop a better understanding on the different parameters, like the crystallization pathway, evaporation temperature, and type of building block (molecularly dissolved chains or preformed micelles) that define the final morphology.

We herein describe the formation of microparticles from a linear polystyrene-*block*-polyethylene-*block*-poly(methyl methacrylate) triblock terpolymer (PS-*b*-PE-*b*-PMMA, S<sub>32</sub>E<sub>36</sub>M<sub>32</sub>)<sup>93</sup> with a crystallizable PE middle block by evaporation-induced confinement assembly (EICA). Microparticles with various lamellar morphologies or inner hexagonal lattice could be generated from the same terpolymer through different evaporation/crystallization routes, indicating the existence of a competition between microphase separation and crystallization within the spherical confinement of the emulsion droplets.

## Results and Discussion

**Thermal properties of the S<sub>32</sub>E<sub>36</sub>M<sub>32</sub><sup>93</sup> triblock terpolymer.** We first investigated the thermal properties of S<sub>32</sub>E<sub>36</sub>M<sub>32</sub><sup>93</sup> (subscripts denote the block fraction,  $f_S$ ,  $f_E$ , and  $f_M$ , in wt.-% and the superscript the overall number-average molecular weight,  $M_n$ , in kg·mol<sup>-1</sup>; see also Table S6.1 for details) in bulk and solution to define suitable temperature ranges for the confinement assembly. The PE block shows a peak melting temperature of  $T_m = 90$  °C and a peak crystallization temperature of  $T_c = 68$  °C in bulk, as determined by differential scanning calorimetry (DSC) measurements at a scanning rate of 10 K·min<sup>-1</sup> (Figure S6.1A). These melting and crystallization temperatures will become relevant for the behaviour of S<sub>32</sub>E<sub>36</sub>M<sub>32</sub><sup>93</sup> once all toluene has evaporated. Since toluene is a good solvent for PE in the molten state and acts as a plasticizer,<sup>68</sup> we analysed the crystallization temperature ( $T_{c, \text{solution}}$ ) of PE at varying S<sub>32</sub>E<sub>36</sub>M<sub>32</sub><sup>93</sup> concentrations in toluene to define the temperatures at which PE is expected to crystallize. Micro differential scanning calorimetry ( $\mu$ DSC) measurements are given in Figure S6.1B and the corresponding peak melting ( $T_{m, \text{solution}}$ ) and crystallization ( $T_{c, \text{solution}}$ ) temperatures are summarized in Table S6.2 and plotted in Figure 6.1 for S<sub>32</sub>E<sub>36</sub>M<sub>32</sub><sup>93</sup> concentrations between  $c_P = 1$  g·L<sup>-1</sup> - 500 g·L<sup>-1</sup>. According to this data, the melting temperature of the PE block is significantly decreased in toluene ( $T_{m, \text{solution}} = 51 - 66$  °C). Heating the terpolymer in toluene (or the emulsion) to 80 °C should therefore be sufficient to completely melt the PE block and, thus, to obtain molecularly dissolved S<sub>32</sub>E<sub>36</sub>M<sub>32</sub><sup>93</sup>. Once dissolved,  $T_{c, \text{solution}}$  will define the temperature at which the PE block starts to crystallize. Due to the increasing polymer concentration during toluene evaporation  $T_{c, \text{solution}}$  continuously rises from 26 °C ( $c_P = 1$  g·L<sup>-1</sup>) to 47°C ( $c_P = 500$  g·L<sup>-1</sup>), and reaches its maximum at  $T_c = 68$  °C. Hence, crystallization will not occur when toluene evaporation takes places at  $T_{\text{evap}} > T_c$ , while evaporation and crystallization will occur simultaneously at  $T_{\text{evap}} < T_c$ , with most pronounced effects expected at 30 °C. This allows to select between microphase separation taking place before crystallization and microphase separation occurring simultaneously with crystallization by proper choice of the evaporation temperature.

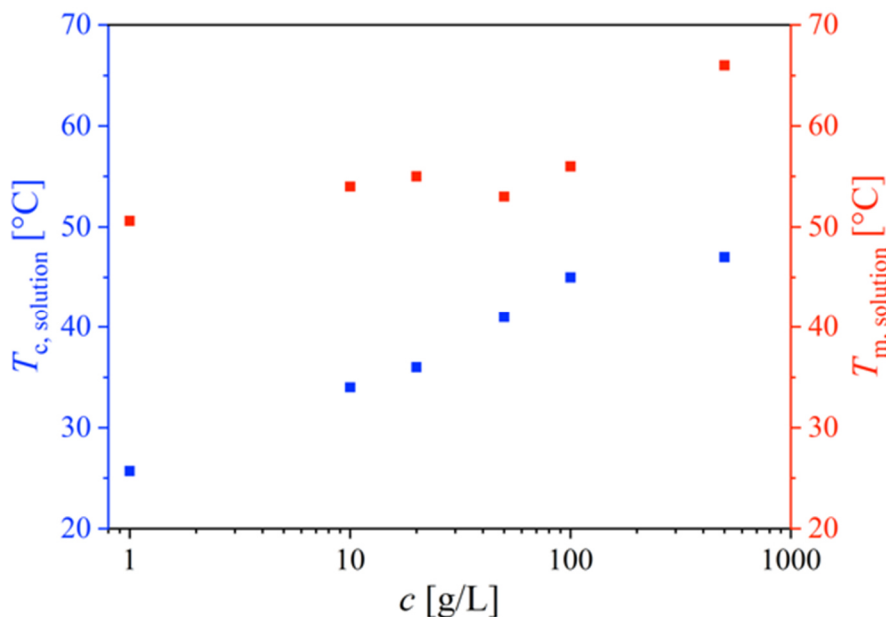


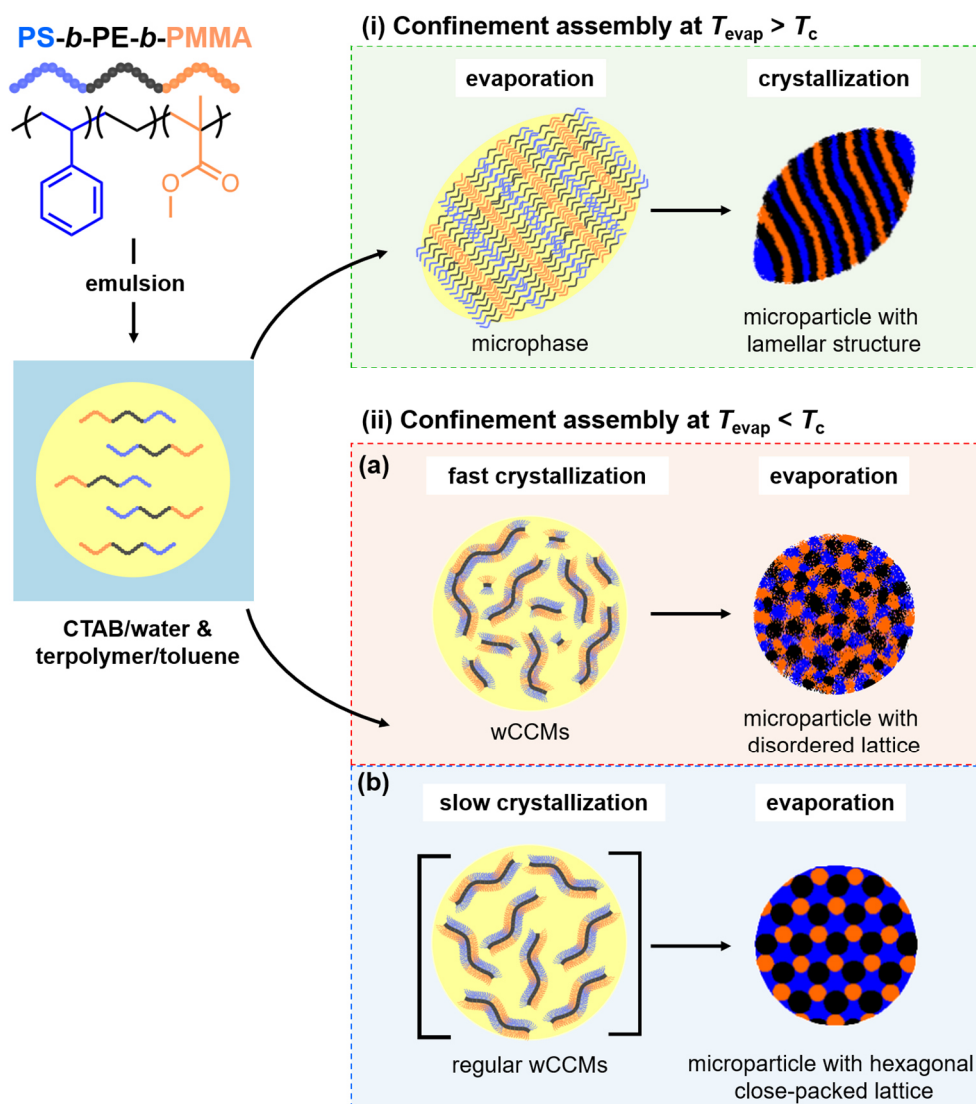
**Figure 6.1.** Peak crystallization ( $T_{c, \text{solution}}$ ) and melting ( $T_{m, \text{solution}}$ ) temperatures of the PE block with increasing polymer concentration as derived from  $\mu$ DSC measurements on  $S_{32}E_{36}M_{32}^{93}$  solutions in toluene (scanning rate:  $0.5 \text{ K} \cdot \text{min}^{-1}$ ).

**Routes for microparticle preparation.** Scheme 6.1 summarizes the general process to form microparticles of the  $S_{32}E_{36}M_{32}^{93}$  triblock terpolymer *via* evaporation-induced confinement assembly. For all routes, the polymer solution with a starting concentration of  $c_P = 1 \text{ g} \cdot \text{L}^{-1}$  or  $c_P = 10 \text{ g} \cdot \text{L}^{-1}$  in toluene was heated to  $80 \text{ }^\circ\text{C}$  for at least 2 h, which is well above the melting temperature of the PE block in toluene ( $T_{m, \text{solution}} < 66 \text{ }^\circ\text{C}$ , Table S6.2). This annealing step eliminated any thermal history and gave a homogeneous solution of molecularly dissolved terpolymer chains. The polymer solution was then emulsified with an aqueous cetyltrimethylammonium bromide (CTAB,  $c_S = 10 \text{ g} \cdot \text{L}^{-1}$ ) solution at  $80 \text{ }^\circ\text{C}$  by vortex mixing for 1 min. Microparticles were formed according to two different evaporation/crystallization protocols:

- (i) *Confinement assembly at  $T_{\text{evap}} > T_c$  – evaporation first:* The emulsion was first evaporated at  $T_{\text{evap}} = 80 \text{ }^\circ\text{C}$  for 4 h, where PE is not able to crystallize, followed by annealing at  $T < T_c$  for 48 h to induce crystallization of the PE block within the preformed microphase-separated microparticles. This route resembles the classical confinement assembly of amorphous BCPs into microparticles.
- (ii) *Confinement assembly at  $T_{\text{evap}} < T_c$  – crystallization first:* The emulsion was first cooled from  $80 \text{ }^\circ\text{C}$  to  $T_{\text{evap}} < T_c$ , which should induce CDSA of  $S_{32}E_{36}M_{32}^{93}$  into worm-like

crystalline-core micelles (wCCMs) prior to toluene evaporation. This route is related to colloidal aggregation of preformed wCCMs with different average lengths.

**Scheme 6.1.** Schematic illustration of two different routes for the 3D confinement self-assembly of  $S_{32}E_{36}M_{32}^{93}$ .<sup>a</sup>



<sup>a</sup> Emulsification of  $S_{32}E_{36}M_{32}^{93}$  in toluene with CTAB/water followed by two evaporation/crystallization protocols: (i) Confinement assembly at  $T_{\text{evap}} > T_c$  – evaporation first. (ii) Confinement assembly at  $T_{\text{evap}} < T_c$  – crystallization first.

**Confinement assembly at  $T_{\text{evap}} > T_c$  – Evaporation first.** Having confirmed the thermal properties of  $S_{32}E_{36}M_{32}^{93}$ , we applied conditions where microphase separation occurs in confinement prior to PE crystallization. The  $S_{32}E_{36}M_{32}^{93}$  triblock terpolymer has comparable weight fractions of the different blocks,  $f_{\text{PS}} \approx f_{\text{PE}} \approx f_{\text{PMMA}}$ , and forms a lamella-lamella (*ll*)-morphology in bulk. The transmission electron microscopy (TEM) micrograph in Figure S6.2 shows the cross-section of a  $S_{32}E_{36}M_{32}^{93}$  film cast from toluene at  $T_{\text{evap}} = 70$  °C, *i.e.*, above the crystallization temperature of the PE middle block ( $T_c = 68$  °C). Toluene was chosen as the least selective solvent with comparable solubility parameters to PS, PMMA, and PE ( $\delta_{\text{PS}} = 18.5 \text{ MPa}^{1/2}$ ,  $\delta_{\text{PE}} = 17.0 \text{ MPa}^{1/2}$ ,  $\delta_{\text{PMMA}} = 19.0 \text{ MPa}^{1/2}$ , and  $\delta_{\text{toluene}} = 18.3 \text{ MPa}^{1/2}$ ).<sup>69,70</sup> At 70 °C, microphase separation first led to a *ll*-morphology, where the molten PE lamellae are sandwiched in between the PS and PMMA lamellae. Upon cooling, the PE block crystallized within the confinement of the *ll*-morphology thereby retaining the morphology.

For confinement assembly, a  $S_{32}E_{36}M_{32}^{93}$ /toluene solution was heated to 80 °C, emulsified with the aqueous CTAB solution at 80 °C, and toluene evaporated at  $T_{\text{evap}} = 80$  °C for 4 h. After  $S_{32}E_{36}M_{32}^{93}$  formed amorphous microparticles, the dispersion was cooled to 30 °C for crystallization, and microparticles were analysed with TEM and scanning electron microscopy (SEM). For a  $c_P = 10 \text{ g}\cdot\text{L}^{-1}$ , microparticles generally had a larger diameter of  $D = 600\text{-}800 \text{ nm}$ , while they were smaller ( $D = 100\text{-}300 \text{ nm}$ ) at  $c_P = 1 \text{ g}\cdot\text{L}^{-1}$  due to the overall lower polymer mass content. In both cases, about 95 % of microparticles contained a *ll*-morphology with a variety of different orientations.

A  $S_{32}E_{36}M_{32}^{93}$  microparticle with axially stacked *ll*-morphology (pupa-like) is exemplified in Figure 6.2A. Here, the PS/PE/PMMA lamellae are essentially 2D discs that are stacked in axial direction giving the microparticles a strongly anisotropic, prolate ellipsoid shape (aspect ratios were typically  $\alpha > 2$ ). The polymer microdomains can be distinguished based on their contrast: PS appeared darkest due to  $\text{RuO}_4$  staining, while PE and PMMA had close to identical contrast. Still, PE can be distinguished from PMMA by thin dark lines, as the staining agent preferentially accumulated at microdomain interfaces. Since evaporation of toluene took place at 80 °C, the PE block of  $S_{32}E_{36}M_{32}^{93}$  formed an amorphous PE lamella first, followed by confined crystallization of the PE block within the *ll*-morphology upon cooling the dispersion below the crystallization temperature of PE (here 30 °C).<sup>43,50</sup> In order to form pupa-like microparticles, all three polymer blocks need to locate at the CTAB/water interface. Based on the solubility parameters ( $\delta_{\text{PS}} = 18.5 \text{ MPa}^{1/2}$ ,  $\delta_{\text{PMMA}} = 19.0 \text{ MPa}^{1/2}$ ), PS and PMMA should have similar affinities to the CTAB/water interface. Since the PE middle block is covalently linked

to the PS/PMMA end blocks, PE likewise has to locate at the interface irrespective of its compatibility. In addition, it was previously shown on other BCPs that CTAB lowers the interfacial tension for each block to comparable values, increasing the probability for all blocks to share the interface.<sup>25</sup> Further, kinetic aspects need to be considered that contribute to axial lamellae, as fast solvent evaporation at 80°C will cause fast collapse of terpolymers chains at the interface, preventing rearrangement into concentric lamella (onion-like particles).<sup>24</sup>

Crystallization also influenced the microparticle surface as can be seen on the pronounced corrugations and necking at the PE/PMMA microphases attributed to the contraction of PE during crystallization. Although PMMA experiences *e*-beam damage during imaging, which contributes to shrinking of the PMMA microdomain, such strong surface corrugation was not observed for microparticles formed by polystyrene-*block*-polybutadiene-*block*-poly(methyl methacrylate) (SBM) triblock terpolymers.<sup>17,27</sup> Since SBM is the precursor polymer for the synthesis of S<sub>32</sub>E<sub>36</sub>M<sub>32</sub><sup>93</sup> (hydrogenation of PB to PE), the main difference is the crystallizable PE block.

Another difference to amorphous BCPs is the preference of the crystalline PE block to form planar structures with high bending rigidity. The conflict between growth of the crystalline microdomain and the curved confining barrier of the ellipsoidal particle resulted in slightly twisted PE lamellae in some cases that cannot connect in-plane to form a complete PE disc. Instead, this offset created dislocations as visible in Figure 6.2B. Dislocations are common in rigid, crystalline lattices, but have not been observed before for in confinement assembly of BCPs. The PS lamellae share a direct interface with the PMMA lamella at these dislocations, which is uncommon as both microdomains are usually separated by a PE layer. If the pitch, *p*, of these twisted PE lamellae matched the distance to the next PE lamella after one revolution (here *p* = 55 nm), lamellae were able to connect into a helical screw spiralling from ellipsoid pole to pole (Figure 6.2C). This helical progression of lamellae is likewise attributed to the peculiar behaviour of crystalline BCPs in confinement. In addition to this helical screw, we identified double helical spirals in several cases (Figure 6.2D) for which the 3D arrangement of the microdomains is rather puzzling and difficult to understand through mere TEM projection imaging.

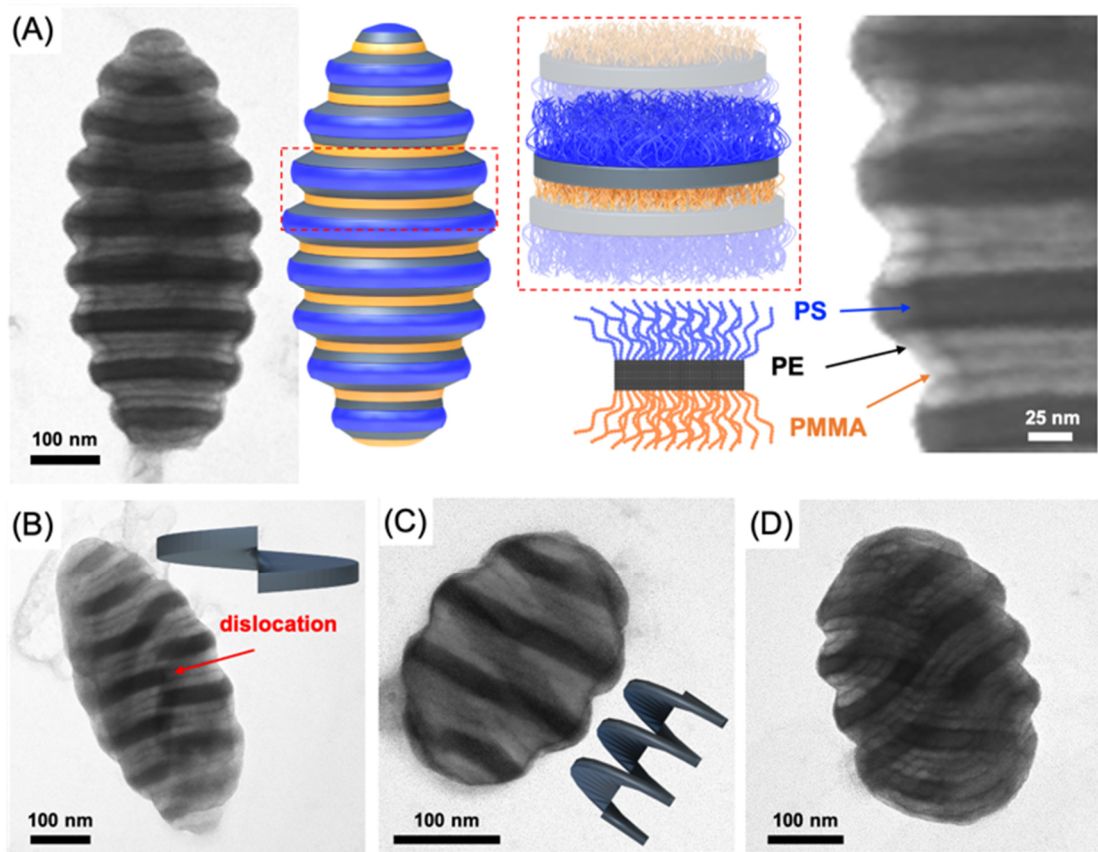


**Figure 6.2.** Lamella morphologies of  $S_{32}E_{36}M_{32}^{93}$  through evaporation at  $T_{\text{evap}} > T_c$ . (A) TEM image of prolate ellipsoid microparticle with axially stacked lamellae of PS/PE/PMMA; TEM inset and schematics clarifying the arrangement of polymer chains (PS domains appear dark due to  $\text{RuO}_4$  staining). (B)  $ll$ -morphology with dislocations. (C) Helical spiral morphology, and (D) double helical spiral morphology.

In order to get more information about the double spiral morphology, we analysed a representative particle with TEM tomography (Figure 6.3). For that, images were taken at varying tilt angles in a tilt angle range of  $\alpha = \pm 69^\circ$  with  $3^\circ$  increments. Figure 6.3A shows selected images of the tilt-series at  $\alpha = +47.6^\circ$ ,  $\alpha = -0.9^\circ$ , and  $\alpha = -49.4^\circ$ . Figure 6.3B illustrates the double spiral progression of the PS, PE and PMMA lamellae at the one pole of the ellipsoid. The dark PS lamella is most visible and connected into a 3D Fermat spiral noticeable on the twists, where the lamella bends twice around two  $+1/2$  disclinations in an  $180^\circ$  angle (blue in Figure 6.3C). Since the PE lamellae are adjacent to PS, they likewise formed a 3D Fermat spiral (black in Figure 6.3C). The PMMA lamella on the other hand exhibited two terminal points coinciding with two  $+1$  disclinations resembling 3D Archimedean spirals that are not connected (orange in Figure 6.3C). Overall, the combination of these defects satisfies the Gauss-Bonnet theorem of topology describing the defect strength

for spherical (or ellipsoidal) objects ( $\chi = +2$ ). Since the microdomains are not solely located on the surface, but span across the entire core as lamella (or helical screws) they have to perfectly fit into each other to create this intriguing structure.

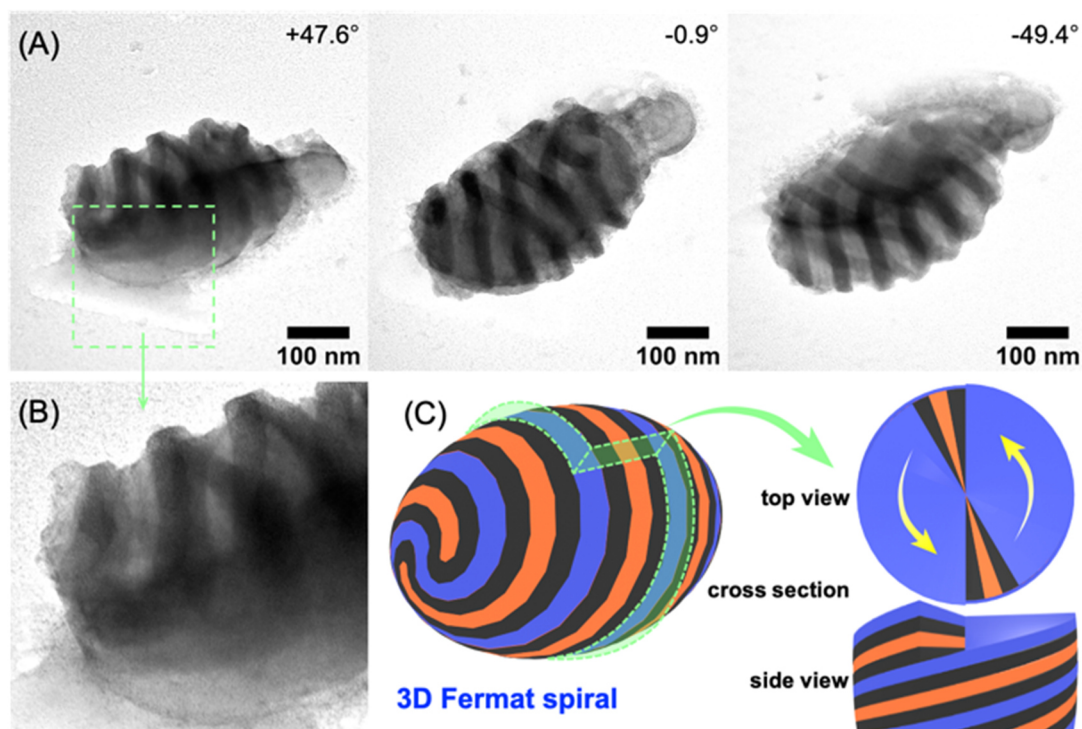


**Figure 6.3.** TEM tilt series of double spiral lamellar morphology. (A) Selected TEM tilt series images and (B) close-up showing the twisting of the PS/PE lamellae and the terminal points of the PMMA lamella (PS appears dark due to RuO<sub>4</sub> staining). (C) Schematic clarifying the microdomain orientation on the ellipsoid surface as well as their progression on the inside.

Aside from these axially-directed lamellae, we also identified a range of other coexisting *ll*-orientations that are more severely influenced by the curved confinement (Figure 6.4). For instance, Figure 6.4A shows a bud-like microparticle, which essentially is a hemisphere with concentric lamellae cut in half, while there can be a pronounced stacking of hemispherical shells as seen in the SEM. These bud-like microparticles have been observed for amorphous BCPs in confinement as intermediate morphology during structural transitions between axial lamellae and concentric lamellae (*e.g.*, thermal or solvent annealing) or at specific evaporation rates.<sup>12,24,71</sup> Recently, we also observed this morphology for SBM triblock terpolymers with equal-sized end blocks during solvent-adsorption annealing<sup>27</sup> as well as for polystyrene-*block*-polybutadiene-*block*-poly(*tert*-butyl methacrylate) triblock terpolymers.<sup>18</sup> The morphology is interesting in the sense that it allows the formation of cup-shaped nanoparticles after cross-

linking of one hemispherical lamella and redispersion in a common solvent. A variation of the bud-like morphology is shown in Figure 6.4B, where the bottom part still is partially a hemisphere, but the top part is a concentric spiral lamella. The spiral-like winding is better visible in the TEM, while SEM only shows the outermost layer of the spiral appearing as a smooth surface.

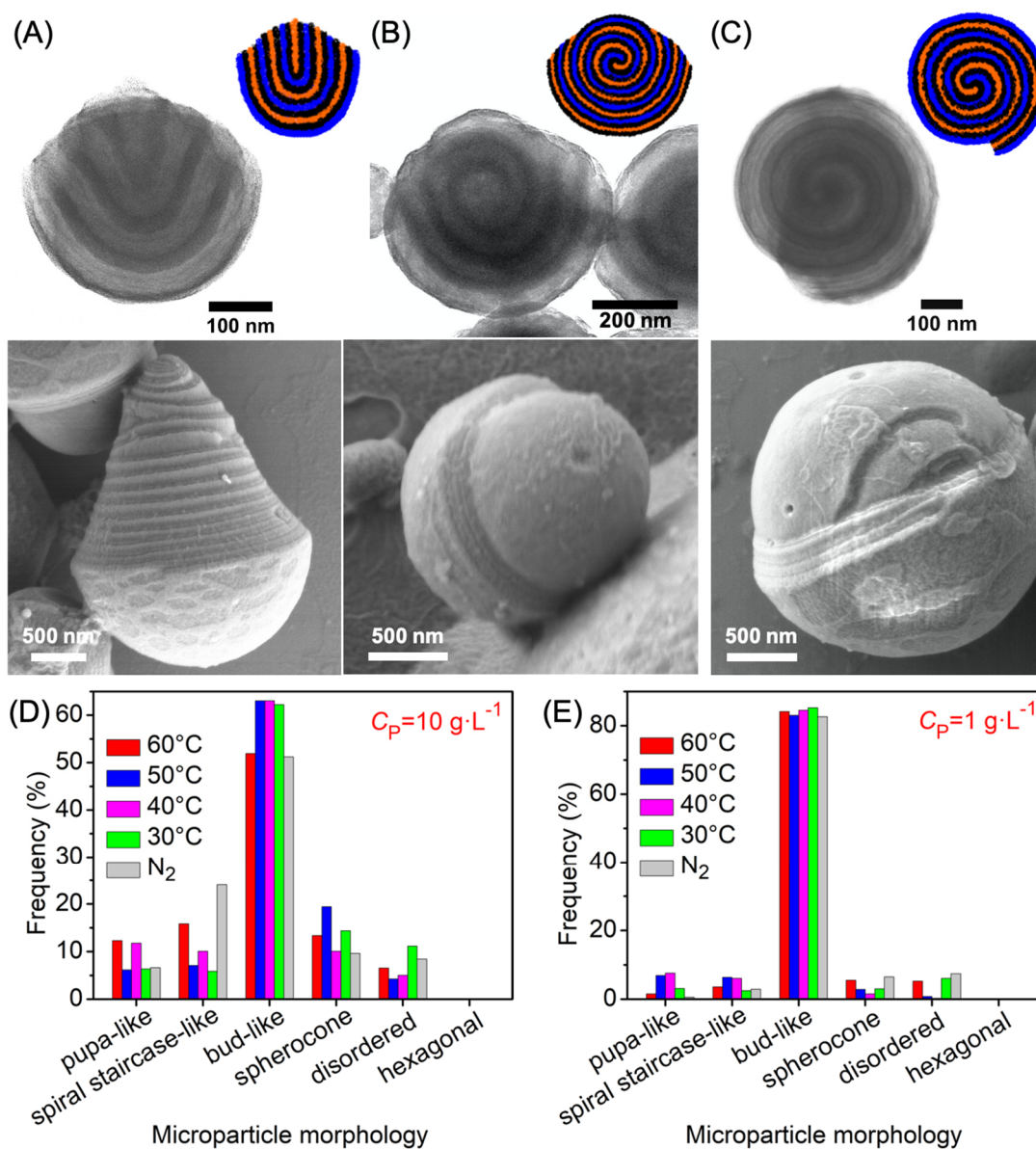


**Figure 6.4.** Evaporation first followed by crystallization at varying temperatures. TEM and SEM images of (A) bud-like, (B) hemisphere/helix, and (C) spherocone morphology. (D, E) Frequency distributions of morphologies at different crystallization temperatures for  $c_P = 10 \text{ g}\cdot\text{L}^{-1}$  in (D) and  $c_P = 1 \text{ g}\cdot\text{L}^{-1}$  in (E).

We also observed complete 3D spherical spiral lamellae in moderate frequency that could be best described as a fully developed spherocone structure (Figure 6.4C).<sup>72</sup> Instead of a closed concentric lamellae, the *ll*-microdomain progresses as one continuous spherical spiral from the centre of the microparticle to the periphery, thereby enveloping the preceding *ll*-microdomains after each revolution. The surface of these spherical microparticles mainly consist of the PS lamella, yet, with a clearly visible fissure in SEM, where the three edges of the PS/PE/PMMA lamella are seen. Spherocoines are complex 3D arrangements and bare similarity to structures found in biomineralization processes (*e.g.*, sea shells).<sup>72</sup> There, soft matter scaffolds direct the growth of crystalline minerals and the conflict between curved soft boundaries and planar crystallization gives rise to a variety of non-trivial 3D structures such as the spherocone. The morphology in Figure 6.4C likely formed due to an incompatibility of the growing rigid PE lamellae along the curved boundary of the ellipsoidal microparticle. The energetic penalty for bending PE lamellae could also explain why the classical onion-like microparticles with radial-symmetric concentric lamella were not observed. In onion-like microparticles, the curvature increases stepwise for each concentric lamella from periphery (lowest) to the particle core (highest). This stress concentration in the core becomes more unfavourable the higher the bending rigidity of the lamellae is. This unfavourable bending energy is alleviated to some extent by forming the spherocone morphology with a less abrupt but more gradual change in curvature.

Figure 6.4D summarizes the frequency distributions obtained by counting more than 200 microparticles of the observed morphologies for  $c_P = 10 \text{ g}\cdot\text{L}^{-1}$  at different crystallization temperatures, *i.e.*, 60 °C, 50 °C, 40 °C and 30 °C as well as a reference sample that was directly frozen in liquid nitrogen after toluene evaporation at 80 °C to prevent any further structural reorganization (denoted as N<sub>2</sub>). Respective TEM overview images of the formed microparticles are summarized in Figure S6.3. We found that the frequency of the morphologies did not change noticeably irrespective of the crystallization temperature, supporting the assumption that microphase separation into the *ll*-morphology with molten PE lamellae had occurred first, followed by confined crystallization of PE. The bud-like microparticles were rather frequent with about 50-60 % as compared to other morphologies averaging at 10-15% (including 10% disordered). There was however a drastic change in frequency for all morphologies by reducing the polymer concentration to  $c_P = 1 \text{ g}\cdot\text{L}^{-1}$ , where bud-like particles became much more prominent with > 85% (Figure 6.4E). Nevertheless, ordered lamellae (pupa-like, spiral staircase-like, bud-like, and spherocone) are the dominant morphology with 89% and 93% for  $10 \text{ g}\cdot\text{L}^{-1}$  and  $1 \text{ g}\cdot\text{L}^{-1}$ , respectively, confirming that under these conditions microphase

separation is the structure directing force and not crystallization. However, the evaluation of the microparticle size distribution (Table S6.3) did not provide any obvious correlation between microparticle size and morphology.

**Confinement assembly at  $T_{\text{evap}} < T_c$  – Crystallization first.** According to the  $\mu$ DSC data, the  $T_{c, \text{solution}}$  of PE is 34 °C for a polymer solution with  $c_P = 10 \text{ g}\cdot\text{L}^{-1}$  (Figure 6.1, Table S6.2). We therefore assumed a substantially different assembly behaviour of  $\text{S}_{32}\text{E}_{36}\text{M}_{32}^{93}$  at 30 °C as compared to amorphous BCPs that would lead to deviations from the expected *ll*-morphology. The as-prepared  $\text{S}_{32}\text{E}_{36}\text{M}_{32}^{93}$ /toluene solution at 80 °C was cooled to 5 °C and annealed for 10 min in order to induce CDSA of  $\text{S}_{32}\text{E}_{36}\text{M}_{32}^{93}$  into wCCMs. The wCCM dispersion was emulsified with an aqueous CTAB solution at 30 °C and toluene was evaporated at  $T_{\text{evap}} = 30 \text{ °C}$  over the course of 4 days, *i.e.*, well below the melting temperature of the PE block in toluene ( $T_{m, \text{solution}} = 54 \text{ °C}$ , Figure 6.1, Table S6.2). From the TEM and SEM images in Figure 6.5A and B, it becomes evident that this process exclusively resulted in microparticles with a somewhat microphase-separated interior but without recognizable order. This can be attributed to the formation of polydisperse wCCMs during crystallization at 5 °C prior to emulsification and evaporation.<sup>56,60</sup> TEM of the cooled  $\text{S}_{32}\text{E}_{36}\text{M}_{32}^{93}$  solution before emulsification confirmed the presence of wCCMs with an average length of  $L_n = 300 \pm 50 \text{ nm}$ , a PE core with a width of  $10 \pm 3 \text{ nm}$ , and a patchy PS/PMMA corona (both are  $10 \pm 3 \text{ nm}$  in diameter) (Figure S6.4). By crystallizing the BCP prior to evaporation, wCCMs formed first, and confinement assembly during evaporation is more related to the packing of preformed wCCMs in confinement than to microphase separation of BCPs. Since the wCCMs grew rather fast and uncontrolled into polydisperse worm-like micelles, they merely entangled into spherical bundles with the observed distorted structure. This is in stark contrast to the evaporation first route. However, heating a preformed wCCM solution to 80 °C, followed by evaporation of toluene and rapid cooling to 30 °C for PE crystallization, we again exclusively obtained microparticles with a lamellar inner structure (Figure S6.5). Heating the emulsion to 80 °C erased the thermal history of  $\text{S}_{32}\text{E}_{36}\text{M}_{32}^{93}$ , *i.e.*, the preformed wCCMs “have molten”, which led to the same starting conditions as for the evaporation first route. This path dependence confirms our results discussed before. It is worth noting that bud-like microparticles were obtained in even higher fractions ( $> 97 \%$ ) using the heated wCCM dispersion ( $c_P = 1 \text{ g}\cdot\text{L}^{-1}$ ) as compared to the direct evaporation first route. We hypothesize that the high interfacial activity of patchy wCCMs<sup>73</sup> may have reduced the size of the emulsion droplets, which in turn affects evaporation rate and fosters growth of bud-like particles.<sup>24</sup>

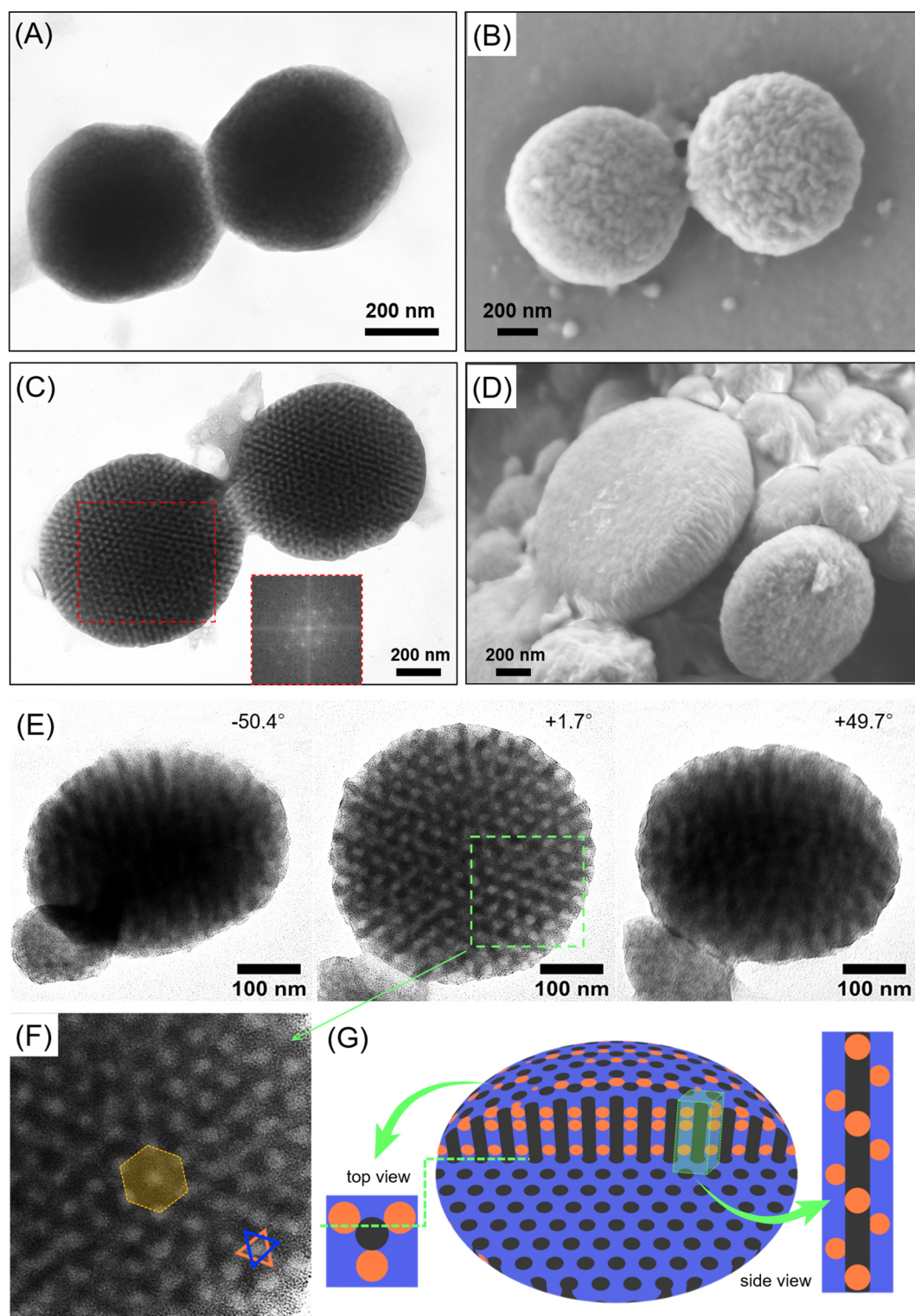


**Figure 6.5.** Crystallization first at varying evaporation temperatures ( $c_P = 10 \text{ g}\cdot\text{L}^{-1}$ ). (A, B) TEM and SEM image of disordered  $S_{32}E_{36}M_{32}^{93}$  microparticles after crystallization at  $5^\circ\text{C}$  and emulsification/evaporation at  $30^\circ\text{C}$ . (C, D) TEM and SEM image of hexagonally ordered  $S_{32}E_{36}M_{32}^{93}$  microparticles after cooling the emulsion from  $80^\circ\text{C}$  to  $30^\circ\text{C}$ , followed by simultaneous crystallization and evaporation at  $30^\circ\text{C}$ . (E) TEM tilt series images, tilt angles are as marked in the images. (F) Close-up showing the three microphases of PS, PE and PMMA (PS domains appear dark due to  $\text{RuO}_4$  staining). (G) Schematic clarifying the packing of the blocks.

We then considered to slow down the crystallization of  $S_{32}E_{36}M_{32}^{93}$  to obtain better defined wCCMs. We heated and emulsified the  $S_{32}E_{36}M_{32}^{93}$  solution ( $c_P = 10 \text{ g}\cdot\text{L}^{-1}$ ) at  $80 \text{ }^\circ\text{C}$ , followed by direct quenching to  $30 \text{ }^\circ\text{C}$  and immediate evaporation, *i.e.*, just below  $T_{c, \text{solution}} = 34 \text{ }^\circ\text{C}$ . As a result, the PE blocks crystallized slowly into patchy wCCMs<sup>60</sup> accompanied by simultaneous slow evaporation of toluene and confinement assembly. After evaporation, less than 4 % of the microparticles were lamellar, supporting the crystallization pathway. However, in addition to the disordered microparticles, a considerable fraction of particles ( $\sim 34\%$ , Figure S6.5) exhibited a highly ordered hexagonal close-packed lattice with an overall lenticular shape (Figure 6.5C and D). Figure 6.5E shows a TEM tilt-series of an oblate ellipsoidal microparticle with hexagonal ordered lattices at tilt angles of  $\alpha = -50.4^\circ$ ,  $\alpha = +1.7^\circ$ , and  $\alpha = +49.7^\circ$ . These microparticles most likely consisted of a close-packed lattice of patchy wCCMs with crystalline PE cores that formed during evaporation. This arrangement is highly interesting as the matrix must consist of two immiscible polymers, PS and PMMA, which suggests that the matrix itself should be ordered as well. On closer inspection of the inner structure (Figure 6.5F), it is noticeable that the central PE core ( $12 \pm 2 \text{ nm}$  in diameter) of the CCMs is surrounded by somewhat triangular distributed PS/PMMA microdomains, likely originating from the corona patches of the wCCMs. A tilting series video further confirmed this hexagonally packed morphology as schematically shown in Figure 6.5G.

This morphology was exclusively found for  $c_P = 10 \text{ g}\cdot\text{L}^{-1}$  at  $T_{\text{evap}} = 30 \text{ }^\circ\text{C}$ . For  $c_P = 1 \text{ g}\cdot\text{L}^{-1}$ , the crystallization temperature of the PE block in solution is below the evaporation temperature ( $T_{c, \text{solution}} = 26 \text{ }^\circ\text{C}$ ) and the formation of patchy wCCMs is hindered. Cooling the emulsion directly from  $80 \text{ }^\circ\text{C}$  to  $T_{\text{evap}} = 40 \text{ }^\circ\text{C}$ ,  $50 \text{ }^\circ\text{C}$ , and  $60 \text{ }^\circ\text{C}$ , no hexagonal close-packed lattice was observed, while the fraction of *ll*-morphologies discussed for the evaporation first route continuously increased (see frequency distributions and TEM overview images in Figure S6.6). Bud-like microparticles were obtained with 47% and 93% for  $c_P = 10 \text{ g}\cdot\text{L}^{-1}$  and  $1 \text{ g}\cdot\text{L}^{-1}$  at  $60 \text{ }^\circ\text{C}$ . This is reasonable, as for  $T_{\text{evap}} > 40 \text{ }^\circ\text{C}$  the PE block is not able to crystallize at the initial  $c_P$  (compare Figure 6.1). Evaporation will occur first, followed by slow crystallization of PE when the critical concentration for crystallization in toluene is reached, *e.g.*,  $c_{\text{critical}} = 50 \text{ g}\cdot\text{L}^{-1}$  for  $T_{c, \text{solution}} = 40 \text{ }^\circ\text{C}$  (Table S6.2). This effect was more pronounced for a higher  $T_{\text{evap}}$  and lower initial  $c_P$ . At  $T_{\text{evap}} = 60 \text{ }^\circ\text{C}$ , microparticles with a lamellar structure are almost exclusively formed, since the PE block is not able to crystallize irrespective of concentration.<sup>44,45</sup> These trends in the frequency distributions of microparticle morphologies at different evaporation temperature are in good agreement with our previous hypothesis and underline the existence of two fundamentally different structure-formation routes. Increasing  $T_{\text{evap}}$  systematically

accelerated solvent evaporation, while slowing down or inhibiting crystallization of PE. Accordingly, the structure-directing process gradually changed from crystallization to microphase separation.

**Confined microphase separation versus crystallization.** In order to summarize the above results, the morphologies and their frequencies of  $S_{32}E_{36}M_{32}^{93}$  microparticles using two different evaporation/crystallization protocols but with the same  $T_{\text{evap}} = 30\text{ }^{\circ}\text{C}$  are given in Figure 6.6. Figure 6.6A-C displays the TEM overview images of  $S_{32}E_{36}M_{32}^{93}$  microparticles with disordered inner structure (A) and hexagonal close-packed lattice (B) formed through the “crystallization first” protocol based on wCCMs, while lamellar structures (C) formed through the “evaporation first” protocol based on molecularly dissolved triblock terpolymers. The corresponding frequency distributions of the microparticle morphologies are summarized in Figure 6.6D. The “crystallization first” route with less defined wCCMs (red) led to 100 % microparticles with disordered structure for both polymer concentrations. CDSA of wCCMs with simultaneous evaporation (blue) resulted in more than 96 % microparticles with disordered (63 %) and hexagonal (33 %) structure for  $c_P = 10\text{ g}\cdot\text{L}^{-1}$ . On the other hand, the “evaporation first” protocol (green) provided 89% and 93% microparticles with lamella structure (pupa-like, spiral staircase-like, bud-like, and spherocone) for  $c_P = 10\text{ g}\cdot\text{L}^{-1}$  and  $1\text{ g}\cdot\text{L}^{-1}$ , respectively. Overall, a large range of different microparticle morphologies could be obtained from the same triblock terpolymer by adjusting the crystallization/evaporation parameters.

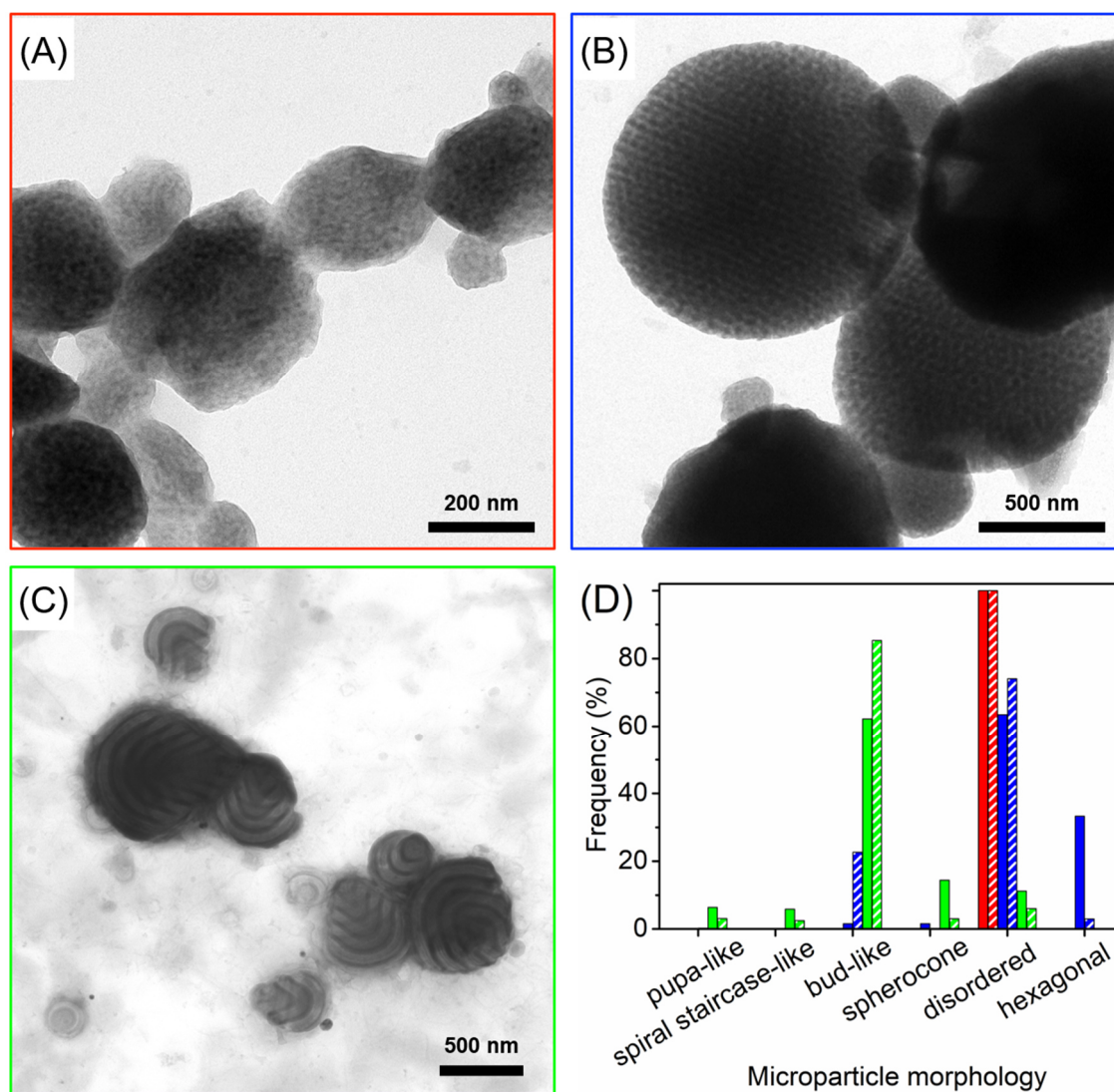


**Figure 6.6.** TEM overview images of  $S_{32}E_{36}M_{32}^{93}$  microparticles formed at  $T_{\text{evap}} = 30\text{ }^{\circ}\text{C}$ . “Crystallization first” with (A) preformed wCCMs and (B) simultaneous CDSA of wCCMs during evaporation, and “evaporation first” with molecularly dissolved triblock terpolymers in (C). (D) Frequency distributions of microparticle morphologies from A (red), B (blue) and C (green) using  $10\text{ g}\cdot\text{L}^{-1}$  (solid colour) or  $1\text{ g}\cdot\text{L}^{-1}$  (striped pattern). (PS domains appear dark due to  $\text{RuO}_4$  staining).

## Conclusion

In summary, we reported the 3D soft confinement self-assembly of a semicrystalline triblock terpolymer in O/W emulsions resulting in a variety of frustrated multicompart ment microparticles, whose morphologies depend on the preparation route and the conflict between crystallization and the confining barrier. When crystallization occurs before microparticle formation (“crystallization first”), microparticles with latticed inner structure are favoured, while microparticles with lamellar inner structure are exclusively formed when confined microphase separation occurs first (“evaporation first”). Depending on the preparation route and attributed to the semi-crystalline character of one of the blocks, we identified a range of microparticle morphologies from one single triblock terpolymer including hexagonally packed cylinders with compartmentalized matrix, helical and double stair case morphologies, as well as spherocones. TEM tomography aided in the analysis of the partially complex arrangement of inner structures. The herein presented  $S_{32}E_{36}M_{32}^{93}$  microparticle morphologies might be disassembled into crystalline-core nano-particles with a variety of shapes<sup>17,18</sup> that could be used as seeds for the controlled epitaxial growth of crystalline-core micelles upon addition of unimers to create hierarchical superstructures.<sup>52,61</sup> For example, bud-like microparticles could be disassembled into nanocups, as previously demonstrated for another triblock terpolymer,<sup>18</sup> yet, in case of a crystalline wall, nanocups would exhibit high shape persistence. Our results give a preliminary understanding of self-assembly of semicrystalline triblock terpolymer under 3D soft confinement, and provide an alternative strategy for complex morphological control that may have important implications on future applications of semicrystalline (e.g., conductive) polymers.

## Methods

**Materials.** Cetyltrimethylammonium bromide (CTAB) ( $\geq 99.9\%$ , Sigma-Aldrich) and toluene (analytical grade, Merck) were used as received. Deionized water with a resistivity of  $18.2 \text{ M}\Omega\cdot\text{cm}$  was prepared with a Milli-Q A+ system (Millipore SAS, France). The dialysis membrane (Sigma-Aldrich, average flat width 33 mm) had a molecular weight cut-off of 12-14 kDa and was equilibrated in deionized water prior to use. The  $\text{S}_{32}\text{E}_{36}\text{M}_{32}^{93}$  triblock terpolymer ( $D = 1.03$ , subscripts denote the respective block in wt.-% and superscript denotes the number-average molecular weight in  $\text{kg}\cdot\text{mol}^{-1}$ ) was synthesized by a combination of living anionic polymerization and subsequent catalytic hydrogenation as described previously (see also Table S6.1).<sup>56,60</sup>

**Confinement Self-Assembly.** Molecularly dissolved  $\text{S}_{32}\text{E}_{36}\text{M}_{32}^{93}$  in toluene ( $c = 1$  or  $10 \text{ g}\cdot\text{L}^{-1}$ ) was prepared by heating the polymer solutions to  $80 \text{ }^\circ\text{C}$  for at least 2 h. After that, 0.1 mL of the polymer solution was emulsified with 3 mL of a preheated aqueous CTAB solution ( $c = 10 \text{ g}\cdot\text{L}^{-1}$ ,  $80 \text{ }^\circ\text{C}$ ) by vortex mixing for 1 min in a 10 mL vial (22 mm in diameter) with snap-caps. Subsequently, two different evaporation/crystallization protocols were employed: (i) Evaporation first: the emulsions were first evaporated at  $80 \text{ }^\circ\text{C}$  for 4 h by drilling a small hole of about  $1.5 \text{ mm}^2$  in the cap refer to previous report,<sup>24</sup> followed by crystallization at  $T_{\text{crist}} = 30, 40, 50,$  and  $60 \text{ }^\circ\text{C}$  for 48 h. (ii) Crystallization first: the emulsions were rapidly cooled from  $80 \text{ }^\circ\text{C}$  to the desired evaporation temperature ( $T_{\text{evap}} = 30, 40, 50,$  and  $60 \text{ }^\circ\text{C}$ ) and evaporation/crystallization was allowed to occur simultaneously for 48 h. As a reference, the as-prepared  $\text{S}_{32}\text{E}_{36}\text{M}_{32}^{93}$  solution was quenched from  $80 \text{ }^\circ\text{C}$  to  $5 \text{ }^\circ\text{C}$  followed by annealing for 10 min to prepare a dispersion of worm-like crystalline-core micelles (wCCMs) *via* CDSA, first. Subsequent emulsification (with  $30 \text{ }^\circ\text{C}$  CTAB solution) and solvent evaporation were both done at  $30 \text{ }^\circ\text{C}$ . In all cases, excess CTAB was removed by dialysis against deionized water after solid microparticles were formed.

**Differential Scanning Calorimetry (DSC).** Calorimetric measurements on the  $\text{S}_{32}\text{E}_{36}\text{M}_{32}^{93}$  bulk film were performed with a Phoenix 204 F1 (Netzsch) instrument using aluminum crucibles (pierced lid) and nitrogen as protective gas. The temperature range was selected from  $0\text{-}150 \text{ }^\circ\text{C}$  at a scanning rate of  $10 \text{ K}\cdot\text{min}^{-1}$ . The displayed heating trace corresponds to the second heating run to exclude effects from thermal history.

**Micro Differential Scanning Calorimetry ( $\mu$ DSC).** For thermal analysis of  $S_{32}E_{36}M_{32}^{93}$  solutions in toluene at different concentrations ( $c = 1, 10, 20, 50, 100,$  and  $500 \text{ g}\cdot\text{L}^{-1}$ ), a SETARAM Micro DSC III instrument equipped with sealed measuring cells ("batch cells",  $V = 1 \text{ mL}$ ) was used. A scanning rate of  $0.5 \text{ K}\cdot\text{min}^{-1}$  was employed and pure toluene was used as reference.

**Transmission Electron Microscopy (TEM).** Samples were prepared by placing one drop of  $S_{32}E_{36}M_{32}^{93}$  microparticles dispersion on a carbon-coated copper grid (400 mesh, Science Services). Excess solution was blotted with a filter paper after 2 min and the grid was dried at room temperature for at least 12 h. The PS block was selectively stained with ruthenium tetroxide ( $\text{RuO}_4$ ) vapor for 15 min before measurements. TEM measurements were performed on a JEOL JEM-1400 Plus TEM (JEOL, Japan), operated at an acceleration voltage of 120 kV, a point resolution of 0.38 nm and a line resolution of 0.2 nm. Images were recorded with a 16-bit  $4096\times 4096$ -pixel CMOS digital camera and processed with FIJI open-source software package. TEM tilt series were recorded between  $\pm 69^\circ$  in  $3^\circ$  increments with SerialEM software package (version 3.2.2).

**Scanning Electron Microscopy (SEM).** Samples were prepared by placing one drop of  $S_{32}E_{36}M_{32}^{93}$  microparticles dispersion on a silicon wafer, excess solution was blotted with filter paper after 2 min and the wafer was dried at room temperature for at least 12 h. A layer of 10 nm platinum was sputtered onto the samples using a Quorum PP3010T-Cryo chamber with integrated Q150T-Es high-end sputter coater and Pt-Cd target before measurements. SEM measurements were performed on a cryo-field emission SEM (Crossbeam 540 FIB, ZEISS, Germany) equipped with in lens-, chamber-, and energy-selective detectors for 16-bit image series acquisition with up to  $40,000\times 50,000$ -pixel resolution.

## Supporting Information

The supporting information is available free of charge at <https://pubs.acs.org/doi/>

Molecular characteristics of the used triblock terpolymer, additional DSC and  $\mu$ DSC data of  $S_{32}E_{36}M_{32}^{93}$  in bulk and in toluene, size evaluation of  $S_{32}E_{36}M_{32}^{93}$  microparticles prepared from evaporation first protocol, and additional TEM images of  $S_{32}E_{36}M_{32}^{93}$  bulk film, microparticles and wCCMs (PDF), as well as TEM tilt series of double spiral staircase-like and hexagonal microparticles.

## Acknowledgements

We made use of the facilities of the Imaging Centre Essen (IMCES). X.D. is grateful for financial support from the Sino-German (CSC-DAAD) Postdoc Scholarship Program, 2018 (No. 57395819). X.Q. is grateful for financial support from China Scholarship Council (CSC) and Institute of Chemical Materials, CAEP. C.H. and H.S. acknowledge support by the collaborative research centre SFB 840 (project A2) and by the Graduate School of the University of Bayreuth (C.H.). A.H.G. thanks the German Research Foundation (DFG) for funding an Emmy Noether Research Group (GR 5075/2-1).

## References

- (1) Cabral, H.; Miyata, K.; Osada, K.; Kataoka, K. Block Copolymer Micelles in Nanomedicine Applications. *Chem. Rev.* **2018**, *118* (14), 6844–6892.
- (2) Gaitzsch, J.; Huang, X.; Voit, B. Engineering Functional Polymer Capsules toward Smart Nanoreactors. *Chem. Rev.* **2016**, *116* (3), 1053–1093.
- (3) Orilall, M. C.; Wiesner, U. Block Copolymer Based Composition and Morphology Control in Nanostructured Hybrid Materials for Energy Conversion and Storage: Solar Cells, Batteries, and Fuel Cells. *Chem. Soc. Rev.* **2011**, *40* (2), 520–535.
- (4) Yoo, H. G.; Byun, M.; Jeong, C. K.; Lee, K. J. Performance Enhancement of Electronic and Energy Devices via Block Copolymer Self-Assembly. *Adv. Mater.* **2015**, *27* (27), 3982–3998.
- (5) Stefik, M.; Guldin, S.; Vignolini, S.; Wiesner, U.; Steiner, U. Block Copolymer Self-Assembly for Nanophotonics. *Chem. Soc. Rev.* **2015**, *44* (15), 5076–5091.
- (6) Ku, K. H.; Shin, J. M.; Yun, H.; Yi, G. R.; Jang, S. G.; Kim, B. J. Multidimensional Design of Anisotropic Polymer Particles from Solvent-Evaporative Emulsion. *Adv. Funct. Mater.* **2018**, *28* (42), 1802961.
- (7) Wong, C. K.; Qiang, X.; Müller, A. H. E.; Gröschel, A. H. Self-Assembly of Block Copolymers into Internally Ordered Microparticles. *Prog. Polym. Sci.* **2020**, *102*, 101211.
- (8) Yan, N.; Zhu, Y.; Jiang, W. Recent Progress in the Self-Assembly of Block Copolymers Confined in Emulsion Droplets. *Chem. Commun.* **2018**, *54* (94), 13183–13195.
- (9) Shin, J. M.; Kim, Y.; Ku, K. H.; Lee, Y. J.; Kim, E. J.; Yi, G. R.; Kim, B. J. Aspect Ratio-Controlled Synthesis of Uniform Colloidal Block Copolymer Ellipsoids from Evaporative Emulsions. *Chem. Mater.* **2018**, *30* (18), 6277–6288.

- (10) Yan, N.; Zhang, Y.; He, Y.; Zhu, Y.; Jiang, W. Controllable Location of Inorganic Nanoparticles on Block Copolymer Self-Assembled Scaffolds by Tailoring the Entropy and Enthalpy Contributions. *Macromolecules* **2017**, *50* (17), 6771–6778.
- (11) Xu, J.; Yang, Y.; Wang, K.; Li, J.; Zhou, H.; Xie, X.; Zhu, J. Additives Induced Structural Transformation of ABC Triblock Copolymer Particles. *Langmuir* **2015**, *31* (40), 10975–10982.
- (12) Xu, J.; Wang, K.; Li, J.; Zhou, H.; Xie, X.; Zhu, J. ABC Triblock Copolymer Particles with Tunable Shape and Internal Structure through 3D Confined Assembly. *Macromolecules* **2015**, *48* (8), 2628–2636.
- (13) Shin, J. J.; Kim, E. J.; Ku, K. H.; Lee, Y. J.; Hawker, C. J.; Kim, B. J. 100th Anniversary of Macromolecular Science Viewpoint: Block Copolymer Particles: Tuning Shape, Interfaces, and Morphology. *ACS Macro Lett.* **2020**, *9* (3), 306–317.
- (14) Lee, J.; Ku, K. H.; Park, C. H.; Lee, Y. J.; Yun, H.; Kim, B. J. Shape and Color Switchable Block Copolymer Particles by Temperature and PH Dual Responses. *ACS Nano* **2019**, *13* (4), 4230–4237.
- (15) Deng, R.; Liang, F.; Li, W.; Liu, S.; Liang, R.; Cai, M.; Yang, Z.; Zhu, J. Shaping Functional Nano-Objects by 3D Confined Supramolecular Assembly. *Small* **2013**, *9* (24), 4099–4103.
- (16) Deng, R.; Liang, F.; Zhou, P.; Zhang, C.; Qu, X.; Wang, Q.; Li, J.; Zhu, J.; Yang, Z. Janus Nanodisc of Diblock Copolymers. *Adv. Mater.* **2014**, *26* (26), 4469–4472.
- (17) Steinhaus, A.; Chakroun, R.; Müllner, M.; Nghiem, T.-L.; Hildebrandt, M.; Gröschel, A. H. Confinement Assembly of ABC Triblock Terpolymers for the High-Yield Synthesis of Janus Nanorings. *ACS Nano* **2019**, *13* (6), 6269–6278.
- (18) Qiang, X.; Steinhaus, A.; Chen, C.; Chakroun, R.; Gröschel, A. H. Template-Free Synthesis and Selective Filling of Janus Nanocups. *Angew. Chem. Int. Ed.* **2019**, *58* (21), 7122–7126.
- (19) Stadler, R.; Auschra, C.; Beckmann, J.; Krappe, U.; Voigt-Martin, I.; Leibler, L. Morphology and Thermodynamics of Symmetric Poly(A-Block-B-Block-C) Triblock Copolymers. *Macromolecules* **1995**, *28* (9), 3080–3097.
- (20) Goldacker, T.; Abetz, V.; Stadler, R.; Erukhimovich, I.; Leibler, L. Non-Centrosymmetric Superlattices in Block Copolymer Blends. *Nature* **1999**, *398* (6723), 137–139.

- (21) Ludwigs, S.; Böker, A.; Abetz, V.; Müller, A. H. E.; Krausch, G. Phase Behavior of Linear Polystyrene-Block-Poly(2-Vinylpyridine)-Block-Poly(tert-Butyl Methacrylate) Triblock Terpolymers. *Polymer* **2003**, *44* (22), 6815–6823.
- (22) Abetz, V.; Stadler, R. ABC and BAC Triblock Copolymers - Morphological Engineering by Variation of the Block Sequence. *Macromol. Symp.* **1997**, *113*, 19–26.
- (23) Yabu, H.; Higuchi, T.; Jinnai, H. Frustrated Phases: Polymeric Self-Assemblies in a 3D Confinement. *Soft Matter* **2014**, *10* (17), 2919–2931.
- (24) Shin, J. M.; Kim, Y.; Yun, H.; Yi, G. R.; Kim, B. J. Morphological Evolution of Block Copolymer Particles: Effect of Solvent Evaporation Rate on Particle Shape and Morphology. *ACS Nano* **2017**, *11* (2), 2133–2142.
- (25) Yan, N.; Liu, X.; Zhu, J.; Zhu, Y.; Jiang, W. Well-Ordered Inorganic Nanoparticle Arrays Directed by Block Copolymer Nanosheets. *ACS Nano* **2019**, *13* (6), 6638–6646.
- (26) Saito, N.; Takekoh, R.; Nakatsuru, R.; Okubo, M. Effect of Stabilizer on Formation of “Onionlike” Multilayered Polystyrene-Block-Poly(Methyl Methacrylate) Particles. *Langmuir* **2007**, *23* (11), 5978–5983.
- (27) Qiang, X.; Dai, X.; Steinhaus, A.; Gröschel, A. H. Multicompartment Microparticles with Patchy Topography through Solvent-Adsorption Annealing. *ACS Macro Lett.* **2019**, *8* (12), 1654–1659.
- (28) Zhu, Y.; Jiang, W. Self-Assembly of Diblock Copolymer Mixtures in Confined States: A Monte Carlo Study. *Macromolecules* **2007**, *40* (8), 2872–2881.
- (29) Stewart-Sloan, C. R.; Thomas, E. L. Interplay of Symmetries of Block Polymers and Confining Geometries. *Eur. Polym. J.* **2011**, *47* (4), 630–646.
- (30) Wyman, I.; Njikang, G.; Liu, G. When Emulsification Meets Self-Assembly: The Role of Emulsification in Directing Block Copolymer Assembly. *Prog. Polym. Sci.* **2011**, *36* (9), 1152–1183.
- (31) Klinger, D.; Wang, C. X.; Connal, L. A.; Audus, D. J.; Jang, S. G.; Kraemer, S.; Killops, K. L.; Fredrickson, G. H.; Kramer, E. J.; Hawker, C. J. A Facile Synthesis of Dynamic, Shape-Changing Polymer Particles. *Angew. Chem. Int. Ed.* **2014**, *53* (27), 7018–7022.
- (32) Schmidt, B. V. K. J.; Elbert, J.; Scheid, D.; Hawker, C. J.; Klinger, D.; Gallei, M. Metallopolymer-Based Shape Anisotropic Nanoparticles. *ACS Macro Lett.* **2015**, *4* (7), 731–735.
- (33) Pelras, T.; Mahon, C. S.; Müllner, M. Synthesis and Applications of Compartmentalised Molecular Polymer Brushes. *Angew. Chem. Int. Ed.* **2018**, *57* (24), 6982–6994.

- (34) Steinhaus, A.; Pelras, T.; Chakroun, R.; Gröschel, A. H.; Müllner, M. Self-Assembly of Diblock Molecular Polymer Brushes in the Spherical Confinement of Nanoemulsion Droplets. *Macromol. Rapid Commun.* **2018**, *39* (19), 1800177.
- (35) He, Q.; Ku, K. H.; Vijayamohanan, H.; Kim, B. J.; Swager, T. M. Switchable Full-Color Reflective Photonic Ellipsoidal Particles. *J. Am. Chem. Soc.* **2020**, *142* (23), 10424–10430.
- (36) Song, D. P.; Zhao, T. H.; Guidetti, G.; Vignolini, S.; Parker, R. M. Hierarchical Photonic Pigments *via* the Confined Self-Assembly of Bottlebrush Block Copolymers. *ACS Nano* **2019**, *13* (2), 1764–1771.
- (37) Zhang, W.; Kochovski, Z.; Lu, Y.; Schmidt, B. V. K. J.; Antonietti, M.; Yuan, J. Internal Morphology-Controllable Self-Assembly in Poly(Ionic Liquid) Nanoparticles. *ACS Nano* **2016**, *10* (8), 7731–7737.
- (38) Vacogne, C. D.; Wei, C.; Tauer, K.; Schlaad, H. Self-Assembly of  $\alpha$ -Helical Polypeptides into Microscopic and Enantiomorphic Spirals. *J. Am. Chem. Soc.* **2018**, *140* (36), 11387–11394.
- (39) Quintieri, G.; Saccone, M.; Spengler, M.; Giese, M.; Gröschel, A. H. Supramolecular Modification of ABC Triblock Terpolymers in Confinement Assembly. *Nanomaterials* **2018**, *8* (12), 1029.
- (40) Rider, D. A.; Chen, J. I. L.; Eloi, J. C.; Arsenault, A. C.; Russell, T. P.; Ozin, G. A.; Manners, I. Controlling the Morphologies of Organometallic Block Copolymers in the 3-Dimensional Spatial Confinement of Colloidal and Inverse Colloidal Crystals. *Macromolecules* **2008**, *41* (6), 2250–2259.
- (41) Wang, H.; Wu, C.; Xia, G.; Ma, Z.; Mo, G.; Song, R. Semi-Crystalline Polymethylene-*b*-Poly(Acrylic Acid) Diblock Copolymers: Aggregation Behavior, Confined Crystallization and Controlled Growth of Semicrystalline Micelles from Dilute DMF Solution. *Soft Matter* **2015**, *11* (9), 1778–1787.
- (42) Botiz, I.; Darling, S. B. Self-Assembly of Poly(3-Hexylthiophene)-Block-Polylactide Block Copolymer and Subsequent Incorporation of Electron Acceptor Material. *Macromolecules* **2009**, *42* (21), 8211–8217.
- (43) Zhu, L.; Cheng, S. Z. D.; Calhoun, B. H.; Ge, Q.; Quirk, R. P.; Thomas, E. L.; Hsiao, B. S.; Yeh, F.; Lotz, B. Crystallization Temperature-Dependent Crystal Orientations within Nanoscale Confined Lamellae of a Self-Assembled Crystalline - Amorphous Diblock Copolymer. *J. Am. Chem. Soc.* **2000**, *122* (25), 5957–5967.

- (44) Loo, Y. L.; Register, R. A.; Ryan, A. J. Modes of Crystallization in Block Copolymer Microdomains: Breakout, Templated, and Confined. *Macromolecules* **2002**, *35* (6), 2365–2374.
- (45) Kim, J. S.; Lee, Y. J.; Coote, J. P.; Stein, G. E.; Kim, B. J. Confined, Templated, and Break-Through Crystallization Modes in Poly(3-Dodecylthiophene)-Block-Poly(Ethyl Methacrylate) Block Copolymers. *Macromolecules* **2019**, *52*, 4475–4482.
- (46) Müller, A. J.; Balsamo, V.; Arnal, M. L.; Jakob, T.; Schmalz, H.; Abetz, V. Homogeneous Nucleation and Fractionated Crystallization in Block Copolymers. *Macromolecules* **2002**, *35* (8), 3048–3058.
- (47) Schmalz, H.; Knoll, A.; Müller, A. J.; Abetz, V. Synthesis and Characterization of ABC Triblock Copolymers with Two Different Crystalline End Blocks: Influence of Confinement on Crystallization Behavior and Morphology. *Macromolecules* **2002**, *35* (27), 10004–10013.
- (48) Michell, R. M.; Müller, A. J. Confined Crystallization of Polymeric Materials. *Prog. Polym. Sci.* **2016**, *54–55*, 183–213.
- (49) Boschetti-de-Fierro, A.; Lorenzo, A. T.; Müller, A. J.; Schmalz, H.; Abetz, V. Crystallization Kinetics of PEO and PE in Different Triblock Terpolymers: Effect of Microdomain Geometry and Confinement. *Macromol. Chem. Phys.* **2008**, *209* (5), 476–487.
- (50) Loo, Y. L.; Register, R. A.; Ryan, A. J.; Dee, G. T. Polymer Crystallization Confined in One, Two, or Three Dimensions. *Macromolecules* **2001**, *34* (26), 8968–8977.
- (51) Zhu, L.; Mimnaugh, B. R.; Ge, Q.; Quirk, R. P.; Cheng, S. Z. D.; Thomas, E. L.; Lotz, B.; Hsiao, B. S.; Yeh, F.; Liu, L. Hard and Soft Confinement Effects on Polymer Crystallization in Microphase Separated Cylinder-Forming PEO-*b*-PS/PS Blends. *Polymer* **2001**, *42* (21), 9121–9131.
- (52) Schmelz, J.; Schedl, A. E.; Steinlein, C.; Manners, I.; Schmalz, H. Length Control and Block-Type Architectures in Worm-Like Micelles with Polyethylene Cores. *J. Am. Chem. Soc.* **2012**, *134* (34), 14217–14225.
- (53) Kim, Y. J.; Cho, C. H.; Paek, K.; Jo, M.; Park, M. K.; Lee, N. E.; Kim, Y. J.; Kim, B. J.; Lee, E. Precise Control of Quantum Dot Location within the P3HT-*b*-P2VP/QD Nanowires Formed by Crystallization-Driven 1D Growth of Hybrid Dimeric Seeds. *J. Am. Chem. Soc.* **2014**, *136* (7), 2767–2774.
- (54) Tong, Z.; Li, Y.; Xu, H.; Chen, H.; Yu, W.; Zhuo, W.; Zhang, R.; Jiang, G. Corona Liquid Crystalline Order Helps to Form Single Crystals When Self-Assembly Takes Place

- in the Crystalline/Liquid Crystalline Block Copolymers. *ACS Macro Lett.* **2016**, *5* (7), 867–872.
- (55) Ganda, S.; Stenzel, M. H. Concepts, Fabrication Methods and Applications of Living Crystallization-Driven Self-Assembly of Block Copolymers. *Prog. Polym. Sci.* **2020**, *101*, 101195.
- (56) Mihut, A. M.; Walther, A.; Schweimer, K.; Drechsler, M.; Yuan, J.; Schmalz, H.; Schmelz, J. Thermo-Reversible Formation of Wormlike Micelles with a Microphase-Separated Corona from a Semicrystalline Triblock Terpolymer. *Macromolecules* **2008**, *41* (9), 3235–3242.
- (57) Gilroy, J. B.; Gädt, T.; Whittell, G. R.; Chabanne, L.; Mitchels, J. M.; Richardson, R. M.; Winnik, M. A.; Manners, I. Monodisperse Cylindrical Micelles by Crystallization-Driven Living Self-Assembly. *Nat. Chem.* **2010**, *2* (7), 566–570.
- (58) Inam, M.; Cambridge, G.; Pitto-Barry, A.; Laker, Z. P. L.; Wilson, N. R.; Mathers, R. T.; Dove, A. P.; O'Reilly, R. K. 1D vs. 2D Shape Selectivity in the Crystallization-Driven Self-Assembly of Polylactide Block Copolymers. *Chem. Sci.* **2017**, *8* (6), 4223–4230.
- (59) Gädt, T.; Jeong, N. S.; Cambridge, G.; Winnik, M. A.; Manners, I. Complex and Hierarchical Micelle Architectures from Diblock Copolymers Using Living, Crystallization-Driven Polymerizations. *Nat. Mater.* **2009**, *8* (2), 144–150.
- (60) Schmelz, J.; Karg, M.; Hellweg, T.; Schmalz, H. General Pathway toward Crystalline-Core Micelles with Tunable Morphology and Corona Segregation. *ACS Nano* **2011**, *5* (12), 9523–9534.
- (61) Hudson, Z. M.; Boott, C. E.; Robinson, M. E.; Rupar, P. A.; Winnik, M. A.; Manners, I. Tailored Hierarchical Micelle Architectures Using Living Crystallization-Driven Self-Assembly in Two Dimensions. *Nat. Chem.* **2014**, *6* (10), 893–898.
- (62) Qiu, H.; Hudson, Z. M.; Winnik, M. A.; Manners, I. Multidimensional Hierarchical Self-Assembly of Amphiphilic Cylindrical Block Comicelles. *Science* **2015**, *347* (6228), 1329–1332.
- (63) Li, X.; Wolanin, P. J.; MacFarlane, L. R.; Harniman, R. L.; Qian, J.; Gould, O. E. C.; Dane, T. G.; Rudin, J.; Cryan, M. J.; Schmaltz, T.; Frauenrath, H.; Winnik, M. A.; Faul, C. F.J.; Manners, I. Uniform Electroactive Fibre-Like Micelle Nanowires for Organic Electronics. *Nat. Commun.* **2017**, *8* (1), 15909.
- (64) Wang, X.; Guerin, G.; Wang, H.; Wang, Y.; Manners, I.; Winnik, M. A. Cylindrical Block Copolymer Micelles and Co-Micelles of Controlled Length and Architecture. *Science* **2007**, *317* (5838), 644–647.

- (65) Oliver, A. M.; Gwyther, J.; Boott, C. E.; Davis, S.; Pearce, S.; Manners, I. Scalable Fiber-Like Micelles and Block Co-Micelles by Polymerization-Induced Crystallization-Driven Self-Assembly. *J. Am. Chem. Soc.* **2018**, *140* (51), 18104–18114.
- (66) Xu, J.; Zhou, H.; Yu, Q.; Guerin, G.; Manners, I.; Winnik, M. A. Synergistic Self-Seeding in One-Dimension: A Route to Patchy and Block Comicelles with Uniform and Controllable Length. *Chem. Sci.* **2019**, *10* (8), 2280–2284.
- (67) Yu, W.; Inam, M.; Jones, J. R.; Dove, A. P.; O'Reilly, R. K. Understanding the CDSA of Poly(Lactide) Containing Triblock Copolymers. *Polym. Chem.* **2017**, *8* (36), 5504–5512.
- (68) Iv, P.; Theory, A.; Flory, P. J. Thermodynamics of Crystallization in High Polymers. IV. A Theory of Crystalline States and Fusion in Polymers, Copolymers, and Their Mixtures with Diluents. *J. Chem. Phys.* **1949**, *17* (3), 223–240.
- (69) Abetz, V.; Goldacker, T. Formation of Superlattices *via* Blending of Block Copolymers. *Macromol. Rapid Commun.* **2002**, *21* (1), 16–34.
- (70) Barton, A. F. M. Determination of Polymer Cohesion Parameters. *CRC Handbook of Solubility Parameters and Other Cohesion Parameters*, 2nd Ed.; CRC Press: Boca Raton, Florida, 1991; pp 406–446.
- (71) Deng, R.; Liang, F.; Li, W.; Yang, Z.; Zhu, J. Reversible Transformation of Nanostructured Polymer Particles. *Macromolecules* **2013**, *46* (17), 7012–7017.
- (72) Kutugin, R. V. Shell Shapes of Permian Ammonoids from Northeastern Russia. *Paleontol. J.* **1998**, *32* (1), 19–29.
- (73) Schmelz, J.; Pirner, D.; Krekhova, M.; Ruhland, T. M.; Schmalz, H. Interfacial Activity of Patchy Worm-Like Micelles. *Soft Matter* **2013**, *9* (47), 11173.

## Supporting Information

**Table S6.1.** Molecular characteristics of S<sub>32</sub>E<sub>36</sub>M<sub>32</sub><sup>93</sup>.

Polymer <sup>a</sup>	Polymer <sup>b</sup>	$\bar{D}$ <sup>c</sup>	Ethyl branches <sup>d</sup>
S <sub>32</sub> E <sub>36</sub> M <sub>32</sub> <sup>93</sup>	S <sub>280</sub> E <sub>1190</sub> M <sub>300</sub>	1.03	2.6

<sup>a</sup> Subscripts denote the weight fraction of each block in wt.-% and superscript the number-average molecular weight in kg/mol. <sup>b</sup> Subscripts denote the number-average degree of polymerization. <sup>c</sup> Dispersity of the polystyrene-*block*-poly(1,4-butadiene)-*block*-poly(methyl methacrylate) (SBM) triblock terpolymer before hydrogenation as obtained by THF-SEC using a polystyrene calibration. <sup>d</sup> Average amount of ethyl branches per 100 main chain carbon atoms resulting from 1,2-addition during the polymerization of PB, determined by <sup>1</sup>H-NMR on the SBM precursor.

**Table S6.2.** Thermal properties of S<sub>32</sub>E<sub>36</sub>M<sub>32</sub><sup>93</sup> in bulk and in toluene.

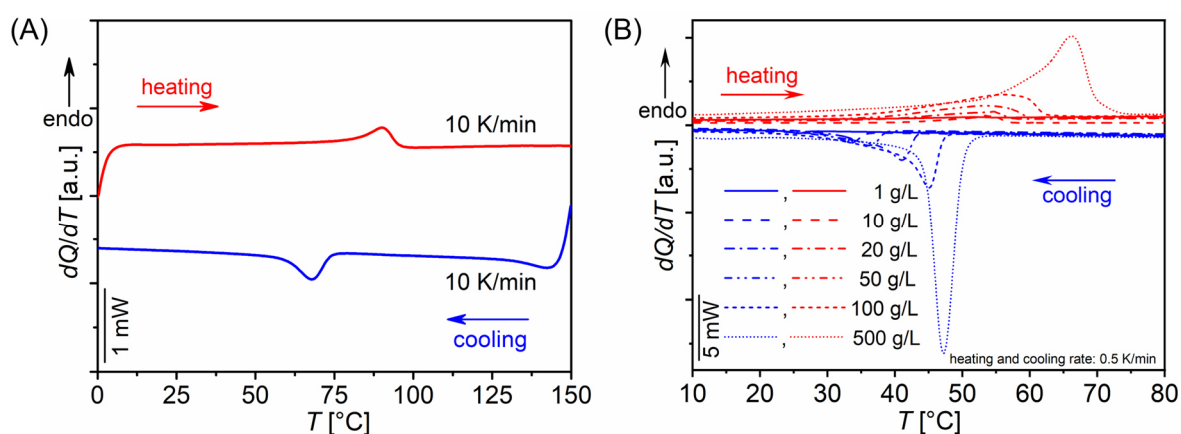
Type	Concentration	$T_c$ (°C)	$T_m$ (°C)
Bulk	/	68	90
	500	47	66
Toluene	100	45	56
	50	41	53
	20	36	55
	10	34	54
	1	26	51

**Table S6.3.** Size statistics of  $S_{32}E_{36}M_{32}^{93}$  microparticles prepared from evaporation first protocol.

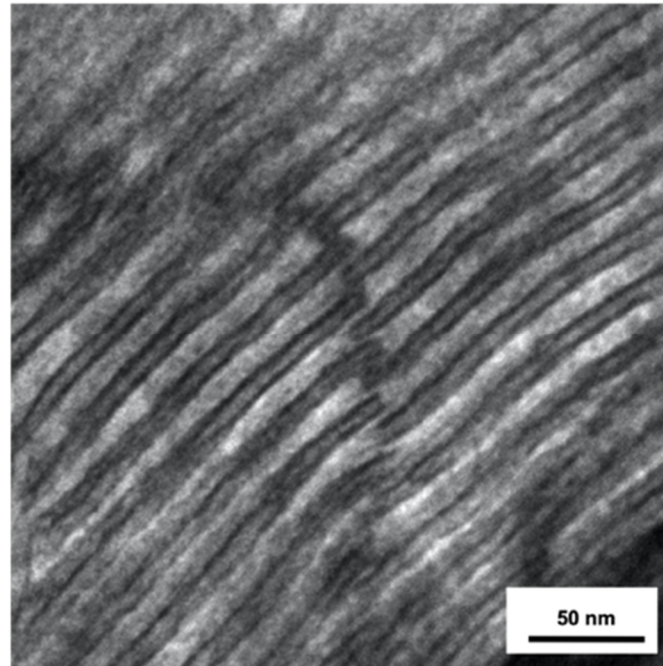
Morphology	Average length, $L$ (nm) <sup>a</sup>		Average diameter, $D$ (nm) <sup>a</sup>		Average aspect ratio, $R$ ( $L/D$ ) <sup>a</sup>	
	$c_P = 10 \text{ g}\cdot\text{L}^{-1}$	$c_P = 1 \text{ g}\cdot\text{L}^{-1}$	$c_P = 10 \text{ g}\cdot\text{L}^{-1}$	$c_P = 1 \text{ g}\cdot\text{L}^{-1}$	$c_P = 10 \text{ g}\cdot\text{L}^{-1}$	$c_P = 1 \text{ g}\cdot\text{L}^{-1}$
Pupa-like	435 (128)	363 (89)	208 (62)	172 (44)	2.10 (0.19)	2.15 (0.35)
Single spiral staircase-like <sup>b</sup>	388 (91)	369 (82)	235 (52)	203 (43)	1.66 (0.19)	1.84 (0.28)
Double spiral staircase-like <sup>b</sup>	521 (151)	464 (104)	316 (107)	304 (67)	1.68 (0.23)	1.56 (0.30)
Bud-like	329 (216)	287 (118)	336 (205)	302 (115)	0.97 (0.07)	0.95 (0.10)
Hemisphere/helix <sup>c</sup>	538 (177)	457 (102)	496 (231)	468 (109)	1.10 (0.12)	0.98 (0.09)
Spherocone <sup>c</sup>	687 (202)	423 (161)	686 (202)	388 (149)	1.00 (0.00)	1.09 (0.08)
Disordered	596 (300)	377 (107)	558 (294)	339 (91)	1.08 (0.12)	1.11 (0.07)
Hexagonal	/	/	/	/	/	/

<sup>a</sup> Average size was obtained by counting more than 200 microparticles of each morphology at all temperatures (including 60 °C, 50 °C, 40 °C, 30 °C, and in liquid nitrogen); data in brackets indicate the standard deviation. <sup>b</sup> Both single and double spiral staircase-like particle are classified as spiral staircase-like particle in morphology frequency statistics. <sup>c</sup> Both hemisphere/helix and spherocone particle are classified as spherocone particle in morphology frequency statistics.

### Thermal properties of $S_{32}E_{36}M_{32}^{93}$ in bulk and in toluene

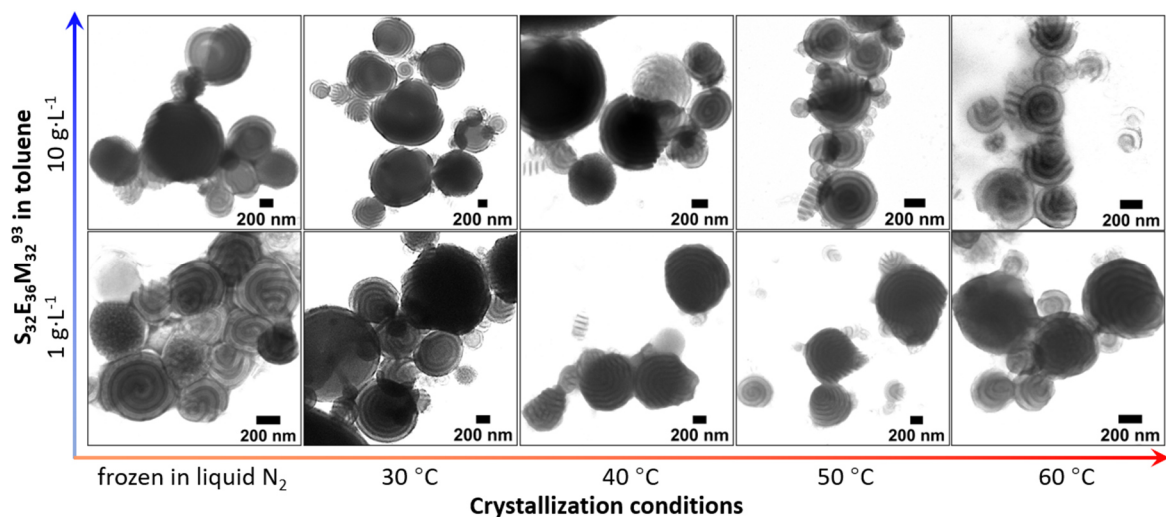


**Figure S6.1.** (A) DSC heating (red) and cooling (blue) traces of a  $S_{32}E_{36}M_{32}^{93}$  bulk sample monitored at a scanning rate of  $10 \text{ K}\cdot\text{min}^{-1}$ ; (B)  $\mu$ DSC heating (red) and cooling (blue) traces of  $S_{32}E_{36}M_{32}^{93}$  solutions in toluene at different concentrations (scanning rate:  $0.5 \text{ K}\cdot\text{min}^{-1}$ ). The displayed heating traces correspond to the second heating runs to exclude effects resulting from any previous thermal history.

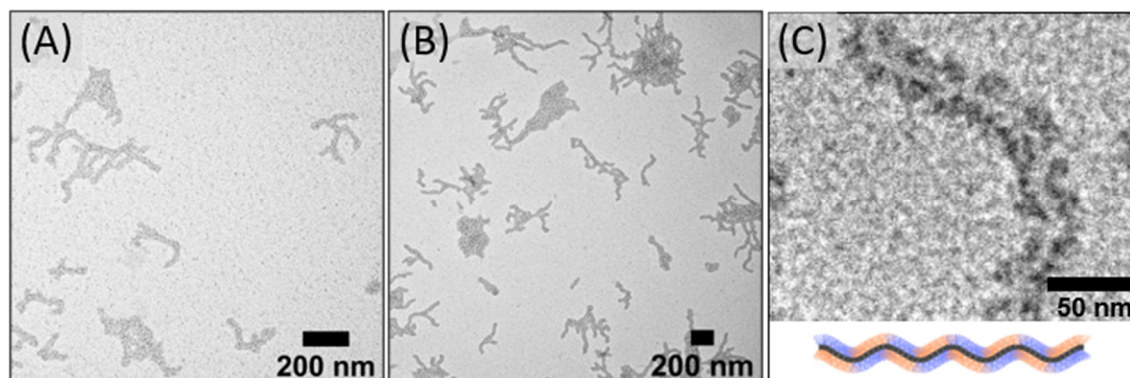
Bulk morphology of  $S_{32}E_{36}M_{32}^{93}$ 

**Figure S6.2.** TEM micrograph of a  $S_{32}E_{36}M_{32}^{93}$  bulk film cast from toluene at 70 °C, stained with  $RuO_4$  to enhance the contrast of PS.

Microparticles of  $S_{32}E_{36}M_{32}^{93}$  through “confinement assembly at  $T_{evap} > T_c$  - evaporation first” protocol at different temperatures



**Figure S6.3.** TEM overview images of  $S_{32}E_{36}M_{32}^{93}$  microparticles formed through “confinement assembly at  $T_{evap} > T_c$  - evaporation first” at different  $T_{cryst}$  (frozen in liquid nitrogen ( $N_2$ ), 30 °C, 40 °C, 50 °C, and 60 °C) using 10  $g \cdot L^{-1}$  and 1  $g \cdot L^{-1}$   $S_{32}E_{36}M_{32}^{93}$  polymer solutions in toluene. The PS microdomains appear dark due to  $RuO_4$  staining.

Worm-like crystalline-core micelles of  $S_{32}E_{36}M_{32}^{93}$ 

**Figure S6.4.** TEM micrographs of patchy worm-like crystalline-core micelles (wCCMs) formed by crystallization-driven self-assembly (CDSA) of  $S_{32}E_{36}M_{32}^{93}$  in toluene at 5 °C for 10 min ( $c = 10 \text{ g}\cdot\text{L}^{-1}$  (A) and  $1 \text{ g}\cdot\text{L}^{-1}$  (B)). (C) Close up of the structure of wCCMs with a crystallizable PE core and an amorphous patchy corona (PS and PMMA blocks) in toluene. The PS compartments appear dark due to  $\text{RuO}_4$  staining, the PE core and PMMA patches appear bright.

Microparticles of  $S_{32}E_{36}M_{32}^{93}$  through “confinement assembly at  $T_{\text{evap}} > T_c$  - evaporation first” protocol with preformed wCCMs.

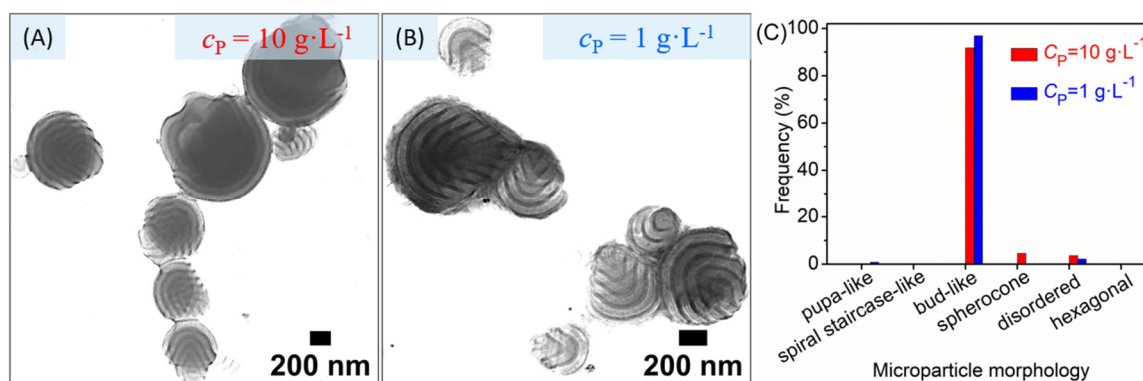


**Figure S6.5.** TEM overview images of  $S_{32}E_{36}M_{32}^{93}$  microparticles formed through “confinement assembly at  $T_{\text{evap}} > T_c$  - evaporation first” protocol with preformed  $10 \text{ g}\cdot\text{L}^{-1}$  (A) and  $1 \text{ g}\cdot\text{L}^{-1}$  (B) wCCMs. The emulsions containing a dispersion of preformed wCCMs were reheated to 80 °C for evaporation before rapid cooling to 30 °C for crystallization. (C) Frequency distributions of microparticle morphologies (PS microdomains appear dark due to  $\text{RuO}_4$  staining).

Microparticles of  $S_{32}E_{36}M_{32}^{93}$  through “confinement assembly at  $T_{\text{evap}} < T_c$  - crystallization first” protocol at different temperatures

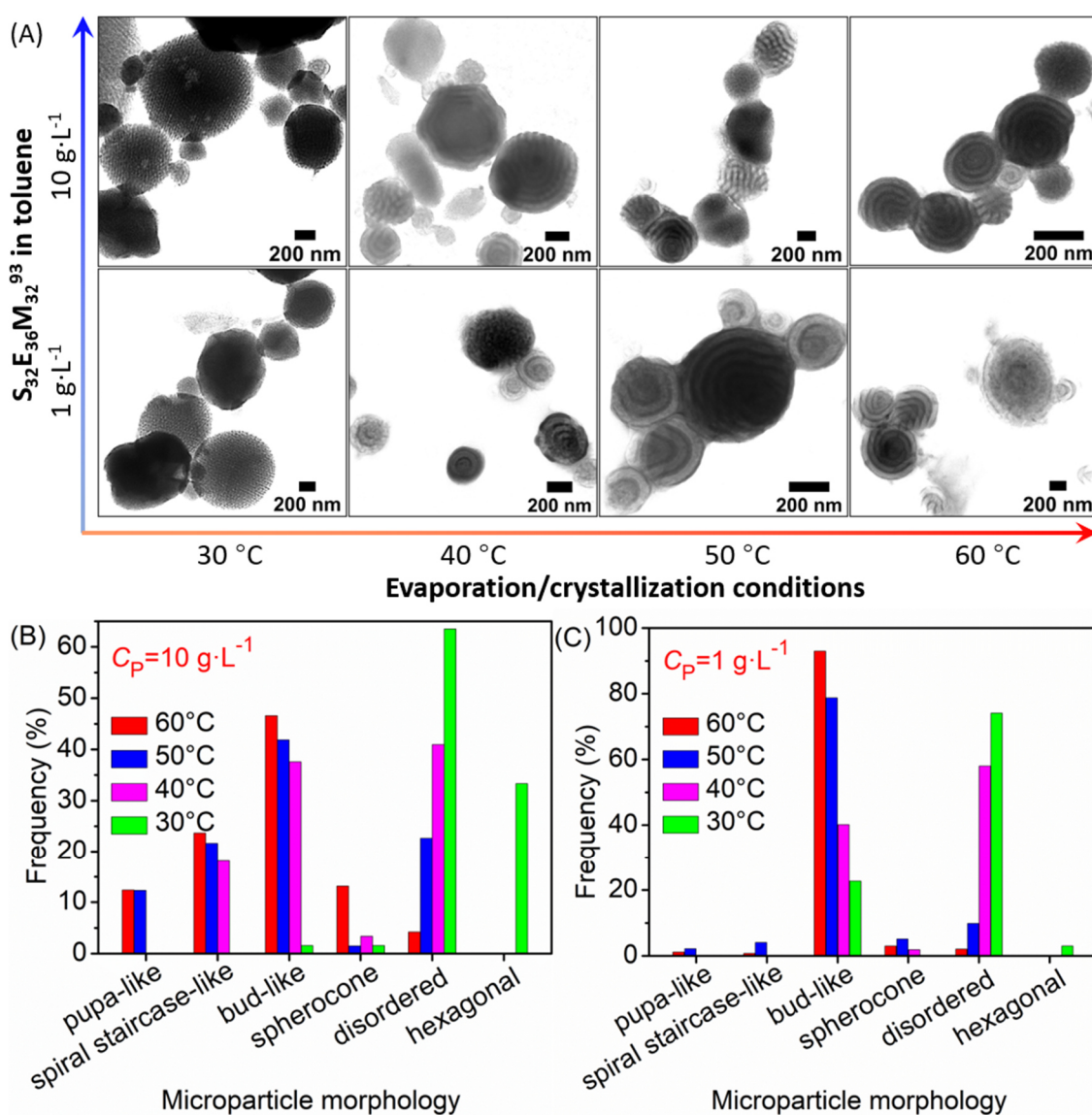


**Figure S6.6.** (A) TEM overview images of  $S_{32}E_{36}M_{32}^{93}$  microparticles formed through “Confinement assembly at  $T_{\text{evap}} < T_c$  - crystallization first” protocol at different evaporation/crystallization temperatures (30 °C, 40 °C, 50 °C, and 60 °C) using  $10 \text{ g}\cdot\text{L}^{-1}$  and  $1 \text{ g}\cdot\text{L}^{-1}$   $S_{32}E_{36}M_{32}^{93}$  polymer solutions in toluene as precursors. The PS microdomains appear dark due to  $\text{RuO}_4$  staining. (B) and (C) Frequency distributions of the corresponding morphologies.



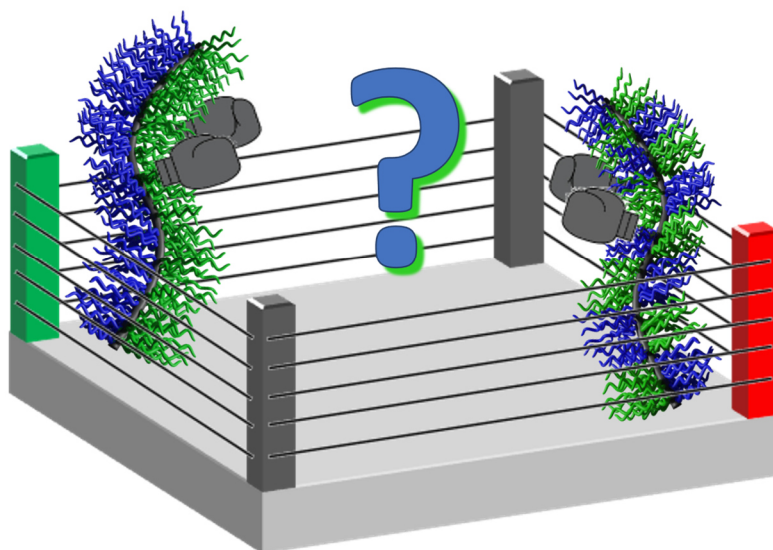
## 7 Janus or patchy: Who Wins the Battle in Crystallization-Driven Self-Assembly of Double Crystalline Triblock Terpolymers?

Christian Hils,<sup>[a]</sup> Joachim Schmelz,<sup>[a]</sup> Markus Drechsler<sup>[b]</sup> and Holger Schmalz<sup>[a,c]\*</sup>

[a] Macromolecular Chemistry II, University of Bayreuth, Universitätsstraße 30, 95447 Bayreuth (Germany)

[b] Bavarian Polymer Institute, Keylab Electron and Optical Microscopy, Universitätsstraße 30, 95447 Bayreuth (Germany)

[c] Bavarian Polymer Institute, Keylab Synthesis and Molecular Characterization, Universitätsstraße 30, 95447 Bayreuth (Germany)



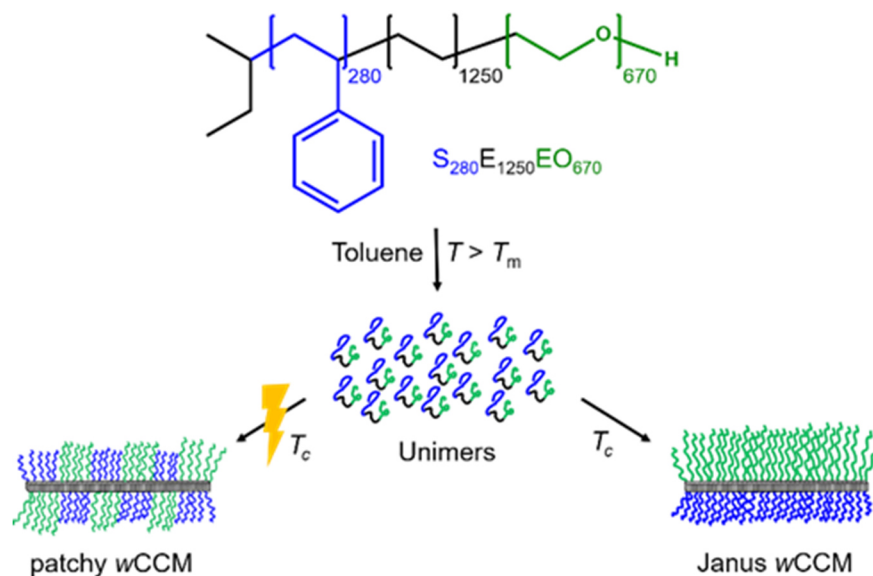
Submitted to *J. Am. Chem. Soc.*

## **Abstract**

Surface-compartmentalized micellar nanostructures (Janus and patchy micelles) have gained increasing interest due to their unique properties opening highly relevant applications, e.g., as efficient particulate surfactants, compatibilizers in polymer blends, or templates for catalytically active nanoparticles. Here, we present a facile method for the production of amphiphilic, worm-like Janus micelles based on crystallization-driven self-assembly of a double crystalline triblock terpolymer with a crystallizable polyethylene middle block and two strongly incompatible corona blocks, polystyrene and poly(ethylene oxide) (PEO). The combination of strongly incompatible corona blocks with the ability of the PEO corona to crystallize fosters the formation of Janus micelles via a comparably simple heating and cooling protocol.

Surface-compartmentalized polymeric nanostructures are of substantial interest, as their unique corona structure paves the way to a multitude of highly relevant applications.[1–6] In general, they can be divided in Janus and patch-like (patchy) particles. Janus particles (or micelles) exhibit two opposing faces with different chemistry and/or polarity, whereas patchy micelles are characterized by a patch-like microphase-separated corona, consisting of several compartments. Janus particles and micelles have been intensively studied in the past with a strong focus on spherical structures, which is owed to the fact that cylindrical (1D) or platelet-like (2D) Janus structures are more difficult to realize.[7–13] Janus particles can be applied in a broad range of applications, for example as highly efficient particulate surfactants for emulsion stabilization or compatibilization of polymer blends, as optical nanoprobe and biosensors, for self-propulsion, interfacial catalysis, superhydrophobic and anti-ice coatings, and many more. 1D (cylindrical or worm-like) patchy micelles can be produced in an efficient manner employing crystallization-driven self-assembly (CDSA) and living CDSA, which allows control over length, length distribution and corona chemistries.[14–19] There are two main concepts for the fabrication of 1D patchy micelles: i) CDSA of linear triblock terpolymers with a crystallizable middle blocks,[19–21] or of  $\mu$ -ABC miktoarm star terpolymers,[22] ii) CDSA of a mixture of diblock copolymers bearing a common crystallizable block[23–26]. The patchy structure of the micellar corona gives rise to specific applications, like for example as templates for the regio-selective incorporation of different nanoparticle types,[19] in heterogeneous catalysis,[27,28] as compatibilizers in polymer blends or their use as highly efficient particulate surfactants,[29,30] and for the construction of hierarchical superstructures[31]. So far, CDSA of triblock terpolymers with crystallizable middle blocks has always resulted in cylindrical micelles with a patchy corona. Nevertheless, a Janus-type structure of the corona might also be feasible when the two soluble corona blocks have a sufficiently high incompatibility or if there is another driving force promoting microphase separation in the corona. This has been predicted theoretically and observed experimentally for two-component bottle brush copolymers, featuring a polymer backbone that is densely grafted with two strongly immiscible amorphous polymer segments.[32–36] Interestingly, introducing crystallizable grafts has shown to foster the formation of Janus structures for two-component bottle brushes as well as amphiphilic, double-grafted hyperbranched polymers.[37–41] Thus, we speculated, whether the replacement of one incompatible end block by a highly incompatible and crystallizable block can guide the formation of Janus-type worm-like micelles in the CDSA of triblock terpolymers with a crystallizable polyethylene (PE) middle

block in solution. In this context, only a few studies on CDSA of double crystalline block copolymers are currently available that address crystallization in the micelle corona.[42–44]



**Scheme 7.1.** CDSA of a double crystalline PS-*b*-PE-*b*-PEO triblock terpolymer in toluene favours formation of Janus micelles with a crystalline PE core.

In this communication, we report the formation of amphiphilic Janus micelles by CDSA of a double crystalline polystyrene-*block*-polyethylene-*block*-poly(ethylene oxide) (PS-*b*-PE-*b*-PEO:  $S_{280}E_{1350}EO_{670}$ , indices denote number average degrees of polymerization of the respective blocks) triblock terpolymer in toluene (Scheme 7.1). The  $S_{280}E_{1250}EO_{670}$  triblock terpolymer was synthesized by a combination of sequential anionic polymerization and catalytic hydrogenation, according to a previously reported method.[45] Details on synthesis and molecular characteristics of  $S_{280}E_{1250}EO_{670}$  are given in the Supporting Information (Table S7.1, Figures S7.1,S7.2). Toluene was chosen as solvent for CDSA, as it is a good solvent for PE in the molten state and, thus, promotes the formation of worm-like micelles with a crystalline PE core.[14,20] Micro-differential scanning calorimetry ( $\mu$ -DSC) measurements clearly prove that the PEO corona block is able to crystallize, revealing a fractionated crystallization behavior with two pronounced crystallization exotherms (Figure 7.1A).

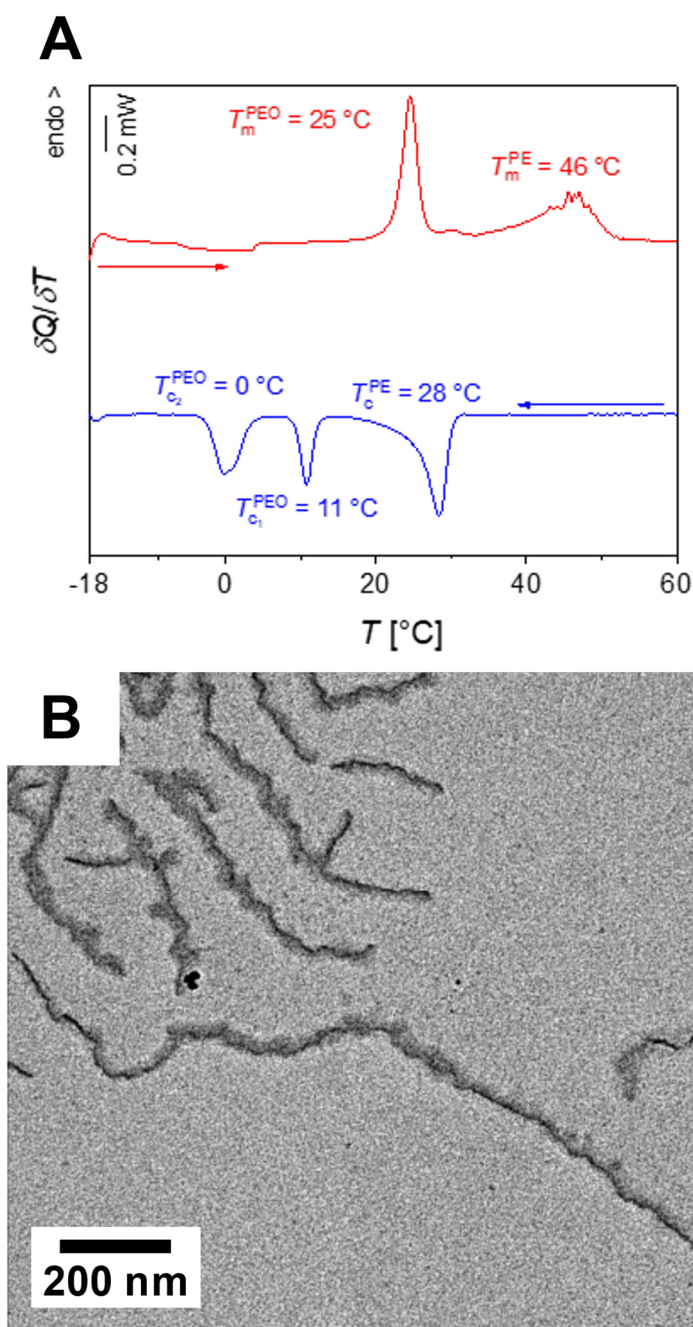


**Figure 7.1.** A)  $\mu$ -DSC heating and cooling traces for  $S_{280}E_{1250}EO_{670}$  in toluene ( $c = 10 \text{ g}\cdot\text{L}^{-1}$ ) and B) TEM micrograph of worm-like Janus micelles formed by CDSA at  $T_c = 28.5^\circ\text{C}$  ( $\text{OsO}_4$  staining).

Notably, the crystallization temperatures ( $T_c$ ) of the PEO block ( $T_{c1} = 11^\circ\text{C}$  and  $T_{c2} = 0^\circ\text{C}$ ) are significantly higher compared to that observed for neat PEO in toluene at identical PEO concentration ( $T_c \approx -11^\circ\text{C}$ , Figure S7.3). Besides, only one melting endotherm at  $T_m = 25^\circ\text{C}$  was observed. The PE block shows a melting point at  $T_m = 46^\circ\text{C}$  and crystallization at  $T_c = 28^\circ\text{C}$ , respectively, in line with the behaviour of other triblock terpolymers with crystalline PE middle blocks.[19,20] This indicates a certain impact of the crystalline PE core on the

crystallization of the PEO block in the corona of the formed worm-like crystalline-core micelles (wCCMs), which might also influence corona segregation.

The transmission electron microscopy (TEM) image of the wCCMs formed by CDSA in toluene at  $T_c = 28.5$  °C (for details please see Supporting Information) nicely confirms this assumption, as in contrast to the usually observed patchy corona a Janus-type corona segregation is formed (Figure 7.1B). Here, staining with OsO<sub>4</sub> was employed in order to weakly stain the PEO domains in the corona.[46] The PE core appears dark due to the dense chain packing in the PE crystallites in the core, and only one half of the corona is discernable as light grey regions predominantly located on one side of the micelles.

We have systematically studied the influence of staining on the corona structure of the formed wCCMs in order to confirm the presence of a Janus-type microphase separation. Janus and patchy micelles are characterized by a comparable interfacial activity and also in 2D <sup>1</sup>H nuclear *Overhauser* effect spectroscopy (NOESY), a NMR technique probing internuclear distances, cross peaks are absent for both structures.[29,47] Thus, the differentiation between a Janus-type or patch-like microphase-separated corona is only feasible using imaging techniques. From Figures 7.2A,B it can be clearly deduced that the pristine micelles (no staining, overview TEM image in Figure S7.4A) and the micelles after staining with OsO<sub>4</sub> show an identical corona structure, where only one half of the corona, that is the PEO hemi-corona, is visible.

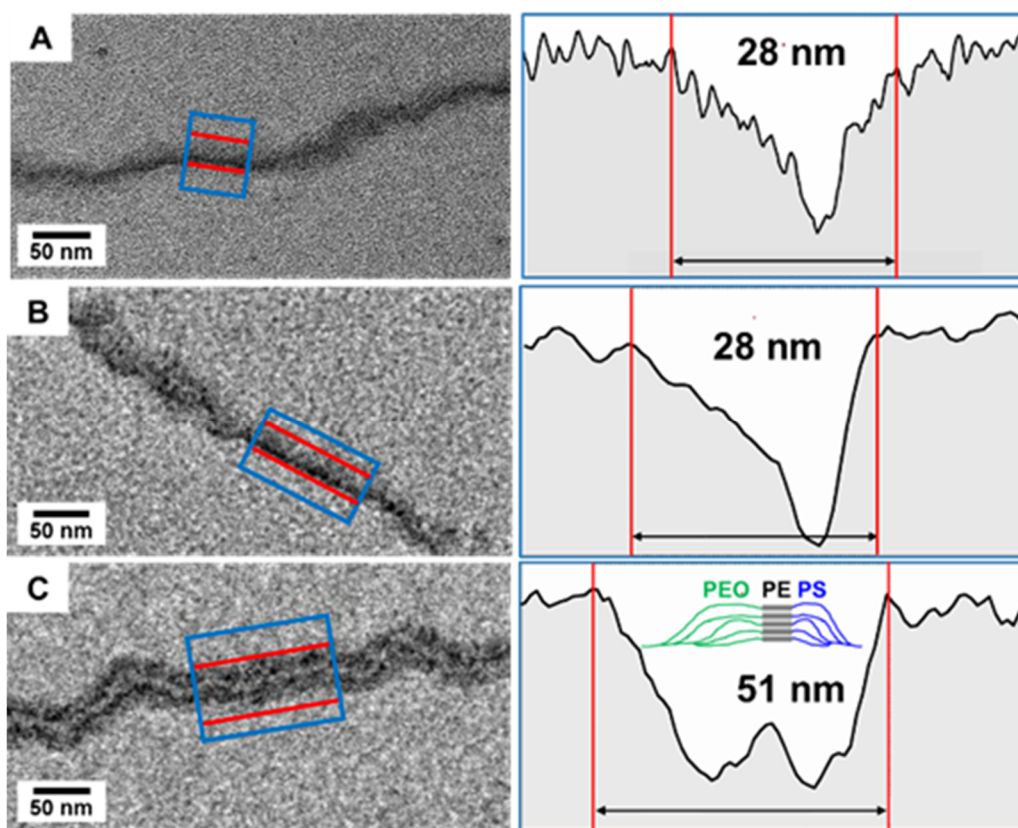


**Figure 7.2.** TEM micrographs (left) and corresponding grey scale analyses of the indicated regions (right) for  $S_{280}E_{1250}EO_{670}$  Janus micelles: A) not stained, B) stained with  $OsO_4$  vapour for 30 sec (under vacuum, ca. 50 mbar), and C) with  $RuO_4$  vapour for 7 min (ambient conditions).

In contrast, staining with  $RuO_4$ , which stains both the PEO and PS parts of the corona, resulted in micelles with a homogeneously dark corona with the bright appearing PE core being located in the center of the micelles (Figures 7.2C, S7.4B). This is supported by grey scale analyses over selected cross sectional areas (Figure 7.2, right panels), revealing an almost double micelle width in case of  $RuO_4$  staining compared to the widths obtained for  $OsO_4$  staining or without staining. Thus, a Janus-type microphase separated corona seems to be preferred over the entropically more favoured patchy structure when two strongly incompatible corona blocks, PS and PEO, are combined with the ability of one corona block (here PEO) to crystallize.

In addition, the presence of a Janus-type corona structure can be verified by comparing the behaviour with a  $S_{330}E_{1360}M_{760}$  ( $M$  = poly(methyl methacrylate)) triblock terpolymer, which features weakly incompatible PS and PMMA end blocks and, thus, forms patchy  $wCCMs$  in toluene (Figure S7.4C).[48] Upon dialysis in a solvent mixture, here acetone/*iso*-propanol (4/1 v/v), being selective for the PEO and PMMA corona blocks, respectively, is expected to result in different corona structures. For  $S_{330}E_{1360}M_{760}$  the patchy structure of the corona should

remain upon collapse of the insoluble PS patches, whereas for  $S_{280}E_{1350}EO_{670}$  the corona should exhibit a continuous structure consisting of two hemicylinders, PEO and the collapsed PS phase. This is confirmed by the TEM images shown in Figure 7.3 (top row), where for  $S_{330}E_{1360}M_{760}$  the patchy structure of the corona is clearly visible (PS patches were selectively stained with  $RuO_4$  and appear dark, overview TEM in Figure S7.4D), whereas for  $S_{280}E_{1350}EO_{670}$  a homogeneous corona is observed for both  $OsO_4$  and  $RuO_4$  staining. As  $OsO_4$  is only a weak staining agent for PEO, the darker hemicylinder corresponds to the PE core plus the collapsed PS hemi-corona, and the light grey part to PEO (Figures 7.3B,S7.4E). Consequently, for  $RuO_4$  staining (stains PS and PEO) both hemicylinders appear dark and the PE core bright (Figures 7.3C,S7.4F). The width of the Janus  $wCCMs$  is significantly smaller (ca. 40 nm, according to grey scale analyses shown in Figures 7.3C,D (bottom row)) compared to that observed for  $S_{280}E_{1350}EO_{670}$  Janus  $wCCMs$  in toluene (ca. 50 nm, Figure 7.2C (right panel)). This is reasonable, as due to the collapse of the insoluble PS chains in acetone/*iso*-propanol the PS hemi-cylinder shrinks in size.

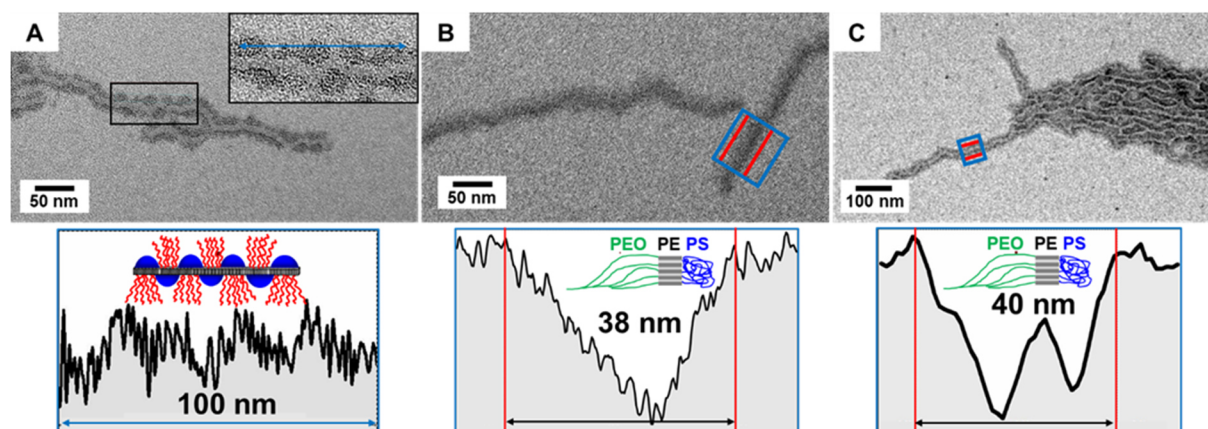


**Figure 7.3.** TEM micrographs (top) and corresponding grey scale analyses of the indicated regions (bottom) for A) patchy  $S_{330}E_{1360}M_{760}$  micelles stained with  $RuO_4$  for 7 min, and  $S_{280}E_{1250}EO_{670}$  Janus micelles stained with B)  $OsO_4$  for 30 sec and C)  $RuO_4$  for 7 min. Staining with  $OsO_4$  vapour was conducted under vacuum (ca. 50 mbar) and staining with  $RuO_4$  vapour under ambient conditions, respectively.

One unique property of Janus and patchy micelles is their out-standing interfacial activity, being attributed to the synergy between their particulate nature (“Pickering effect”) and the amphiphilicity of the microphase-separated corona.[7,11,12,29] Janus and patchy cylindrical micelles with PS and PMMA corona compartments have been shown to exhibit identical interfacial activities at comparable micelle lengths.[29] This can be attributed to the ability of the patchy corona to adapt to the interface by selective collapse/swelling of the respective insoluble/soluble corona block, forming an “in-situ Janus” structure at the interface. Hence, for the produced  $S_{280}E_{1250}EO_{670}$  Janus micelles an even higher interfacial activity compared to that

of patchy SEM micelles might be expected because of the stronger amphiphilic character of the PS/PEO corona.

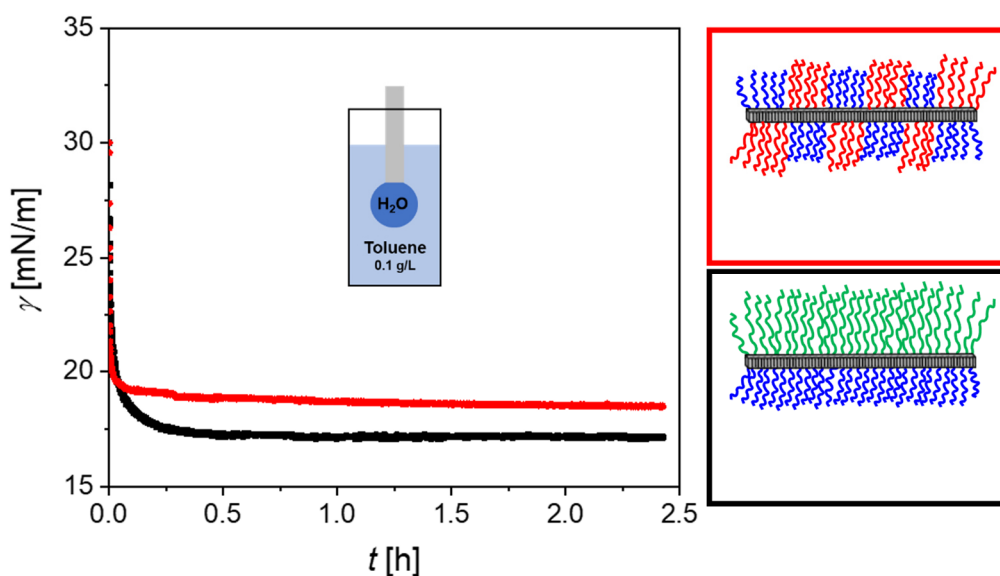


**Figure 7.4.** Interfacial tension isotherms of amphiphilic  $S_{280}E_{1250}EO_{670}$  Janus micelles compared with patchy  $S_{330}E_{1360}M_{760}$  micelles at the water/toluene interface ( $c = 0.1 \text{ g}\cdot\text{L}^{-1}$ ). Interfacial tension of pristine water/toluene interface:  $\gamma = 33.2 \text{ mN}\cdot\text{m}^{-1}$ .

Figure 7.4 displays the results from pendant drop tensiometer measurements at the water/toluene interface for worm-like, patchy  $S_{330}E_{1360}M_{760}$  and Janus-type  $S_{280}E_{1250}EO_{670}$  micelles with comparable lengths ( $l \approx 700 \text{ nm}$ , Table S7.1) and corona blocks of comparable degrees of polymerization. Already at a very low concentration of  $c = 0.1 \text{ g}\cdot\text{L}^{-1}$  the  $S_{280}E_{1250}EO_{670}$  Janus micelles reduce the quasi-equilibrium interfacial tension to  $\gamma = 17.2 \pm 0.03 \text{ mN}\cdot\text{m}^{-1}$ , being significantly lower compared to the value reached by the patchy  $S_{330}E_{1360}M_{760}$  micelles ( $\gamma = 18.5 \pm 0.02 \text{ mN}\cdot\text{m}^{-1}$ ). This convincingly demonstrates the impact of the more amphiphilic nature of the PS/PEO corona on the interfacial activity of  $S_{280}E_{1250}EO_{670}$  Janus micelles.

In conclusion, this work shows that worm-like, amphiphilic Janus micelles with a crystalline PE core are accessible via CDSA of a double crystalline triblock terpolymer, polystyrene-*block*-poly-ethylene-*block*-poly(ethylene oxide) (PS-*b*-PE-*b*-PEO). The combination of two strongly incompatible corona blocks (PS and PEO) together with the ability of the PEO corona block to crystallize seems to be decisive for the formation of a Janus-type microphase-separated corona. Hence, enthalpy (in terms of incompatibility and crystallization) wins over entropy, which would instead favour a patch-like microphase-separated corona. The excellent interfacial activity of these amphiphilic Janus micelles could be applied in the stabilization of emulsions

or for the compatibilization of polymer blends. Furthermore, this approach might stimulate further research on CDSA of double crystalline triblock terpolymers for the preparation of 1D (cylindrical or worm-like) Janus micelles, which are more difficult to prepare compared to spherical Janus micelles. This in turn can open new routes to hierarchical self-assemblies based on 1D Janus micelles. A more fundamental, but highly relevant aspect is the impact of the crystalline core-forming block on the crystallization of the corona block upon CDSA, which will be addressed in future work.

## Acknowledgements

This project was financed by the German Research Foundation within SFB 840, project A2. We thank E. Fuchs, A. Schedl and D. Pirner for their support during preliminary studies. CH acknowledges support by the Graduate School of the University of Bayreuth.

**Keywords:** Janus • patchy • worm-like micelles • triblock terpolymers • crystallization-driven self-assembly

## References

- [1] A. H. Gröschel, A. H. E. Müller, *Nanoscale* **2015**, *7*, 11841–11876.
- [2] J. Du, R. K. O'Reilly, *Chem. Soc. Rev.* **2011**, *40*, 2402.
- [3] U. Trichler, S. Pearce, J. Gwyther, G. R. Whittell, I. Manners, *Macromolecules* **2017**, *50*, 3439–3463.
- [4] K. Zhang, M. Jiang, D. Chen, *Prog. Polym. Sci.* **2012**, *37*, 445–486.
- [5] I. W. Wyman, G. Liu, *Polymer* **2013**, *54*, 1950–1978.
- [6] W. Li, H. Palis, R. Mérindol, J. Majimel, S. Ravaine, E. Duguet, *Chem. Soc. Rev.* **2020**, *49*, 1955–1976.
- [7] K. Chen, X. Hu, N. Zhu, K. Guo, *Macromol. Rapid Commun.* **2020**, *41*, 2000357.
- [8] A. Kirillova, C. Marschelke, A. Synytska, *ACS Appl. Mater. Interfaces* **2019**, *11*, 9643–9671.
- [9] C. Marschelke, A. Fery, A. Synytska, *Colloid Polym. Sci.* **2020**, *298*, 841–865.
- [10] T. Pelras, C. S. Mahon, M. Müllner, *Angew. Chem. Int. Ed.* **2018**, *57*, 6982–6994.
- [11] A. Walther, A. H. E. Müller, *Chem. Rev.* **2013**, *113*, 5194–5261.

- [12] Q. Yang, K. Loos, *Polym. Chem.* **2017**, *8*, 641–654.
- [13] J. Zhang, B. A. Grzybowski, S. Granick, *Langmuir* **2017**, *33*, 6964–6977.
- [14] C. Hils, I. Manners, J. Schöbel, H. Schmalz, *Polymers* **2021**, *13*, 1481.
- [15] X. Wang, G. Guerin, H. Wang, Y. Wang, I. Manners, M. A. Winnik, *Science* **2007**, *317*, 644–647.
- [16] J. B. Gilroy, T. Gädt, G. R. Whittell, L. Chabanne, J. M. Mitchels, R. M. Richardson, M. A. Winnik, I. Manners, *Nat. Chem.* **2010**, *2*, 566–570.
- [17] S. Ganda, M. H. Stenzel, *Prog. Polym. Sci.* **2020**, *101*, 101195.
- [18] L. MacFarlane, C. Zhao, J. Cai, H. Qiu, I. Manners, *Chem. Sci.* **2021**, *12*, 4661–4682.
- [19] J. Schöbel, C. Hils, A. Weckwerth, M. Schlenk, C. Bojer, M. C. A. Stuart, J. Breu, S. Förster, A. Greiner, M. Karg, H. Schmalz, *Nanoscale* **2018**, *10*, 18257–18268.
- [20] J. Schmelz, M. Karg, T. Hellweg, H. Schmalz, *ACS Nano* **2011**, *5*, 9523–9534.
- [21] A. M. Oliver, J. Gwyther, M. A. Winnik, I. Manners, *Macromolecules* **2018**, *51*, 222–231.
- [22] A. Nunns, G. R. Whittell, M. A. Winnik, I. Manners, *Macromolecules* **2014**, *47*, 8420–8428.
- [23] J. Xu, H. Zhou, Q. Yu, G. Guerin, I. Manners, M. A. Winnik, *Chem. Sci.* **2019**, *10*, 2280–2284.
- [24] J. Xu, H. Zhou, Q. Yu, I. Manners, M. A. Winnik, *J. Am. Chem. Soc.* **2018**, *140*, 2619–2628.
- [25] J. R. Finnegan, D. J. Lunn, O. E. C. Gould, Z. M. Hudson, G. R. Whittell, M. A. Winnik, I. Manners, *J. Am. Chem. Soc.* **2014**, *136*, 13835–13844.
- [26] S. Song, X. Liu, E. Nikbin, J. Y. Howe, Q. Yu, I. Manners, M. A. Winnik, *J. Am. Chem. Soc.* **2021**, *143*, 6266–6280.
- [27] J. Schöbel, M. Burgard, C. Hils, R. Dersch, M. Dulle, K. Volk, M. Karg, A. Greiner, H. Schmalz, *Angew. Chem. Int. Ed.* **2017**, *56*, 405–408.
- [28] C. Hils, M. Dulle, G. Sitaru, S. Gekle, J. Schöbel, A. Frank, M. Drechsler, A. Greiner, H. Schmalz, *Nanoscale Adv.* **2020**, *2*, 438–452.
- [29] J. Schmelz, D. Pirner, M. Krekhova, T. M. Ruhland, H. Schmalz, *Soft Matter* **2013**, *9*, 11173.
- [30] T. Gegenhuber, M. Krekhova, J. Schöbel, A. H. Gröschel, H. Schmalz, *ACS Macro Lett.*

- 2016**, *5*, 306–310.
- [31] A. Frank, C. Hils, M. Weber, K. Kreger, H. Schmalz, H. Schmidt, *Angew. Chem. Int. Ed.* **2021**, anie.202105787.
- [32] I. Erukhimovich, P. E. Theodorakis, W. Paul, K. Binder, *J. Chem. Phys.* **2011**, *134*, 054906.
- [33] G. Xie, P. Krys, R. D. Tilton, K. Matyjaszewski, *Macromolecules* **2017**, *50*, 2942–2950.
- [34] T. Stephan, S. Muth, M. Schmidt, *Macromolecules* **2002**, *35*, 9857–9860.
- [35] R. Stepanyan, A. Subbotin, G. ten Brinke, *Macromolecules* **2002**, *35*, 5640–5648.
- [36] P. E. Theodorakis, W. Paul, K. Binder, *Eur. Phys. J. E* **2011**, *34*, 52.
- [37] Y. Li, E. Themistou, J. Zou, B. P. Das, M. Tsianou, C. Cheng, *ACS Macro Lett.* **2012**, *1*, 52–56.
- [38] A. Z. Samuel, S. Ramakrishnan, *Macromolecules* **2012**, *45*, 2348–2358.
- [39] S. Chakraborty, S. G. Ramkumar, S. Ramakrishnan, *Macromolecules* **2017**, *50*, 5004–5013.
- [40] R. Sarkar, E. B. Gowd, S. Ramakrishnan, *Polym. Chem.* **2019**, *10*, 1730–1740.
- [41] D. Neugebauer, M. Theis, T. Pakula, G. Wegner, K. Matyjaszewski, *Macromolecules* **2006**, *39*, 584–593.
- [42] T. Rudolph, M. Von Der Lühe, M. Hartlieb, S. Norsic, U. S. Schubert, C. Boisson, F. D’Agosto, F. H. Schacher, *ACS Nano* **2015**, *9*, 10085–10098.
- [43] T. Rudolph, A. Nunns, S. Stumpf, C. Pietsch, F. H. Schacher, *Macromol. Rapid Commun.* **2015**, *36*, 1651–1657.
- [44] H. Shaikh, X.-H. Jin, R. L. Harniman, R. M. Richardson, G. R. Whittell, I. Manners, *J. Am. Chem. Soc.* **2020**, *142*, 13469–13480.
- [45] A. Boschetti-de-Fierro, A. T. Lorenzo, A. J. Müller, H. Schmalz, V. Abetz, *Macromol. Chem. Phys.* **2008**, *209*, 476–487.
- [46] S. Yeh, K. Wei, Y. Sun, U. Jeng, K. S. Liang, *Macromolecules* **2003**, *36*, 7903–7907.
- [47] H. Schmalz, J. Schmelz, M. Drechsler, J. Yuan, A. Walther, K. Schweimer, A. M. Mihut, *Macromolecules* **2008**, *41*, 3235–3242.
- [48] J. Schmelz, H. Schmalz, *Polymer* **2012**, *53*, 4333–4337.

## Supporting Information

### Experimental Procedures and Methods

**Materials.** All chemicals were used as received unless otherwise noted. Poly(ethylene oxide) (PEO,  $M_n = 10.000$ , Sigma-Aldrich), tris(triphenylphosphine)rhodium(I) chloride (Wilkinson's catalyst, 99.9% trace metals basis, Sigma-Aldrich), *iso*-propanol (*i*PrOH, p.a., ACS reagent,  $\geq 99.8\%$  (GC), Sigma-Aldrich), deuterated chloroform ( $CDCl_3$ , 99.8%, Deutero), hydrochloric acid (37 wt% in water, VWR), ruthenium(III) chloride hydrate (ReagentPlus<sup>®</sup>, Sigma-Aldrich), sodium hypochlorite solution (NaOCl, 10 – 15 wt% in water, Sigma-Aldrich), osmium tetroxide ( $OsO_4$ , ReagentPlus<sup>®</sup>, 99.8%, Sigma-Aldrich), tetrahydrofuran (THF,  $\geq 99.9\%$ , Sigma-Aldrich), toluene ( $\geq 99.5\%$ , AnalaR NORMAPUR<sup>®</sup> ACS, VWR), acetone (p.a., ACS reagent,  $\geq 99.5\%$  (GC), Sigma-Aldrich) and dialysis membrane (Spectra/Por<sup>®</sup> 3).

**Synthesis of the SEEO triblock terpolymer.** The polystyrene-*block*-polyethylene-*block*-poly(ethylene oxide) (SEEO) triblock terpolymer was synthesized by a combination of sequential living anionic polymerization to yield the corresponding polystyrene-*block*-poly(1,4-butadiene)-*block*-poly(ethylene oxide) (PS-*b*-PB-*b*-PEO) precursor, followed by catalytic hydrogenation. The sequential anionic polymerization of styrene, butadiene and ethylene oxide was conducted in toluene with *sec*-BuLi as initiator utilizing the phosphazene base *t*-BuP<sub>4</sub> to promote polymerization of ethylene oxide in the presence of Li<sup>+</sup> counter ions.[1] The polymerization of butadiene under the conditions employed led to a preferential 1,4-addition, which is essential to obtain the corresponding “pseudo-polyethylene” structure after hydrogenation. The hydrogenation of the obtained S<sub>280</sub>B<sub>630</sub>EO<sub>640</sub> triblock terpolymer (indices denote the average degrees of polymerization of the respective blocks) resulted in the corresponding S<sub>280</sub>E<sub>1250</sub>EO<sub>670</sub> triblock terpolymer. Homogeneous catalytic hydrogenation was carried out with Wilkinson's catalyst (1 mol% with respect to double bonds) in toluene at 60 °C and 60 bar H<sub>2</sub> pressure for 3 d. The used S<sub>330</sub>E<sub>1360</sub>M<sub>760</sub> triblock terpolymer is identical to that described in our previous work.[2]

**Preparation of worm-like crystalline core micelles (wCCMs).** The Janus and patchy wCCMs were prepared by crystallization-driven self-assembly (CDSA) of the triblock terpolymers S<sub>280</sub>E<sub>1250</sub>EO<sub>670</sub> and S<sub>330</sub>E<sub>1360</sub>M<sub>760</sub> in toluene, respectively.[3] To this end, the triblock terpolymers were dissolved in toluene ( $c = 10 \text{ g}\cdot\text{L}^{-1}$ ) at 80 °C for 30 min and subsequently

cooled to the crystallization temperature ( $T_c$ , Table S7.1) of the polyethylene (PE) middle block, using a thermostated shaker unit (HLC-MKR 13, Ditabis). The self-assembly process was allowed to proceed for 24 h at a shaking rate of 200 rpm. Afterwards, the PE core was annealed at  $T_a$  (Table S7.1) for 5 min followed by cooling to 20 °C. In addition, micellar dispersions ( $c = 0.5 \text{ g}\cdot\text{L}^{-1}$  in toluene) were dialyzed for 6 d against acetone/*i*PrOH (4/1, v/v), followed by dilution to  $c = 0.1 \text{ g}\cdot\text{L}^{-1}$  by slowly adding the same solvent mixture over 2.5 h.

**Table S7.1.** Characteristics of the employed triblock terpolymers and micellar dispersions.

Triblock terpolymer <sup>[a]</sup>	$M_n / \text{kg}\cdot\text{mol}^{-1}$ ( $\mathcal{D}$ ) <sup>[b]</sup>	$T_c / \text{°C}$ <sup>[c]</sup>	$T_a / \text{°C}$ <sup>[c]</sup>	$l(\text{wCCMs}) / \text{nm}$ <sup>[d]</sup>
S <sub>280</sub> E <sub>1250</sub> EO <sub>670</sub>	92 (1.03)	28.5	45.0	686 ± 275
S <sub>330</sub> E <sub>1360</sub> M <sub>760</sub>	148 (1.03)	22.0	41.0	692 ± 269

[a] Indices denote the number average degree of polymerization. [b] Determined from the respective precursor triblock terpolymers with polybutadiene middle blocks using a combination of MALDI-ToF and <sup>1</sup>H-NMR for  $M_n$  calculation, dispersity ( $\mathcal{D}$ ) determined by CHCl<sub>3</sub>-SEC employing a PS calibration. [c] Measured by  $\mu$ -DSC ( $c = 10 \text{ g}\cdot\text{L}^{-1}$ ). [d] Average micelle length ± standard deviation as determined by TEM image analyses of at least 100 micelles.

**Nuclear Magnetic Resonance (NMR) Spectroscopy.** The triblock terpolymers were characterized by <sup>1</sup>H NMR spectroscopy (Bruker Ultrashield 300 spectrometer) using CDCl<sub>3</sub> as solvent. S<sub>280</sub>E<sub>1250</sub>EO<sub>670</sub> was analysed at 52 °C to ensure complete dissolution of the PE block. The signal assignment was supported by simulations with the NMR software MestReNova.

**Size-Exclusion Chromatography (SEC).** SEC measurements were performed on an instrument equipped with two PSS-SDV gel columns (particle size = 5 μm) with porosity range from 10<sup>2</sup> to 10<sup>5</sup> Å (PSS, Mainz, Germany). Chloroform (HPLC grade) was used as solvent (for dissolving polymer and as eluting solvent). The polymers were dissolved and filtered through a 0.22 μm PTFE filter before analysis. The samples were measured on a SEC 1260 Infinity system (Agilent Technologies) at a flow rate of 0.5 mL·min<sup>-1</sup> at 23 °C, using a refractive index detector (Agilent Technologies). The calibration was done with narrowly distributed polystyrene standards (PSS calibration kit) and toluene (HPLC grade) was used as internal standard.

**Micro Differential Scanning Calorimetry ( $\mu$ -DSC).** The measurements were performed on a SETARAM Micro DSC III using sealed measuring cells ("batch cells",  $V = 1$  mL) filled with approx. 0.7 mL of the polymer dispersions ( $c = 10$  g·L<sup>-1</sup> in toluene). A scanning rate of 0.5 K·min<sup>-1</sup> was employed and pure toluene was used as reference.

**Transmission Electron Microscopy (TEM).** The TEM measurements were carried out with a Zeiss CEM902, a ZEISS / LEO EM922 Omega and a JEOL JEM-2200FS field emission TEM. All microscopes are energy filtering transmission electron microscopes (EFTEMs), operated at an acceleration voltage of 80 kV and 200 kV, respectively. Zero-loss filtered micrographs ( $\Delta E \approx 0$  eV) were taken with a side mounted CCD camera system (Orius, Gatan) in case of the Zeiss CEM902, a bottom mounted CCD camera (Ultrascan 1000, Gatan) in case of the ZEISS Omega and a bottom mounted CMOS camera system (OneView, Gatan) for the JEOL JEM-2200FS, respectively. The images were processed with a digital image processing software (Digital Micrograph DM 1.9, DM 2.3 and DM 3.3, Gatan). For TEM analysis of the triblock terpolymer micelle dispersions, the samples were diluted to a concentration of  $c = 0.1$  g·L<sup>-1</sup> and stirred for 30 min at room temperature. Subsequently, 10  $\mu$ L of the respective dispersion was applied to a carbon-coated copper grid and residual solvent was removed by blotting with a filter paper followed by drying of the coated copper grid in a vacuum oven (24 h,  $1 \cdot 10^{-5}$  mbar, room temperature). For RuO<sub>4</sub> staining the samples were treated for 7 min with RuO<sub>4</sub> vapor, which was formed in situ from RuCl<sub>3</sub> hydrate and NaOCl. Staining with OsO<sub>4</sub> was conducted for 30 sec under vacuum (ca. 50 mbar). After staining, the samples were stored for at least 1 h in a fume hood to ensure that any not reacted staining agents were completely removed. The average lengths of the triblock terpolymer micelles were determined by measuring at least 100 micelles using the software ImageJ.[4] The greyscale analyses were performed with the Digital Micrograph software package (Gatan).

**Interfacial Tension** measurements were performed employing a DS25 from Krüss. First, the interfacial tension of pure toluene in a cuvette (10 mm, QS) was determined with the software "Advanced Drop Shape Analysis" (version 1.3.1.0) and the method "Pendant Drop" using a droplet volume of  $V = 35$   $\mu$ L (deionized water). Micellar dispersions were measured with a concentration of  $c = 0.1$  g·L<sup>-1</sup>. The quasi-equilibrium interfacial tensions were determined as average over the last 30 min of the respective measurement, where the interfacial tension levels off.

## Supporting Figures

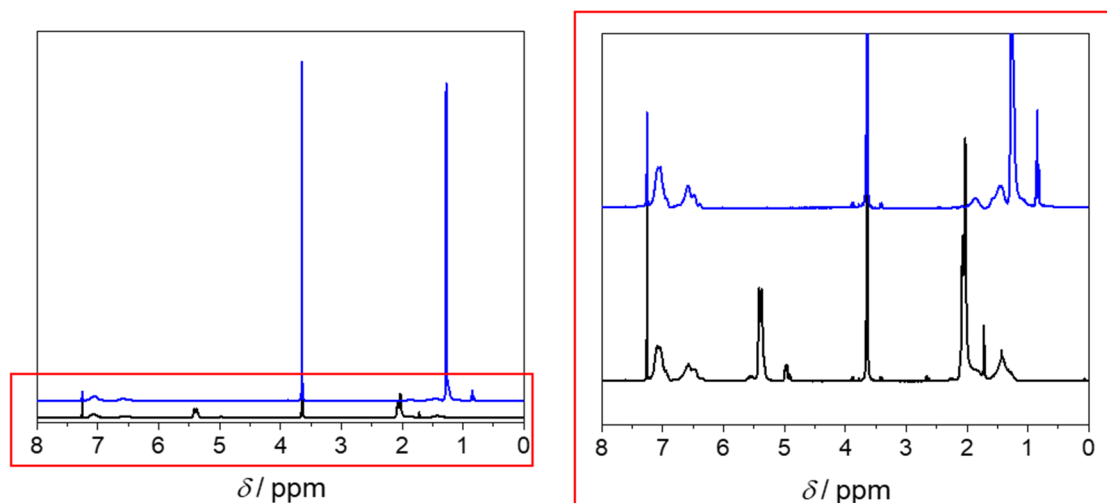


**Figure S7.1.**  $^1\text{H}$  NMR in  $\text{CDCl}_3$  of  $\text{S}_{280}\text{B}_{630}\text{EO}_{640}$  (blue) and  $\text{S}_{280}\text{E}_{1250}\text{EO}_{670}$  (black,  $T = 52\text{ }^\circ\text{C}$ ). Complete hydrogenation of the polybutadiene (PB) middle block to polyethylene is proven by the absence of PB related peaks between ca. 5 – 5.5 ppm in the  $^1\text{H}$  NMR spectrum of  $\text{S}_{280}\text{E}_{1250}\text{EO}_{670}$ .

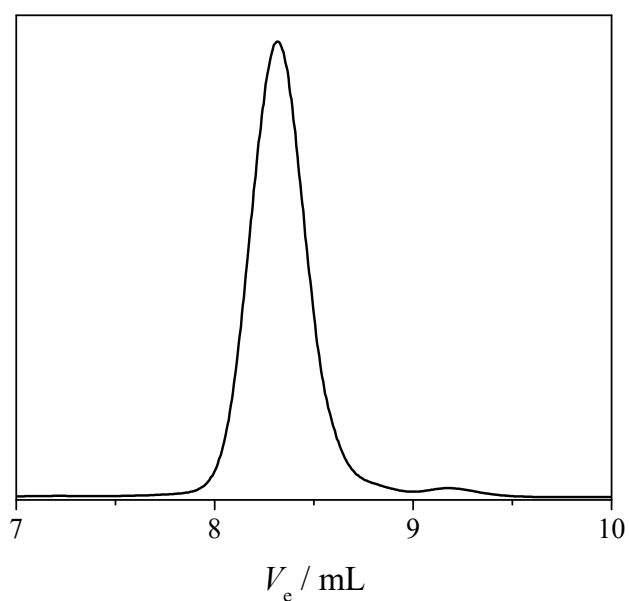


**Figure S7.2.**  $\text{CHCl}_3$ -SEC of the  $\text{S}_{280}\text{B}_{630}\text{EO}_{640}$  triblock terpolymer.

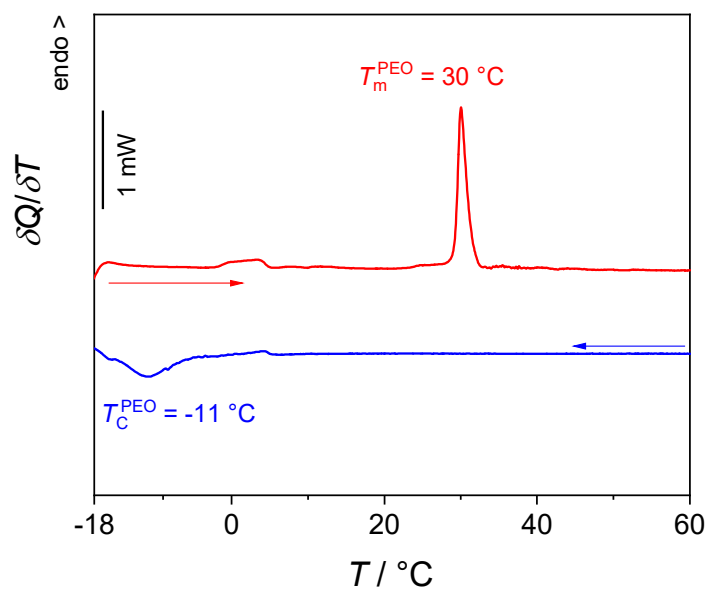


**Figure S7.3.**  $\mu$ -DSC heating and cooling traces of neat PEO in toluene ( $c = 3 \text{ g}\cdot\text{L}^{-1}$ ).

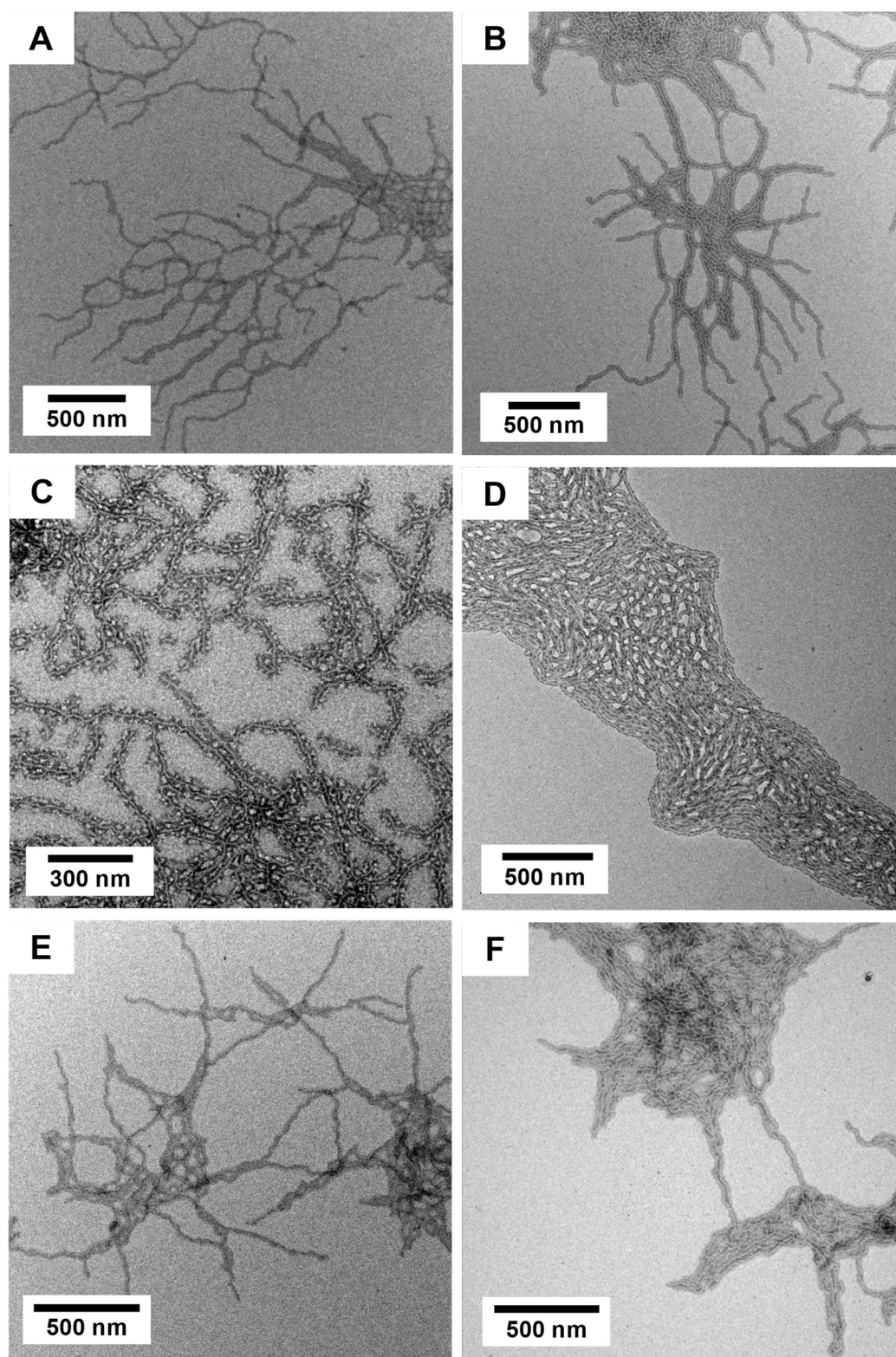


**Figure S7.4.** TEM measurements of worm-like crystalline-core micelles. A)  $S_{280}E_{1250}EO_{670}$  ( $c = 0.1 \text{ g}\cdot\text{L}^{-1}$ , toluene), B)  $S_{280}E_{1250}EO_{670}$  ( $c = 0.1 \text{ g}\cdot\text{L}^{-1}$ , toluene) stained with  $\text{RuO}_4$ , C)  $S_{330}E_{1360}M_{760}$  ( $c = 0.1 \text{ g}\cdot\text{L}^{-1}$ , toluene) stained with  $\text{RuO}_4$ , D)  $S_{330}E_{1360}M_{760}$  ( $c = 0.1 \text{ g}\cdot\text{L}^{-1}$ ) dialysed against acetone/*iso*-propanol (4/1 v/v) and stained with  $\text{RuO}_4$ , E)  $S_{280}E_{1250}EO_{670}$  ( $c = 0.1 \text{ g}\cdot\text{L}^{-1}$ ) dialysed against acetone/*iso*-propanol (4/1 v/v) and stained with  $\text{OsO}_4$ , and F)  $S_{280}E_{1250}EO_{670}$  ( $c = 0.1 \text{ g}\cdot\text{L}^{-1}$ ) dialysed against acetone/*iso*-propanol (4/1 v/v) and stained with  $\text{RuO}_4$ .

## References

- [1] A. Boschetti-de-Fierro, A. T. Lorenzo, A. J. Müller, H. Schmalz, V. Abetz, *Macromol. Chem. Phys.* **2008**, *209*, 476–487.
- [2] J. Schmelz, H. Schmalz, *Polymer* **2012**, *53*, 4333–4337.
- [3] J. Schmelz, M. Karg, T. Hellweg, H. Schmalz, *ACS Nano* **2011**, *5*, 9523–9534.
- [4] W. S. Rasband, *ImageJ*, U. S. National Institutes of Health: Bethesda, Maryland, USA, 1997 - 2018.



## 8 Outlook

The excellent performance of gold nanoparticle loaded patchy fibre mats developed in this thesis could be applied for the construction of further heterogeneous catalysts, also with adapted properties of the template itself. Here, the double-responsive (pH and temperature) solubility of the poly(*N,N*-dialkylaminoethyl methacrylamide) patches, used for the immobilization of nanoparticles, could add further functionality like self-regulation of catalytic reactions. In this context, catalytically active nanoparticles such as palladium or platinum could be of particular interest. As a result, further technologically relevant reactions such as hydrogenation or cross-coupling could be realized. The use of nanoparticles with special optical properties such as photoluminescence or electrical conductivity could pave the way to new applications. Cadmium selenide, lead(II) sulfide or zinc oxide, for example, could be used for this purpose.

New hierarchical structures could be created by using other tailored patchy fibres as well as neat patchy worm-like crystalline-core micelles. In this context, the use of ABC triblock terpolymers with a crystalline component in the corona could be of particular interest, as crystalline corona patches could act as seeds for “grafting-from” crystallization-driven self-assembly. The substitution of polyethylene could lead to the formation of more temperature-stable micelles with a crystalline core. Conceivable here would be, for example, the use of poly(*L*-lactide)/poly(*D*-lactide) stereocomplexes.

Novel microparticle morphologies of triblock terpolymers with a crystallizable middle or end block could be specifically produced by confinement assembly. Of particular interest could also be racemic mixtures of poly(*L*-lactide)- and poly(*D*-lactide)/-based diblock copolymers leading to the formation of complex or "pseudo" triblock copolymer morphologies, respectively.



## Glossary

%	percentage
$[\text{Fe}(\text{CN})_6]^{3-}$	hexacyanoferrate(III)
°	degree
°C	degree Celsius
μ	micro
μg	microgram
μm	micrometre
1D	one-dimensional
2D	two-dimensional
3D	three-dimensional
AuNP	gold nanoparticle
BCP	block copolymer
BSE	back scattered electron
BTA	benzene-1,3,5-tricarboxamide
BTA-Methyl	$N^1, N^3, N^5$ -tris[2-(dimethylamino)-ethyl]-1,3,5-benzenetricarboxamide
$c$	concentration
CCM	crystalline-core micelle
CDSA	crystallization-driven self-assembly
cm <sup>2</sup>	square centimetre
CTAB	cetrimonium bromide
$d$	width
g	gram
$\gamma$	interfacial tension

---

ICP-OES	inductively coupled plasma optical emission spectrometry
kg	kilogram
L	litre
LCST	lower critical solution temperature
$L_n$	number average micelle length
$L_w$	weight average micelle length
MCM	multicompartment core micelle
$m_{seed}$	mass of seeds
$m_{unimer}$	mass of unimers
<i>n</i> -BuOH	<i>n</i> -butanol
NP	nanoparticle
NW	nonwoven
OPV	oligo( <i>p</i> -phenylene vinylene)
OsO <sub>4</sub>	osmium tetroxide
P2VP	poly(2-vinyl pyridine)
P3EHT	poly(3-(2'-ethylhexyl)thiophene)
P3HT	poly(3-hexyl thiophene)
PB	polybutadiene
PCEMA	poly(2-cinnamoyloxyethyl methacrylate)
PDEA	poly( <i>N,N</i> -diethylaminoethyl methacrylamide)
PDHF	poly(di- <i>n</i> -hexylfluorene)
PD <i>i</i> PrA	poly( <i>N,N</i> -diisopropylaminoethyl methacrylamide)
PD <i>x</i> A	poly( <i>N,N</i> -dialkylaminoethyl methacrylamide)
PE	polyethylene
PEO	poly(ethylene oxide)
PFG	poly(ferrocenyl dimethylgermane)

---

PFS	poly(ferrocenyl dimethylsilane)
PGMA	poly(glyceryl monomethacrylate)
PI	polyisoprene
PLLA	poly( <i>L</i> -lactide)
PMMA	poly(methyl methacrylate)
PMVS	poly(methylvinylsiloxane)
<i>Pn</i> BA	poly( <i>n</i> -butyl acrylate)
PNIPAm	poly( <i>N</i> -isopropylacrylamide)
PS	polystyrene
<i>Pt</i> BA	poly( <i>tert</i> -butyl acrylate)
RuO <sub>4</sub>	ruthenium tetroxide
SAXS	small-angle X-ray scattering
<i>s</i> CCM	spherical crystalline-core micelle
SED <sub>x</sub> A	PS- <i>b</i> -PE- <i>b</i> -PD <sub>x</sub> A
SEM	PS- <i>b</i> -PE- <i>b</i> -PMMA
SES	PS- <i>b</i> -PE- <i>b</i> -PS
<i>T</i>	temperature
<i>T</i> <sub>a</sub>	annealing temperature
TBP	4- <i>tert</i> -butylphenol
<i>T</i> <sub>c</sub>	crystallization temperature
TEM	transmission electron microscopy
<i>T</i> <sub>evap</sub>	evaporation temperature
THF	tetrahydrofuran
<i>T</i> <sub>m</sub>	melting temperature
UCST	upper critical solution temperature
UV-Vis	ultraviolet–visible

wCCM	worm-like crystalline-core micelle
wt. %	mass fraction
$\mu$ -SIF	miktoarm PS- <i>arm</i> -PI- <i>arm</i> -PFS

## Acknowledgement

First, I want to thank Prof. Dr. Andreas Greiner and Dr. Holger Schmalz for the opportunity to work on this interesting topic. I appreciated all the scientific discussions, support, suggestions and ideas, which finally led to this thesis. I would also like to thank them for letting me follow my ideas and inspirations and giving me the opportunity to develop myself further. I would like to thank Prof. Dr. Seema Agarwal for the continuous support and academic discussions that helped me to improve my work. I would like to express my gratitude for the financial support from the German Research Foundation within the framework of the *Collaborative Research Centre SFB840* (Project A2).

Next, I want to thank Prof. Dr. Birgit Weber for being my mentor in the *BayNat* program. I would like to thank my cooperation partners for their support and help. Without them, it would not have been possible for me to work on all these topics. I want to thank Dr. Markus Drechsler and Carmen Kunert (TEM), Dr. Ulrich Mansfeld and Andreas Frank (SEM), Dr. Martin Dulle (SAXS) and Rika Schneider (SEC, AF4) for their support and scientific discussions of the different analytical methods.

My special thanks go to all those who supported and acted in the background so that a successful doctoral graduation was possible in the first place. In addition, I want to thank the mechanics workshop around Frank Neumann for many conversions and custom-made products. The team of the glassblower, who also always supported me with plenty of handicraft. I want to thank the pump and electronics workshop for quick and straightforward repairs of our equipment. Furthermore, I want to thank Gaby Oliver, Niko Plocher, Ramona Lechner, Christina Lindörfer and Sieglinde Hörath for supporting the bureaucracy and organizing appointments. Likewise, I also thank the post office in the NWII, and especially Reinhold Schoberth, who always provided us with plenty of parcels. I want to thank Annette Krökel for ordering and organizing new chemicals.

Furthermore, I want to thank the whole MC2 group for the support and scientific discussions. I would like to thank the MC1 group for the pleasant atmosphere and support during my work, as well as for the fun evenings and activities within university life. Especially, I want to thank Thomas, Martin, Adrian, Andreas, Christina, Rika and Lisa who all gave me incredible support in every situation.

Additionally, I want to thank all my students who did practical lab courses with me: Franziska, Emma and Roman. Thank you for many experiments and discussions and for making my work better.

For the discussions and the support in every situation, I want to thank Judith.

My special thanks go to Lisa's family, who not only took care of my physical well-being, but also supported me in many ways outside the university. Finally, I would like to thank my friends, Lisa and especially my family for the amazing support in every part of my life.

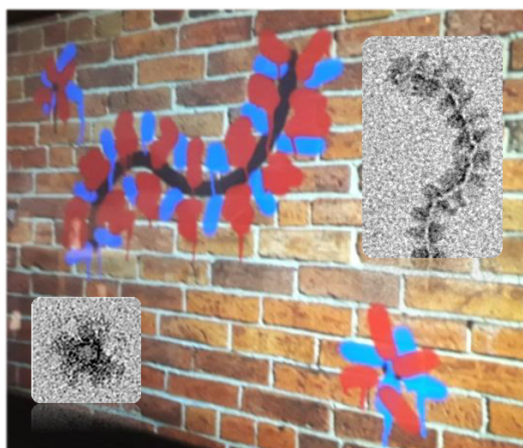
**Thank you!**

## Appendix

### Patchy Micelles with a Crystalline Core: Self-Assembly Concepts, Properties, and Applications

*Christian Hils*<sup>1</sup>, *Ian Manners*<sup>2</sup>, *Judith Schöbel*<sup>3,\*</sup> and *Holger Schmalz*<sup>1,4,\*</sup>

- 1 University of Bayreuth, Macromolecular Chemistry II, Universitätsstraße 30, 95440 Bayreuth, Germany
- 2 University of Victoria, Department of Chemistry, University of Victoria, 3800 Finnerty Road, Victoria, British Columbia V8P 5C2, Canada
- 3 Fraunhofer Institute for Applied Polymer Research IAP, Geiselbergstraße 69, 14476 Potsdam-Golm, Germany
- 4 University of Bayreuth, Bavarian Polymer Institute (BPI), Universitätsstraße 30, 95440 Bayreuth, Germany



Published in: *Polymers*, **2021**, *13*, 1481

Reprinted with permission from MDPI.

**Abstract**

Crystallization-driven self-assembly (CDSA) of block copolymers bearing one crystallizable block has emerged to be a powerful and highly relevant method for the production of one- and two-dimensional micellar assemblies with controlled length, shape, and corona chemistries. This gives access to a multitude of potential applications, from hierarchical self-assembly to complex superstructures, catalysis, sensing, nanomedicine, nanoelectronics, and surface functionalization. Related to these applications, patchy crystalline-core micelles, with their unique, nanometer-sized, alternating corona segmentation, are highly interesting, as this feature provides striking advantages concerning interfacial activity, functionalization, and confinement effects. Hence, this review aims to provide an overview of the current state of the art with respect to self-assembly concepts, properties, and applications of patchy micelles with crystalline cores formed by CDSA. We have also included a more general discussion on the CDSA process and highlight block-type co-micelles as a special type of patchy micelle, due to similarities of the corona structure if the size of the blocks is well below 100 nm.

**Keywords:** crystallization-driven self-assembly (CDSA), crystalline-core micelles, patchy micelles, block copolymers.

## 1. Introduction

The solution self-assembly of block copolymers (BCPs) has paved the way to a vast number of micellar assemblies of various shapes (e.g. spheres, cylinders, vesicles, platelets, core-shell, core-shell-corona, and compartmentalized (core or corona) structures) and hierarchical superstructures, as well as hybrids with fascinating applications in drug delivery and release, as emulsifiers/blend compatibilizers, in nanoelectronics, as responsive materials (temperature, pH, light), templates for nanoparticles, in heterogeneous catalysis, etc. [1–6]. A key prerequisite for controlling/programming the solution self-assembly is the synthesis of well-defined diblock and triblock (linear, star-shaped, ABA- or ABC-type) copolymers via controlled or living polymerization techniques, such as living anionic polymerization, reversible addition–fragmentation chain transfer, nitroxide-mediated, and atom transfer radical polymerization [5–9]. In general, anisotropic polymer micelles can be divided into three main categories: multicompartment core micelles (MCMs), surface-compartmentalized micelles, and a combination of both [2]. MCMs are generally defined as micellar assemblies with a solvophilic corona and a microphase-separated solvophobic core. According to the suggestion of Laschewsky et al., a key feature of multicompartment micelles is that the various subdomains in the micellar core feature substantially different properties to behave as separate compartments [10,11]. MCMs are commonly prepared via hierarchical self-assembly of suitable building blocks, which provide “sticky patches” [12–15]. Depending on the number and geometrical arrangement (linear, triangular, tetrahedral, etc.) of the “sticky patches”, as well as the volume fraction of the solvophilic block, various spherical, cylindrical, sheet-like, and vesicular MCMs are accessible [16–25]. For a deeper insight into this highly relevant topic, the reader is referred to recent extensive reviews on MCMs [26–31]. Surface-compartmentalized micelles are subdivided into micelles with a Janus-type (two opposing faces with different chemistry or polarity) or patch-like, microphase-separated corona, featuring several compartments of different chemistry or polarity (denoted as patchy micelles), as illustrated in Figure 1 for cylindrical micelles. Here, block co-micelles with a block-like arrangement of several (>2) surface compartments along the cylindrical long axis can be regarded as a special case of patchy micelles. It is noted that AB-type diblock co-micelles also represent Janus-type micelles, where the two opposing faces are arranged perpendicular to the cylindrical long axis. The broken symmetry of Janus particles offers efficient and distinctive means of targeting complex materials by hierarchical self-assembly and realize unique

properties and applications, like particulate surfactants, optical nanoproboscopes, biosensors, self-propulsion, and many more [32–41].

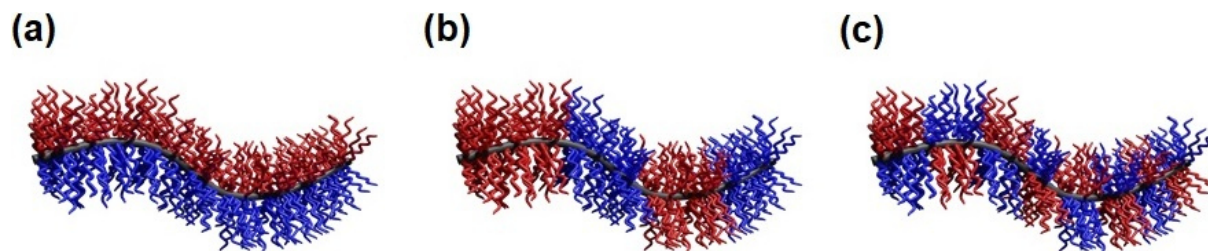


**Figure 1.** Schematic depiction of a cylindrical (a) Janus micelle, (b) block co-micelle, and (c) patchy micelle.

For the preparation of patchy micelles and polymersomes from amorphous BCPs, three main strategies can be applied: (i) self-assembly of ABC triblock terpolymers in selective solvents for the incompatible A and C blocks [42–48]; (ii) co-assembly of AB and CD diblock copolymers with selective interactions between the B and C blocks (e.g. hydrogen bonding, ionic interactions, solvophobic interactions) [49–52], resulting in patchy micelles with an insoluble mixed B/C core; and (iii) co-assembly of AB and BC diblock copolymers [53–56] where the B block forms the insoluble core. However, mostly spherical micelles or polymersomes with a patchy corona have been reported and only a few reports describe the preparation of one-dimensional (worm-like, cylindrical) assemblies with a patch-like compartmentalized corona, even though theoretical work on mixed polymer brushes predict their existence [57–61]. One of the rare but highly intriguing examples are *PtBA*–*b*–*PCEMA*–*b*–*PGMA* (poly(*tert*-butyl acrylate)–*block*–poly(2-cinnamoyloxyethyl methacrylate)–*block*–poly(glyceryl monomethacrylate)) and *PnBA*–*b*–*PCEMA*–*b*–*PtBA* (*PnBA*: poly(*n*-butyl acrylate)) triblock terpolymers [42,43,45]. For self-assembly, the triblock terpolymers were first dissolved in a good solvent for all blocks ( $\text{CH}_2\text{Cl}_2$ ,  $\text{CHCl}_3$ , or THF), followed by the addition of methanol (non-solvent for the middle block) to induce micelle formation. As an intermediate, cylindrical micelles with a patchy corona were formed first, with the *PtBA* blocks forming small circular patches in a corona mainly consisting of *PGMA* or *PnBA*. Upon further decreasing the solvent quality for the *PtBA* block (addition of MeOH), these cylinders can form double and triple helices via hierarchical self-assembly. This concept has also been applied to triblock terpolymers with a poly(2-hydroxyethyl methacrylate) middle block, having the potential for further modification by esterification of the pendant hydroxy functions [42]. Besides, crystallization-driven self-assembly (CDSA) is a highly versatile tool for the

preparation of well-defined cylindrical micelles of controlled length and length distribution, and has proven as a valuable method for the preparation of patchy cylindrical micelles.

This review will focus on the recent developments concerning self-assembly strategies for the production of crystalline-core micelles (CCMs) bearing a patchy corona, and will also address their unique properties and potential applications. As stated above, block co-micelles represent a special case of patchy micelles and thus, will be discussed only briefly. This is not only due to the usually larger size and sequential arrangement of surface compartments in the corona, in contrast to the more alternating arrangement in patchy cylindrical micelles (Figure 1b,c), but is also attributed to the substantially different self-assembly procedure. Block co-micelles are commonly prepared by sequential living CDSA of different diblock copolymers, whereas patchy micelles are formed by simultaneous CDSA of diblock copolymer mixtures or CDSA of ABC triblock terpolymers with crystallizable middle blocks. Hence, this review will be divided into four main sections, starting with a general consideration of CDSA. The second part gives a compact overview over self-assembly strategies used to form cylindrical and platelet-like block co-micelles. The different self-assembly concepts for patchy micelles with crystalline cores will be reviewed in the third section, followed by a discussion on properties and applications of these interesting compartmentalized nanostructures.

## 2. Crystallization-Driven Self-Assembly (CDSA)

As pointed out in the introduction, the preparation of one-dimensional (1D) cylindrical (or worm-like) micelles with controlled dimensions, low-length dispersities, and tailored corona structures and functionalities still remains a challenge in the self-assembly of fully amorphous BCPs. Besides, the introduction of a crystallizable block, which adds an additional and strong driving force for micelle formation, has turned out to be a highly efficient route to solve these issues. Consequently, the self-assembly of such BCPs, bearing crystallizable blocks, is termed crystallization-driven self-assembly (CDSA) [1,62,63]. This field was pioneered by studies on poly(ferrocenyl dimethylsilane) (PFS)-containing BCPs and is gaining increasing importance for the preparation of well-defined 1D and two-dimensional (2D) assemblies, especially since the discovery of living CDSA (Figure 2) [63–67]. Analogous to the living polymerization of monomers, CDSA can proceed in a living manner, employing small micellar fragments as seeds (Figure 2a: seeded growth) for the addition of unimers (molecularly dissolved BCPs with a crystallizable block). In this approach, the micellar seeds, also termed “stub-like” micelles,

are produced by vigorous sonication of long, polydisperse cylindrical micelles prepared by conventional CDSA. Owing to its living nature, the length of the produced cylindrical micelles shows a linear dependence on the unimer/seed ratio employed, and length dispersities are very low ( $L_w/L_n$  typically well below 1.1; where  $L_n$  is the number average and  $L_w$  the weight average micelle length).

Living CDSA can also be realized by using spherical CCMs as seeds [68], by self-seeding [69-71] (Figure 2a), and even directly by polymerization-induced CDSA (Fig. 2b) [72-74], i.e., via polymerization in the presence of seed micelles. The self-seeding approach also uses small micellar fragments that are heated in dispersion to a specific annealing temperature ( $T_a$ ), where most of the crystalline core is molten/dissolved and only a very minor fraction of crystallites survive. These act as seeds in the subsequent CDSA upon cooling (Figure 2a: self-seeding), and the length of the micelles can be controlled by a proper choice of  $T_a$ . If  $T_a$  is too low, the crystalline cores will not melt/dissolve, and the length distribution of the employed micellar fragments remains unchanged. On the other hand, if  $T_a$  is too high, the crystalline cores will melt/dissolve completely, and no crystallites will survive that could act as seeds. As a result, in between these two limiting cases, an increase in micelle length with increasing  $T_a$  is observed, as the fraction of surviving crystallites (seeds) decreases with  $T_a$ . This range of self-seeding temperatures can be very restricted, making length control difficult. Another drawback of these seed-based protocols is the low amount of cylindrical micelles that can be produced, as commonly rather dilute solutions have to be used. This can be overcome by the living polymerization-induced CDSA approach, enabling the production of uniform cylindrical micelles with concentrations up to ca. 10–20% (*w/w* solids) within a few hours. In a recent report, it was shown that living CDSA can even be stimulated by light, utilizing the photo-induced cis-trans isomerization in oligo(*p*-phenylenevinylene) (OPV)-based BCPs [75].

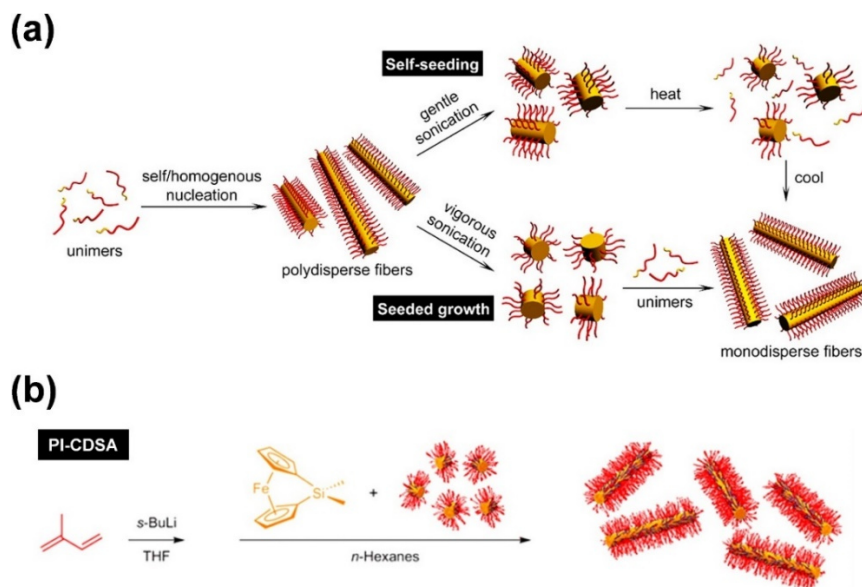


**Figure 2.** (a) Concepts for living CDSA, enabling the production of cylindrical micelles with defined length and narrow length distribution. Self-seeding employing seeds produced by thermal treatment of micelle fragments (top) and seeded growth using small micellar fragments (“stub”-like micelles) as seeds (bottom). (b) Living polymerization-induced CDSA (PI-CDSA) utilizing micellar seeds during anionic polymerization of the PFS block. After complete conversion, the reaction was quenched with 4-*tert*-butylphenol. (a) Reproduced from [76] with permission of the American Chemical Society (ACS).

Living CDSA has paved the way to a myriad of 1D and 2D micellar assemblies of controlled dimensions, including patchy and block co-micelles (both will be addressed in the next sections) [65,68,77–80], branched micelles [76], platelet-like micelles and co-micelles [81–86], and hierarchical assemblies [81,87–91]. Next to BCPs with a PFS block, a variety of other crystallizable polymer blocks were employed in CDSA, e.g. polyethylene (PE) [68,92–94], poly(ethylene oxide) [95], polyesters (poly( $\epsilon$ -caprolactone) (PCL) or poly(*L*-lactide) (PLLA)) [86,96–101], polycarbonate [102], poly(2-*iso*-propyl-2-oxazoline) (PiPrOx) [103,104], liquid crystalline polymers [71,105], poly(vinylidene fluoride) [106], polypeptoids [107,108], and various conjugated polymers (e.g., poly(3-hexyl thiophene) (P3HT) and OPV) [75,109–113].

### 3. Short Excursion on Block Co-Micelles

Block co-micelles represent a special type of patchy CCM, because of the sequential arrangement of surface compartments and the precisely adjustable size of the blocks, usually leading to larger corona segments than commonly observed for patchy CCMs. Analogous to the synthesis of BCPs, block co-micelles are produced by sequential living CDSA. The characteristic of this process is that the micelles' termini remain "active" after unimer addition is completed. Consequently, addition of a different type of unimer leads to the formation of a blocky structure (Figure 3a) [65,114]. This feature allows for precise control over the block length by adjusting the amount of added unimer.

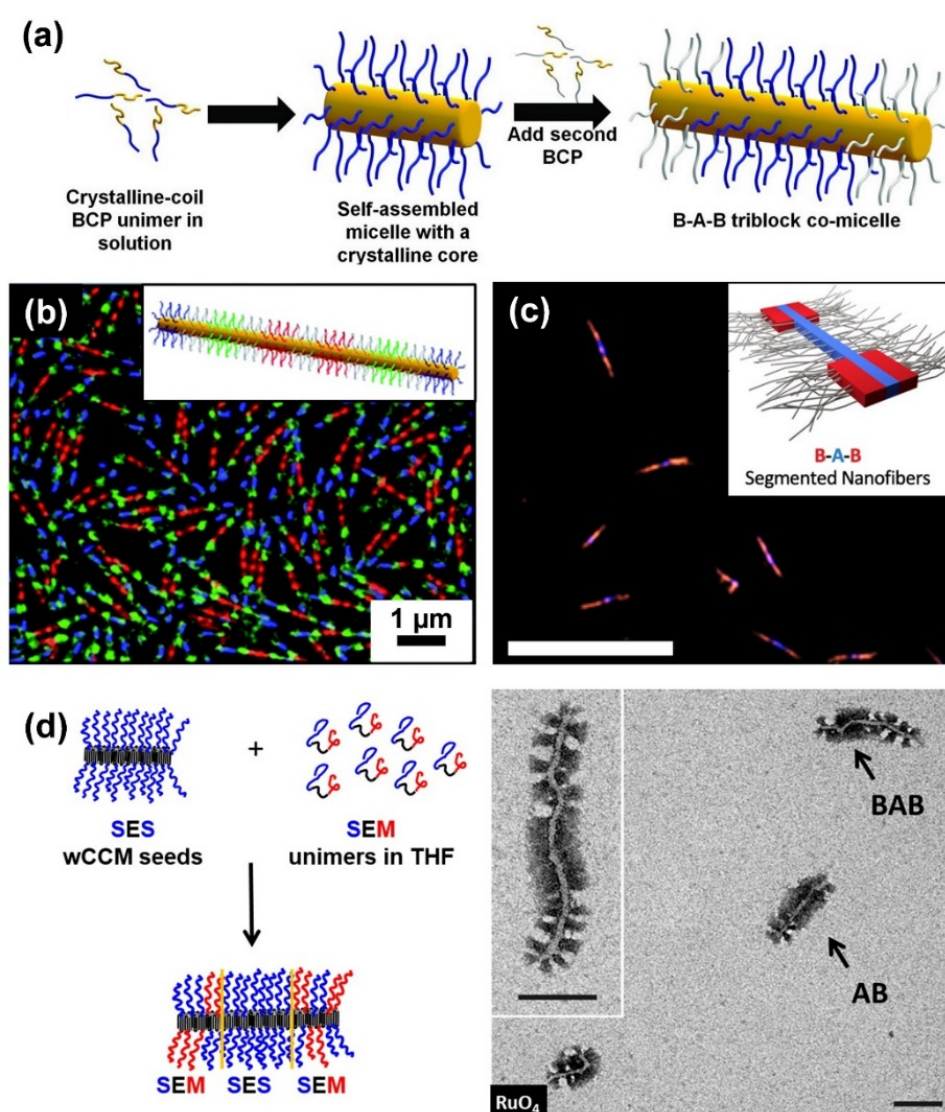


**Figure 3.** (a) Formation of B–A–B triblock co-micelles via sequential living CDSA in selective solvents for the corona blocks. (b) Structured illumination microscopy image of symmetrical 11-block co-micelles with red, green, and blue fluorescent corona blocks separated by non-fluorescent PDMS spacer blocks. (c) Laser-scanning confocal microscopy image of solid-state,

donor–acceptor, coaxial heterojunction nanowires based on B–A–B segmented nanofibers with a semi-crystalline PDHF core (depicted in blue) and a semi-crystalline P3EHT shell (depicted in red) in the outer corona blocks, taken with both blue (PDHF) and red (P3EHT) channels (scale bar: 10  $\mu\text{m}$ ). Blue emission from the central PDHF core, as well as red/orange emission from the outer P3EHT segments, due to Förster resonance energy transfer (FRET) were observed. **(d)** Schematic depiction of the formation of B–A–B triblock co-micelles with patchy outer corona blocks, starting from SES wCCMs as seed micelles and subsequent living CDSA of SEM unimers in THF (left) and corresponding TEM image of patchy block co-micelles (scale bar: 100 nm). **(a)** Reproduced from [79] with permission of the American Association for the Advancement of Science (AAAS), **(b)** reproduced from [67] with permission of the Royal Society of Chemistry (RSC), **(c)** reproduced from [105], and **(d)** reproduced from [68] with permission of ACS.

Similar to living polymerization techniques, in which the reactivity of the first monomer limits the choice of a second monomer, unimers need to fulfill certain requirements for successful co-crystallization. For example, the micellar cores need to be compatible for epitaxial crystallization, i.e., they should exhibit a similar crystal lattice spacing [115,116]. A common way to fulfill this prerequisite is the use of diblock copolymers bearing the same crystallizable block that induces homoepitaxial growth, as shown first for PFS-containing diblock copolymers to produce B–A–B triblock co-micelles [65]. Within this work, PFS–*b*–polyisoprene (PFS–*b*–PI) cylindrical micelles served as seeds for the nucleation of PFS–*b*–polymethylvinylsilane (PFS–*b*–PMVS) and PFS–*b*–polydimethylsiloxane (PFS–*b*–PDMS) unimers, respectively. For heteroepitaxial growth, different PFS-containing seed micelles were applied to induce CDSA of polyferrocenylgermane (PFG)-containing diblock copolymers [73,83,89]. The crystal lattice spacing of the two core-forming blocks only differs by about 6%, enabling the formation of tri- and pentablock co-micelles as well as 2D co-assemblies.

Living CDSA has opened the door to a huge variety of one dimensional, PFS-containing block co-micelles with tailored numbers, lengths, and composition of corona blocks [114,117–121]. Centrosymmetric and non-centrosymmetric block co-micelles are accessible, and give rise to broad structural complexity [79]. In particular, the introduction of fluorescent corona blocks marks an important step in the development of block co-micelles, since this enables the formation of barcode and RGB micelles (Figure 3b) [67,77,122]. Up to that point, the fabrication of cylindrical nanomaterials with precise, color-tunable compartments of predictable length and number was challenging. Moreover, it is possible to induce fluorescence in the semicrystalline core-forming block by replacing the PFS block by a poly(*n*-hexylfluorene) (PDHF) block [78]. B–A–B triblock co-micelles with PDHF core and P3HT outer corona blocks were found to show long-range exciton transport (>200 nm). Inducing secondary crystallization of a poly(3-(2'-hexylethyl)thiophene) (P3EHT) corona block even

rendered solid-state donor–acceptor heterojunctions possible (Figure 3c) [105]. These materials bear a high potential for applications in optoelectronics, device fabrication, and sensing [123].

Several other semicrystalline, core-forming blocks—for example, PFG [73,83,89], polycarbonate [102,124], poly(3-heptylselenophene) [109], P3HT [125], OPV [75,126,127], PLLA [128], and PE [68]—were used for the production of block co-micelles. As an example, sequential living CDSA of a polystyrene–*block*–polyethylene–*block*–polystyrene (PS–*b*–PE–*b*–PS; SES) triblock copolymer with a PS–*b*–PE–*b*–PMMA (SEM; PMMA: poly(methyl methacrylate)) triblock terpolymer yielded B–A–B- or A–B–A-type triblock co-micelles with patchy outer or inner B blocks, respectively (Figure 3d) [68]. Interestingly, the choice of seed micelles was crucial for the successful formation of triblock co-micelles, as worm-like SES micelles are accessible on both micelle ends for epitaxial growth, whereas patchy, worm-like SEM micelles show diverse growth behavior, which is predefined by the arrangement of the corona chains at the micelles' ends.

The scope of complex micellar assemblies is further extended by hierarchical self-assembly, using block co-micelles as building blocks for the formation of 2D and three-dimensional (3D) superstructures. There are different strategies to realize hierarchical assemblies—for example, coordination-driven co-assembly [129] or dialysis of amphiphilic block co-micelles against selective solvents, enabling highly efficient side-by-side or end-to-end stacking (Figure 4a,b) [88,130,131], or spatially confined hydrogen-bonding interactions [132,133]. The latter opens access to numerous hierarchical 2D morphologies, such as “I”-shaped, cross, shish-kebab (Figure 4c) or windmill-like (Figure 4d) structures, by precisely tailored interactions between hydrogen donor and hydrogen acceptor units within the block co-micelles. However, not only the attractive interactions by hydrogen-bonding have to be taken into account, but also repulsive interactions caused by steric hindrance of the corona chains. To overcome this problem, tuning the length of the hydrogen acceptor blocks has proven to be a suitable solution, rendering 3D assemblies possible. It is noted that 2D platelet-like hierarchical superstructures, as well as more complex micelle architectures like double- and single-headed, spear-like micelles [90], scarf-like micelles [89], diamond-fiber hybrid structures [81], or platelets with various shapes (rectangular, quasi-hexagonal, and diamond platelet micelles) [82–85] are accessible.

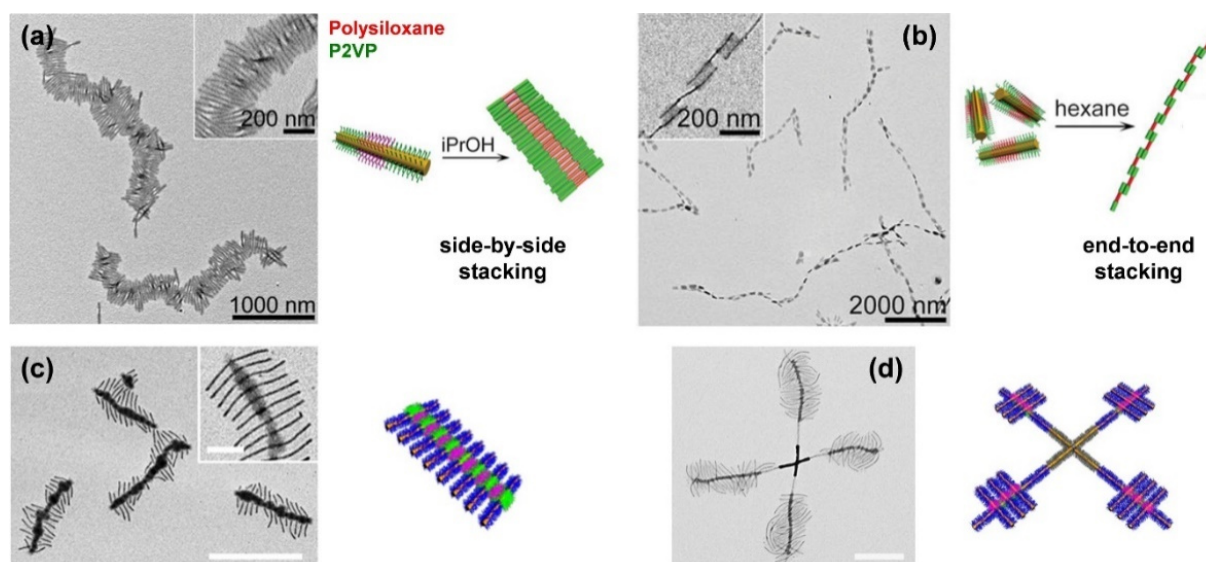


**Figure 4.** One-dimensional supermicelles by (a) side-by-side and (b) end-to-end stacking in selective solvents for the outer and middle corona block of B–A–B triblock co-micelles (PFS core), respectively. (c) “Shish-kebab” supermicelles (scale bar = 1  $\mu\text{m}$ , inset = 200 nm) formed by hydrogen-bond (H-bond)-mediated co-assembly of an H-bond donor homopolymer (hydroxyl-functionalized poly(vinylmethylsiloxane) (PMVSOH), colored in pink) with B–A–B triblock co-micelles with “neutral” outer corona blocks (poly(*t*-butyl acrylate) (PtBA), colored in blue, no H-bond interactions) and an H-bond acceptor middle corona block (P2VP, colored in green). (d) “Windmill”-like supermicelles via living CDSA of a PFS-*b*-PtBA diblock copolymer from “cross” supermicelles (scale bar = 0.5  $\mu\text{m}$ ). The “cross” supermicelles featured an H-bond acceptor corona block (P2VP) at the termini, onto which short CCMs with H-bond donor corona blocks (PMVSOH) that served as seeds for the subsequent living CDSA of the PFS-*b*-PtBA diblock copolymer (color code identical to (c)) were immobilized. (a,b) reproduced from [88] with permission of AAAS, (c) reproduced from [133] with permission of ACS, and (d) from [132] with permission of Springer Nature.

## 4. Self-Assembly Concepts for Patchy Micelles with Crystalline Cores

### 4.1. CDSA of Linear and Star-Shaped Triblock Terpolymers

The most widely used route toward crystalline-core patchy micelles is the CDSA of linear ABC triblock terpolymers with a crystallizable middle block (Table 1) [134]. In contrast to block co-micelles, where the sequential living CDSA of different diblock copolymers results in a block-type segmentation of the corona, the incompatibility of the corona-forming blocks is the driving force for corona segregation in CDSA of triblock terpolymers. This affects the average width of the patches and leads to an alternating, chess-board-like arrangement of the corona patches [135]. Worm-like CCMs (wCCMs) with a patchy corona were first reported in 2008 for triblock terpolymers with a semicrystalline PE middle block and two amorphous outer blocks, namely PS and PMMA (SEM) [93]. Since patchy, worm-like (or cylindrical) CCMs based on these

triblock terpolymers have been intensively studied, the self-assembly mechanism will be elucidated in detail on this example.

**Table 1.** Overview of self-assembly concepts for patchy micelles with a crystalline core.

Self-Assembly Concept	Employed BCPs	Special Feature	Reference
<b>CDSA of triblock terpolymers</b>			
Linear triblock terpolymers	PS- <i>b</i> -PE- <i>b</i> -PMMA	Control over micelle morphology, length control through seeded growth, co-crystallization with PS- <i>b</i> -PE- <i>b</i> -PS	[93,94,134–136]
	PS- <i>b</i> -PE- <i>b</i> -PDxA <sup>1</sup>	Functional groups for NP incorporation	[137,138]
	PS- <i>b</i> -PFS- <i>b</i> -PMMA	Control over patch size, co-crystallization with diblock co-polymers of varying PS and PMMA block lengths	[140]
	PS- <i>b</i> -PFS- <i>b</i> -PMVS, PI- <i>b</i> -PFS- <i>b</i> -PMMA	Length control through seeded growth	[141]
Star-shaped triblock terpolymers	$\mu$ -SIF	Seeded growth, block co-micelles with patchy $\mu$ -SIF outer blocks, and middle block based on PFS- <i>b</i> -PDMS	[142]
Non-covalent grafting on carbon nanotubes	PS- <i>b</i> -PE- <i>b</i> -PMMA	Temperature-stable patchy hybrid materials	[139]
<b>Co-assembly of diblock copolymers</b>			
Sterically demanding co-unimers	PFS- <i>b</i> -PMVS, PFS- <i>b</i> -PMVS(C18) <sup>2</sup>	Gradual coassembly of linear and brush-type BCPs	[143]
Strong difference in Flory-Huggins interaction parameters of corona chains	PFS- <i>b</i> -PDMS, PFS- <i>b</i> -PMVS, PFS- <i>b</i> -PI	Different patch arrangements accessible (helical, hemispherical)	[144]
Manipulation of the epitaxial growth rate or the critical dissolution temperature	PFS- <i>b</i> -P2VP, PFS- <i>b</i> -PNiPAM, PFS- <i>b</i> -P2VPQ <sup>3</sup>	Patchy or blocky structures accessible	[80,145]
Addition of crystallizable homopolymer, heating-cooling-aging approach	PFS, PFS- <i>b</i> -PDMS, PFS- <i>b</i> -PI, PFS- <i>b</i> -PMVS, PFS- <i>b</i> -P2VP	PFS crystal fragments serve as seeds, patchy or blocky structures, easy up-scaling	[146]

<sup>1</sup> PDxA: poly(*N,N*-dialkylaminoethyl methacrylamide). <sup>2</sup> PMVS block alkylated by C18 alkyl chains. <sup>3</sup> Quaternized P2VP.

Initially, the SEM triblock terpolymers are placed in a good solvent for the amorphous blocks and heated above the melting temperature of the semicrystalline PE block in the given solvent (Figure 5a) [94]. Depending on the solvent quality for the PE middle block, different micelle

morphologies are formed. In good solvents for the molten PE block (for example, THF or toluene), the triblock terpolymers are molecularly dissolved, i.e., unimers are formed. In bad solvents for PE (for example 1,4-dioxane), the molten PE block collapses, and spherical micelles with an amorphous (molten) PE core are observed. Cooling of the corresponding unimer solution (in good solvents) or dispersion of spherical micelles (bad solvents) results in the nucleation of PE crystallization. In good solvents, the nuclei are stable and able to initiate the bidirectional, 1D epitaxial growth of the remaining unimers to generate wCCMs. However, in bad solvents, the spherical shape of the micelles dictates the final morphology of the CCMs. Consequently, confined crystallization of PE in the respective micellar cores leads to the generation of spherical CCMs. In both cases, the micelle corona exhibits a patch-like, microphase-separated (patchy) structure, whereas for wCCMs the patchy structure of the corona is more pronounced (Figure 5b,c). For wCCMs, an almost alternating arrangement of the PS and PMMA patches in the corona can be deduced from transmission electron microscopy (TEM) [94], and was also confirmed by small-angle neutron scattering studies [135].

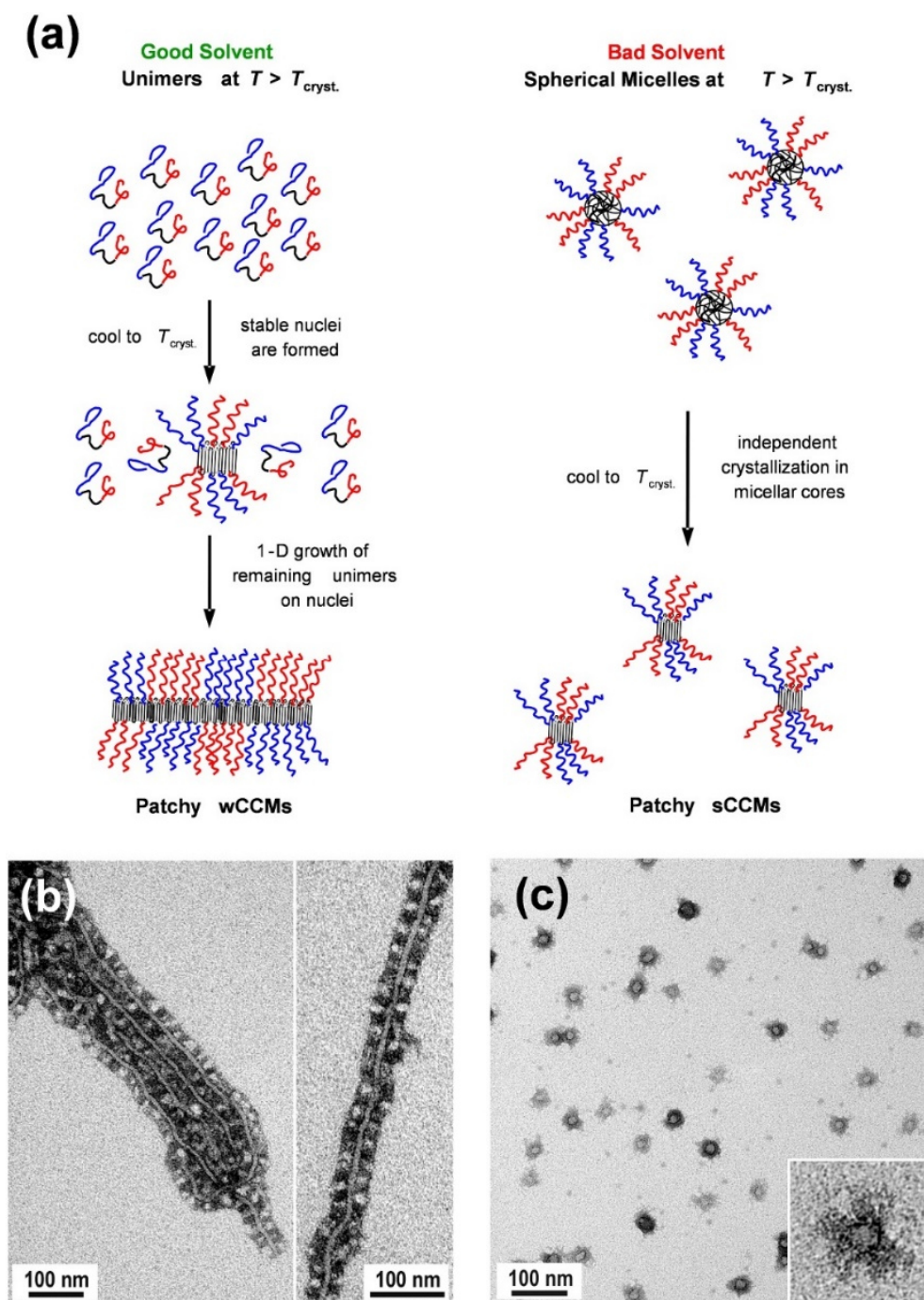


**Figure 5.** (a) Schematic representation of the proposed mechanism for the formation of patchy worm-like and spherical crystalline-core micelles (wCCMs and sCCMs, respectively) from SEM triblock terpolymers (PS blocks are represented in blue, PE in black, and PMMA in red). TEM images of (b) patchy  $S_{340}E_{700}M_{360}$  wCCMs prepared by CDSA in THF and subsequent annealing at 45 °C for 3 h, and (c) patchy  $S_{340}E_{700}M_{360}$  sCCMs formed in dimethylacetamide (subscripts denote the respective average degrees of polymerization, PS was selectively stained with  $\text{RuO}_4$  vapor and appears dark). Reproduced from [94] with permission of ACS.

A facile way to tailor the sizes of the PS and PMMA corona patches is random co-crystallization of an SEM triblock terpolymer with a corresponding SES triblock copolymer,

bearing two PS end blocks [136]. A systematic increase of the SES fraction led to a decrease of the PMMA patch size (Figure 6a). Thus, this approach allows to tune the corona structure by a simple co-assembly without the need to synthesize new triblock terpolymers for each desired corona composition. Another efficient way to modify the corona patches is the introduction of functional groups via selective amidation of the PMMA block in SEM triblock terpolymers with different *N,N*-dialkylethylenediamines [137,138]. CDSA in THF led to patchy wCCMs, for which the patch size and shape could be tuned by varying the block length ratio of the corona blocks (Figure 6b,c) and selective solvent interactions. The functionalized, patchy corona enables an application of these wCCMs as templates for the incorporation of inorganic nanoparticles (NPs), which will be discussed in detail in Section 5.2.

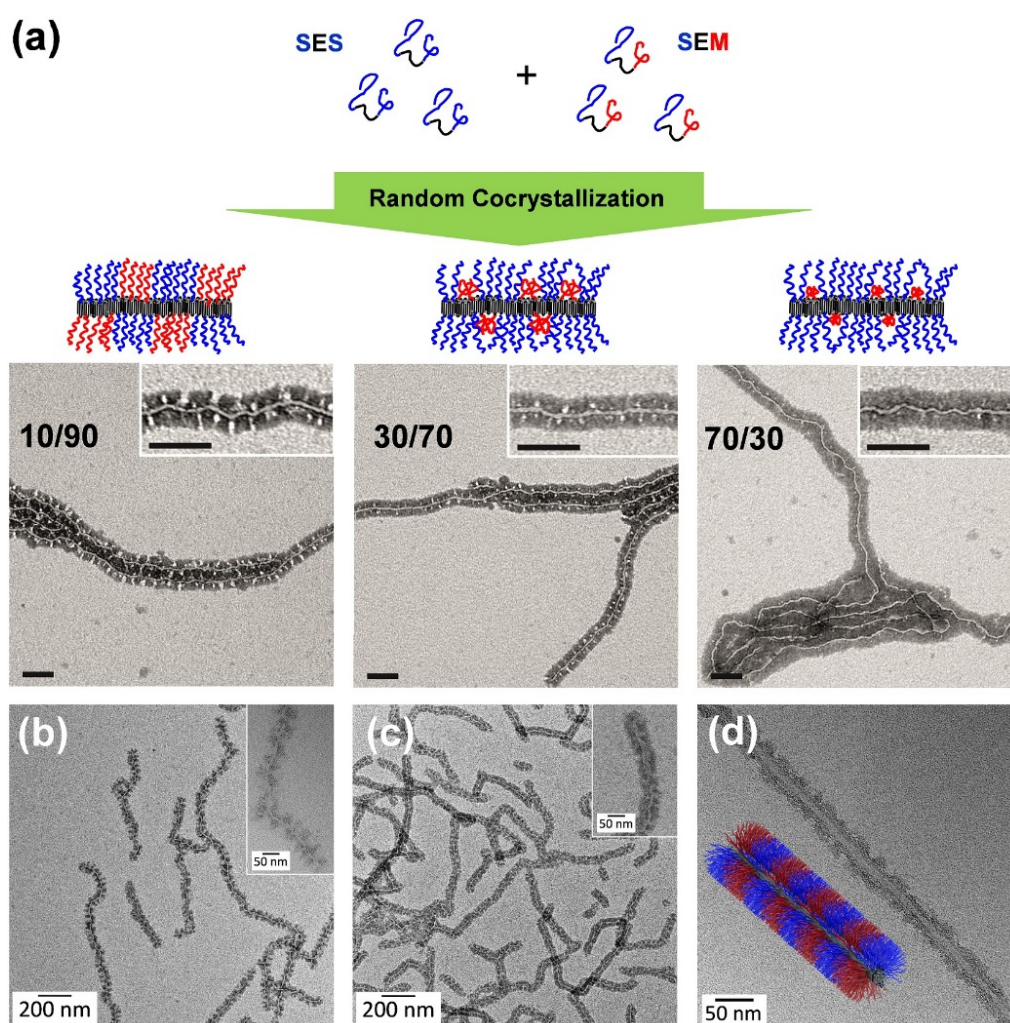


**Figure 6.** (a) Random co-crystallization of a SES triblock co- and a SEM triblock, in order to tune the size of the corona patches. TEM images of patchy wCCMs obtained by co-crystallization of  $S_{380}E_{880}S_{390}$  with  $S_{340}E_{700}M_{360}$  in THF (subscripts denote the respective average degrees of polymerization), revealing a decreasing size of the bright-appearing PMMA corona patches with an increasing amount of  $S_{380}E_{880}S_{390}$  (scale bars: 100 nm). TEM images of patchy (b)  $S_{415}E_{830}DMA_{420}$  and (c)  $S_{660}E_{1350}DMA_{350}$  wCCMs (DMA: *N,N*-

dimethylaminoethyl methacrylamide), as well as **(d)** 1D patchy hybrids with a CNT core and a patchy PS/PMMA corona prepared by ultrasound-assisted, non-covalent grafting of an SEM triblock terpolymer onto CNTs. For all samples, PS was selectively stained with RuO<sub>4</sub> vapor and appears dark. **(a)** Reproduced from [136] with permission of Elsevier, **(b,c)** reprinted from [138] with permission of RSC, and **(d)** reproduced from [139] with permission of ACS.

The patchy corona structure of SEM wCCMs can also be transferred to multiwalled carbon nanotubes (CNTs) by a non-covalent grafting approach that forms 1D patchy hybrids (Figure 6d) [139]. In contrast to CDSA, which is commonly used to obtain patchy wCCMs, these patchy hybrids were prepared by an ultrasound-assisted process. Here, the PE block selectively adsorbs onto the CNT surface, while the soluble PS and PMMA blocks form the patchy corona. The driving force for CNT functionalization is the high affinity of the PE block to the CNT surface, which was supported by the use of a SEM triblock terpolymer, which is not able to crystallize at room temperature, but successfully generates patchy CNT hybrids.

Different attempts were made to exchange the PE block with another crystallizable block in order to generate patchy wCCMs. Successful examples are triblock terpolymers of PS-*b*-PFS-*b*-PMMA, PS-*b*-PFS-*b*-PMVS, and PI-*b*-PFS-*b*-PMMA [140,141], as well as  $\mu$ -ABC miktoarm star terpolymers with a crystallizable PFS block (Figure 7a) [142]. The PFS-containing triblock terpolymers were able to undergo a seeded growth protocol for living CDSA in different solvents to form patchy wCCMs of predictable length (Figure 7b). Remarkably, the living CDSA of all triblock terpolymers proceeded rather slowly compared to PFS-containing diblock copolymers, which was attributed to two effects: (i) the comparably high steric hindrance caused by the two corona blocks surrounding the core-forming block, and (ii) the choice of solvent, which did not sufficiently support the crystallization of PFS. For the PS-*b*-PFS-*b*-PMMA triblock terpolymers, the corona chain length (core to total corona block ratio) was varied, and co-crystallization of the resulting triblock terpolymers resulted in block co-micelles with a patchy corona. Interestingly, the different micelle blocks were still discernible by TEM analysis because of the different corona thicknesses (Figure 7c).

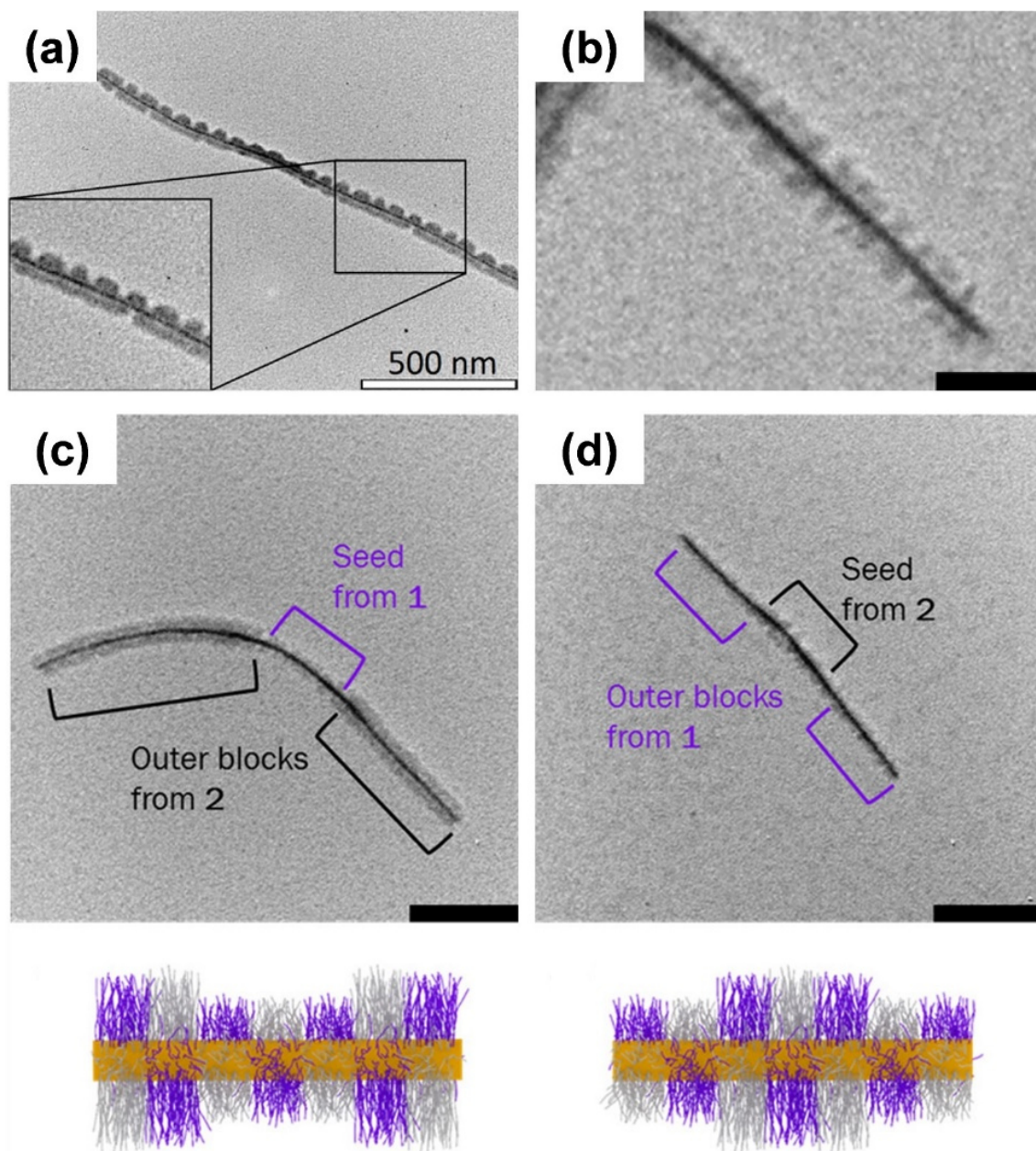


**Figure 7.** (a) Patchy micelles formed by CDSA of a  $\mu$ -SIF (polystyrene-*arm*-polyisoprene-*arm*-poly(ferrocenyl dimethylsilane)) miktoarm star terpolymer in ethyl acetate. (b) Patchy cylindrical micelles and (c,d) patchy ABA-type triblock co-micelles with a crystalline PFS core and a patchy PS/PMMA corona prepared in acetone (scale bars = 100 nm). In (c,d), triblock terpolymers with PS and PMMA blocks of different lengths were used to alter the width of the patchy corona in the middle and outer blocks of the triblock co-micelles (in the sketches PS is depicted in light grey and PMMA in purple). (a) Reprinted from [142], and (b–d) from [140] with permission of ACS.

#### 4.2. Co-assembly of Diblock Copolymers

The simultaneous co-assembly of PFS-based diblock copolymers represents an alternative way of producing patchy, cylindrical CCMs, next to the use of synthetically more demanding linear or star-shaped triblock terpolymers (Table 1). However, the corona patches of the resulting micelles are usually arranged in a blocky rather than an alternating manner. Consequently, the micelles produced with this approach represent a special case of patchy CCMs. The first example of these patchy block co-micelles was reported in 2014, and is based on the co-crystallization of linear and brush-type BCPs with a crystallizable PFS block [143]. Starting from a linear PFS-*b*-PMVS diblock copolymer, the PMVS corona block was alkylated via thiol-ene functionalization, in order to yield a brush-type BCP with pendant C18 alkyl chains. The brush-type BCPs showed poor crystallization behavior, due to the steric repulsion of the alkyl moieties. However, simultaneous co-crystallization with the linear BCP, applying cylindrical PFS-*b*-PDMS seed micelles, resulted in a gradual integration of the brush-type unimers. Hence, a patchy corona segmentation of the end blocks was observed for the produced B-A-B triblock co-micelles by TEM and atomic force microscopy (AFM) (Figure 8a).

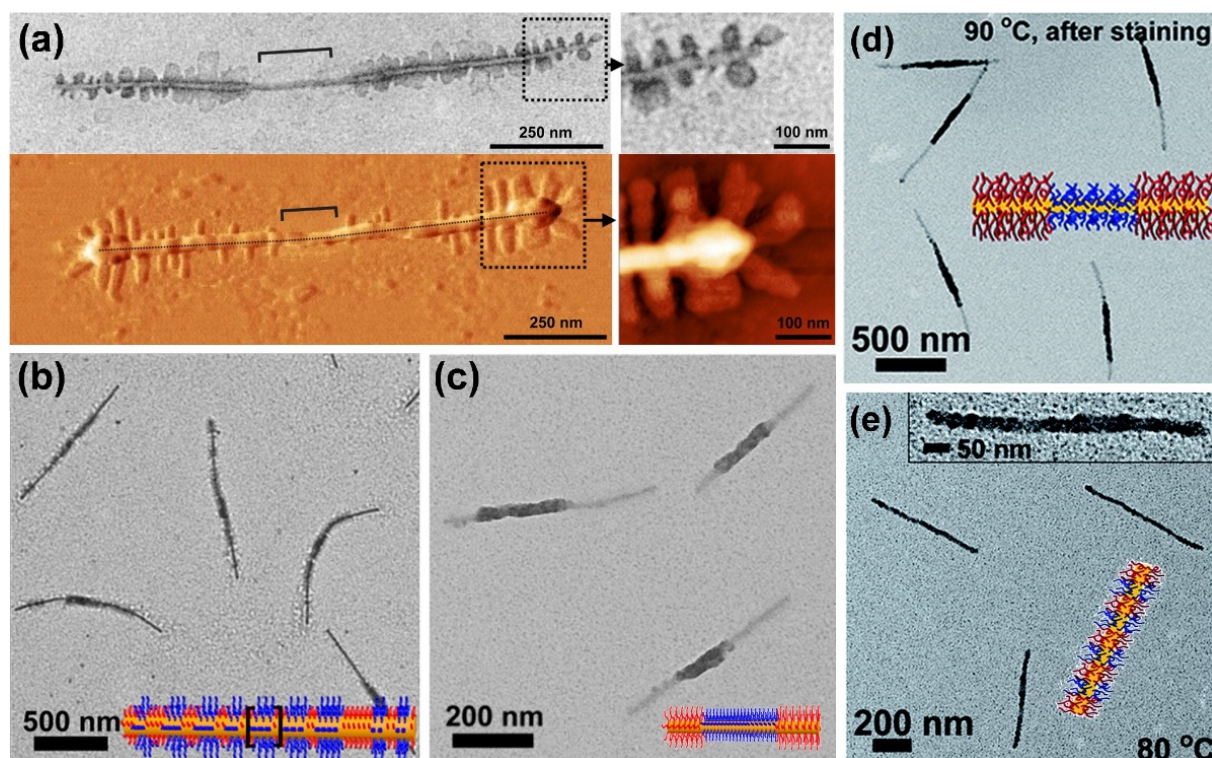


**Figure 8.** (a) TEM (top), as well as AFM topography (bottom left) and phase (bottom right) images of B-A-B triblock co-micelles with patchy end blocks prepared by the co-crystallization of linear and brush-type BCPs with a crystallizable PFS block, employing cylindrical PFS-*b*-PDMS seed micelles. (b) Patch-like segmented and (c) B-A-B triblock co-micelles produced by controlling the epitaxial growth rate of PFS-*b*-PNiPAM over PFS-*b*-PMVS.

P2VP onto cylindrical PFS-*b*-P2VP seed micelles. Comparable growth rates resulted in patch-like segmentation and dissimilar growth rates in a blocky structure of the corona. **(d)** B-A-B triblock co-micelles and **(e)** patch-like, segmented co-micelles prepared by synergistic self-seeding of a mixture of short PFS-*b*-PNiPAM and PFS-*b*-P2VP cylindrical micelles. In **(d)**, the P2VP middle block corona was selectively stained with platinum NPs. **(b–e)** In the respective sketches, PFS is colored in light orange, P2VP in blue, and PNiPAM in red. **(a)** Reprinted from [143], **(b,c)** reprinted from [145] with permission of ACS, and **(d,e)** reproduced from [80] with permission of RSC.

The preparation of patchy block co-micelles is not limited to sterically demanding co-blocks, but can be induced by a strong difference in the Flory–Huggins interaction parameter between the corona-forming blocks [144]. Blends of PFS-*b*-PDMS with PFS-*b*-PMVS and PFS-*b*-PI, respectively, were co-crystallized, resulting in a blocky corona segmentation. Staining with Karstedt's catalyst (selective for PI and PMVS) revealed the small corona patches and made two different patch arrangements visible (helical pattern and hemispherical shape). In a subsequent study, the competitive seeded-growth kinetics of the simultaneous co-crystallization of diblock copolymers bearing different corona blocks was investigated [145]. To this end, PFS-*b*-poly(2-vinylpyridine) (PFS-*b*-P2VP) was co-crystallized with two different PFS-*b*-poly(*N*-isopropyl acrylamide) (PFS-*b*-PNiPAM) diblock copolymers using short PFS-*b*-P2VP seed micelles. The length of the PFS block was similar in all used diblock copolymers, but the corona block length of the PFS-*b*-PNiPAM diblock copolymers differed, which affected the epitaxial growth rate of the PFS-*b*-PNiPAM unimers on the seed micelles. If this growth rate was comparable to that of the competing PFS-*b*-P2VP unimers, patchy micelles were observed (Figure 8b). If, on the other hand, the growth rates of the two competing diblock copolymers differed significantly, the formation of block co-micelles was preferred (Figure 8c). Additionally, the epitaxial growth rate of the PFS-*b*-P2VP diblock copolymers was manipulated by quaternization of the P2VP block, which generated a permanent positive charge within the corona chains. Co-crystallization with a PFS-*b*-PNiPAM diblock copolymer, which yielded a patchy structure with the non-quaternized PFS-*b*-P2VP, then led to a blocky arrangement of the patches, which could again be attributed to the differing epitaxial growth rates.

Beyond changes in the epitaxial growth rate by manipulation of the corona chains, the crystallization behavior of the PFS core block can also be altered [80]. A variation in the PFS block length affects the so-called critical dissolution temperature ( $T_c$ ). This temperature describes the point at which the initial average micelle length doubles upon cooling. Heating a mixture of two different micelle fragments with similar  $T_c$  values to an annealing temperature ( $T_a$ ), and  $T_a < T_c$  results in separate micelle fragments. If  $T_a$  is in the range of the  $T_c$  of both

micellar fragments, the micellar fragments dissolve partly, and tadpole-shaped fragments are observable. If  $T_a > T_c$ , self-seeding is taking place and the growth kinetics are dictated by the epitaxial growth rates of the two competing unimer types, i.e., a patchy morphology is observed for similar growth rates and a blocky arrangement of the patches results from dissimilar growth rates (Figure 8d). The self-seeding behavior changes if two diblock copolymers with different  $T_c$  values are employed. If  $T_a$  is raised above the  $T_c$  of one of the diblock copolymers, but is still lower than the  $T_c$  of the other diblock copolymer, the diblock copolymer with the lower  $T_c$  will partly or almost fully dissolve and epitaxially grow from the remaining micelle seed fragments of both diblock copolymers. This results in either match stick-like micelles or block co-micelles. If  $T_a$  is increased well above the  $T_c$  of both diblock copolymers, again the growth kinetics determine the final observable corona arrangement – i.e., for similar growth rates, a patchy segmentation is generated (Figure 8e). This concept can also be transferred to mixtures of PFS homopolymers and PFS-based BCPs [146]. Due to the higher  $T_c$  of the PFS homopolymer, a certain fraction of PFS homopolymer crystal fragments will survive upon proper choice of  $T_a$ ; these fragments then act as seeds upon subsequent cooling and annealing. This not only allows the production of cylindrical micelles of uniform length, but also of well-defined block co-micelles or patchy micelles employing a mixture of PFS with different PFS-based BCPs. An important feature of this approach with respect to applications is the comparably easy scale-up, enabling the production of uniform cylindrical micelles of controlled architecture up to concentrations of 10% (*w/w* solids) or more.

## 5. Properties and Applications

### 5.1. Interfacial Activity and Blend Compatibilization

The alternating, patch-like arrangement in the corona of worm-like (or cylindrical) patchy CCMs offers a high potential for a variety of applications. As was shown for amorphous Janus micelles, polymer particles exhibiting two opposing faces made of PS and PMMA (or poly(*tert*-butyl methacrylate)) serve as excellent particulate surfactants and compatibilizers in polymer blends [147–158]. This originates from the unique interfacial activity of these materials [38]. Patchy wCCMs were proven to show not only a superior interfacial activity compared to cylindrical micelles with a homogeneous PS corona, but also an identical interfacial activity compared to that of Janus micelles at a water–toluene interface (Figure 9a) [159]. Although Janus particles consist of only two clearly separated compartments (or faces), which facilitates the orientation at interfaces, the unique corona structure of patchy micelles is

able to adapt to the requirements of the interface, i.e., the respective insoluble block will collapse and the soluble block will expand. Depending on the molecular weight of the corona-forming blocks and thus, the thickness of the corona, the interfacial activity could be tuned, and was shown to increase with thickness (at constant micelle length), which is in good agreement with theoretical predictions [160]. Interestingly, patchy SEM wCCMs can also be hierarchically assembled by a confinement process through emulsification in a toluene-in-water emulsion and subsequent evaporation of the solvents. This leads to microparticles with a highly ordered hexagonal close-packed lattice structure [161].

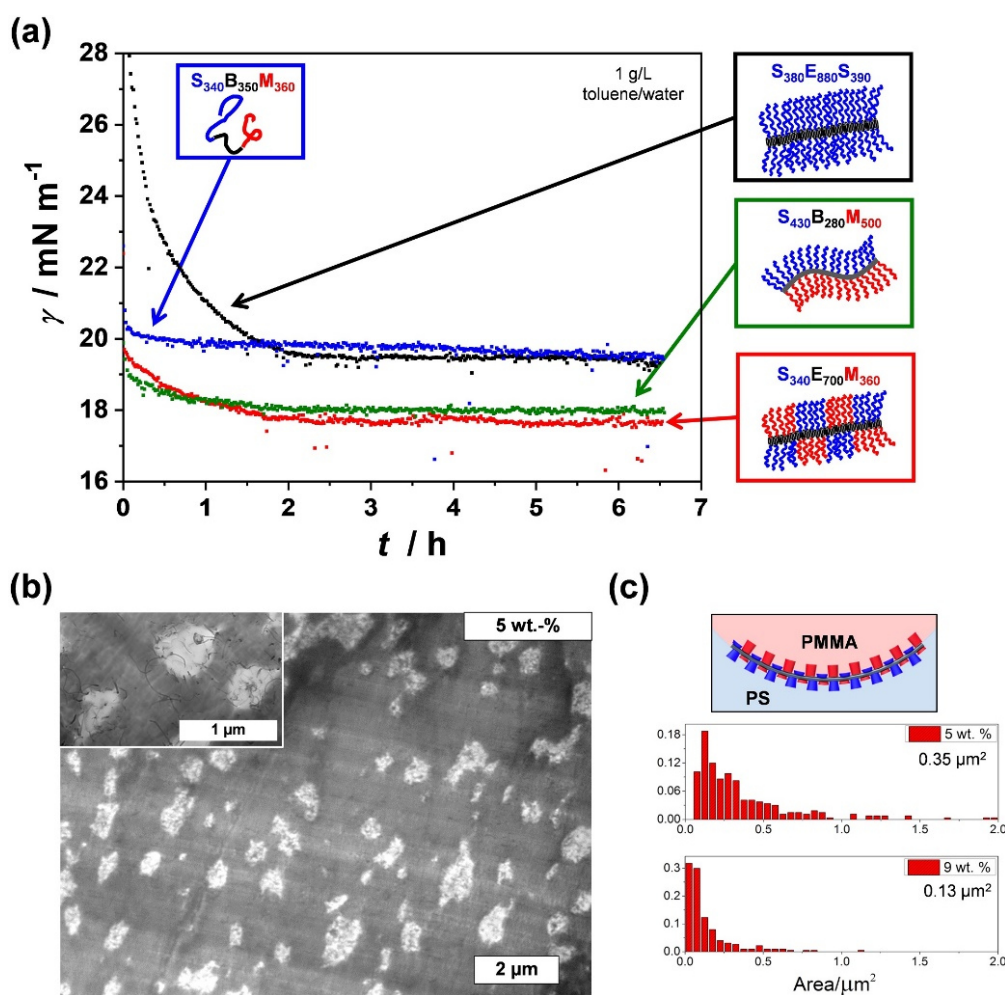


**Figure 9.** (a) Comparison of interfacial tension isotherms of 1 g·L<sup>-1</sup> solutions containing SBM unimers, SES wCCMs with a homogeneous PS corona, SEM wCCMs with a patchy PS/PMMA corona, and SBM-based Janus cylinders with opposing PS and PMMA faces (given subscripts correspond to average degrees of polymerization of the respective blocks). (b) TEM image of a solvent-cast PS/PMMA blend (80/20 w/w) compatibilized with 5 wt. % patchy CNTs (PS/PMMA corona). (c) Schematic representation of the adaption of the patchy PS/PMMA corona to the PS/PMMA blend interface by selective collapse/expansion of the incompatible/compatible corona blocks (top) and histograms of PMMA domain areas for blends with 5 wt. % and 9 wt. % patchy CNTs (bottom). (a) Reproduced from [159] with permission of Elsevier and (b,c) reproduced from [162] with permission of ACS.

The excellent interfacial activity of patchy *w*CCMs can be harnessed for the efficient compatibilization of polymer blends, as reported for solvent-cast PS/PMMA (80/20 *w/w*) blends [162]. In this work, SEM triblock terpolymers were non-covalently grafted onto the surface of multiwalled CNTs, in order to obtain temperature-stable hybrid compatibilizers with a patchy PS/PMMA corona (patchy CNTs, Figure 6d). The performance of these hybrid compatibilizers was studied depending on their weight fraction, revealing that an increasing filler content considerably reduced the size of the PMMA droplets (minority component) in the blends down to  $0.13 \mu\text{m}^2$  for the blend with 9 wt. % patchy CNTs (Figure 9b,c). Remarkably, the obtained PMMA domain areas were significantly lower compared to that achieved by using Janus cylinders ( $L = 2.3 \mu\text{m}$ , biphasic PS/PMMA corona) as compatibilizers, resulting in domain areas of  $10.2 \mu\text{m}^2$  and  $1.77 \mu\text{m}^2$  for 5 wt. % and 10 wt. % Janus cylinders (PS/PMMA = 80/20 *w/w*), respectively [163]. In addition, the TEM image taken at higher magnification (inset of Figure 9b) shows that well-dispersed patchy CNTs are not only located at the PS/PMMA interface, but are also homogeneously distributed in the PS and PMMA phase. The homogeneous distribution of the patchy CNTs, together with their superior compatibilizing efficiency, can be again attributed to the unique feature of the patchy corona, being able to adapt to their surroundings (PS/PMMA interface, or neat PS and PMMA phases) by selective collapse/expansion of the corona blocks.

### 5.2. Nanoparticle Templates/Hybrids

Metal and metal oxide NPs are highly attractive materials for a multitude of applications, such as optics, medicine, electronics, or catalysis, originating from their unique optical properties and high surface-to-volume ratio [164–171]. However, the high surface area is an ambivalent feature, as it is useful, for example, in catalysis, but considerably limits the overall stability of NP dispersions, due to agglomeration and Ostwald ripening. Here, the stabilization of NPs with ligands has proven to be a convenient solution to overcome this substantial drawback [172–175]. Another highly efficient method is the use of micellar nanostructures to selectively embed the NPs within functional surface compartments, which not only act as ligands for the NPs, but also keep the NPs' surface accessible and inhibits agglomeration due to spatial separation [38,117,118,127,137,176,177].

In particular, patchy *w*CCMs, with their well-defined, alternating segmented coronas, have been shown to be versatile NP templates, and even allow the regio-selective incorporation of two different NP types, since the chemistry of the two corona-forming blocks can be tailored to the specific needs of the respective NP [137,138]. In order to obtain these binary-loaded

hybrid materials, based on patchy PS-*b*-PE-*b*-poly(dimethylaminoethyl methacrylamide) (SEDMA) *w*CCMs, a two-step procedure for the selective decoration of the patches with NPs was developed (Figure 10a). In the first step, preformed, PS-stabilized gold NPs were mixed with a dispersion of the functional patchy *w*CCMs, followed by the addition of acetone as a selective solvent for the PDMA block, resulting in a collapse of the PS chains. Due to selective interactions of the PS corona block and the PS-stabilized gold NPs, the NPs were enclosed within the PS patches upon collapse of the PS chains. In the following step, preformed, acetate-stabilized zinc oxide NPs were incorporated in the functional patches by a ligand exchange method. Intrinsic staining provided by the inorganic NPs facilitated an examination of the resulting structures via TEM (Figure 10b,c). The different types of NPs are clearly discernible by their different diameters ( $D$ ;  $D_{\text{gold NP}} = 9 \text{ nm}$ ,  $D_{\text{zinc oxide NP}} = 2.7 \text{ nm}$ ) and the contrast (heavy metals generate a higher contrast in TEM compared to transition metal oxides). Interestingly, despite the small size of the corona patches ( $<20 \text{ nm}$ ), it seems that more than one NP per patch is observable. This might be attributed to the extremely small size of the chosen inorganic NPs ( $<10 \text{ nm}$ ).

The selective functionalization of surface-compartmentalized polymeric micelles with inorganic NPs was also shown for PFS-containing triblock co-micelles, featuring a quaternized P2VP corona in the middle [117,118]. Through electrostatic interactions, the middle block was selectively loaded with mercaptoacetic acid-stabilized gold NPs, PbS quantum dots and dextran-magnetite NPs, demonstrating the versatility of block co-micelles as NP templates. Furthermore, NP hybrid materials with block co-micelles derived from co-assembly of diblock copolymers were reported. Here, the spatially confined incorporation of platinum NPs and CdSe quantum dots was enabled by selective interactions with functional corona patches [146,178].

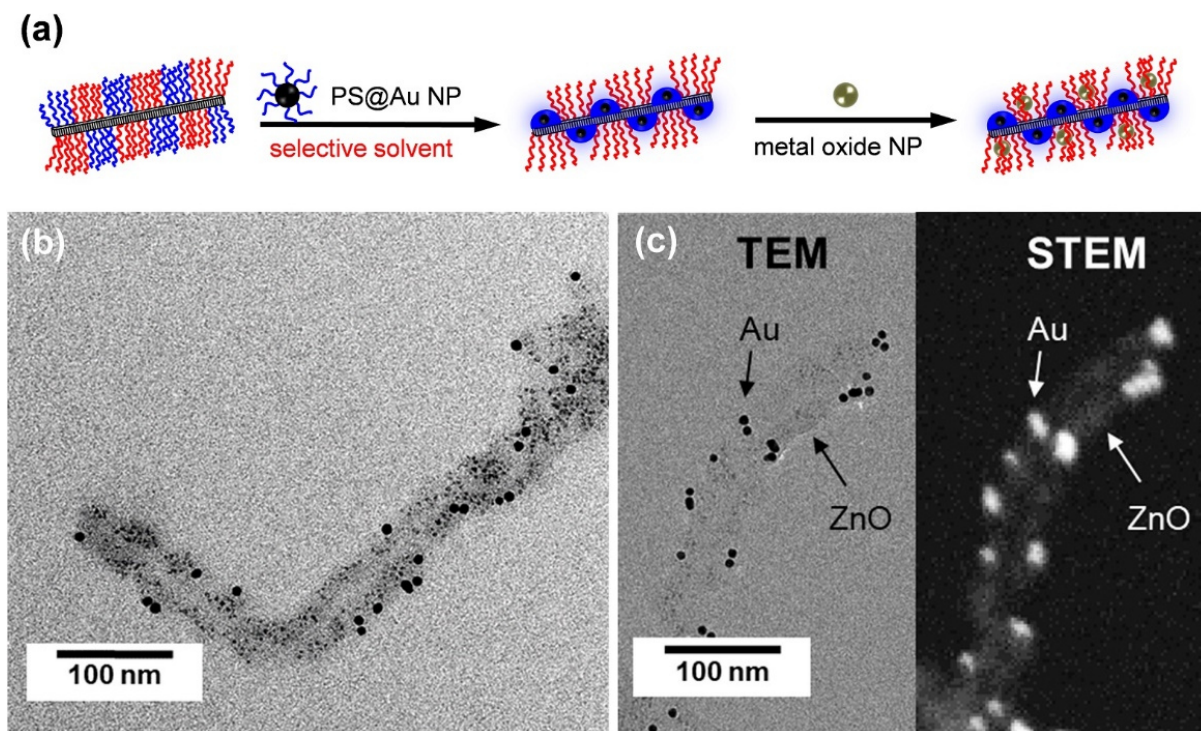


**Figure 10.** (a) Schematic depiction of the regio-selective, binary loading of patchy SEDMA wCCMs with PS-stabilized gold (Au) NPs and zinc oxide (ZnO) NPs, respectively (PS is displayed in blue, PE in black, and PDMA in red). (b) TEM image of  $S_{415}E_{830}DMA_{420}$  wCCMs binary-loaded with Au and ZnO NPs. (c) Bright-field (left) and high-angle annular dark-field scanning transmission electron microscopy (HAADF-STEM, right) images, clearly revealing the binary loading with two different NP types. Reproduced and adapted from [138] with permission of RSC.

### 5.3. Heterogeneous Catalysis

As mentioned in the previous section, an application of noble metal and metal oxide NPs in catalysis is highly desirable, because of the high catalytically active surface area of the employed NPs. However, ligands, which are needed for stabilization of the NPs, might inhibit the superior catalytic activity of the NPs by blocking the surface. Even for tailor-made ligands, this is a distinct drawback, since these materials are usually hard to recover after usage. A separation of the catalytically active species from the reaction medium is challenging and expensive. Immobilizing the catalytically active NPs on suitable supports (e.g., inorganic, polymeric) solves this problem of recoverability, while preserving the activity and accessibility of the NPs' surface [179–185]. Nonetheless, agglomeration of the inorganic NPs on the surface of the heterogeneous supports can occur if the NPs are insufficiently confined, resulting in a significant loss of activity over several consecutive catalysis cycles.

The highly regular, alternating arrangement of the corona compartments in patchy *w*CCMs allows us to efficiently confine inorganic NPs. However, these micellar templates have to be immobilized on a solid support, which provides high accessibility of the reactants to the catalytically active NPs and easy recovery in order to harness these structures for heterogeneous catalysis. This issue was overcome by coating different patchy PS-*b*-PE-*b*-poly(dialkylaminoethyl methacrylamide) *w*CCMs onto the surface of PS nonwovens by means of coaxial electrospinning (Figure 11a,b) [186,187]. The resulting patchy nonwovens were loaded with gold NPs through a simple dip-coating process (Figure 11c), which was driven by a ligand exchange reaction. The hybrid nonwovens were successfully applied as catalysts for the alcoholysis of dimethylphenylsilane (Figure 11d) at room temperature, showing a comparable or even higher catalytic activity than other supports reported before [188–193]. Moreover, the employed patchy hybrid nonwovens were easily recoverable from the reaction medium and reusable in at least 10 consecutive catalysis cycles.

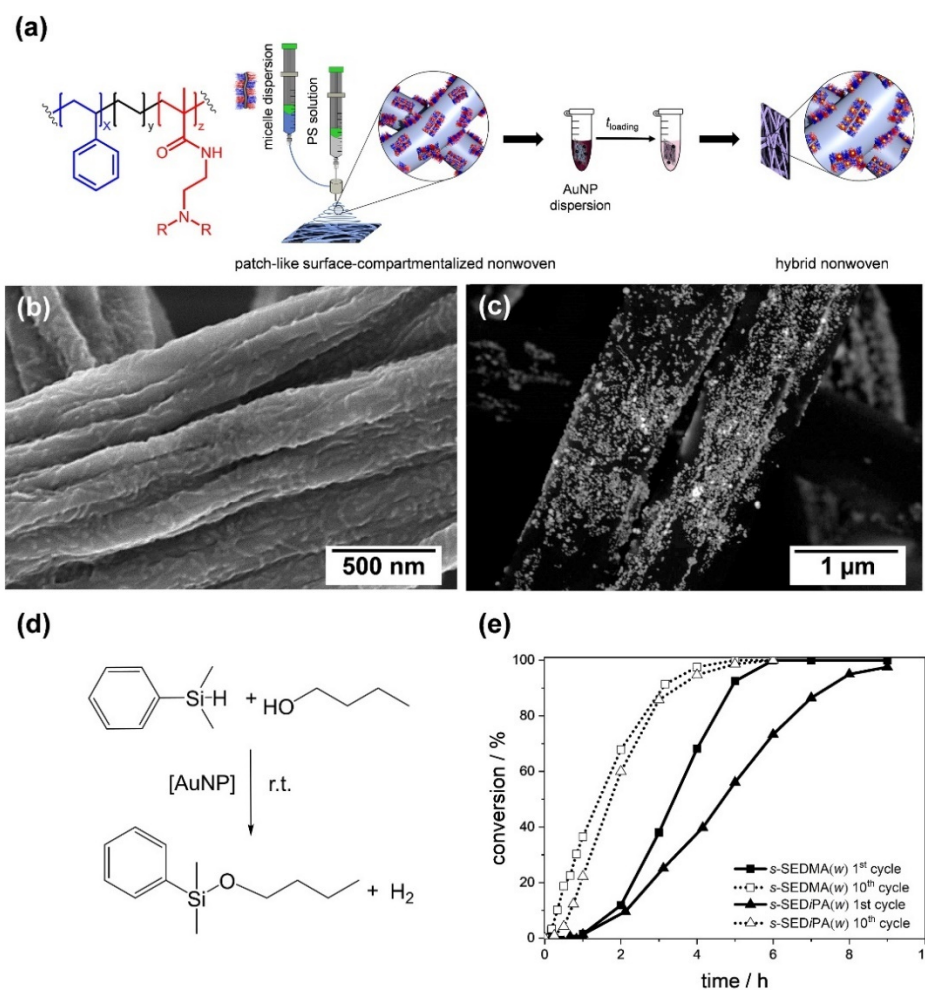


**Figure 11.** (a) Catalytically active, hybrid nonwovens prepared by a combination of bottom-up (CDSA) and top-down (coaxial electrospinning) approaches. In the first step, patchy

nonwovens were prepared by decorating a PS nonwoven with functional, patchy PS-*b*-PE-*b*-poly(dialkylaminoethyl methacrylamide) *w*CCMs by coaxial electrospinning (PS patches are depicted in blue and the functional, tertiary amino group containing patches in red). Subsequently, the patchy nonwovens were loaded with citrate-stabilized Au NPs via a ligand exchange process (citrate against tertiary amino groups in functional patches). **(b)** Scanning electron microscopy images of a patchy nonwoven (based on S<sub>415</sub>E<sub>830</sub>DMA<sub>420</sub> *w*CCMs) before and **(c)** after loading with Au NPs (back-scattered electron detector). **(d)** Au NP-catalyzed alcoholysis of dimethylphenylsilane in *n*-butanol. **(e)** Kinetics of the Au NP-catalyzed alcoholysis of dimethylphenylsilane in *n*-butanol, employing patchy hybrid nonwovens as catalysts (DiPA = poly(*diis*opropylaminoethyl methacrylamide). Reproduced from [186] with permission from RSC.

Since this system offers different possibilities to tune the catalytic activity, an in-depth study on the influence of the patch size and chemistry on the reaction kinetics was conducted. Here, an extended first-order kinetics model was employed, which includes the induction periods observed in the catalytic alcoholysis of dimethylphenylsilane in *n*-butanol. This study revealed a strong dependence on the accessibility of the reactants to the gold NPs' surface, being mainly controlled by the swellability of the functional patches in *n*-butanol. The latter depends on both patch chemistry, i.e., poly(*N,N*-dimethylaminoethyl methacrylamide) (PDMA, more hydrophilic) vs. poly(*N,N*-*diis*opropylaminoethyl methacrylamide) (PDiPA, more hydrophobic) patches, as well as size. As a result, significantly longer induction ( $t_{\text{ind}}$ ) and reaction ( $t_{\text{R}}$ ) times were observed for the first catalysis cycles compared to the tenth cycles (Figure 11e). Nonwovens with more polar PDMA patches were the most efficient in NP stabilization (prevention of agglomeration), but showed a significantly lower  $t_{\text{R}}$  in the first catalysis cycle, due to a strong interaction with the gold NPs' surface. Thus, precise tuning of the patch size and chemistry is needed to optimize the catalysts performance. However, the modular design of the patchy hybrid nonwovens enables a facile adaption to the needs of different catalysis systems – for example, by an exchange of the support material or by varying the type of NPs. Moreover, it is possible to render the functionalized patches thermo-responsive[194], which opens access to catalytic reactions regulated by an inherent temperature control.

## 6. Conclusions and Outlook

From a conceptual point of view, several strategies exist for the production of patchy micelles with crystalline cores, such as CDSA of triblock terpolymers with crystallizable middle blocks, miktoarm stars, or the co-assembly of diblock copolymers with a common crystallizable block but different corona-forming blocks. However, so far, patchy micelles have been reported only for BCPs with PE or PFS as crystallizable blocks, despite the fact that a large variety of crystallizable polymer blocks has already been utilized in CDSA. Here, ring-opening polymerization of lactones or lactides, in combination with controlled radical polymerization techniques, might be another promising alternative, as BCPs based on PCL or PLLA as crystallizable blocks are readily accessible. Moreover, PFS could be replaced by ruthenocene-based BCPs, which show a higher degree of crystallinity but are less studied for CDSA. Finally, patchy micelles could be derived from the simultaneous heteroepitaxial growth of two crystallizable di- or triblock copolymers bearing different core- and corona-forming blocks, inducing segmentation within the core as well as in the corona.

The alternating arrangement of the corona patches emerges as an excellent feature for the stabilization and confinement of metal and metal oxide nanoparticles, opening applications in heterogeneous catalysis. Yet this has been shown only for the gold nanoparticle-catalyzed alcoholysis of silanes, and it is anticipated that this concept can be transferred to other relevant catalytic processes like heterogeneous hydrogenation. By incorporating different nanoparticle types, even cascade reactions might be realizable. Most interestingly, the interfacial activity of patchy, worm-like (or cylindrical) micelles is equivalent to that of Janus micelles, the latter being, however, more difficult to produce. Thus, patchy micelles might be utilized in interfacial catalysis, as well as in the efficient stabilization of emulsions or compatibilization of polymer blends.

**Author Contributions:** C.H., I.M., J.S., and H.S. contributed to writing (review and editing). All authors have read and agreed to the published version of the manuscript.

**Funding:** This research was funded by the German Research Foundation within the collaborative research center SFB 840 (project A2).

**Institutional Review Board Statement:** Not applicable.

**Informed Consent Statement:** Not applicable.

**Data Availability Statement:** The data presented in this study are available on request from the corresponding author.

Acknowledgments: C.H. acknowledges support by the Graduate School of the University of Bayreuth.

Conflicts of Interest: The authors declare no conflict of interest.

## 7 References

1. Tritschler, U.; Pearce, S.; Gwyther, J.; Whittell, G.R.; Manners, I. 50th Anniversary Perspective: Functional Nanoparticles from the Solution Self-Assembly of Block Copolymers. *Macromolecules* **2017**, *50*, 3439–3463.
2. Du, J.; O'Reilly, R.K. Anisotropic particles with patchy, multicompartment and Janus architectures: Preparation and application. *Chem. Soc. Rev.* **2011**, *40*, 2402–2416.
3. Wyman, I.W.; Liu, G. Micellar structures of linear triblock terpolymers: Three blocks but many possibilities. *Polymer* **2013**, *54*, 1950–1978.
4. Schacher, F.H.; Ruper, P.A.; Manners, I. Functional Block Copolymers: Nanostructured Materials with Emerging Applications. *Angew. Chem. Int. Ed.* **2012**, *51*, 7898–7921.
5. Matyjaszewski, K., Möller, M. (Eds.) *Polymer Science: A Comprehensive Reference*; Elsevier Science: Amsterdam, The Netherlands, 2012; ISBN 978-0-08-087862-1.
6. Feng, H.; Lu, X.; Wang, W.; Kang, N.-G.; Mays, J.W. Block Copolymers: Synthesis, Self-Assembly, and Applications. *Polymers* **2017**, *9*, 494.
7. Müller, A.H.E., Matyjaszewski, K. (Eds.) *Controlled and Living Polymerizations*; Wiley: Hoboken, NJ, USA, 2009; ISBN 9783527324927.
8. Jennings, J.; He, G.; Howdle, S.M.; Zetterlund, P.B. Block copolymer synthesis by controlled/living radical polymerisation in heterogeneous systems. *Chem. Soc. Rev.* **2016**, *45*, 5055–5084.
9. Hadjichristidis, N.; Pitsikalis, M.; Iatrou, H. Synthesis of Block Copolymers. In: Abetz V. (eds) *Block Copolymers I. Advances in Polymer Science*, vol 189. Springer, Berlin, Heidelberg.
10. Lutz, J.; Laschewsky, A. Multicompartment Micelles: Has the Long-Standing Dream Become a Reality? *Macromol. Chem. Phys.* **2005**, *206*, 813–817.
11. Laschewsky, A. Polymerized micelles with compartments. *Curr. Opin. Colloid Interface Sci.* **2003**, *8*, 274–281.

12. Gröschel, A.H.; Walther, A.; Löbbling, T.I.; Schacher, F.H.; Schmalz, H.; Müller, A.H.E. Guided hierarchical co-assembly of soft patchy nanoparticles. *Nature* **2013**, *503*, 247–251.
13. Li, W.; Palis, H.; Mérindol, R.; Majimel, J.; Ravaine, S.; Duguet, E. Colloidal molecules and patchy particles: Complementary concepts, synthesis and self-assembly. *Chem. Soc. Rev.* **2020**, *49*, 1955–1976.
14. Lunn, D.J.; Finnegan, J.R.; Manners, I. Self-assembly of “patchy” nanoparticles: A versatile approach to functional hierarchical materials. *Chem. Sci.* **2015**, *6*, 3663–3673.
15. Zhang, K.; Jiang, M.; Chen, D. Self-assembly of particles—The regulatory role of particle flexibility. *Prog. Polym. Sci.* **2012**, *37*, 445–486.
16. Löbbling, T.I.; Ikkala, O.; Gröschel, A.H.; Müller, A.H.E. Controlling Multicompartment Morphologies Using Solvent Conditions and Chemical Modification. *ACS Macro Lett.* **2016**, *5*, 1044–1048.
17. Fang, B.; Walther, A.; Wolf, A.; Xu, Y.; Yuan, J.; Müller, A.H.E. Undulated Multicompartment Cylinders by the Controlled and Directed Stacking of Polymer Micelles with a Compartmentalized Corona. *Angew. Chem. Int. Ed.* **2009**, *48*, 2877–2880.
18. Lee, S.; Jang, S.; Kim, K.; Jeon, J.; Kim, S.-S.; Sohn, B.-H. Branched and crosslinked supracolloidal chains with diblock copolymer micelles having three well-defined patches. *Chem. Commun.* **2016**, *52*, 9430–9433.
19. Walther, A.; Müller, A.H.E. Formation of hydrophobic bridges between multicompartment micelles of miktoarm star terpolymers in water. *Chem. Commun.* **2009**, *7*, 1127–1129.
20. Kong, W.; Jiang, W.; Zhu, Y.; Li, B. Highly Symmetric Patchy Multicompartment Nanoparticles from the Self-Assembly of ABC Linear Terpolymers in C-Selective Solvents. *Langmuir* **2012**, *28*, 11714–11724.
21. Kim, K.; Jang, S.; Jeon, J.; Kang, D.; Sohn, B.-H. Fluorescent Supracolloidal Chains of Patchy Micelles of Diblock Copolymers Functionalized with Fluorophores. *Langmuir* **2018**, *34*, 4634–4639.
22. Nghiem, T.; Chakroun, R.; Janoszka, N.; Chen, C.; Klein, K.; Wong, C.K.; Gröschel, A.H. pH-Controlled Hierarchical Assembly/Disassembly of Multicompartment Micelles in Water. *Macromol. Rapid Commun.* **2020**, *41*, 2000301.
23. Skrabania, K.; Berlepsch, H.V.; Böttcher, C.; Laschewsky, A. Synthesis of Ternary, Hydrophilic–Lipophilic–Fluorophilic Block Copolymers by Consecutive RAFT

- Polymerizations and Their Self-Assembly into Multicompartment Micelles. *Macromolecules* **2010**, *43*, 271–281.
24. Löbbling, T.I.; Borisov, O.; Haataja, J.S.; Ikkala, O.; Gröschel, A.H.; Müller, A.H.E. Rational design of ABC triblock terpolymer solution nanostructures with controlled patch morphology. *Nat. Commun.* **2016**, *7*, 12097.
  25. Nghiem, T.-L.; Löbbling, T.I.; Gröschel, A.H. Supracolloidal chains of patchy micelles in water. *Polym. Chem.* **2017**, *9*, 1583–1592.
  26. Moughton, A.O.; Hillmyer, M.A.; Lodge, T.P. Multicompartment Block Polymer Micelles. *Macromolecules* **2012**, *45*, 2–19.
  27. Wang, L.; Lin, J. Discovering multicore micelles: Insights into the self-assembly of linear ABC terpolymers in midblock-selective solvents. *Soft Matter* **2011**, *7*, 3383–3391.
  28. Gröschel, A.H.; Müller, A.H.E. Self-assembly concepts for multicompartment nanostructures. *Nanoscale* **2015**, *7*, 11841–11876.
  29. Wong, C.K.; Qiang, X.; Müller, A.H.E.; Gröschel, A.H. Self-Assembly of block copolymers into internally ordered microparticles. *Prog. Polym. Sci.* **2020**, *102*, 101211.
  30. Pelras, T.; Mahon, C.S.; Müllner, M. Synthesis and Applications of Compartmentalised Molecular Polymer Brushes. *Angew. Chem. Int. Ed.* **2018**, *57*, 6982–6994.
  31. Nayanathara, U.; Kermaniyan, S.S.; Such, G.K. Multicompartment Polymeric Nanocarriers for Biomedical Applications. *Macromol. Rapid Commun.* **2020**, *41*, 2000298.
  32. Marschelke, C.; Fery, A.; Synytska, A. Janus particles: From concepts to environmentally friendly materials and sustainable applications. *Colloid Polym. Sci.* **2020**, *298*, 841–865.
  33. Fan, X.; Yang, J.; Loh, X.J.; Li, Z. Polymeric Janus Nanoparticles: Recent Advances in Synthetic Strategies, Materials Properties, and Applications. *Macromol. Rapid Commun.* **2019**, *40*, 1800203.
  34. Agrawal, G.; Agrawal, R. Janus Nanoparticles: Recent Advances in Their Interfacial and Biomedical Applications. *ACS Appl. Nano Mater.* **2019**, *2*, 1738–1757.
  35. Zhang, J.; Grzybowski, B.A.; Granick, S. Janus Particle Synthesis, Assembly, and Application. *Langmuir* **2017**, *33*, 6964–6977.
  36. Deng, R.; Liang, F.; Zhu, J.; Yang, Z. Recent advances in the synthesis of Janus nanomaterials of block copolymers. *Mater. Chem. Front.* **2016**, *1*, 431–443.

37. Pang, X.; Wan, C.; Wang, M.; Lin, Z. Strictly Biphasic Soft and Hard Janus Structures: Synthesis, Properties, and Applications. *Angew. Chem. Int. Ed.* **2014**, *53*, 5524–5538.
38. Walther, A.; Müller, A.H.E. Janus Particles: Synthesis, Self-Assembly, Physical Properties, and Applications. *Chem. Rev.* **2013**, *113*, 5194–5261.
39. Hu, J.; Zhou, S.; Sun, Y.; Fang, X.; Wu, L. Fabrication, properties and applications of Janus particles. *Chem. Soc. Rev.* **2012**, *41*, 4356–4378.
40. Loget, G.; Kuhn, A. Bulk synthesis of Janus objects and asymmetric patchy particles. *J. Mater. Chem.* **2012**, *22*, 15457–15474.
41. Wurm, F.; Kilbinger, A.F.M. Polymeric Janus Particles. *Angew. Chem. Int. Ed.* **2009**, *48*, 8412–8421.
42. Dou, H.; Liu, G.; Dupont, J.; Hong, L. Triblock terpolymer helices self-assembled under special solvation conditions. *Soft Matter* **2010**, *6*, 4214–4222.
43. Dupont, J.; Liu, G.; Niihara, K.-I.; Kimoto, R.; Jinnai, H. Self-Assembled ABC Triblock Copolymer Double and Triple Helices. *Angew. Chem. Int. Ed.* **2009**, *48*, 6144–6147.
44. Hoppenbrouwers, E.; Li, Z.; Liu, G. Triblock Nanospheres with Amphiphilic Coronal Chains. *Macromolecules* **2003**, *36*, 876–881.
45. Hu, J.; Njikang, G.; Liu, G. Twisted ABC Triblock Copolymer Cylinders with Segregated A and C Coronal Chains. *Macromolecules* **2008**, *41*, 7993–7999.
46. Liu, X.; Ding, Y.; Liu, J.; Lin, S.; Zhuang, Q. Evolution in the morphological behaviour of a series of fluorine-containing ABC miktoarm star terpolymers. *Eur. Polym. J.* **2019**, *116*, 342–351.
47. Njikang, G.; Han, D.; Wang, J.; Liu, G. ABC Triblock Copolymer Micelle-Like Aggregates in Selective Solvents for A and C. *Macromolecules* **2008**, *41*, 9727–9735.
48. Zhang, W.; He, J.X.; Liu, Q.; Ke, G.Q.; Dong, X. Synthesis of Block Terpolymer PS-PDMAEMA-PMMA via ATRP and its Self-Assembly in Selective Solvents. *Adv. Mater. Res.* **2014**, *1049–1050*, 137–141.
49. Kuo, S.-W.; Tung, P.-H.; Lai, C.-L.; Jeong, K.-U.; Chang, F.-C. Supramolecular Micellization of Diblock Copolymer Mixtures Mediated by Hydrogen Bonding for the Observation of Separated Coil and Chain Aggregation in Common Solvents. *Macromol. Rapid Commun.* **2007**, *29*, 229–233.
50. Kuo, S.-W.; Tung, P.-H.; Chang, F.-C. Hydrogen bond mediated supramolecular micellization of diblock copolymer mixture in common solvents. *Eur. Polym. J.* **2009**, *45*, 1924–1935.

51. Voets, I.K.; De Keizer, A.; Leermakers, F.A.; Debuigne, A.; Jérôme, R.; Detrembleur, C.; Stuart, M.A.C. Electrostatic hierarchical co-assembly in aqueous solutions of two oppositely charged double hydrophilic diblock copolymers. *Eur. Polym. J.* **2009**, *45*, 2913–2925.
52. Lopresti, C.; Massignani, M.; Fernyhough, C.; Blanazs, A.; Ryan, A.J.; Madsen, J.; Warren, N.J.; Armes, S.P.; Lewis, A.L.; Chirasatitsin, S.; et al. Controlling Polymersome Surface Topology at the Nanoscale by Membrane Confined Polymer/Polymer Phase Separation. *ACS Nano* **2011**, *5*, 1775–1784.
53. Hu, J.; Liu, G. Chain Mixing and Segregation in B–C and C–D Diblock Copolymer Micelles. *Macromolecules* **2005**, *38*, 8058–8065.
54. Srinivas, G.; Pitera, J.W. Soft Patchy Nanoparticles from Solution-Phase Self-Assembly of Binary Diblock Copolymers. *Nano Lett.* **2008**, *8*, 611–618.
55. Zheng, R.; Liu, G.; Yan, X. Polymer Nano- and Microspheres with Bumpy and Chain-Segregated Surfaces. *J. Am. Chem. Soc.* **2005**, *127*, 15358–15359.
56. Christian, D.A.; Tian, A.; Ellenbroek, W.G.; Levental, I.; Rajagopal, K.; Janmey, P.A.; Liu, A.J.; Baumgart, T.; Discher, D.E. Spotted vesicles, striped micelles and Janus assemblies induced by ligand binding. *Nat. Mater.* **2009**, *8*, 843–849.
57. Hsu, H.-P.; Paul, W.; Binder, K. One- and Two-Component Bottle-Brush Polymers: Simulations Compared to Theoretical Predictions. *Macromol. Theory Simul.* **2007**, *16*, 660–689.
58. De Jong, J.; ten Brinke, G. Conformational Aspects and Intramolecular Phase Separation of Alternating Copolymacromonomers: A Computer Simulation Study. *Macromol. Theory Simul.* **2004**, *13*, 318–327.
59. Stepanyan, R.; Subbotin, A.; ten Brinke, G. Comb Copolymer Brush with Chemically Different Side Chains. *Macromolecules* **2002**, *35*, 5640–5648.
60. Theodorakis, P.E.; Paul, W.; Binder, K. Interplay between Chain Collapse and Microphase Separation in Bottle-Brush Polymers with Two Types of Side Chains. *Macromolecules* **2010**, *43*, 5137–5148.
61. Hsu, H.-P.; Paul, W.; Binder, K. Intramolecular phase separation of copolymer “bottle brushes”: No sharp phase transition but a tunable length scale. *EPL Europhys. Lett.* **2006**, *76*, 526–532.
62. He, W.-N.; Xu, J.-T. Crystallization assisted self-assembly of semicrystalline block copolymers. *Prog. Polym. Sci.* **2012**, *37*, 1350–1400.

63. Ganda, S.; Stenzel, M.H. Concepts, fabrication methods and applications of living crystallization-driven self-assembly of block copolymers. *Prog. Polym. Sci.* **2020**, *101*, 101195.
64. Hailes, R.L.N.; Oliver, A.M.; Gwyther, J.; Whittell, G.R.; Manners, I. Polyferrocenylsilanes: Synthesis, properties, and applications. *Chem. Soc. Rev.* **2016**, *45*, 5358–5407.
65. Wang, X.; Guerin, G.; Wang, H.; Wang, Y.; Manners, I.; Winnik, M.A. Cylindrical Block Copolymer Micelles and Co-Micelles of Controlled Length and Architecture. *Science* **2007**, *317*, 644–647.
66. Gilroy, J.B.; Gädt, T.; Whittell, G.R.; Chabanne, L.; Mitchels, J.M.; Richardson, R.M.; Winnik, M.A.; Manners, I. Monodisperse cylindrical micelles by crystallization-driven living self-assembly. *Nat. Chem.* **2010**, *2*, 566–570.
67. MacFarlane, L.; Zhao, C.; Cai, J.; Qiu, H.; Manners, I. Emerging applications for living crystallization-driven self-assembly. *Chem. Sci.* **2021**, *12*, 4661–4682.
68. Schmelz, J.; Schedl, A.E.; Steinlein, C.; Manners, I.; Schmalz, H. Length Control and Block-Type Architectures in Worm-like Micelles with Polyethylene Cores. *J. Am. Chem. Soc.* **2012**, *134*, 14217–14225.
69. Qian, J.; Lu, Y.; Chia, A.; Zhang, M.; Rugar, P.A.; Gunari, N.; Walker, G.C.; Cambridge, G.; He, F.; Guerin, G.; et al. Self-Seeding in One Dimension: A Route to Uniform Fiber-like Nanostructures from Block Copolymers with a Crystallizable Core-Forming Block. *ACS Nano* **2013**, *7*, 3754–3766.
70. Qian, J.; Guerin, G.; Lu, Y.; Cambridge, G.; Manners, I.; Winnik, M.A. Self-Seeding in One Dimension: An Approach To Control the Length of Fiberlike Polyisoprene-Polyferrocenylsilane Block Copolymer Micelles. *Angew. Chem. Int. Ed.* **2011**, *50*, 1622–1625.
71. Li, X.; Jin, B.; Gao, Y.; Hayward, D.W.; Winnik, M.A.; Luo, Y.; Manners, I. Monodisperse Cylindrical Micelles of Controlled Length with a Liquid-Crystalline Perfluorinated Core by 1D “Self-Seeding”. *Angew. Chem. Int. Ed.* **2016**, *55*, 11392–11396.
72. Boott, C.E.; Gwyther, J.; Harniman, R.L.; Hayward, D.W.; Manners, I. Scalable and uniform 1D nanoparticles by synchronous polymerization, crystallization and self-assembly. *Nat. Chem.* **2017**, *9*, 785–792.

- 
73. Oliver, A.M.; Gwyther, J.; Boott, C.E.; Davis, S.; Pearce, S.; Manners, I. Scalable Fiber-like Micelles and Block Co-micelles by Polymerization-Induced Crystallization-Driven Self-Assembly. *J. Am. Chem. Soc.* **2018**, *140*, 18104–18114.
  74. Sha, Y.; Rahman, A.; Zhu, T.; Cha, Y.; McAlister, C.W.; Tang, C. ROMPI-CDSA: Ring-opening metathesis polymerization-induced crystallization-driven self-assembly of metallo-block copolymers. *Chem. Sci.* **2019**, *10*, 9782–9787.
  75. Shin, S.; Menk, F.; Kim, Y.; Lim, J.; Char, K.; Zentel, R.; Choi, T.-L. Living Light-Induced Crystallization-Driven Self-Assembly for Rapid Preparation of Semiconducting Nanofibers. *J. Am. Chem. Soc.* **2018**, *140*, 6088–6094.
  76. Qiu, H.; Gao, Y.; Du, V.A.; Harniman, R.; Winnik, M.A.; Manners, I. Branched Micelles by Living Crystallization-Driven Block Copolymer Self-Assembly under Kinetic Control. *J. Am. Chem. Soc.* **2015**, *137*, 2375–2385.
  77. Hudson, Z.M.; Lunn, D.J.; Winnik, M.A.; Manners, I. Colour-tunable fluorescent multiblock micelles. *Nat. Commun.* **2014**, *5*, 3372.
  78. Jin, X.-H.; Price, M.B.; Finnegan, J.R.; Boott, C.E.; Richter, J.M.; Rao, A.; Menke, S.M.; Friend, R.H.; Whittell, G.R.; Manners, I. Long-range exciton transport in conjugated polymer nanofibers prepared by seeded growth. *Science* **2018**, *360*, 897–900.
  79. Rupar, P.A.; Chabanne, L.; Winnik, M.A.; Manners, I. Non-Centrosymmetric Cylindrical Micelles by Unidirectional Growth. *Science* **2012**, *337*, 559–562.
  80. Xu, J.; Zhou, H.; Yu, Q.; Guerin, G.; Manners, I.; Winnik, M.A. Synergistic self-seeding in one-dimension: A route to patchy and block comicelles with uniform and controllable length. *Chem. Sci.* **2019**, *10*, 2280–2284.
  81. He, X.; He, Y.; Hsiao, M.-S.; Harniman, R.L.; Pearce, S.; Winnik, M.A.; Manners, I. Complex and Hierarchical 2D Assemblies via Crystallization-Driven Self-Assembly of Poly(L-lactide) Homopolymers with Charged Termini. *J. Am. Chem. Soc.* **2017**, *139*, 9221–9228.
  82. He, X.; Hsiao, M.-S.; Boott, C.E.; Harniman, R.L.; Nazemi, A.; Li, X.; Winnik, M.A.; Manners, I. Two-dimensional assemblies from crystallizable homopolymers with charged termini. *Nat. Mater.* **2017**, *16*, 481–488.
  83. Nazemi, A.; He, X.; Macfarlane, L.R.; Harniman, R.L.; Hsiao, M.-S.; Winnik, M.A.; Faul, C.F.J.; Manners, I. Uniform “Patchy” Platelets by Seeded Heteroepitaxial Growth of Crystallizable Polymer Blends in Two Dimensions. *J. Am. Chem. Soc.* **2017**, *139*, 4409–4417.

84. Pearce, S.; He, X.; Hsiao, M.-S.; Harniman, R.L.; Macfarlane, L.R.; Manners, I. Uniform, High-Aspect-Ratio, and Patchy 2D Platelets by Living Crystallization-Driven Self-Assembly of Crystallizable Poly(ferrocenyldimethylsilane)-Based Homopolymers with Hydrophilic Charged Termini. *Macromolecules* **2019**, *52*, 6068–6079.
85. Qiu, H.; Gao, Y.; Boott, C.E.; Gould, O.E.C.; Harniman, R.L.; Miles, M.J.; Webb, S.E.D.; Winnik, M.A.; Manners, I. Uniform patchy and hollow rectangular platelet micelles from crystallizable polymer blends. *Science* **2016**, *352*, 697–701.
86. Inam, M.; Cambridge, G.; Pitto-Barry, A.; Laker, Z.P.L.; Wilson, N.R.; Mathers, R.T.; Dove, A.P.; O'Reilly, R.K. 1D vs. 2D shape selectivity in the crystallization-driven self-assembly of polylactide block copolymers. *Chem. Sci.* **2017**, *8*, 4223–4230.
87. Gould, O.E.; Qiu, H.; Lunn, D.J.; Rowden, J.; Harniman, R.L.; Hudson, Z.M.; Winnik, M.A.; Miles, M.J.; Manners, I. Transformation and patterning of supermicelles using dynamic holographic assembly. *Nat. Commun.* **2015**, *6*, 10009.
88. Qiu, H.; Hudson, Z.M.; Winnik, M.A.; Manners, I. Multidimensional hierarchical self-assembly of amphiphilic cylindrical block comicelles. *Science* **2015**, *347*, 1329–1332.
89. Gädt, T.; Jeong, N.S.; Cambridge, G.; Winnik, M.A.; Manners, I. Complex and hierarchical micelle architectures from diblock copolymers using living, crystallization-driven polymerizations. *Nat. Mater.* **2009**, *8*, 144–150.
90. Hudson, Z.M.; Boott, C.E.; Robinson, M.E.; Rupar, P.A.; Winnik, M.A.; Manners, I. Tailored hierarchical micelle architectures using living crystallization-driven self-assembly in two dimensions. *Nat. Chem.* **2014**, *6*, 893–898.
91. Dou, H.; Li, M.; Qiao, Y.; Harniman, R.; Li, X.; Boott, C.E.; Mann, S.; Manners, I. Higher-order assembly of crystalline cylindrical micelles into membrane-extendable colloidosomes. *Nat. Commun.* **2017**, *8*, 426.
92. Fan, B.; Liu, L.; Li, J.-H.; Ke, X.-X.; Xu, J.-T.; Du, B.-Y.; Fan, Z.-Q. Crystallization-driven one-dimensional self-assembly of polyethylene-*b*-poly(*tert*-butylacrylate) diblock copolymers in DMF: Effects of crystallization temperature and the corona-forming block. *Soft Matter* **2015**, *12*, 67–76.
93. Schmalz, H.; Schmelz, J.; Drechsler, M.; Yuan, J.; Walther, A.; Schweimer, K.; Mihut, A.M. Thermo-Reversible Formation of Wormlike Micelles with a Microphase-Separated Corona from a Semicrystalline Triblock Terpolymer. *Macromolecules* **2008**, *41*, 3235–3242.

- 
94. Schmelz, J.; Karg, M.; Hellweg, T.; Schmalz, H. General Pathway toward Crystalline-Core Micelles with Tunable Morphology and Corona Segregation. *ACS Nano* **2011**, *5*, 9523–9534.
  95. Xiong, H.; Chen, C.-K.; Lee, K.; Van Horn, R.M.; Liu, Z.; Ren, B.; Quirk, R.P.; Thomas, E.L.; Lotz, B.; Ho, R.-M.; et al. Scrolled Polymer Single Crystals Driven by Unbalanced Surface Stresses: Rational Design and Experimental Evidence. *Macromolecules* **2011**, *44*, 7758–7766.
  96. Coe, Z.; Weems, A.; Dove, A.P.; O'Reilly, R.K. Synthesis of Monodisperse Cylindrical Nanoparticles via Crystallization-driven Self-assembly of Biodegradable Block Copolymers. *J. Vis. Exp.* **2019**, *20*, e59772.
  97. Arno, M.C.; Inam, M.; Coe, Z.; Cambridge, G.; MacDougall, L.J.; Keogh, R.; Dove, A.P.; O'Reilly, R.K. Precision Epitaxy for Aqueous 1D and 2D Poly( $\epsilon$ -caprolactone) Assemblies. *J. Am. Chem. Soc.* **2017**, *139*, 16980–16985.
  98. Petzetakis, N.; Dove, A.P.; O'Reilly, R.K. Cylindrical micelles from the living crystallization-driven self-assembly of poly(lactide)-containing block copolymers. *Chem. Sci.* **2011**, *2*, 955–960.
  99. Arno, M.C.; Inam, M.; Weems, A.C.; Li, Z.; Binch, A.L.A.; Platt, C.I.; Richardson, S.M.; Hoyland, J.A.; Dove, A.P.; O'Reilly, R.K. Exploiting the role of nanoparticle shape in enhancing hydrogel adhesive and mechanical properties. *Nat. Commun.* **2020**, *11*, 1–9.
  100. Yu, W.; Inam, M.; Jones, J.R.; Dove, A.P.; O'Reilly, R.K. Understanding the CDSA of poly(lactide) containing triblock copolymers. *Polym. Chem.* **2017**, *8*, 5504–5512.
  101. Tong, Z.; Su, Y.; Jiang, Y.; Xie, Y.; Chen, S.; O'Reilly, R.K. Spatially Restricted Templated Growth of Poly( $\epsilon$ -caprolactone) from Carbon Nanotubes by Crystallization-Driven Self-Assembly. *Macromolecules* **2021**, *54*, 2844–2851.
  102. Finnegan, J.R.; He, X.; Street, S.T.G.; Garcia-Hernandez, J.D.; Hayward, D.W.; Harniman, R.L.; Richardson, R.M.; Whittell, G.R.; Manners, I. Extending the Scope of “Living” Crystallization-Driven Self-Assembly: Well-Defined 1D Micelles and Block Comicelles from Crystallizable Polycarbonate Block Copolymers. *J. Am. Chem. Soc.* **2018**, *140*, 17127–17140.
  103. Rudolph, T.; von der L uhe, M.; Hartlieb, M.; Norsic, S.; Schubert, U.S.; Boisson, C.; D'Agosto, F.; Schacher, F.H. Toward Anisotropic Hybrid Materials: Directional Crystallization of Amphiphilic Polyoxazoline-Based Triblock Terpolymers. *ACS Nano* **2015**, *9*, 10085–10098.

104. Finnegan, J.; Pilkington, E.; Alt, K.; Rahim, A.; Kent, S.J.; Davis, T.P.; Kempe, K. Stealth Nanorods via the Aqueous Living Crystallisation-Driven Self-Assembly of Poly(2-oxazoline)s. *Chem. Sci.* **2021**, doi:10.1039/D1SC00938A.
105. Shaikh, H.; Jin, X.-H.; Harniman, R.L.; Richardson, R.M.; Whittell, G.R.; Manners, I. Solid-State Donor-Acceptor Coaxial Heterojunction Nanowires via Living Crystallization-Driven Self-Assembly. *J. Am. Chem. Soc.* **2020**, *142*, 13469–13480.
106. Folgado, E.; Mayor, M.; Cot, D.; Ramonda, M.; Godiard, F.; Ladmiral, V.; Semsarilar, M. Preparation of well-defined 2D-lenticular aggregates by self-assembly of PNIPAM-*b*-PVDF amphiphilic diblock copolymers in solution. *Polym. Chem.* **2021**, *12*, 1465–1475.
107. Kang, L.; Chao, A.; Zhang, M.; Yu, T.; Wang, J.; Wang, Q.; Yu, H.; Jiang, N.; Zhang, D. Modulating the Molecular Geometry and Solution Self-Assembly of Amphiphilic Polypeptoid Block Copolymers by Side Chain Branching Pattern. *J. Am. Chem. Soc.* **2021**, *143*, 5890–5902.
108. Wei, Y.; Liu, F.; Li, M.; Li, Z.; Sun, J. Dimension control on self-assembly of a crystalline core-forming polypeptoid block copolymer: 1D nanofibers versus 2D nanosheets. *Polym. Chem.* **2021**, *12*, 1147–1154.
109. Kynaston, E.L.; Nazemi, A.; MacFarlane, L.R.; Whittell, G.R.; Faul, C.F.J.; Manners, I. Uniform Polyselenophene Block Copolymer Fiberlike Micelles and Block Comicelles via Living Crystallization-Driven Self-Assembly. *Macromolecules* **2018**, *51*, 1002–1010.
110. Kim, Y.-J.; Cho, C.-H.; Paek, K.; Jo, M.; Park, M.-K.; Lee, N.-E.; Kim, Y.-J.; Kim, B.J.; Lee, E. Precise Control of Quantum Dot Location within the P3HT-*b*-P2VP/QD Nanowires Formed by Crystallization-Driven 1D Growth of Hybrid Dimeric Seeds. *J. Am. Chem. Soc.* **2014**, *136*, 2767–2774.
111. Patra, S.K.; Ahmed, R.; Whittell, G.R.; Lunn, D.J.; Dunphy, E.L.; Winnik, M.A.; Manners, I. Cylindrical Micelles of Controlled Length with a  $\pi$ -Conjugated Polythiophene Core via Crystallization-Driven Self-Assembly. *J. Am. Chem. Soc.* **2011**, *133*, 8842–8845.
112. Li, X.; Wolanin, P.J.; MacFarlane, L.R.; Harniman, R.L.; Qian, J.; Gould, O.E.C.; Dane, T.G.; Rudin, J.; Cryan, M.J.; Schmaltz, T.; et al. Uniform electroactive fibre-like micelle nanowires for organic electronics. *Nat. Commun.* **2017**, *8*, 15909.

- 
113. MacFarlane, L.R.; Shaikh, H.; Garcia-Hernandez, J.D.; Vespa, M.; Fukui, T.; Manners, I. Functional nanoparticles through  $\pi$ -conjugated polymer self-assembly. *Nat. Rev. Mater.* **2021**, *6*, 7–26.
114. Boott, C.E.; Laine, R.F.; Mahou, P.; Finnegan, J.R.; Leitao, E.M.; Webb, S.E.D.; Kaminski, C.F.; Manners, I. In Situ Visualization of Block Copolymer Self-Assembly in Organic Media by Super-Resolution Fluorescence Microscopy. *Chem. Eur. J.* **2015**, *21*, 18539–18542.
115. Wittmann, J.C.; Hodge, A.M.; Lotz, B. Epitaxial crystallization of polymers onto benzoic acid: Polyethylene and paraffins, aliphatic polyesters, and polyamides. *J. Polym. Sci. Polym. Phys. Ed.* **1983**, *21*, 2495–2509.
116. Wittmann, J.C.; Lotz, B. Epitaxial crystallization of polyethylene on organic substrates: A reappraisal of the mode of action of selected nucleating agents. *J. Polym. Sci. Polym. Phys. Ed.* **1981**, *19*, 1837–1851.
117. Wang, H.; Lin, W.; Fritz, K.P.; Scholes, G.D.; Winnik, M.A.; Manners, I. Cylindrical Block Co-Micelles with Spatially Selective Functionalization by Nanoparticles. *J. Am. Chem. Soc.* **2007**, *129*, 12924–12925.
118. Wang, H.; Patil, A.J.; Liu, K.; Petrov, S.; Mann, S.; Winnik, M.A.; Manners, I. Fabrication of Continuous and Segmented Polymer/Metal Oxide Nanowires Using Cylindrical Micelles and Block Comicelles as Templates. *Adv. Mater.* **2009**, *21*, 1805–1808.
119. Rupar, P.A.; Cambridge, G.; Winnik, M.A.; Manners, I. Reversible Cross-Linking of Polyisoprene Coronas in Micelles, Block Comicelles, and Hierarchical Micelle Architectures Using Pt(0)–Olefin Coordination. *J. Am. Chem. Soc.* **2011**, *133*, 16947–16957.
120. Nazemi, A.; Boott, C.E.; Lunn, D.J.; Gwyther, J.; Hayward, D.W.; Richardson, R.M.; Winnik, M.A.; Manners, I. Monodisperse Cylindrical Micelles and Block Comicelles of Controlled Length in Aqueous Media. *J. Am. Chem. Soc.* **2016**, *138*, 4484–4493.
121. Qiu, H.; Cambridge, G.; Winnik, M.A.; Manners, I. Multi-Armed Micelles and Block Co-micelles via Crystallization-Driven Self-Assembly with Homopolymer Nanocrystals as Initiators. *J. Am. Chem. Soc.* **2013**, *135*, 12180–12183.
122. He, F.; Gädt, T.; Manners, I.; Winnik, M.A. Fluorescent “Barcode” Multiblock Co-Micelles via the Living Self-Assembly of Di- and Triblock Copolymers with a Crystalline Core-Forming Metalloblock. *J. Am. Chem. Soc.* **2011**, *133*, 9095–9103.

123. Street, S.T.G.; He, Y.; Jin, X.-H.; Hodgson, L.; Verkade, P.; Manners, I. Cellular uptake and targeting of low dispersity, dual emissive, segmented block copolymer nanofibers. *Chem. Sci.* **2020**, *11*, 8394–8408.
124. He, X.; Finnegan, J.R.; Hayward, D.W.; MacFarlane, L.R.; Harniman, R.L.; Manners, I. Living Crystallization-Driven Self-Assembly of Polymeric Amphiphiles: Low-Dispersity Fiber-like Micelles from Crystallizable Phosphonium-Capped Polycarbonate Homopolymers. *Macromolecules* **2020**, *53*, 10591–10600.
125. Qian, J.; Li, X.; Lunn, D.J.; Gwyther, J.; Hudson, Z.M.; Kynaston, E.; Rupar, P.A.; Winnik, M.A.; Manners, I. Uniform, High Aspect Ratio Fiber-like Micelles and Block Co-micelles with a Crystalline  $\pi$ -Conjugated Polythiophene Core by Self-Seeding. *J. Am. Chem. Soc.* **2014**, *136*, 4121–4124.
126. Tao, D.; Feng, C.; Cui, Y.; Yang, X.; Manners, I.; Winnik, M.A.; Huang, X. Monodisperse Fiber-like Micelles of Controlled Length and Composition with an Oligo(*p*-phenylenevinylene) Core via “Living” Crystallization-Driven Self-Assembly. *J. Am. Chem. Soc.* **2017**, *139*, 7136–7139.
127. Tao, D.; Wang, Z.; Huang, X.; Tian, M.; Lu, G.; Manners, I.; Winnik, M.A.; Feng, C. Continuous and Segmented Semiconducting Fiber-like Nanostructures with Spatially Selective Functionalization by Living Crystallization-Driven Self-Assembly. *Angew. Chem. Int. Ed.* **2020**, *59*, 8232–8239.
128. He, Y.; Eloi, J.-C.; Harniman, R.L.; Richardson, R.M.; Whittell, G.R.; Mathers, R.T.; Dove, A.P.; O’Reilly, R.K.; Manners, I. Uniform Biodegradable Fiber-Like Micelles and Block Comicelles via “Living” Crystallization-Driven Self-Assembly of Poly(L-lactide) Block Copolymers: The Importance of Reducing Unimer Self-Nucleation via Hydrogen Bond Disruption. *J. Am. Chem. Soc.* **2019**, *141*, 19088–19098.
129. Lunn, D.J.; Gould, O.E.C.; Whittell, G.R.; Armstrong, D.P.; Mineart, K.P.; Winnik, M.A.; Spontak, R.J.; Pringle, P.G.; Manners, I. Microfibres and macroscopic films from the coordination-driven hierarchical self-assembly of cylindrical micelles. *Nat. Commun.* **2016**, *7*, 12371.
130. Li, X.; Gao, Y.; Boott, C.E.; Hayward, D.W.; Harniman, R.; Whittell, G.R.; Richardson, R.M.; Winnik, M.A.; Manners, I. “Cross” Supermicelles via the Hierarchical Assembly of Amphiphilic Cylindrical Triblock Comicelles. *J. Am. Chem. Soc.* **2016**, *138*, 4087–4095.
131. Qiu, H.; Russo, G.; Rupar, P.A.; Chabanne, L.; Winnik, M.A.; Manners, I. Tunable Supermicelle Architectures from the Hierarchical Self-Assembly of Amphiphilic

- Cylindrical B-A-B Triblock Co-Micelles. *Angew. Chem. Int. Ed.* **2012**, *51*, 11882–11885.
132. Li, X.; Gao, Y.; Boott, C.E.; Winnik, M.A.; Manners, I. Non-covalent synthesis of supermicelles with complex architectures using spatially confined hydrogen-bonding interactions. *Nat. Commun.* **2015**, *6*, 8127.
133. Li, X.; Gao, Y.; Harniman, R.; Winnik, M.; Manners, I. Hierarchical Assembly of Cylindrical Block Comicelles Mediated by Spatially Confined Hydrogen-Bonding Interactions. *J. Am. Chem. Soc.* **2016**, *138*, 12902–12912.
134. Schmelz, J.; Schacher, F.H.; Schmalz, H. Cylindrical crystalline-core micelles: Pushing the limits of solution self-assembly. *Soft Matter* **2013**, *9*, 2101–2107.
135. Rosenfeldt, S.; Lüdel, F.; Schulreich, C.; Hellweg, T.; Radulescu, A.; Schmelz, J.; Schmalz, H.; Harnau, L. Patchy worm-like micelles: Solution structure studied by small-angle neutron scattering. *Phys. Chem. Chem. Phys.* **2012**, *14*, 12750–12756.
136. Schmelz, J.; Schmalz, H. Corona structure on demand: Tailor-made surface compartmentalization in worm-like micelles via random cocrystallization. *Polymer* **2012**, *53*, 4333–4337.
137. Schöbel, J.; Karg, M.; Rosenbach, D.; Krauss, G.; Greiner, A.; Schmalz, H. Patchy Wormlike Micelles with Tailored Functionality by Crystallization-Driven Self-Assembly: A Versatile Platform for Mesostructured Hybrid Materials. *Macromolecules* **2016**, *49*, 2761–2771.
138. Schöbel, J.; Hils, C.; Weckwerth, A.; Schlenk, M.; Bojer, C.; Stuart, M.C.A.; Brey, J.; Förster, S.; Greiner, A.; Karg, M.; et al. Strategies for the selective loading of patchy worm-like micelles with functional nanoparticles. *Nanoscale* **2018**, *10*, 18257–18268.
139. Gegenhuber, T.; Gröschel, A.H.; Löbbling, T.I.; Drechsler, M.; Ehlert, S.; Förster, S.; Schmalz, H. Noncovalent Grafting of Carbon Nanotubes with Triblock Terpolymers: Toward Patchy 1D Hybrids. *Macromolecules* **2015**, *48*, 1767–1776.
140. Oliver, A.M.; Gwyther, J.; Winnik, M.A.; Manners, I. Cylindrical Micelles with “Patchy” Coronas from the Crystallization-Driven Self-Assembly of ABC Triblock Terpolymers with a Crystallizable Central Polyferrocenyldimethylsilane Segment. *Macromolecules* **2017**, *51*, 222–231.
141. Oliver, A.M.; Spontak, R.J.; Manners, I. Solution self-assembly of ABC triblock terpolymers with a central crystallizable poly(ferrocenyldimethylsilane) core-forming segment. *Polym. Chem.* **2019**, *10*, 2559–2569.

142. Nunns, A.; Whittell, G.R.; Winnik, M.A.; Manners, I. Crystallization-Driven Solution Self-Assembly of  $\mu$ -ABC Miktoarm Star Terpolymers with Core-Forming Polyferrocenylsilane Blocks. *Macromolecules* **2014**, *47*, 8420–8428.
143. Finnegan, J.R.; Lunn, D.J.; Gould, O.E.C.; Hudson, Z.M.; Whittell, G.R.; Winnik, M.A.; Manners, I. Gradient Crystallization-Driven Self-Assembly: Cylindrical Micelles with “Patchy” Segmented Coronas via the Coassembly of Linear and Brush Block Copolymers. *J. Am. Chem. Soc.* **2014**, *136*, 13835–13844.
144. Cruz, M.; Xu, J.; Yu, Q.; Guerin, G.; Manners, I.; Winnik, M.A. Visualizing Nanoscale Coronal Segregation in Rod-Like Micelles Formed by Co-Assembly of Binary Block Copolymer Blends. *Macromol. Rapid Commun.* **2018**, *39*, 1800397.
145. Xu, J.; Zhou, H.; Yu, Q.; Manners, I.; Winnik, M.A. Competitive Self-Assembly Kinetics as a Route To Control the Morphology of Core-Crystalline Cylindrical Micelles. *J. Am. Chem. Soc.* **2018**, *140*, 2619–2628.
146. Song, S.; Liu, X.; Nikbin, E.; Howe, J.Y.; Yu, Q.; Manners, I.; Winnik, M.A. Uniform 1D Micelles and Patchy & Block Comicelles via Scalable, One-Step Crystallization-Driven Block Copolymer Self-Assembly. *J. Am. Chem. Soc.* **2021**, *143*, 6266–6280.
147. Bahrami, R.; Löbbling, T.I.; Gröschel, A.H.; Schmalz, H.; Müller, A.H.E.; Altstädt, V. The Impact of Janus Nanoparticles on the Compatibilization of Immiscible Polymer Blends under Technologically Relevant Conditions. *ACS Nano* **2014**, *8*, 10048–10056.
148. Bärwinkel, S.; Bahrami, R.; Löbbling, T.I.; Schmalz, H.; Müller, A.H.E.; Altstädt, V. Polymer Foams Made of Immiscible Polymer Blends Compatibilized by Janus Particles-Effect of Compatibilization on Foam Morphology. *Adv. Eng. Mater.* **2016**, *18*, 814–825.
149. Yang, Q.; Loos, K. Janus nanoparticles inside polymeric materials: Interfacial arrangement toward functional hybrid materials. *Polym. Chem.* **2017**, *8*, 641–654.
150. Bahrami, R.; Löbbling, T.I.; Schmalz, H.; Müller, A.H.E.; Altstädt, V. Synergistic effects of Janus particles and triblock terpolymers on toughness of immiscible polymer blends. *Polymer* **2017**, *109*, 229–237.
151. Walther, A.; André, X.; Drechsler, M.; Abetz, V.; Müller, A.H.E. Janus Discs. *J. Am. Chem. Soc.* **2007**, *129*, 6187–6198.
152. Bryson, K.C.; Löbbling, T.I.; Müller, A.H.E.; Russell, T.P.; Hayward, R.C. Using Janus Nanoparticles To Trap Polymer Blend Morphologies during Solvent-Evaporation-Induced Demixing. *Macromolecules* **2015**, *48*, 4220–4227.

- 
153. Ruhland, T.M.; Gröschel, A.H.; Walther, A.; Müller, A.H.E. Janus Cylinders at Liquid–Liquid Interfaces. *Langmuir* **2011**, *27*, 9807–9814.
  154. Walther, A.; Drechsler, M.; Müller, A.H.E. Structures of amphiphilic Janus discs in aqueous media. *Soft Matter* **2009**, *5*, 385–390.
  155. Walther, A.; Matussek, K.; Müller, A.H.E. Engineering Nanostructured Polymer Blends with Controlled Nanoparticle Location using Janus Particles. *ACS Nano* **2008**, *2*, 1167–1178.
  156. Walther, A.; Hoffmann, M.; Müller, A.H.E. Emulsion Polymerization Using Janus Particles as Stabilizers. *Angew. Chem. Int. Ed.* **2008**, *47*, 711–714.
  157. Ruhland, T.M.; Gröschel, A.H.; Ballard, N.; Skelhon, T.S.; Walther, A.; Müller, A.H.E.; Bon, S.A.F. Influence of Janus Particle Shape on Their Interfacial Behavior at Liquid–Liquid Interfaces. *Langmuir* **2013**, *29*, 1388–1394.
  158. Gröschel, A.H.; Löbbling, T.I.; Petrov, P.D.; Müllner, M.; Kuttner, C.; Wieberger, F.; Müller, A.H.E. Janus Micelles as Effective Supracolloidal Dispersants for Carbon Nanotubes. *Angew. Chem. Int. Ed.* **2013**, *52*, 3602–3606.
  159. Schmelz, J.; Pirner, D.; Krekhova, M.; Ruhland, T.M.; Schmalz, H. Interfacial activity of patchy worm-like micelles. *Soft Matter* **2013**, *9*, 11173–11177.
  160. Böker, A.; He, J.; Emrick, T.; Russell, T.P. Self-assembly of nanoparticles at interfaces. *Soft Matter* **2007**, *3*, 1231–1248.
  161. Dai, X.; Qiang, X.; Hils, C.; Schmalz, H.; Gröschel, A.H. Frustrated Microparticle Morphologies of a Semicrystalline Triblock Terpolymer in 3D Soft Confinement. *ACS Nano* **2021**, *15*, 1111–1120.
  162. Gegenhuber, T.; Krekhova, M.; Schöbel, J.; Gröschel, A.H.; Schmalz, H. “Patchy” Carbon Nanotubes as Efficient Compatibilizers for Polymer Blends. *ACS Macro Lett.* **2016**, *5*, 306–310.
  163. Ruhland, T.M. *Janus Cylinders at Interfaces*; University of Bayreuth: Bayreuth, Germany, 2009.
  164. Haruta, M. When Gold Is Not Noble: Catalysis by Nanoparticles. *Chem. Rec.* **2003**, *3*, 75–87.
  165. Daniel, M.-C.; Astruc, D. Gold Nanoparticles: Assembly, Supramolecular Chemistry, Quantum-Size-Related Properties, and Applications toward Biology, Catalysis, and Nanotechnology. *Chem. Rev.* **2004**, *104*, 293–346.
  166. Shenhar, R.; Norsten, T.B.; Rotello, V.M. Polymer-Mediated Nanoparticle Assembly: Structural Control and Applications. *Adv. Mater.* **2005**, *17*, 657–669.

167. Campelo, J.M.; Luna, D.; Luque, R.; Marinas, J.M.; Romero, A.A. Sustainable Preparation of Supported Metal Nanoparticles and Their Applications in Catalysis. *ChemSusChem* **2009**, *2*, 18–45.
168. Rycenga, M.; Cogley, C.M.; Zeng, J.; Li, W.; Moran, C.H.; Zhang, Q.; Qin, D.; Xia, Y. Controlling the Synthesis and Assembly of Silver Nanostructures for Plasmonic Applications. *Chem. Rev.* **2011**, *111*, 3669–3712.
169. Giljohann, D.A.; Seferos, D.S.; Daniel, W.L.; Massich, M.D.; Patel, P.C.; Mirkin, C.A. Gold Nanoparticles for Biology and Medicine. *Angew. Chem. Int. Ed.* **2010**, *49*, 3280–3294.
170. Dykman, L.; Khlebtsov, N. Gold nanoparticles in biomedical applications: Recent advances and perspectives. *Chem. Soc. Rev.* **2011**, *41*, 2256–2282.
171. Saha, K.; Agasti, S.S.; Kim, C.; Li, X.; Rotello, V.M. Gold Nanoparticles in Chemical and Biological Sensing. *Chem. Rev.* **2012**, *112*, 2739–2779.
172. Astruc, D.; Lu, F.; Aranzaes, J.R. Nanoparticles as Recyclable Catalysts: The Frontier between Homogeneous and Heterogeneous Catalysis. *Angew. Chem. Int. Ed.* **2005**, *44*, 7852–7872.
173. Burda, C.; Chen, X.; Narayanan, R.; El-Sayed, M.A. Chemistry and Properties of Nanocrystals of Different Shapes. *Chem. Rev.* **2005**, *105*, 1025–1102.
174. Murphy, C.J.; Sau, T.K.; Gole, A.M.; Orendorff, C.J.; Gao, J.; Gou, L.; Hunyadi, S.E.; Li, T. Anisotropic Metal Nanoparticles: Synthesis, Assembly, and Optical Applications. *J. Phys. Chem. B* **2005**, *109*, 13857–13870.
175. Lu, A.-H.; Salabas, E.-L.; Schüth, F. Magnetic Nanoparticles: Synthesis, Protection, Functionalization, and Application. *Angew. Chem. Int. Ed.* **2007**, *46*, 1222–1244.
176. Wang, J.; Li, W.; Zhu, J. Encapsulation of inorganic nanoparticles into block copolymer micellar aggregates: Strategies and precise localization of nanoparticles. *Polymer* **2014**, *55*, 1079–1096.
177. Zhou, T.; Dong, B.; Qi, H.; Mei, S.; Li, C.Y. Janus hybrid hairy nanoparticles. *J. Polym. Sci. Part B Polym. Phys.* **2014**, *52*, 1620–1640.
178. Zhang, Y.; Pearce, S.; Eloi, J.-C.; Harniman, R.L.; Tian, J.; Cordoba, C.; Kang, Y.; Fukui, T.; Qiu, H.; Blackburn, A.; et al. Dendritic Micelles with Controlled Branching and Sensor Applications. *J. Am. Chem. Soc.* **2021**, *143*, 5805–5814.
179. Liu, L.; Corma, A. Metal Catalysts for Heterogeneous Catalysis: From Single Atoms to Nanoclusters and Nanoparticles. *Chem. Rev.* **2018**, *118*, 4981–5079.

- 
180. Van Deelen, T.W.; Mejía, C.H.; de Jong, K.P. Control of metal-support interactions in heterogeneous catalysts to enhance activity and selectivity. *Nat. Catal.* **2019**, *2*, 955–970.
181. Li, Z.; Ji, S.; Liu, Y.; Cao, X.; Tian, S.; Chen, Y.; Niu, Z.; Li, Y. Well-Defined Materials for Heterogeneous Catalysis: From Nanoparticles to Isolated Single-Atom Sites. *Chem. Rev.* **2020**, *120*, 623–682.
182. Ishida, T.; Murayama, T.; Taketoshi, A.; Haruta, M. Importance of Size and Contact Structure of Gold Nanoparticles for the Genesis of Unique Catalytic Processes. *Chem. Rev.* **2019**, *120*, 464–525.
183. Shifrina, Z.B.; Matveeva, V.G.; Bronstein, L.M. Role of Polymer Structures in Catalysis by Transition Metal and Metal Oxide Nanoparticle Composites. *Chem. Rev.* **2020**, *120*, 1350–1396.
184. Cai, J.; Li, C.; Kong, N.; Lu, Y.; Lin, G.; Wang, X.; Yao, Y.; Manners, I.; Qiu, H. Tailored multifunctional micellar brushes via crystallization-driven growth from a surface. *Science* **2019**, *366*, 1095–1098.
185. Astruc, D. Introduction: Nanoparticles in Catalysis. *Chem. Rev.* **2020**, *120*, 461–463.
186. Hils, C.; Dulle, M.; Sitaru, G.; Gekle, S.; Schöbel, J.; Frank, A.; Drechsler, M.; Greiner, A.; Schmalz, H. Influence of patch size and chemistry on the catalytic activity of patchy hybrid nonwovens. *Nanoscale Adv.* **2020**, *2*, 438–452.
187. Schöbel, J.; Burgard, M.; Hils, C.; Dersch, R.; Dulle, M.; Volk, K.; Karg, M.; Greiner, A.; Schmalz, H. Bottom-Up Meets Top-Down: Patchy Hybrid Nonwovens as an Efficient Catalysis Platform. *Angew. Chem. Int. Ed.* **2016**, *56*, 405–408.
188. Mitschang, F.; Schmalz, H.; Agarwal, S.; Greiner, A. Tea-Bag-Like Polymer Nanoreactors Filled with Gold Nanoparticles. *Angew. Chem. Int. Ed.* **2014**, *53*, 4972–4975.
189. Taguchi, T.; Isozaki, K.; Miki, K. Enhanced Catalytic Activity of Self-Assembled Monolayer-Capped Gold Nanoparticles. *Adv. Mater.* **2012**, *24*, 6462–6467.
190. Raffa, P.; Evangelisti, C.; Vitulli, G.; Salvadori, P. First examples of gold nanoparticles catalyzed silane alcoholysis and silylative pinacol coupling of carbonyl compounds. *Tetrahedron Lett.* **2008**, *49*, 3221–3224.
191. Mitsudome, T.; Yamamoto, Y.; Noujima, A.; Mizugaki, T.; Jitsukawa, K.; Kaneda, K. Highly Efficient Etherification of Silanes by Using a Gold Nanoparticle Catalyst: Remarkable Effect of O<sub>2</sub>. *Chem. Eur. J.* **2013**, *19*, 14398–14402.

- 
192. Kronawitt, J.; Dulle, M.; Schmalz, H.; Agarwal, S.; Greiner, A. Poly(*p*-xylylene) Nanotubes Decorated with Nonagglomerated Gold Nanoparticles for the Alcoholysis of Dimethylphenylsilane. *ACS Appl. Nano Mater.* **2020**, *3*, 2766–2773.
  193. Isozaki, K.; Taguchi, T.; Ishibashi, K.; Shimoaka, T.; Kurashige, W.; Negishi, Y.; Hasegawa, T.; Nakamura, M.; Miki, K. Mechanistic Study of Silane Alcoholysis Reactions with Self-Assembled Monolayer-Functionalized Gold Nanoparticle Catalysts. *Catalysts* **2020**, *10*, 908.
  194. Hils, C.; Fuchs, E.; Eger, F.; Schöbel, J.; Schmalz, H. Converting Poly(Methyl Methacrylate) into a Triple-Responsive Polymer. *Chem. Eur. J.* **2020**, *26*, 5611–5614.



## **(Eidesstattliche) Versicherungen und Erklärungen**

(§ 9 Satz 2 Nr. 3 PromO BayNAT)

*Hiermit versichere ich eidesstattlich, dass ich die Arbeit selbstständig verfasst und keine anderen als die von mir angegebenen Quellen und Hilfsmittel benutzt habe (vgl. Art. 64 Abs. 1 Satz 6 BayHSchG).*

(§ 9 Satz 2 Nr. 3 PromO BayNAT)

*Hiermit erkläre ich, dass ich die Dissertation nicht bereits zur Erlangung eines akademischen Grades eingereicht habe und dass ich nicht bereits diese oder eine gleichartige Doktorprüfung endgültig nicht bestanden habe.*

(§ 9 Satz 2 Nr. 4 PromO BayNAT)

*Hiermit erkläre ich, dass ich Hilfe von gewerblichen Promotionsberatern bzw. -vermittlern oder ähnlichen Dienstleistern weder bisher in Anspruch genommen habe noch künftig in Anspruch nehmen werde.*

(§ 9 Satz 2 Nr. 7 PromO BayNAT)

*Hiermit erkläre ich mein Einverständnis, dass die elektronische Fassung meiner Dissertation unter Wahrung meiner Urheberrechte und des Datenschutzes einer gesonderten Überprüfung unterzogen werden kann.*

(§ 9 Satz 2 Nr. 8 PromO BayNAT)

*Hiermit erkläre ich mein Einverständnis, dass bei Verdacht wissenschaftlichen Fehlverhaltens Ermittlungen durch universitätsinterne Organe der wissenschaftlichen Selbstkontrolle stattfinden können.*

.....  
Ort, Datum, Unterschrift